

Soil properties from seismic intrinsic dispersion

Soil properties from seismic intrinsic dispersion

PROEFSCHRIFT

ter verkrijging van de graad van doctor
aan de Technische Universiteit Delft,
op gezag van de Rector Magnificus prof.ir. K.C.A.M. Luyben,
voorzitter van het College voor Promoties,
in het openbaar te verdedigen op donderdag 15 mei 2014 om 12:30 uur

door Alimzhan Sabyrzhhanovich ZHUBAYEV

Master of Physics and Applied Mathematics MIPT
Bachelor of Physics and Applied Mathematics MIPT
(Moscow Institute of Physics and Technology, Moscow, Russia)
geboren te Aktobe, Kazachstan.

Dit proefschrift is goedgekeurd door de promotoren:
Prof.dr.ir. C.P.A. Wapenaar

Copromotor:
Dr. R. Ghose

Samenstelling promotiecommissie:

Rector Magnificus,	Technische Universiteit Delft, voorzitter
Prof.dr.ir. C.P.A. Wapenaar,	Technische Universiteit Delft, promotor
Dr. R. Ghose,	Technische Universiteit Delft, copromotor
Prof.dr.ir. D.M.J. Smeulders,	Technische Universiteit Eindhoven
Prof.dr. K. Holliger,	Univeriste de Lausanne
Prof.dr. R.J. Schotting,	Universiteit Utrecht
Dr. J. van Deen,	Deltares
Prof.dr. C. Jommi,	Technische Universiteit Delft

This work is financially supported by Deltares and the Delft Earth research programme of the Delft University of Technology.

ISBN 978-90-8891-883-4

© 2014 by A.S. Zhubayev. Some rights reserved. Chapter 4.2 is reproduced by permission of the Acoustical Society of America (Zhubayev & Ghose, 2012a). Chapter 5 is reproduced by permission of the European Association of Geoscientists and Engineers (Zhubayev & Ghose, 2012b). No part of this publication may be reproduced or distributed in any form or by any means, or stored in a database or retrieval system, without the prior written permission of the publishers.

Published by: Uitgeverij BOX Press, Oisterwijk, The Netherlands
Printed by: Proefschriftmaken.nl
Cover by: Alimzhan Zhubayev and Alex Kirichek

Dedicated to my friend, Adilet Imambekov

Adilet Imambekov



Adilet Imambekov

was a brilliant young physicist in the field of quantum many-body physics. Adilet has influenced and inspired many of us who were lucky to know him. On 18th July 2012 Adilet passed away while climbing Khan Tengri mountain in Kyrgyzstan.

Adilet was born in 1981 and spent his childhood in Zhambyl and Almaty, Kazakhstan. At the age of 15, Adilet moved to Moscow, after winning National Kazakhstan physics and mathematics competitions. In Moscow, he continued his study in one of the best science high school in the former Soviet Union—Kolmogorov Physics and Math-

ematics High School. He graduated the school with the highest honors and was the only student of the school to receive a gold medal in 14 years. In 1997 and 1998 he won the National Russian Physics Olympiad, and a Gold Medal at the International Physics Olympiad (IPhO) held in Reykjavik, Iceland in 1998. The same year, Adilet received two awards from Presidents of Russian Federation and Kazakhstan for extraordinary successes in high school studies.

Adilet continued his Bachelor studies in Moscow Institute of Physics and Technology (MIPT) at the Department of General and Applied Physics. During his years at MIPT, Adilet seriously started to develop his knowledge in the field of theoretical physics at the Theoretical Group of Landau Institute, where he passed several exams of the challenging Landau's Theoretical Minimum. The most notable awards during his bachelor studies in MIPT are ISSEP (Soros) Student Fellowship (1998–1999) and Landau Prize (2000–2001). Adilet received Bachelor's degree *summa cum laude* in 2002 and published his first research article in the Journal of Experimental and Theoretical Physics (JETP) Letters the same year.

After bachelor studies, being invited to world top universities including Caltech, Harvard, MIT, Princeton, Stanford, UC Berkeley, Adilet joined Condensed Matter Theory Group of Harvard University to pursue his PhD degree in physics in 2002. During PhD studies at Harvard, by combining deep physical understanding and

mathematical skills, Adilet made his first important contribution to physics of cold atoms. He received Purcell Fellowship of Harvard University (2002–2003).

After obtaining a PhD degree in physics, Adilet continued his research as a postdoc at Yale University in 2007, where he became interested in the dynamics of one-dimensional quantum liquids. He made a crucial contribution in building a nonlinear Luttinger liquid theory. These results were published in *Science* in 2009.

Adilet joined Rice University as Assistant Professor of Physics and Astronomy in 2009. During his tenure-track position at Rice, Adilet received two prestigious awards—A.P. Sloan Foundation Research Fellowship (2010–2012) and National Science Foundation Career Award.

In spite of his short career, Adilet made a tremendous contribution to science and physical society. He authored and coauthored thirty two research articles in top physics journals such as *JETP Lett.*, *Ann. Phys.*, *Rev. Mod. Phys.*, *New J. Phys.*, *Phys. Rev. A*, *Phys. Rev. B*, *Phys. Rev. X*, *Phys. Rev. Lett.*, *Nature*, and *Science*.

Besides his intense passion for physics, Adilet was an avid marathoner, triathlete, cyclist and mountain climber. He climbed Muztagh Ata, the second highest (7546 m) of the mountains which form the northern edge of the Tibetan Plateau. Adilet won his full Ironman triathlon competition in May, 2012 (swim: 1h44m15s, bike/cycle: 5h51m57s and run: 4h10m24s, total time: 11h52m33s). He was also a dedicated husband and a father of two kids.

Adilet was like a brother to me who significantly influenced my life and development. His exceptional advice and wise guidance were always invaluable. Adilet, you will be always in my heart.

Articles in memory of Adilet Imambekov can be found in
Physics Today 66(4), 68 (2013) by Abanin et al., and
<http://ufn.ru/dates/inmemoria/imambekov.pdf>

Contents

Adilet Imambekov	vii
1 Introduction	1
1.1 Background and Motivation	1
1.2 Research objectives and outline of the thesis	4
2 Seismic wave propagation in unconsolidated granular earth materials	7
2.1 Introduction	7
2.2 The principle of least action	8
2.3 Dissipative forces in Lagrange's mechanics	9
2.3.1 Macroscopic Lagrange's equations for fluid-saturated elastic solids: Biot's theory	10
2.3.2 The Biot-Stoll model	14
2.3.3 The Biot-Stoll model with contact squirt flow and shear drag	15
2.4 Wave propagation in partially saturated granular earth materials . .	19
2.4.1 Effective fluid model	19
2.4.2 Patchy saturation	21
2.5 Conclusions	23
3 Stress-dependent seismic dispersion in unconsolidated TI media	25
3.1 Introduction	25
3.2 Stress-dependent seismic dispersion in TI media	26
3.2.1 Stress-dependent elastic moduli	27
3.2.2 Stress-dependent transport properties	30
3.2.3 Numerical tests	35
3.3 Conclusions	37
3.4 Appendix A: Coefficients and roots of cubic equation	39
4 Contrasting behaviour between dispersive seismic velocity and attenuation: Advantages in subsoil characterization	41
4.1 Introduction	41
4.2 Fully saturated media	42

4.2.1	Porosity and permeability from integrated velocity and attenuation dispersion	42
4.2.2	Effective stress and permeability from integrated velocity and attenuation dispersion: TI media	48
4.3	Partially saturated media	52
4.3.1	Porosity and water saturation from dispersive velocity and attenuation: effective-fluid model	52
4.3.2	Porosity and water saturation from elastic P - and S -wave velocity integration: effective-fluid model	53
4.3.3	Porosity and water saturation from elastic P - and S -wave velocity integration: patchy saturation model	56
4.3.4	Porosity and water saturation from integrated seismic and GPR velocities	58
4.4	Conclusions	61
5	Physics of shear-wave intrinsic dispersion and estimation of in-situ soil properties: a synthetic VSP appraisal	63
5.1	Introduction	63
5.2	Physics of S -wave intrinsic dispersion in water-saturated soils	64
5.3	Tests on poroelastic synthetic VSP data	68
5.3.1	Generation of synthetic poroelastic VSP data	69
5.3.2	Estimation of layer-specific intrinsic dispersion from VSP data: effect on n and k estimates	71
5.3.3	Noisy data and error in estimated dispersion: effect on n and k estimates	79
5.3.4	Error in model: effect on n and k estimates	83
5.4	Discussion	87
5.5	Conclusions	88
6	Global optimization to obtain soil properties using poroelasticity theory	89
6.1	Introduction	89
6.2	Optimization	90
6.2.1	Cost function	92
6.2.2	Coordinate rotation	92
6.2.3	Simulated annealing	95
6.2.4	Is viscosity change discernible?	99
6.3	Application to field database of shear wave dispersion	99
6.3.1	Dispersion in field database	99
6.3.2	Results and discussion	102
6.4	Conclusions	106
7	Soil properties from S-wave dispersion: tests on shallow downhole field data	109
7.1	Introduction	109

7.2	<i>k</i> and <i>n</i> from <i>S</i> -wave dispersion: effect of noise and unknown parameter values	110
7.3	Field experiment	112
7.3.1	Estimating dispersion	112
7.3.2	Results and discussion	113
7.4	Conclusions	118
8	Seismic signatures of fluid mobility: Field observation	119
8.1	Introduction	119
8.2	Field zero-offset VSP and well log measurements	122
8.3	Estimation of effective attenuation and velocity dispersion from VSP data	122
8.4	<i>P</i> -wave velocities from VSP and sonic log data	126
8.5	Estimation of scattering attenuation	128
8.6	Intrinsic attenuation in high- and low-mobility zones	130
8.7	Poroelastic inversion using a rotated coordinate system and simulated annealing	131
8.7.1	Forward model	131
8.7.2	Cost-function	133
8.7.3	Estimation of rotated coordinates and parameter bounds	133
8.7.4	Inversion results and discussion	137
8.8	Conclusions	138
9	Conclusions	141
Bibliography		145
Summary		155
Samenvatting		157
Acknowledgments		160
Curriculum Vitae		163

Chapter 1

Introduction

1.1 Background and Motivation

The majority of solid earth materials have some internal structures. This is because these materials are composed of different components such as sand, concrete and interacting fluids. Materials such as soil and rocks may contain micro-cracks and isolated and/or interconnected pores. These cracks and pores can be empty, but generally they are partly or fully saturated with fluids such as water, oil, gas etc.

In general, the physical behaviour of dry granular materials can be explained with relative success by means of continuum mechanics. It disregards the internal cracky-porous structures of the media by replacing them with some average or effective characteristics.

However, classical continuum mechanics, dealing with only a single material component, in principle, cannot model the filtration processes which may occur due to the relative motion between the fluid and the solid phases. This leads to the necessity of a combined consideration of mechanics and thermodynamics of a heterogeneous medium. In fact, the fluid motion in such a system is not purely mechanical. However, this motion can still be described by Lagrange's equations, if the frequencies of the mechanical oscillations are small compared to the characteristic dissipation frequencies in the medium. This yields the equation of motion for wave propagation in a fluid-saturated medium.

In general, there are three main challenges in the study and utilization of wave propagation in porous materials:

1. understanding better the underlying physics that convert mechanical energy into heat in a porous medium (forward modelling),
2. measuring reliably seismic dispersion (i.e., frequency-dependent seismic velocity and attenuation) in a broad frequency range (field and laboratory measurements),
3. developing robust methodologies for quantitative material characterization (inverse problems).

The theory of seismic wave propagation in fluid-saturated porous media was first presented by Frenkel (1944) who was investigating the seismoelectric phenomenon caused by elastic wave propagation through a moist soil. He was the first to predict the existence of a second or slow compressional (P) wave. Subsequently, an extensive investigation on the nature of the second P wave was carried out by Biot (1956a,b, 1962). Importantly, by introducing the concept of wave-induced capillary flow in the porous material, Biot arrived at the characteristic equations for wave propagation in a fluid-filled medium. In this way, the mechanics and thermodynamics were intrinsically coupled. Biot provided a general framework to link seismic measurements to soil/rock properties. It is now well-known that Biot loss mechanism can predict rather well the seismic velocity dispersion, but it greatly underestimates seismic attenuation in both soils and rocks.

The Biot theory has been subjected to critical investigations in relation to its applicability to unconsolidated (e.g., soft soil, marine sediments) and consolidated (e.g., sandstones, siltstones, shale, mudstones) formations. Concerning unconsolidated sediments, which are commonly encountered in shallow land or shallow marine environments, extensive numerical and experimental studies of the loss mechanisms responsible for seismic attenuation and dispersion have been performed by many researchers (e.g., Stoll, 1977; Hamilton, 1980; Hovem & Ingram, 1979; Holland & Brunson, 1988; Buchanan, 2006; Chotiros & Isakson, 2004; Buchanan, 2006; Buckingham, 2004; Leurer, 1997). Most of these studies suggest that in addition to viscous loss due to capillary flow at macro scale (Biot loss), additional global friction losses in the skeletal frame possibly take place (Stoll, 1977). To explain the relatively high level of seismic attenuation, Chotiros & Isakson (2004), on the other hand, argue that the wave-induced squirt flow (grain or micro scale loss) between the sand grains can be an important mechanism, due to the loose nature of the unconsolidated coarse-grained sand or gravel. To justify the broadband attenuation in water-saturated fine-grained marine sediments, Leurer (1997) proposed an “effective grain model”, where the single elastic solid grain is replaced by an effective medium made up of solid grain and low-aspect-ratio inclusions representing the intracrystalline water layers in the swelling clay minerals. The validity of these mechanisms has been tested against field and laboratory experimental data.

Concerning experimental studies on unconsolidated sediments, extensive investigation of intrinsic acoustic (P -wave) dispersion has been directed to marine sediments with operational frequencies between 1 kHz and 500 kHz (e.g., Stoll, 1977; Hamilton, 1980; Holland & Brunson, 1988; Buchanan, 2006; Buckingham, 2004; Leurer, 1997). Such high frequencies are not encountered in land seismic measurements. At the same time, dispersion of shear waves (S) has received little attention and only a few studies have looked at its frequency-dependent attenuation and dispersion (e.g., Stoll, 2002; Bowles, 1997). In the context of unconsolidated soils in land environment, there are few investigations related to frequency-dependent S -wave velocity and attenuation (e.g., Kudo & Shima, 1970; Michaels, 1998; Jongmans, 1990), and even fewer studies on P -wave dispersion (Badri & Mooney, 1987). Because in soils P waves generally travel much faster than S waves, for the very short propagation distance in the shallow subsoil, it is rather difficult to estimate P -wave dispersion,

which explains why there are relatively few studies on this topic. Earlier observations of S -wave intrinsic dispersion in soft soils (e.g., Kudo & Shima, 1970; Michaels, 1998) have not led to a quantitative approach for estimation of soil properties like porosity, permeability, stress, etc. from the low-frequency field S -wave seismic data. Generally speaking, the relationship between seismic dispersion and soil properties remains still unclear.

The energy dissipation mechanisms responsible for seismic dispersion in deeper reservoir rocks have received relatively much more attention. The accumulation of hydrocarbon in this type of consolidated formations is the reason for the great interest. In particular, the permeability in porous reservoir rocks has been a target property to estimate from the seismic dispersion data. Field and laboratory estimates of seismic velocity dispersion and attenuation in hard rocks have revealed strong sensitivity to rock permeability (Adam *et al.*, 2009; Marketos & Best, 2010; Batzle *et al.*, 2006; Quan & Harris, 1997; Payne *et al.*, 2007). Different models at meso- (White, 1975; Dutta & Ode, 1979b,a; Smeulders & van Dongen, 1997; Johnson, 2001; Pride *et al.*, 2004) and micro- (Mavko & Nur, 1975; Dvorkin & Nur, 1993; Pride *et al.*, 2004) scales have been proposed to establish relationship between permeability and seismic attenuation.

In order to estimate the intrinsic dispersion, determining and subtracting the effect of scattering attenuation from the observed effective (or apparent) attenuation has been a challenging task. This has been a subject of research for several decades (Aki & Wu, 1988). Research on scattering attenuation has focused principally on seismic transmission data such as vertical seismic profile (VSP), crosswell and sonic-log data. Since the earth's crust is generally modelled as finely layered, there are several techniques available in quantifying scattering attenuation of seismic waves due to multiple reflections in such a layered medium (e.g., O'Doherty & Anstey, 1971; Wapenaar *et al.*, 2004). These methods require properties of the fine layers, which can be estimated from the well logs. Reliable determination of scattering-related dispersion is crucial in correctly estimating intrinsic seismic dispersion. Once estimated correctly, the intrinsic seismic dispersion can potentially address soil and rock properties.

Purely elastic or viscoelastic models are generally unable to predict the broadband seismic dispersion data. The poroelasticity models, on the other hand, require a multitude of parameters. Some of these parameters can be estimated with relative success from well-log measurements and rock-physics models. However, a few other parameters are difficult or virtually impossible to measure (e.g., tortuosity or structure factor). The inversion of seismic data for poroelasticity parameters becomes more complicated as the number of unknowns increases. Additionally, several parameters are interrelated. Such large numbers of inversion parameters generally produce many local minima during inversion and this requires use of Monte Carlo global search algorithms. For example Isakson & Neilsen (2006) invert for Biot parameters using synthetic reflection loss measurements over a large frequency band (10^2 – 10^6 Hz) and simulated annealing. Their study reveals the relative sensitivity of reflection data to each poroelastic parameter and the ability of the inversion process to converge at different frequencies. Pride *et al.* (2003) discuss how permeability can

be obtained from attenuation and velocity dispersion of P and S waves coupled to a mesoscopic flow model. In an ideal situation, extraction of poroelastic parameters from full-waveform three-component data appear promising (De Barros *et al.*, 2010); however, full-waveform inversion is computationally intensive and it demands high data quality (Pride *et al.*, 2003).

In this research, we aim to address the above-mentioned challenges pertaining to the study and utilization of seismic intrinsic dispersion, especially dispersion to S waves, in water-saturated near-surface soils. One final motivation of this study derives from the recent technological possibilities which allow obtaining high-quality broadband seismic data in near-surface soils using specialized seismic sources and receiver systems (e.g., Ghose *et al.*, 1996, 1998; Ghose, 2012).

1.2 Research objectives and outline of the thesis

Near-surface soil layers are typically more porous than the deeper, compacted formations. Therefore, dispersion of seismic waves is more relevant and potentially more informative for the shallow subsoil layers. Understanding the mechanisms responsible for seismic wave dispersion in shallow subsoil and the possibility of and the means for extracting soil properties from the observed dispersion data have so far received little attention. In this thesis, we investigate the feasibility and reliability of extraction of intrinsic seismic dispersion (velocity and attenuation) from the low-frequency field seismic data. We then explore the possibility of using the extracted seismic dispersion information to obtain estimates of in-situ soil properties e.g., porosity, permeability and stress. Particularly, S wave dispersion at low seismic frequencies will be the central topic of this thesis, as it has a good potential to address the properties of unconsolidated subsoil.

Chapters 3 to 8 of this thesis are composed in the format of independent journal articles, which is the reason for some overlaps in the content of these chapters.

We start by deriving the wave equation in a fluid-saturated porous medium based on the macroscopic Lagrangian formulation (Chapter 2). We show how different loss mechanisms can be introduced in the equation of wave propagation and discuss its total effect on the broadband seismic data.

In Chapter 3, we investigate how the effective stress applied to a fluid-saturated porous medium can affect the wave propagation. We develop a new stress-dependent Biot (SDB) model by introducing elastic and transport properties as a function of stress, in a transverse isotropic (TI) medium. The physical reason and the importance of stress-dependent elastic and transport properties in a porous material are illustrated through Lagrange's mechanics. The sensitivity of the dispersive velocity and attenuation of different seismic wavetypes travelling at different incident angles as a function of stress are investigated.

In Chapter 4, we demonstrate that seismic velocity dispersion and attenuation have contrasting behaviour in combined property domains, such as porosity-permeability, porosity-water-saturation and effective stress-permeability. Such a contrasting behaviour between independent measurements leads to the possibility of a judicious integration of these quantities to estimate in-situ soil properties with a greater re-

liability. In addition to seismic data, the potential integration of high-frequency electromagnetic wave propagation is also briefly looked at.

In Chapter 5, we rigorously test the concept of integration, proposed in Chapter 4, on realistic synthetic VSP data to obtain estimates of in-situ porosity and permeability in the shallow soil layers, and check accuracy and stability. The effects of error in the estimation of layer-specific, frequency-dependent velocity and attenuation from the VSP data without and with noise, as well as error in the used poroelasticity model, on the estimated values of porosity and permeability are investigated.

In Chapter 6, we explore a multiparameter cost function and the use of Monte Carlo global search (e.g., simulated annealing) to obtain poroelastic parameters. We test this approach on a newly compiled near-surface shear-wave dispersion database for water-saturated land sediments.

In Chapter 7, we test the method discussed in Chapters 4 and 5 on field VSP dataset obtained in a sand-peat-clay site and estimate in-situ flow properties of the very shallow soil layers.

Although this research primarily addresses the in-situ properties of the unconsolidated soil layers, we had the opportunity to test the validity of the concept and the applicability of the developed methodology to deeper, more consolidated formations. We have tested the approach on exploration-scale vertical seismic profiling (VSP) dataset at a site with hydrocarbon accumulation. The results are presented in Chapter 8.

Finally, in Chapter 9 we summarize the main conclusions of this research and briefly present our outlook for the future.

Chapter 2

Seismic wave propagation in unconsolidated granular earth materials

2.1 Introduction

In order to address the properties of unconsolidated, granular earth materials that are fully or partially saturated with fluids (like water in case of shallow subsoil), one needs to look carefully into the basic equations of wave propagation. The fundamentals of wave propagation in fluid-saturated porous media find their origin in classical mechanics and thermodynamics. A phenomenological theory of elastic waves in fluid-filled granular media was first proposed by Biot (1956a,b). It elegantly connects from first principles the rock physics properties to wave phenomena by introducing the interaction between the solid and the fluid phases. The complex viscous fluid-solid interaction causes the energy of a seismic wave to dissipate. This leads to wave broadening or wave dispersion.

Modern studies of the physics of poroelasticity go beyond the studies originally proposed by Biot, and aim to develop different diffusive processes at *meso* and *micro* scales (e.g., Mavko & Nur, 1975; White, 1975; Budiansky & O'Connell, 1976; Dutta & Ode, 1979b; Dutta & Ode, 1979a; Dvorkin & Nur, 1993; Dvorkin *et al.*, 1994; Dvorkin *et al.*, 1995; Smeulders & van Dongen, 1997; Johnson, 2001; Pride & Berryman, 2003a; Pride & Berryman, 2003b; Chotiros & Isakson, 2004; Muller & Gurevich, 2005), therefore incorporating more complex dissipative processes at different scales caused by the heterogeneous nature of the earth material. The main motivation of introducing new poroelastic models is due to the inability of Biot's theory to explain adequately the observed seismic attenuation. However, Biot's theory does provide a general framework for wave propagation in porous media and offers a direct link between seismic measurements and properties of porous formations.

In this chapter, we first review the theory of wave propagation in fluid-saturated

porous material based on the Lagrangian formulation (Biot, 1962). With an accent on the unconsolidated sediments, we look at different loss mechanisms proposed earlier (Stoll & Bryan, 1970, Chotiros & Isakson, 2004) incorporated in the so-called *global flow*, which may occur while the mechanical waves propagate through a granular medium.

One of the fundamental observations pertaining to the physics of granular materials is that seismic velocity and attenuation are sensitive to pore fluids (Bourbie *et al.*, 1987; Mavko *et al.*, 2009). In this context, we show how the partial saturation can be modelled using Biot's theory for the case when the phases are finely mixed. In this way, seismic velocity dispersion and attenuation are studied as a function of fluid saturation and frequency. Finally, the difference between the effective fluid model and the patchy saturation model in the quasistatic limit is studied.

Prior to the derivation of the constitutive governing equations of wave propagation in fluid-saturated media, the principle of least action is derived.

2.2 The principle of least action

According to the principle of least action, also known as the Hamilton's principle, every mechanical system is characterised by a definite function $\mathcal{L}(q, \dot{q}, t)$ and the system is satisfied by the following condition (Landau & Lifshitz, 1976, §2). The mechanical system moves in such a way that the integral

$$S = \int_{t_1}^{t_2} \mathcal{L}(q, \dot{q}, t) dt \quad (2.1)$$

takes the least possible value, where \mathcal{L} is the Lagrangian of the mechanical system, and the integral (2.1) - the action. q is the generalised coordinate, t is time, and $\dot{q} = \frac{dq}{dt}$ is the generalised velocity.

Having the fact that the Lagrangian contains only q and \dot{q} but no higher order time derivatives implies that the mechanical system can be completely identified by the coordinates and the velocities. From a mathematical point of view, this means that if q and \dot{q} are given, the acceleration \ddot{q} is defined uniquely.

Without a loss generality, let us consider the system which has only one degree of freedom. We now need to derive the differential equations which solve the problem of minimisation of the integral (2.1).

If $q(t)$ is the function for which S is a minimum, then any function of the form $q(t) + \delta q(t)$ will increase S , where $\delta q(t)$ is the variation of $q(t)$ and it is small in the interval between t_1 and t_2 . Since, all the functions in $q(t) + \delta q(t)$ must take the values $q^{(1)} = q(t_1)$ and $q^{(2)} = q(t_2)$, this leads to

$$\delta q(t_1) = \delta q(t_2) = 0. \quad (2.2)$$

The necessary condition for action S to have a minimum (generally speaking an extremum) is:

$$\delta S = \delta \int_{t_1}^{t_2} \mathcal{L}(q, \dot{q}, t) dt = 0, \quad (2.3)$$

or applying the variation

$$\int_{t_1}^{t_2} \left(\frac{\partial \mathcal{L}}{\partial q} \delta q + \frac{\partial \mathcal{L}}{\partial \dot{q}} \delta \dot{q} \right) dt = 0. \quad (2.4)$$

Noting that $\delta \dot{q} = \frac{d}{dt} \delta q$, integrating the second term of the integral (2.4) by parts gives

$$\delta S = \frac{\partial \mathcal{L}}{\partial \dot{q}} \delta q \Big|_{t_1}^{t_2} + \int_{t_1}^{t_2} \left(\frac{\partial \mathcal{L}}{\partial q} - \frac{d}{dt} \frac{\partial \mathcal{L}}{\partial \dot{q}} \right) \delta q dt = 0. \quad (2.5)$$

The first term in equation (2.5) is zero, since the condition in equation (2.2) is applied. Therefore, the second part of the equation (2.5) vanishes for all values of δq if the following condition holds.

$$\frac{d}{dt} \frac{\partial \mathcal{L}}{\partial \dot{q}} - \frac{\partial \mathcal{L}}{\partial q} = 0. \quad (2.6)$$

For the system with more than one degree of freedom, the s different functions $q_i(t)$ must be varied independently in the principle of least action. We then obtain s independent equations

$$\frac{d}{dt} \frac{\partial \mathcal{L}}{\partial \dot{q}_i} - \frac{\partial \mathcal{L}}{\partial q_i} = 0, \quad (2.7)$$

where $i=1,2,\dots,s$. These differential equations are called *Lagrange's equations*. If the Lagrangian of a mechanical system is known, the equations (2.7) provide the equations of motion of the system.

2.3 Dissipative forces in Lagrange's mechanics

In Section 2.2, the general equations of Lagrange mechanics are derived. There we have only dealt with a mechanical system where there is no dissipation. In other words, the effect of the surrounding media to the mechanical system is neglected. In reality, however, drag forces will occur during a mechanical motion, which will tend to retard the motion. The mechanical energy is, therefore, dissipated and converted into heat. The change of internal energy of the system is based on the first law of thermodynamics. Therefore, a motion under these conditions is not purely mechanical, and the change of the entropy of such media and the mechanical system cannot be neglected.

However, there are some cases when a mechanical motion in a medium can still be described by Lagrange's equations by introducing additional terms in the equation of motion. Such cases correspond to situations where the frequencies of the mechanical oscillations are small compared to the characteristic dissipation frequencies in the medium. If this is the case, then we may consider that the frictional force acting on a body is a function of only its velocity. For a system with more than one degree of

freedom, the frictional forces corresponding to the generalised coordinates q_i can be written as (Landau & Lifshitz, 1976, §25)

$$f_{i,fr} = -a_{ik}\dot{q}_k. \quad (2.8)$$

Throughout this thesis we assume that the summation convention applies for repeated subscripts, unless mentioned otherwise. Based on the methods of statistical physics (Landau & Lifshitz, 1980, §120),

$$a_{ik} = a_{ki}. \quad (2.9)$$

Hence the equation (2.8) can be written as

$$f_{i,fr} = -\frac{\partial \mathcal{F}}{\partial \dot{q}_i}, \quad (2.10)$$

where \mathcal{F} is

$$2\mathcal{F} = a_{ik}\dot{q}_i\dot{q}_k. \quad (2.11)$$

\mathcal{F} represents a dissipative function. By adding the frictional force to the right-hand side of the Lagrange's equations (2.7) yields

$$\frac{d}{dt}\frac{\partial \mathcal{L}}{\partial \dot{q}_i} - \frac{\partial \mathcal{L}}{\partial q_i} = -\frac{\partial \mathcal{F}}{\partial \dot{q}_i}. \quad (2.12)$$

2.3.1 Macroscopic Lagrange's equations for fluid-saturated elastic solids: Biot's theory

We now extend the classical elasticity theory to the theory of poroelasticity. This extension implies an introduction of a fluid phase into the solid body and model the dynamics of a coupled solid-fluid physical system. We present a general derivation of equation of motion by constructing the Lagrangian for a fluid-saturated porous material and dissipative function for such a system.

The following assumptions are made in order to derive the dynamic equations for wave propagation in fluid-filled granular materials (Biot, 1956a,b):

1. The fluid phase is Newtonian, compressible, and fully interconnected. The fluid may flow relative to the solid phase, causing the system to dissipate.
2. A representative elementary volume (REV) under consideration is small relative to the wavelength of the elastic waves and large (even in the high-frequencies) compared to the scale of the individual grain and pore.
3. All minerals making up the granular medium have the same bulk and shear moduli.
4. The granular material is completely fluid-saturated.

5. The fluid-solid interaction is isothermal - all thermal and chemical reactions are disregarded. The internal energy change is, therefore, ignored.

The Lagrangian for a mechanical system of particles can be written as (Landau & Lifshitz, 1976, §5)

$$\mathcal{L} = \mathcal{T} - \Pi, \quad (2.13)$$

where \mathcal{T} and Π are, respectively, the kinetic and the potential energy of the mechanical system. Since the fluid is viscous, dissipative forces in equation (2.12) cannot be ignored.

Following classical theory of elasticity and the assumptions above, the potential strain energy per unit volume of a poroelastic medium yields (Biot, 1962):

$$2\Pi = \tau_{11}e_{11} + \tau_{22}e_{22} + \tau_{33}e_{33} + 2\tau_{12}e_{12} + 2\tau_{31}e_{31} + 2\tau_{23}e_{23} + p_f\zeta, \quad (2.14)$$

with

$$\zeta = \nabla \cdot (n(\mathbf{u} - \mathbf{U})) = -\nabla \cdot \mathbf{w}, \quad (2.15)$$

where vectors \mathbf{u} and \mathbf{U} are the solid and fluid displacement vectors, respectively. Vector \mathbf{w} represents the fluid flow relative to the solid phase in volume per unit area, and n is the porosity. τ_{ij} and e_{ij} are the stresses and strains of the solid phase, respectively. Omitting the higher order terms of the displacements, the small-strain tensors for the solid e_{ij} can be defined as (Landau & Lifshitz, 1970, §1)

$$e_{ij} = \frac{1}{2} \left(\frac{\partial u_i}{\partial x_j} + \frac{\partial u_j}{\partial x_i} \right), \quad (2.16)$$

where $i, j = 1, 2, 3$. It should be noted, that the symmetry of stresses and strains are used in the equation (2.14), i.e. $\tau_{ij} = \tau_{ji}$, $e_{ij} = e_{ji}$. This can be shown using the balance momentum equation of a body (Sivukhin, 2005). By expressing Π in terms of elastic coefficients H , C , M and G for an isotropic case, and taking partial derivatives of Π with respect to the strains of the solid e_{ij} and the increment of fluid content ζ , we obtain stress-strain relations for a porous solid saturated with a fluid. Stress-strain relations for anisotropic case will be discussed in Chapter 3. Thus,

$$\tau_{ij} = 2Ge_{ij} + (H - 2G)e\delta_{ij} - C\zeta\delta_{ij} \quad (2.17)$$

$$p_f = M\zeta - Ce, \quad (2.18)$$

where $e = e_{11} + e_{22} + e_{33}$, and δ_{ij} is the Kronecker delta and is defined as

$$\delta_{ij} = \begin{cases} 1, & i = j, \\ 0, & i \neq j. \end{cases} \quad (2.19)$$

The relations of H , C , M and G with physical quantities of the solid and the fluid

phases are given by (Biot, 1962; Stoll, 1977)

$$H = K_b + \frac{4}{3}G + \frac{(K_s - K_b)^2}{D - K_b}, \quad (2.20)$$

$$C = \frac{K_s(K_s - K_b)}{D - K_b}, \quad (2.21)$$

$$M = \frac{K_s^2}{D - K_b}, \quad (2.22)$$

with

$$D = K_s \left(1 + n \left(\frac{K_s}{K_f} - 1 \right) \right), \quad (2.23)$$

where G is the shear rigidity, K_s , K_f , and K_b are, respectively, the bulk modulus of the individual grains, the fluid and the porous matrix. The methods for measuring the bulk modulus of grains and the porous matrix were described by Biot & Willis (1957). These are also known as *unjacketed* and *jacketed* tests, respectively.

For a medium with statistical isotropy, the macroscopic kinetic energy of a porous solid of unit volume containing the fluid can be expressed in terms of density, porosity, tortuosity and velocity fields (Biot, 1962):

$$\mathcal{T} = \frac{1}{2} \rho \dot{u}_i \dot{u}_i + \rho_f \dot{u}_i \dot{w}_i + \frac{1}{2} m \dot{w}_i \dot{w}_i, \quad (2.24)$$

where $\rho = (1 - n)\rho_s + n\rho_f$. Here ρ_s and ρ_f are the density of the solid and the fluid phase, respectively. m is called the added mass and is defined as

$$m = \frac{\gamma}{n} \rho_f, \quad (2.25)$$

where γ is tortuosity (or structure factor) and is introduced due to the heterogeneous nature of the medium at pore scales. Another explanation is that not all of the fluid moves in the direction of the microscopic pressure gradient due to different shapes of the pores and the grains.

In order to obtain a dissipative function for a fluid-saturated porous medium, we follow Eq. (2.11). Therefore, the dissipation function per unit volume can be written in a quadratic form. Assuming the isotropy of the medium, the dissipation function can be expressed as (Biot, 1962):

$$\mathcal{F} = \frac{1}{2} \frac{\eta}{k} \dot{w}_i \dot{w}_i, \quad (2.26)$$

where η/k is a drag coefficient. Here η and k are the fluid viscosity and the permeability of the porous medium, respectively.

Finally, by combining equations (2.12), (2.13), (2.14), (2.17), (2.18), (2.24) and (2.26), we obtain the equations of motion

$$G \nabla^2 \mathbf{u} + (H - G) \nabla \nabla \cdot \mathbf{u} + C \nabla \nabla \cdot \mathbf{w} = \frac{\partial^2}{\partial t^2} (\rho \mathbf{u} + \rho_f \mathbf{w}), \quad (2.27)$$

$$\nabla (C \nabla \cdot \mathbf{u} + M \nabla \cdot \mathbf{w}) = \frac{\partial^2}{\partial t^2} (\rho_f \mathbf{u} + m \mathbf{w}) + \frac{\eta}{k} \frac{\partial \mathbf{w}}{\partial t}. \quad (2.28)$$

Due to the statistical isotropy, equations (2.27) and (2.28) can be decoupled to dilatational and rotational waves by using

$$\nabla \cdot \mathbf{u} = e, \quad -\nabla \cdot \mathbf{w} = \zeta, \quad (2.29)$$

$$\nabla \times \mathbf{u} = \boldsymbol{\omega}, \quad -\nabla \times \mathbf{w} = \boldsymbol{\Omega}. \quad (2.30)$$

These lead to the equation of motion for dilatational and rotational waves, respectively as:

$$\nabla^2(He - C\zeta) = \frac{\partial^2}{\partial t^2}(\rho e - \rho_f \zeta), \quad (2.31)$$

$$\nabla^2(Ce - M\zeta) = \frac{\partial^2}{\partial t^2}(\rho_f e - m\zeta) - \frac{\eta}{k} \frac{\partial \zeta}{\partial t}, \quad (2.32)$$

$$G\nabla^2\boldsymbol{\omega} = \frac{\partial^2}{\partial t^2}(\rho\boldsymbol{\omega} - \rho_f\boldsymbol{\Omega}), \quad (2.33)$$

$$0 = \frac{\partial^2}{\partial t^2}(\rho_f\boldsymbol{\omega} - m\boldsymbol{\Omega}) - \frac{\eta}{k} \frac{\partial \boldsymbol{\Omega}}{\partial t}. \quad (2.34)$$

These are the equations of wave propagation in fully-saturated poroelastic media as derived by Biot (1956a,b, 1962) for the low-frequency regime, where it is assumed that the relative fluid flow is of the Poiseuille type. For an extension from the low to the high frequencies, Biot made the ratio η/k to be frequency-dependent and introduced the so-called viscous correction factor F to correct for the deviation from the Poiseuille flow. Then the ratio becomes $\eta F/k$. F is introduced by solving the equation of motion for the fluid in a straight duct with a circular cross-section of radius a :

$$F = \frac{1}{4} \left(\frac{\xi T(\xi)}{1 + 2iT(\xi)/\xi} \right), \quad (2.35)$$

where

$$T(\xi) = \frac{\text{ber}'(\xi) + i\text{bei}'(\xi)}{\text{ber}(\xi) + i\text{bei}(\xi)}, \quad (2.36)$$

with

$$\xi = a \sqrt{\frac{\omega \rho_f}{\eta}}. \quad (2.37)$$

Here, the functions $\text{ber}(\xi)$ and $\text{bei}(\xi)$ are the real and imaginary parts of the Kelvin function and ω is the angular frequency. Stoll (1974) found the values of a to be between 1/6th and 1/7th of the mean grain diameter, in order get a good agreement with the experimental data reported earlier by several investigators.

2.3.2 The Biot-Stoll model

In an attempt to explain wave attenuation which is typically observed in exploration seismic frequencies (1 to 500 Hz) and also at higher frequencies in case of marine-sediment-acoustics (up to 100 kHz), where Biot's theory fails, Stoll & Bryan (1970) suggested a modification of the Biot's theory (Section 2.3.1). This extension is known as Biot-Stoll model. It models the small-strain wave propagation in saturated sediments and leads to a new model where two loss mechanisms are involved. The first loss is due to the viscous fluid motion in the interconnected pores (Biot's loss) and the second is due to the inelasticity of the skeletal frame (Stoll & Bryan, 1970; Stoll, 1977). By revisiting the poroelastic coefficients H , C , M and G (see equations 2.20, 2.21, 2.22), Bryan and Stoll replace them by introducing linear or slightly nonlinear operators that characterize elastic and inelastic response of the frame. They can be expressed in terms of the following complex moduli:

$$H^* = H_R(\omega) - iH_I(\omega), \quad (2.38)$$

$$C^* = C_R(\omega) - iC_I(\omega), \quad (2.39)$$

$$M^* = H_R(\omega) - iM_I(\omega), \quad (2.40)$$

$$G^* = G_R(\omega) - iG_I(\omega), \quad (2.41)$$

with subscripts R and I denoting respectively the real and imaginary parts of the complex coefficients. By considering the bulk moduli of the solid (K_s) and the fluid (K_f) as real-valued, and the bulk modulus of the skeletal frame (K_b) and the shear rigidity (G) as complex-valued, it is possible to derive the various energy dissipations like grain-to-grain friction and other contact relaxations. Further, introduction of the logarithmic bulk and shear decrements (δ_p and δ_s , respectively) leads to the complex bulk and shear modulus of the frame as:

$$K_b^* = K_b \left(1 - i \frac{\delta_p}{\pi} \right), \quad (2.42)$$

$$G^* = G \left(1 - i \frac{\delta_s}{\pi} \right), \quad (2.43)$$

where $K_b = \text{Re}(K_b^*)$ and $G = G_R = \text{Re}(G^*)$. Recalling the change of the ratio from η/k to $\eta F/k$, the Eqs. (2.31), (2.32), (2.33) and (2.34) become, for compressional wave:

$$\nabla^2(H^*e - C^*\zeta) = \frac{\partial^2}{\partial t^2}(\rho e - \rho_f \zeta), \quad (2.44)$$

$$\nabla^2(C^*e - M^*\zeta) = \frac{\partial^2}{\partial t^2}(\rho_f e - m\zeta) - \frac{\eta}{k} F \frac{\partial \zeta}{\partial t}, \quad (2.45)$$

and for shear wave,

$$G^* \nabla^2 \omega = \frac{\partial^2}{\partial t^2}(\rho \omega - \rho_f \Omega), \quad (2.46)$$

$$0 = \frac{\partial^2}{\partial t^2}(\rho_f \omega - m \Omega) - \frac{\eta}{k} F \frac{\partial \Omega}{\partial t}. \quad (2.47)$$

The physical meaning of δ_P and δ_S can be readily appreciated by considering the *locked* motion of the fluid and the solid phases, i.e. when there is no relative fluid motion ($\mathbf{u}=\mathbf{U}$). In this case, all losses are simply attributed to the inelastic mechanisms in the skeletal frame.

Now, substituting the solutions of the form $e^{-i\omega t}$ in equations (2.44) and (2.45) gives two equations in the frequency domain. For dilatational wave we have:

$$\begin{vmatrix} H^* \kappa^2 - \rho \omega^2 & \rho_f \omega^2 - C^* \kappa^2 \\ C^* \kappa^2 - \rho_f \omega^2 & m \omega^2 - M^* \omega^2 + \frac{i \omega F \eta}{k} \end{vmatrix} = 0, \quad (2.48)$$

from which we get two complex roots - κ_{P1} and κ_{P2} , corresponding to the fast and slow compressional waves, respectively. Their velocities and attenuations can be calculated as follows:

$$V_{P1,2} = \frac{\omega}{\text{Re}(\kappa_{P1,2})}, \quad (2.49)$$

$$Q_{P1,2}^{-1} = \frac{2\text{Im}(\kappa_{P1,2})}{\text{Re}(\kappa_{P1,2})}. \quad (2.50)$$

Following the same procedure for equations (2.46) and (2.47) we get:

$$\begin{vmatrix} \rho \omega^2 - G^* \kappa^2 & \rho_f \omega^2 \\ \rho_f \omega^2 & m \omega^2 + \frac{i \omega F \eta}{k} \end{vmatrix} = 0, \quad (2.51)$$

from which the complex roots - κ_s , corresponding to the shear wave, can be obtained. The velocity and attenuation of shear wave can be calculated as:

$$V_s = \frac{\omega}{\text{Re}(\kappa_s)}, \quad (2.52)$$

$$Q_s^{-1} = \frac{2\text{Im}(\kappa_s)}{\text{Re}(\kappa_s)}. \quad (2.53)$$

2.3.3 The Biot-Stoll model with contact squirt flow and shear drag

Although the Biot-Stoll model has earlier been found to be capable of explaining well the experimental data for soft marine sediments (Beebe, 1982; Holland & Brunson, 1988; Buchanan, 2006), it fails sometimes to predict accurately the high velocity dispersion which is characteristic of coarse grained sediments, e.g. gravel, coarse sands, etc. To meet this challenge, Chotiros & Isakson (2004, 2008) presented the idea of contact squirt flow and shear drag (BICSQS) to explain the highly dispersive velocity observed in unconsolidated sandy sediments. By idealizing the grain-to-grain contact (see Figure 2.1), they considered the water to permeate into the grain-to-grain contact region. The existing gap (thin fluid film) between the grains is responsible for a squirt flow when the media is stressed by an elastic wave. The microscale response due to the normal and tangential forces in terms of the gap can

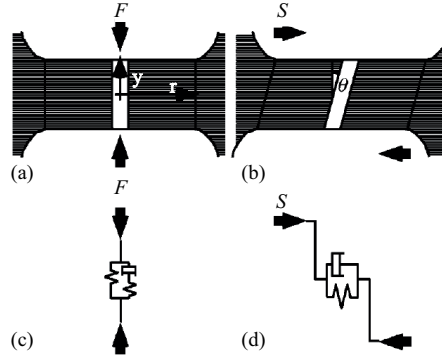


Figure 2.1: Grain contact models of (a) compression, (b) shear, and their equivalents (c) and (d) (after Chotiros & Isakson, 2004).

be written as follows (see Figure 2.1):

$$F = (k_c + k_y)(y - y_0) + c_r(r - r_0), \quad (2.54)$$

$$0 = k_y(y - y_0) + c_r(r - r_0) + b \frac{dr}{dt}, \quad (2.55)$$

and

$$\frac{S}{y_0} = g\theta + h \frac{d\theta}{dt}, \quad (2.56)$$

where F and S are the compressional and shear forces, k_c is the elastic coefficient at the solid contact, k_y and c_r are bulk reaction of the fluid film with respect to changes in y and r , respectively, g is shear stiffness, and b and h are the compressional (with respect to r) and shear drag coefficients. Using the solution in the form $e^{-i\omega t}$, the applied force amplitudes (A_F, A_S) relative to the displacement amplitudes (A_y, A_θ) for compressional and tangential components can be obtained as follows:

$$\frac{A_F}{A_y} = k_c + \frac{k_y}{1 + i \left(\frac{\omega_p}{\omega} \right)}, \quad (2.57)$$

$$\frac{A_S}{A_\theta} = g \left(1 - i \frac{\omega}{\omega_s} \right), \quad (2.58)$$

with $\omega_p = c_r/b$ and $\omega_s = g/h$ being the bulk and shear relaxation frequencies. On a macroscopic scale, considering the statistical isotropy of the grain contact orientations, the effective bulk and shear moduli are

$$K_b^* = K_c + \frac{K_y}{1 + i \left(\frac{\omega_p}{\omega} \right)}, \quad (2.59)$$

$$G^* = G \left(1 - i \frac{\omega}{\omega_s} \right), \quad (2.60)$$

with K_c and G being the asymptotic frame bulk and shear moduli at the quasistatic or the low-frequency limit. K_y is the difference in the bulk moduli of the media between the low and the high frequency limits. It should be noted that at high frequencies, the shear viscous drag may increase infinitely with frequency (see Eq. 2.60), which is nonphysical. For this reason, Chotiros & Isakson (2008) introduced the correction factor for the shear viscous drag, similar to Biot (1956b). Considering the Couette flow (Landau & Lifshitz, 1987, §18), the viscous fluid between two parallel plates moves in the opposite direction. Since the laminar flow breaks down at higher frequencies, the viscosity is taken as ηF_s to correct for the deviation from the Poiseuille flow, so that

Parameter	Unit	Biot	Biot-Stoll	BICSQS
Porosity, n	-	0.44	0.44	0.44
Permeability, k	μm^2	17.5	17.5	17.5
Pore size, a	μm	20	20	20
Viscosity, η	$\text{Pa}\cdot\text{s}$	0.001	0.001	0.001
Shear rigidity, G	MPa	24	24	24
Frame bulk modulus, K_b	MPa	52	52	-
Grain bulk modulus, K_s	GPa	36	36	36
Fluid bulk modulus, K_f	GPa	2.3	2.3	2.3
Density of solid, ρ_s	kg/m^3	2650	2650	2650
Density of fluid, ρ_f	kg/m^3	1000	1000	1000
Tortuosity, γ	-	1.25	1.25	1.25
Bulk log decrement, δ_p	-	-	0.15	-
Shear log decrement, δ_s	-	-	0.15	-
Asymp. frame bulk mod., $K_{c,(\omega \rightarrow 0)}$	MPa	-	-	26.3
Frame bulk mod. difference, K_y	MPa	-	-	675
Bulk relaxation frequency, $\frac{\omega_p}{2\pi}$	kHz	-	-	30
Shear relaxation frequency, $\frac{\omega_s}{2\pi}$	kHz	-	-	∞
Half gap width, a_1	μm	-	-	1

Table 2.1: Values of parameters used in the Biot, Biot-Stoll and BICSQS model (see Fig. 2.2).

$$G^* = G \left(1 - i F_s \frac{\omega}{\omega_s} \right), \quad (2.61)$$

where

$$F_s(\xi_1) = \frac{\xi_1 \sqrt{-i} \cosh(\xi_1 \sqrt{-i})}{\sinh(\xi_1 \sqrt{-i})}, \quad (2.62)$$

with ξ_1 and half gap width a_1 related as

$$\xi_1 = a_1 \sqrt{\frac{\omega \rho_f}{\eta}}. \quad (2.63)$$

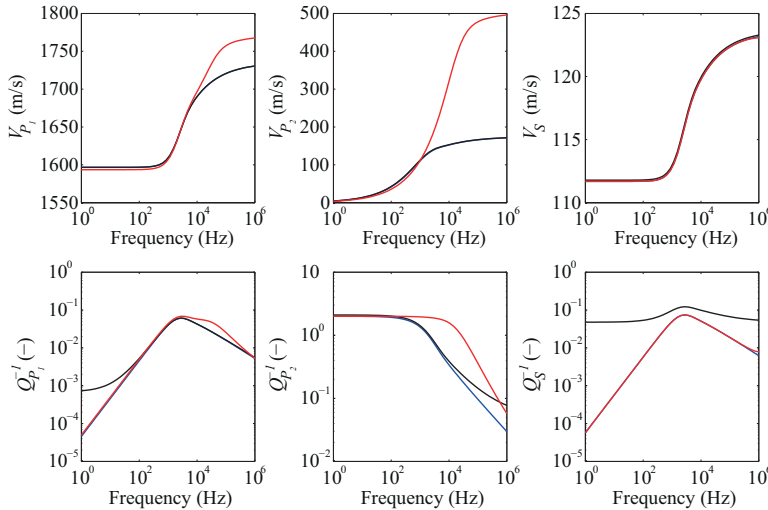


Figure 2.2: Theoretical velocity and attenuation for the Biot (blue line), Biot-Stoll (black line) and BICSQS (red line). The input parameters are shown in Table 2.1.

Now, in order to calculate the velocity and attenuation of a propagating wave, Eqs. (2.59) and (2.61) should be substituted into Eqs. (2.31)-(2.34) through Eqs. (2.20)-(2.23).

Figure 2.2 shows a comparison between the Biot, Biot-Stoll and BICSQS models. The input parameters are taken from Chotiros & Isakson (2004) for unconsolidated sandy sediments. At low seismic frequencies the Biot and the BICSQS models behave similarly. This can be explained by the fact that the bulk relaxation frequency ω_p due to the squirt flow is at 30 kHz and higher than the Biot's characteristic frequency, which is $\omega_c = \eta n / (k \rho_f) \approx 4$ kHz. The result, however, may dramatically change if ω_p decreases and approaches the field seismic frequency. This is possible when the viscous drag forces at grain contacts are large. The Biot-Stoll model shows much larger attenuation for fast P and S waves at low frequencies, which is caused by grain-to-grain friction or other types of inelastic loss at the solid matrix. At high frequencies, the BICSQS model predicts relatively high velocities compared to Biot and Biot-Stoll models. By setting $\omega_s = \infty$, we simply ignore the shear drag forces in the BICSQS, and as a result, the velocity of shear wave coincides with that from Biot and Biot-Stoll models. However, the situation may change with an increase in shear drag forces and hence a decrease in shear relaxation frequencies. It is of our interest to understand which loss mechanisms might occur in reality, particularly in the context of unconsolidated fully-saturated subsoil/sediments. This will be discussed in Chapter 6.

2.4 Wave propagation in partially saturated granular earth materials

2.4.1 Effective fluid model

We have so far looked at waves propagating through fully-saturated porous sediments. We also have shown different loss mechanisms which may occur when the passage of elastic waves is responsible for the extra stress in the fluid-filled granular media. In this section, we show how seismic wave velocity and attenuation change with varying fluids or gases in the formation. We focus on the role of the properties of the fluid/gas.

Possibly the most common approach in modelling the effect of partial saturation on seismic velocity and attenuation is the replacement of multiple fluid phases by one effective fluid. This is also known as the *effective fluid model*. However, before replacing by one effective fluid, one needs to make a preliminary assumption. Since bulk moduli of the different fluid constituents will have different stress-induced pore pressure, the time necessary to equilibrate between these pore pressures should be small compared to $\tau = 1/f$, where f is the seismic frequency. This is possible when the fluid phases are intimately mixed at the finest scales so that the pore-pressure increments equilibrate with each other to a single effective value, or following the definition of the characteristic relaxation or the diffusion time (Mavko *et al.*, 2009, Section 6.17):

$$\tau \cong \frac{L_s^2}{\mathcal{D}}, \quad (2.64)$$

where the heterogeneous pore pressure of scale L_s should satisfy the following condition:

$$L_s \leq \sqrt{\tau \mathcal{D}} = \sqrt{\mathcal{D}/f}, \quad (2.65)$$

in which $\mathcal{D} = kK_f/\eta$ is the diffusivity coefficient, k is permeability, K_f and η , respectively, denote fluid bulk modulus and viscosity. If this condition is satisfied, then the effective fluid bulk modulus can be described well by the Reuss average (Mavko *et al.*, 2009, Section 6.17):

$$\frac{1}{K_f} = \sum \frac{S_i}{K_i}, \quad (2.66)$$

where S_i and K_i denote, respectively, saturation and bulk modulus of the i^{th} fluid constituent.

Let us consider a simple case in which the porous material is saturated with air and water. Thus Eq. (2.66) becomes

$$\frac{1}{K_f} = \frac{S_w}{K_w} + \frac{S_a}{K_a}, \quad (2.67)$$

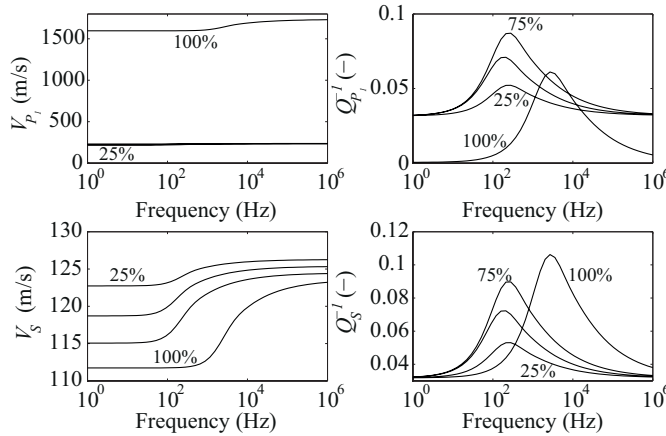


Figure 2.3: Phase velocities and attenuations as a function of water saturation and frequency for P_1 - and S -waves.

where $S_a + S_w = 1$. Subscripts w and a stand for water and air, respectively. In order to find effective fluid viscosity of the mixture of fluids, we again use Reus average:

$$\frac{1}{\eta} = \frac{S_w}{\eta_w} + \frac{S_a}{\eta_a}. \quad (2.68)$$

Fluid density can be calculated as follows:

$$\rho_f = S_w \rho_w + S_a \rho_a. \quad (2.69)$$

Now, assuming that the condition given in Eq. (2.65) is always satisfied at all frequencies, then we can replace fluid bulk modulus, viscosity and fluid density defined in Section 2.3 by the effective fluid bulk modulus, viscosity and fluid density from Eqs. (2.67), (2.68) and (2.69), respectively. This yields the equation of motion in porous media saturated with multiple fluid phases.

Parameter	Unit	Value
Viscosity of air, η_a	Pa·s	$1.8 \cdot 10^{-5}$
Air bulk modulus, K_a	MPa	0.101
Density of air, ρ_a	kg/m ³	1.2
Bulk log decrement, δ_p	-	0.1
Shear log decrement, δ_s	-	0.1

Table 2.2: Values of parameters used in the Biot-Stoll with partial saturation (see Fig. 2.3).

Figure 2.3 shows the phase velocity and attenuation of P_1 (fast compressional) and S waves as a function of frequency, using the Biot-Stoll model. The different curves here correspond to different degrees of water saturation, varying from 25% to

100% at a step of 25%. This synthetic frequency-saturation analysis is performed for the porous, partially saturated earth material with additional properties as shown in Table 2.2. Typical values are taken for air. In addition to these, other properties are the same as in Table 2.1 for the Biot model. When the medium is partially saturated with water, the phase velocity of the P_1 wave is small compared to the P wave velocity in water, whereas in case of full saturation the change is dramatic. This has been illustrated previously by other researchers (Bourbie *et al.*, 1987; Dvorkin & Nur, 1998; Berryman *et al.*, 2002; Mavko *et al.*, 2009). This can be explained by the fact that in this case, the effective bulk modulus with partial saturation is small compared to the full-saturation case due to the air inclusions. Since velocity and attenuation are related through the Kramers-Kronig relation, the attenuation change corresponding to the P_1 wave between full and partial saturations is large as well. However, in this case, the change of the Biot's characteristic frequency with the changing degree of saturation is more apparent. The characteristic frequency shifts toward the lower frequencies. These results indicate that attenuation measurements for compressional wave can potentially be used to identify the degree of saturation at seismic frequencies. Since the increase in water saturation leads to an increase in the overall viscosity (i.e. increasing friction between the solid and the fluid) of the mixed fluid, we see, therefore, a monotonic increase in the P_1 wave attenuation at intermediate saturations.

The change in shear-wave velocity and attenuation is attributed to change in effective density and fluid mobility (permeability to viscosity ratio) in the formation. The shear rigidity is the same for dry and saturated conditions because it is not affected by the pore fluid. Therefore, the shear wave is primarily controlled by the effective density which changes monotonically based on a linear saturation argument. As a result, there is no sharp change in the phase velocities (Fig. 2.3). The effect of the degree of saturation on the shear-wave attenuation are similar to those observed for the P_1 wave, excluding only the sharp nature of the change. The increase in viscosity causes the shear drag forces to grow (see Eq.2.8), which explains this behaviour.

In the quasistatic limit (i.e., the frequency approaching zero), the bulk modulus in Biot's equations in the undrained condition reduces to (see Eq.2.20):

$$K_u = H - \frac{4}{3}G = K_b + \frac{(1 - K_b/K_s)^2}{n/K_f + (1 - n)/K_s - K_b/K_s^2}. \quad (2.70)$$

This result was also obtained by Gassmann (with the assumption of homogeneous grain modulus and statistical isotropy) and is known as the fluid substitution equation. This implies that in the quasistatic limit, Biot's theory is consistent with Gassmann's equation and is equivalent to the case of the elasticity theory. The latter equation is found to explain very well the seismic data at low frequencies and is, therefore, commonly used in geophysical applications.

2.4.2 Patchy saturation

In reality, any material is heterogeneous at some scale. This may result in heterogeneous fluid distribution in the porous material. In this case, there will be some

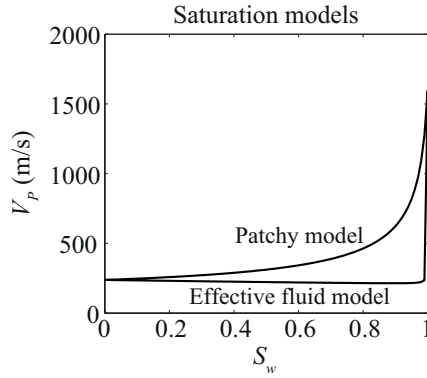


Figure 2.4: P -wave velocity as a function of water saturation for effective fluid and patchy models.

patches with a relatively large size, where the condition in Eq. (2.65) is not satisfied. Fluid phases will be equilibrated within a patch at scales satisfying the condition in Eq. (2.65), but the neighbouring patches, which violate the latter condition, will not be equilibrated. Therefore, the bulk modulus of the media will vary spatially, whereas the shear modulus will be uniform and independent of the pore fluid. Following Dvorkin & Nur (1998), we can use Hill's averaging to calculate the effective bulk modulus in the quasistatic limit, which is independent of shape of the patches:

$$\left(K_u + \frac{4}{3}G\right)^{-1} = S_w \left(K_1 + \frac{4}{3}G\right)^{-1} + S_a \left(K_2 + \frac{4}{3}G\right)^{-1}, \quad (2.71)$$

where K_1 and K_2 are the bulk moduli of the water- and gas-saturated porous earth material, respectively. They can be found from the Gassmann's equation as:

$$K_1 = K_b + \frac{(1 - K_b/K_s)^2}{n/K_w + (1 - n)/K_s - K_b/K_s^2}, \quad (2.72)$$

$$K_2 = K_b + \frac{(1 - K_b/K_s)^2}{n/K_a + (1 - n)/K_s - K_b/K_s^2}. \quad (2.73)$$

Figure 2.4 illustrates the P -wave velocity as a function of water saturation in the quasistatic limit for the effective fluid and patchy models, considering the same input parameters as those used in Fig. (2.3). Note the effect of the two saturation patterns – homogeneous and patchy. In case of homogeneous saturation, where the fluid phases are mixed at the finest scale, one can observe steady decrease in velocity and an abrupt change when the saturation approaches 1. In case of patchy saturation, there is a monotonic increase in velocity and the behaviour is completely different from the homogeneous saturation. Two saturation patterns coincide in the two limits of saturation – 0 and 1. This indicates the two theoretical limits for P -wave velocity. In practice, one should expect the velocity-saturation data to fall into the triangular region between the two theoretical curves.

Here we have looked at the effect of patchy saturation on the P -wave velocity at very low frequencies. However, the heterogeneous nature of the fluid due to the different fluid inclusions may cause wave dispersion due to the fluid pressure equilibration process. In this study, we do not investigate any velocity dispersion and attenuation with patches and stick to the patchy model in the quasistatic limit. An attempt to quantify the velocity dispersion and attenuation due to the patchy saturation are well documented earlier by several researchers (e.g., White, 1975; Dutta & Ode, 1979b,a; Smeulders & van Dongen, 1997; Johnson, 2001).

2.5 Conclusions

In this chapter, we have derived the Lagrange's equations with dissipative functions. These equations were then used to derive equations of motion in fluid-saturated, porous earth materials. We have then looked at different loss mechanisms for propagating seismic waves; these mechanisms are pertinent to unconsolidated sediments/soils. The losses were introduced by extending the undrained bulk and shear material properties and are shown to be frequency-dependent. In the case of Biot-Stoll model, additional loss to those present in the Biot model has been attributed to the inelastic deformations in the porous frame, whereas in the BICSQS model, the loss is ascribed to the squirt-flow and shear drag, which occur due to the thin fluid film present in the grain-to-grain contacts, while the seismic waves propagate through a medium. This microscale (or grain scale) loss mechanism has then been scaled up to describe the macroscopic loss. For this purpose, we have used the statistical isotropy assumption of the grain contact orientation. Finally, we have looked at how the Biot's theory can be extended to the case of partial saturation by introducing the effective fluid modulus based on the isostress Reuss averaging. The frequency-saturation numerical analyses for velocity and attenuation have been performed for both P and S waves. Finally, the effective bulk modulus of the earth material saturated by multiple fluids has been investigated as a function of water saturation. When there are patches with characteristic length larger than L_s , they will not be equilibrated, and only the patch at scales smaller than L_s will be equilibrated. In this case, the bulk modulus will be different between the patches. The effective bulk modulus of the material can be calculated using Hill's average. Theoretical expressions derived in this chapter will be useful in extracting material properties for unconsolidated granular earth materials, which will be discussed in a later chapter.

Chapter 3

Stress-dependent seismic dispersion in unconsolidated TI media

3.1 Introduction

The effect of fluid in a fluid-saturated granular medium on the dispersion of elastic waves has been well-studied in the past. However, the stress-dependence of seismic dispersion has so far received little attention. But this stress-dependence can have important practical implications. In this chapter, we shall develop new theoretical formulations relating stress in unconsolidated, granular earth materials to the dispersive nature of the propagating elastic waves through such materials. In-situ stress in the subsoil and in marine sediments is a key parameter needed in various projects. Here, we will show that frequency-dependent seismic velocity and attenuation at different external stresses are different and this difference can in some cases be significant. This information can be uniquely useful in characterizing the state of in-situ stress in porous, granular soils/sediments, particularly in time-lapse seismic experiments.

The classical approaches to characterize the stress-dependent behaviour of a porous material are empirical: for instance, the ones relating stress to shear-wave velocity in soil (Hardin & Richart, 1963; Drnevich & Richart, 1970; Stokoe *et al.*, 1985; Jamiolkowski & Lo Presti, 1994). The other way of looking at the stress-dependence is the micromechanical approach or the contact theories (Mindlin, 1949; Deresiewicz, 1974). These theories have recently been tested on time-lapse seismic data in the laboratory scale (Ghose, 2010a). These earlier approaches, as well as the crack models involving the effective elastic compliances and their stress-sensitivity (Eshelby, 1957; Nur, 1971) completely ignore the stress-dependent transport properties, and hence stress-dependent seismic dispersion.

A change in stress in a porous material causes changes in both elastic and transport properties. The purpose of the research to be discussed in this chapter is to bridge these two domains – elastic moduli and transport properties. The aim is to understand the dispersive nature of the propagating elastic waves through a

saturated porous medium as a function of the in-situ effective stresses. We derive stress-dependent poroelastic equations by coupling Biot's theory and the mechanics of granular soils/sediments in a transverse isotropic (TI) medium. Thereafter, we concentrate on the stress-dependent transport properties, relying on the general effective-stress laws derived by Berryman (1992). Through such independent consideration of the elastic moduli and the transport properties of the formation, we obtain the stress-dependent Biot's parameters. This results in a new theory for stress-dependent wave propagation in fluid-saturated, porous earth materials. As in the previous chapter, the physical reason and the importance of stress-dependent elastic and transport properties in a porous material are illustrated through Lagrange's mechanics. Finally, the sensitivity of the dispersive velocity and attenuation of different seismic wavetypes travelling at different incidence angles as a function of in-situ stresses are looked at. The practical utility of the theory and insights developed in this chapter will be presented in Chapter 4.

3.2 Stress-dependent seismic dispersion in TI media

In Section 2.3.1 we have derived the dynamic equation of motion for elastic waves in unconsolidated, fluid-saturated porous earth material. There we have considered a statistically isotropic medium in order to study the effect of the transport properties (porosity, permeability, viscosity, tortuosity). In the context of time-lapse seismics, the material properties including the stresses in soils or sediments may change with changes in the external stress. This may lead to a change in both the elastic and the transport properties of the sediment. This, in turn, leads to a stress-dependent change in seismic wave velocity and attenuation. Understanding this physics of stress dependency of seismic wave propagation is potentially important in many applications.

We first develop a theory which relates effective stress to the physical properties of an unconsolidated granular medium. For simplicity, we consider a porous medium with vertical transverse isotropy (VTI), as horizontally layered sediments are represented by this symmetry. We start our derivation by decoupling the solid and the fluid phases that make up the bulk and the transport properties associated with a porous formation, as it is also done in the derivation of the Biot's theory.

The following assumptions are made in addition to those given in Section 2.3.1 in order to derive the dynamic equations of wave propagation in fluid-filled, unconsolidated granular sediments under stress:

1. Poisson's ratio is constant, whereas Young's modulus, bulk modulus and shear modulus of the effective material vary with stress. Experimental studies have shown that, for soft soils, the assumption of independence of Poisson's ratio to the applied stress is acceptable (Yokota & Konno, 1980; El Hosri, 1984; Lade & Nelson, 1987).
2. Purely elastic behaviour of the material is considered during a cycle of loading

along any arbitrary closed-loop stress (or strain) paths associated with an effective stress.

3. The grain diameter, grain density and bulk modulus are constant at different stress states.
4. Properties associated with the fluid phase, i.e. viscosity, fluid bulk modulus and fluid density are constant at different stress states.
5. The bulk transport properties, i.e. porosity, permeability and tortuosity are stress-dependent.

3.2.1 Stress-dependent elastic moduli

Generally speaking, from the point of view of Lagrange's mechanics, a change in stress state of the saturated porous material leads to changes in kinetic energy \mathcal{T} , potential energy Π and the dissipative function \mathcal{F} .

In Section 2.3.1 the generalised Hooke's law was derived for isotropic media (see Eqs. 2.17 and 2.18) based on the strain-potential energy approach. Similarly, the stress-strain relations for the general anisotropic poroelastic media, based on the same principle, are as follows (Biot, 1962; Cheng, 1997):

$$\tau_{ij} = A_{ijkl}e_{kl} - \alpha_{ij}p_f, \quad (3.1)$$

$$p_f = M\zeta - \alpha_{ij}Me_{ij}, \quad (3.2)$$

where A_{ijkl} , α_{ij} and M are the constitutive constants. The physical meaning of A_{ijkl} can be elucidated by setting $p_f = 0$ in Eq. (3.1), which gives

$$\tau_{ij} = A_{ijkl}e_{kl}. \quad (3.3)$$

Here A_{ijkl} are identical to the coefficients present in the theory of elasticity. The corresponding physical experiment is known as the jacketed or drained test, where the internal fluid pressure is constant. Thus, A_{ijkl} are the elastic material coefficients in drained condition. It can be shown (Cheng, 1997) that α_{ij} is a property of a solid constituent only. With the micro-isotropy assumption (i.e., isotropy at the grain scale) of the solid phase, one gets:

$$\alpha_{ij} = \delta_{ij} - \frac{A_{ijkk}}{3K_s}. \quad (3.4)$$

α_{ij} is also known as the Biot-Willis coefficient.

M in Eq. 3.2 is the a modulus associated with the combined fluid-solid compressibility. Based on the micromechanical analysis and the micro-isotropy assumption, one can get a simplified equation (Cheng, 1997):

$$M = \frac{K_s}{\left(1 - \hat{K}_b/K_s\right) - n(1 - K_s/K_f)}, \quad (3.5)$$

in which

$$\hat{K}_b = \frac{A_{iijj}}{9} \quad (3.6)$$

represents the generalized drained bulk modulus.

In case of transverse isotropy, we have eight independent material constants: five A_{ij} , two α_{ij} and one M . The matrix form of the stress-strain relations for the TI media with Ox_3 symmetry axis can be written as:

$$\begin{bmatrix} \tau_{11} \\ \tau_{22} \\ \tau_{33} \\ \tau_{12} \\ \tau_{23} \\ \tau_{31} \\ p_f \end{bmatrix} = \begin{bmatrix} A_{11} & A_{12} & A_{13} & 0 & 0 & 0 & -\alpha_{11}M \\ A_{12} & A_{11} & A_{13} & 0 & 0 & 0 & -\alpha_{11}M \\ A_{13} & A_{13} & A_{33} & 0 & 0 & 0 & -\alpha_{33}M \\ 0 & 0 & 0 & 2G & 0 & 0 & 0 \\ 0 & 0 & 0 & 0 & 2G' & 0 & 0 \\ 0 & 0 & 0 & 0 & 0 & 2G' & 0 \\ -\alpha_{11}M & -\alpha_{11}M & -\alpha_{33}M & 0 & 0 & 0 & M \end{bmatrix} \begin{bmatrix} e_{11} \\ e_{22} \\ e_{33} \\ e_{12} \\ e_{23} \\ e_{31} \\ \zeta \end{bmatrix}, \quad (3.7)$$

where $G = G_{12} = (A_{11} - A_{12})/2$ is the shear modulus in $x_1 - x_2$ (isotropy) plane. G' is the shear modulus perpendicular to the plane of isotropy. From Eq. (3.4) and (3.5) one can obtain:

$$\alpha_{11} = \alpha_{22} = 1 - \frac{A_{11} + A_{12} + A_{13}}{3K_s}, \quad (3.8)$$

$$\alpha_{33} = 1 - \frac{2A_{13} + A_{33}}{3K_s}, \quad (3.9)$$

$$\alpha_{44} = \alpha_{55} = \alpha_{66} = 0, \quad (3.10)$$

$$M = \frac{K_s}{\left(1 - \frac{2(A_{11} + A_{12} + 2A_{13}) + A_{33}}{9K_s}\right) - n\left(1 - \frac{K_s}{K_f}\right)}. \quad (3.11)$$

The drained elastic coefficients A_{ij} can be expressed in terms of more familiar material properties like Young's moduli and Poisson's ratios (Cheng, 1997). Because $E = E_1 = E_2$, $E' = E_3$, $\nu = \nu_{21}$, $\nu' = \nu_{32} = \nu_{31}$, for TI media we have:

$$A_{11} = \frac{E(E' - E\nu'^2)}{(1 + \nu)(E' - E'\nu - 2E\nu'^2)}, \quad (3.12)$$

$$A_{12} = \frac{E(E'\nu + E\nu'^2)}{(1 + \nu)(E' - E'\nu - 2E\nu'^2)}, \quad (3.13)$$

$$A_{13} = \frac{EE'\nu'}{E' - E'\nu - 2E\nu'^2}, \quad (3.14)$$

$$A_{33} = \frac{E'^2(1 - \nu)}{E' - E'\nu - 2E\nu'^2}, \quad (3.15)$$

where E is the drained Young's modulus in the plane of isotropy x_1-x_2 , E' the drained Young's modulus in the Ox_3 direction. $G = E/2(1+\nu)$ is the shear modulus in the plane of isotropy. The drained Poisson's ratio ν is characterizing the strain

reduction in the horizontal plane due to a tensile stress in the same plane. ν' is the drained Poisson's ratio characterizing the strain reduction in the horizontal plane due to a tensile stress perpendicular to the isotropy plane.

Now we have arrived at the convenient expressions, where the drained elastic coefficients are expressed in terms of Young's moduli and Poisson's ratios. Thus, if we are able to introduce stress-dependent Young's moduli ($E(\tau'_{ij}), E'(\tau'_{ij})$) and Poisson's ratios ($\nu(\tau'_{ij}), \nu'(\tau'_{ij})$), then that will bring us to the stress-dependent material coefficients $A_{ij}(\tau'_{ij})$ in the drained condition. This, in turn, will lead us to stress-dependent material coefficients also in the undrained condition $A_{ij}^u(\tau'_{ij})$ (Cheng, 1997):

$$A_{ij}^u(\tau'_{ij}) = A_{ij}(\tau'_{ij}) + \alpha_i(\tau'_{ij})\alpha_j(\tau'_{ij})M(\tau'_{ij}), \quad (3.16)$$

with τ'_{ij} denoting the in-situ effective stress in the porous material.

Strictly speaking,

$$A_{ij}^u = A_{ij}^u(E, E', \nu, \nu', n, K_s, K_f). \quad (3.17)$$

This means that only an introduction of stress-dependent elastic moduli $A_{ij}(\tau'_{ij})$ through the Young's moduli and Poisson's ratios will not completely address the problem. But we can still make the assumptions realistic by setting the bulk moduli of the solid and the fluid constituents (K_f and K_s , respectively) as stress-independent parameters. This is especially true for an unconsolidated medium, where the effect of external stress change on the K_s and K_f is negligible. As mentioned earlier, experimental studies on soils show that Poisson's ratio is nearly independent of the in-situ stress state (Yokota & Konno, 1980; El Hosri, 1984; Lade & Nelson, 1987). Because Poisson's ratio is given by $E/2G - 1$, this will imply that for soft soils the ratio E/G is nearly stress-independent. Therefore, from solely a mechanical point of view, the stress-dependent wave propagation through a fluid-saturated porous material can be addressed by considering the undrained elastic moduli as a function of stress-dependent Young's moduli and porosity (E, E', n), whereas all other parameters can realistically be considered as stress-independent. Now, restricting ourselves to the three parameters - E, E', n - which are stress-dependent, we can derive the mathematical expressions for only effective-stress law for the Young's moduli. Effective-stress laws for the porosity and the transport properties of the granular earth material will be given in Section 3.2.2.

Earlier experimental studies show a strong evidence that elastic moduli E , G and K_b of soil depend primarily on three factors: a) stress state, b) density or void ratio, c) stress history of the material (Hardin & Black, 1968). The general expression for shear modulus can be given in the form:

$$G = AF(e_v)\tau_0'^\mu, \quad (3.18)$$

in which A incorporates empirically the effect of stress history, mineralogy, angularity of grains, etc. $F(e_v)$ is a function describing the influence of void ratio $e_v = n/(1-n)$. Here τ_0' is the effective mean normal stress and μ is a material constant which may

vary between 0.35 and 0.9 for different type of soils but usually taken about 0.5 (Yu & Dakoulas, 1993).

Assuming the stress-independency of Poisson's ratio and by considering the principle of conservation of energy, which means that there is no energy dissipation in the closed-loop stress (or strain) paths, Yu & Dakoulas (1993) derived an expression for the elastic moduli of a transverse isotropic medium:

$$E = n_0 M_0 p_a \left[\left(\frac{I_1}{p_a} \right)^2 + 6 \frac{1+\nu}{1-2\nu} \frac{J_2}{p_a^2} + \frac{3(n_0 - m_0^2)}{1-2\nu} \left(\frac{\tau'_{33}}{p_a} \right)^2 \right]^{\lambda_0}, \quad (3.19)$$

$$E' = M_0 p_a \left[\left(\frac{I_1}{p_a} \right)^2 + 6 \frac{1+\nu}{1-2\nu} \frac{J_2}{p_a^2} + \frac{3(n_0 - m_0^2)}{1-2\nu} \left(\frac{\tau'_{33}}{p_a} \right)^2 \right]^{\lambda_0}, \quad (3.20)$$

where $n_0 = E/E'$, $m_0 = \nu'/\nu$, M_0 and λ_0 are material parameters which can be determined experimentally. p_a is the atmospheric pressure. I_1 and J_2 are, respectively, the first stress invariant and the second deviatoric stress invariant:

$$J_2 = \frac{1}{6} [(\tau'_{11} - \tau'_{22})^2 + (\tau'_{22} - m_0 \tau'_{33})^2 + (m_0 \tau'_{33} - \tau'_{11})^2] + (\tau_{12})^2 + (\alpha_0 \tau_{23})^2 + (\alpha_0 \tau_{31})^2, \quad (3.21)$$

$$I_1 = \tau'_{11} + \tau'_{22} + m_0 \tau'_{33}, \quad (3.22)$$

with $\alpha_0 = \sqrt{G/G'}$. Substitution of Eqs. (3.19) and (3.20) into Eqs. (3.12), (3.13), (3.14) and (3.15) gives finally the stress-dependent Biot's coefficients.

3.2.2 Stress-dependent transport properties

In the previous section, we have investigated the change in strain potential due to a change in the stress state in the fluid-saturated porous solid by introducing stress-dependent elastic moduli. However, the change in porosity with the changing stress has not been considered. In this section, we look at the change in kinetic energy and in the dissipative function caused by the stress state change. This simple analysis will show the need of introduction of stress-dependent transport properties (porosity, permeability, viscosity, and tortuosity) of a geomaterial.

Following Biot (1962), the kinetic energy in an anisotropic medium containing fluid-filled pores can be written as:

$$\mathcal{T} = \frac{1}{2} \rho \dot{u}_i \dot{u}_i + \rho_f \dot{u}_i \dot{w}_i + \frac{1}{2} m_{ij} \dot{w}_i \dot{w}_j. \quad (3.23)$$

Since \dot{u}_i and \dot{w}_i are the generalised coordinates, and assuming that the fluid density and the solid density are stress-independent, the kinetic energy of the system changes only if the added mass m_{ij} (associated with the relative microvelocity fields) and the bulk density ρ change with the stress state:

$$m_{ij} = m_{ij}(\tau'_{ij}) = \frac{\gamma_{ij}(\tau'_{ij})}{n(\tau'_{ij})} \rho_f, \quad (3.24)$$

$$\rho = (1 - n(\tau'_{ij})) \rho_s. \quad (3.25)$$

Here γ_{ij} is the tortuosity tensor. Therefore, the change in porosity and in tortuosity due to stress changes causes a change in the kinetic energy of the system.

On the other hand, as discussed in Section 2.3, the effect of the surrounding media to a mechanical system cannot be neglected due to the presence of drag forces. In fact, the variation in the stress state leads the filtration process (wave-induced fluid flow) to change due to the change in the structure (i.e., tortuosity, permeability) of the porous material. This suggests that the drag force coefficients defined in Eq. (2.8) are stress dependent and inevitably make dissipative function \mathcal{F} to be a function of stress state as well:

$$2\mathcal{F} = a_{ij}(\tau'_{ij})\dot{w}_i\dot{w}_j. \quad (3.26)$$

Recalling the drag coefficients from Biot (1962) one can write:

$$a_{ij} = \frac{\eta}{k_{ij}(\tau'_{ij})}, \quad (3.27)$$

where $k_{ij}(\tau'_{ij})$ is the permeability tensor as a function of effective stress. Note, we have assumed here the viscosity to be stress-independent; this is because the system is considered to be in an isothermal condition. In reality, for a closed system, the pore-fluid pressure may change with an applied confining stress. According to the equation of state of an ideal gas (Clapeyron-Mendeleyev equation) or of a fluid/real gas (Van der Waals equation), the temperature of the system will change as well, causing the viscosity to change. Note that for a deep reservoirs, the assumption of stress-independent viscosity of fluid/gas may not be realistic. But for shallow subsurface studies, this assumption is acceptable.

Assuming that the directions of permeability k_i and tortuosity γ_i coincide with the principle axis x_i for a TI medium, we can write:

$$k_{ij}(\tau'_{ij}) = \begin{bmatrix} k_1 & 0 & 0 \\ 0 & k_1 & 0 \\ 0 & 0 & k_3 \end{bmatrix} \quad (3.28)$$

and

$$\gamma_{ij}(\tau'_{ij}) = \begin{bmatrix} \gamma_1 & 0 & 0 \\ 0 & \gamma_1 & 0 \\ 0 & 0 & \gamma_3 \end{bmatrix}. \quad (3.29)$$

Introduction of $n(\tau'_{ij})$, $k_{ij}(\tau'_{ij})$ and $\gamma_{ij}(\tau'_{ij})$ finally leads to stress-dependent Π , \mathcal{T} , and \mathcal{F} and fully solve the problem of stress-dependent, dispersive elastic wave propagation.

In order to address stress-dependent transport properties, Berryman (1992) derived useful expressions. These expressions relate transport property variations to changes in the effective stresses. These can generally be expressed as (Mavko *et al.*, 2009, Section 2.6):

$$X^l = f^l(p_c - \phi^l p_f). \quad (3.30)$$

This is called the effective stress law for the property X^l , with its associated f^l and ϕ^l (Zimmerman, 1989; Berryman, 1992; Gurevich, 2004). Here ϕ^l is also known as the effective-stress coefficient for X^l . For porosity and permeability under hydrostatic stress $p_c = \frac{1}{3}(\tau_{11}^c + \tau_{22}^c + \tau_{33}^c)$, the effective-stress law for monomineralic porous solid is as follows (Berryman, 1992):

$$\frac{\delta n}{n} = - \left(\frac{\alpha - n}{nK_b} \right) (\delta p_c - \phi^n \delta p_f), \quad (3.31)$$

$$\frac{\delta k}{k} = - \left[h \left(\frac{\alpha - n}{nK_b} \right) + \frac{2}{3K_b} \right] (\delta p_c - \phi^k \delta p_f), \quad (3.32)$$

where $\alpha = 1 - K_b/K_s$ is the Biot-Willis coefficient. Here ϕ^n and ϕ^k are, respectively, the effective-stress coefficients for porosity and permeability:

$$\phi^n = \left(\frac{\beta - n}{\alpha - n} \right) \alpha, \quad (3.33)$$

$$\phi^k = 1 - \frac{2n(1 - \alpha)}{3h(\alpha - n) + 2n} \leq 1, \quad (3.34)$$

in which $\beta = 1 - nK_b/(K_s - K_b)$. Berryman (1992) concluded that the nominal value for h is approximately 4.

In case of anisotropy, Eqs. (3.31) and (3.32) should be adopted accordingly. We have generalized Berryman's effective stress laws for porosity and permeability for the case of full anisotropy. Thus, taking account of the scalar nature of porosity, we have:

$$\frac{\delta n}{n} = - \left(\frac{\hat{\alpha} - n}{n\hat{K}_b} \right) (\delta p_c - \hat{\phi}^n \delta p_f), \quad (3.35)$$

where $\hat{\alpha} = 1 - \hat{K}_b/K_s$. Given the tensor nature of permeability, we can write

$$\begin{aligned} \left(\frac{\delta k}{k} \right)_{ij} = & - \left[h \left(3 \frac{\alpha_{ij} - n}{n(A_{ij11} + A_{ij22} + A_{ij33})} \right) \right. \\ & \left. + \frac{2}{A_{ij11} + A_{ij22} + A_{ij33}} \right] (\delta \tau_{ij}^c - \phi_{ij}^k \delta p_f \delta_{ij}), \end{aligned} \quad (3.36)$$

where τ_{ij}^c is the confining stress tensor. No implicit summation over repeated subscripts is applied in the above equation. The effective-stress coefficient for porosity and permeability are, respectively, given as follows:

$$\phi_{ij}^k = 1 - \frac{2n(1 - \alpha_{ij})}{3h(\alpha_{ij} - n) + 2n} \leq 1, \quad (3.37)$$

$$\hat{\phi}^n = \left(\frac{\hat{\beta} - n}{\hat{\alpha} - n} \right) \hat{\alpha}, \quad (3.38)$$

with $\hat{\beta} = 1 - n\hat{K}_b/(K_s - \hat{K}_b)$.

Eqs. (3.35) and (3.36) represent general effective stress laws for porosity and permeability in case of an anisotropic medium, where micro-isotropy assumption is made for the grains. These equations can easily be adapted to the case of TI or isotropic media.

What is left so far is tortuosity. Next, we derive a new effective-stress law for tortuosity. We start derivation from Kozeny-Carman relationship (Carman, 1937; Chotiros & Isakson, 2004) which gives:

$$\gamma = \frac{a^2 n}{8k}, \quad (3.39)$$

where a is the pore size. By itself a can be a complex function of stress. However, Hovem & Ingram (1979) showed that a can be expressed in terms of grain diameter d_0 and porosity n :

$$a = \frac{d_0 n}{3(1-n)}. \quad (3.40)$$

Substitution of Eq. (3.40) into Eq. (3.39) yields

$$\gamma(d_0, n, k) = \frac{d_0^2 n^3}{72k(1-n)^2}. \quad (3.41)$$

This is a convenient equation since it relates to more familiar physical properties – grain diameter, porosity and permeability. Now, neglecting any change in the grain diameter due to a change in stress, one can write the variation of tortuosity as a function of stress change as follows:

$$d\gamma = \frac{\partial\gamma}{\partial k} dk + \frac{\partial\gamma}{\partial n} dn. \quad (3.42)$$

Calculating the partial derivatives of $\partial\gamma/\partial k$ and $\partial\gamma/\partial n$ from Eq. (3.41), we arrive at

$$\frac{\delta\gamma}{\gamma} = -\frac{\delta k}{k} + \left(\frac{3-n}{1-n}\right) \frac{\delta n}{n}. \quad (3.43)$$

By substituting Eqs. (3.35) and (3.36) into Eq. (3.43) yields the effective-stress law for tortuosity in anisotropic media

$$\left(\frac{\delta\gamma}{\gamma}\right)_{ij} = f_{ij}^\gamma (\delta\tau_{ij}^c - \phi_{ij}^\gamma \delta p_f \delta_{ij}). \quad (3.44)$$

No implicit summation over repeated subscripts is applied in the above equation, where

$$f_{ij}^\gamma = B_{ij}^k - \frac{BB^n}{3} \delta_{ij}, \quad (3.45)$$

$$\phi_{ij}^\gamma = \frac{B_{ij}^k \phi_{ij}^k - BB^n \hat{\phi}^n}{B_{ij}^k - \frac{BB^n}{3} \delta_{ij}}, \quad (3.46)$$

with

$$B_{ij}^k = h \left(3 \frac{\alpha_{ij} - n}{n(A_{ij11} + A_{ij22} + A_{ij33})} \right) + \frac{2}{A_{ij11} + A_{ij22} + A_{ij33}}, \quad (3.47)$$

$$B^n = \frac{\hat{\alpha} - n}{n\hat{K}_b}, \quad (3.48)$$

$$B = \frac{3 - n}{1 - n}. \quad (3.49)$$

Eqs. (3.35), (3.36) and (3.44) are the anisotropic effective-stress laws for porosity, permeability and tortuosity, respectively.

The practical importance of the derived effective-stress law for tortuosity (Eq. 3.43) can readily be seen from the formation factor of a porous material (Archie, 1942):

$$\hat{F} = \frac{\gamma}{n^m}, \quad (3.50)$$

where \hat{F} is the formation factor and m is the cementation exponent which increases as the formation becomes more consolidated. This cementation exponent varies between 1.3 and 2.5 and is close to 1.5 for unconsolidated sands (Carothers, 1968). The formation factor \hat{F} is a crucial parameter in determining reservoir characteristics (e.g., soil/rock type, fluid content, etc.), and in fact, using Eqs. (3.31) and (3.43), one can quantify the change in \hat{F} due to a change in effective stress. Importantly, note that, Eq. (3.50) can be used to check the validity of Eq. (3.43) (or Eq. 3.44 for VTI case). This can be done by calculating \hat{F} as the function of stress and check whether there is a linear trend between $\log(\hat{F})$ and $\log(n)$ (Archie, 1942), which is a general observation for soils and rocks.

Combining Eqs. (2.12), (2.13), (2.14), (3.23) and (3.26) we arrive at the equation of motion in anisotropic media

$$\frac{\partial}{\partial x_j} ((A_{ijkl} + \alpha_{ij}\alpha_{kl}M)e_{kl} - \alpha_{ij}M\zeta) = \frac{\partial^2}{\partial t^2}(\rho u_i + \rho_f w_i), \quad (3.51)$$

$$-\frac{\partial}{\partial x_i}(M\zeta - \alpha_{jk}M e_{jk}) = \frac{\partial^2}{\partial t^2}(\rho_f u_i + m_{ij}w_j) + \frac{\eta}{k_{ij}} \frac{\partial w_j}{\partial t}. \quad (3.52)$$

Considering TI and substituting the stress-dependent elastic moduli (Eqs. 3.12-3.15) and transport rock properties (Eqs. 3.35, 3.36 and 3.44) in Eqs (3.51) and (3.52), we obtain stress-dependent poroelastic equations for a TI medium.

To solve Eqs. (3.51) and (3.52), we seek the plane wave solutions of the form $e^{i(\kappa l_1 x_1 + \kappa l_2 x_2 + \kappa l_3 x_3 - \omega t)}$, where l_i denotes the direction cosines. Without a loss of generality, we consider the motion to be in the x_1 - x_3 plane. Then $l_2 = 0$, $l_1 = \sin(\theta)$, $l_3 = \cos(\theta)$, where θ is the angle between the direction of wave propagation and the Ox_3 axis. This gives two decoupled systems of equations in the frequency domain, from which we obtain four complex roots.

For κ_{P_1} , κ_{P_2} , and κ_{SV} , we have:

$$\begin{vmatrix} \omega^2 \rho - \kappa^2 (A_{11}l_1^2 + A_{44}l_3^2) & -\kappa^2 (A_{13} + A_{44})l_1l_3 & \omega^2 \rho_f + \kappa^2 l_1^2 M_{11} & \kappa^2 l_1 l_3 M_{11} \\ -\kappa^2 (A_{13} + A_{44})l_1l_3 & \omega^2 \rho - \kappa^2 (A_{44}l_1^2 + A_{33}l_3^2) & \kappa^2 l_1 l_3 M_{33} & \omega^2 \rho_f + \kappa^2 l_3^2 M_{33} \\ \omega^2 \rho_f + \kappa^2 l_1^2 M_{11} & \kappa^2 l_1 l_3 M_{33} & m_{11}\omega^2 + i\omega \frac{\eta F_1}{k_1} - \kappa^2 l_1^2 M & -\kappa^2 l_1 l_3 M \\ \kappa^2 l_1 l_3 M_{11} & \omega^2 \rho_f + \kappa^2 l_3^2 M_{33} & -\kappa^2 l_1 l_3 M & m_{33}\omega^2 + i\omega \frac{\eta F_3}{k_3} - \kappa^2 l_3^2 M \end{vmatrix} = 0, \quad (3.53)$$

where F_1 and F_3 are the viscous correction factors for the fluid flow in x_1 and x_3 directions, respectively. The determinant (3.53) yields

$$a_1x^3 + a_2x^2 + a_3x + a_4 = 0, \quad (3.54)$$

where $x = (\kappa_\alpha/\omega)^2$. The solution of Eq. (3.54) is given in Appendix A. Thus, for P - and SV -waves, the velocities and attenuations can be calculated from:

$$V_\alpha = \frac{\omega}{\text{Re}(\kappa_\alpha)}, \quad (3.55)$$

$$Q_\alpha^{-1} = \frac{2\text{Im}(\kappa_\alpha)}{\text{Re}(\kappa_\alpha)}, \quad (3.56)$$

where $\alpha = P_1, P_2$ and SV .

For SH -waves, we have the following equation in the frequency domain:

$$\begin{vmatrix} \omega^2 \rho - \kappa^2 (A_{66}l_1^2 + A_{44}l_3^2) & \omega^2 \rho_f \\ \omega^2 \rho_f & m_{11}\omega^2 + i\omega \frac{\eta F_1}{k_1} \end{vmatrix} = 0. \quad (3.57)$$

SH -wave velocity and attenuation can calculated from:

$$V_{SH} = \frac{\omega}{\text{Re}(\kappa_{SH})}, \quad (3.58)$$

$$Q_{SH}^{-1} = \frac{2\text{Im}(\kappa_{SH})}{\text{Re}(\kappa_{SH})}. \quad (3.59)$$

3.2.3 Numerical tests

In this section, we present results of numerical tests using the new stress-dependent poroelasticity formulations in TI media developed in the previous section. We consider permeability and tortuosity to be in the i^{th} direction. This direction coincides with the principal direction x_i . Figure 3.1 shows the calculated phase velocity and attenuation of all four body waves as a function of frequency. For each wave, the different curves correspond to different values of the angle of propagation with respect to the vertical direction, which vary from 0° to 90° at a step of 22.5° . The frequency-angle forward modelling is performed for unconsolidated sediments with realistic values of the properties, as shown in Table 3.1. In addition, soil properties like n , η , G , K_s , K_f , ρ_s and ρ_f are taken from Table 2.1. Horizontal and vertical Young's moduli (E and E' , respectively) are calculated from Eqs. (3.19) and (3.20) and are used to calculate A_{ij} in Eqs. (3.12)-(3.15). Effective stress applied to the media in vertical and horizontal directions are taken, respectively, $\tau'_{33} = 200$ kPa and $\tau'_{11} = \tau'_{22} = 100$ kPa.

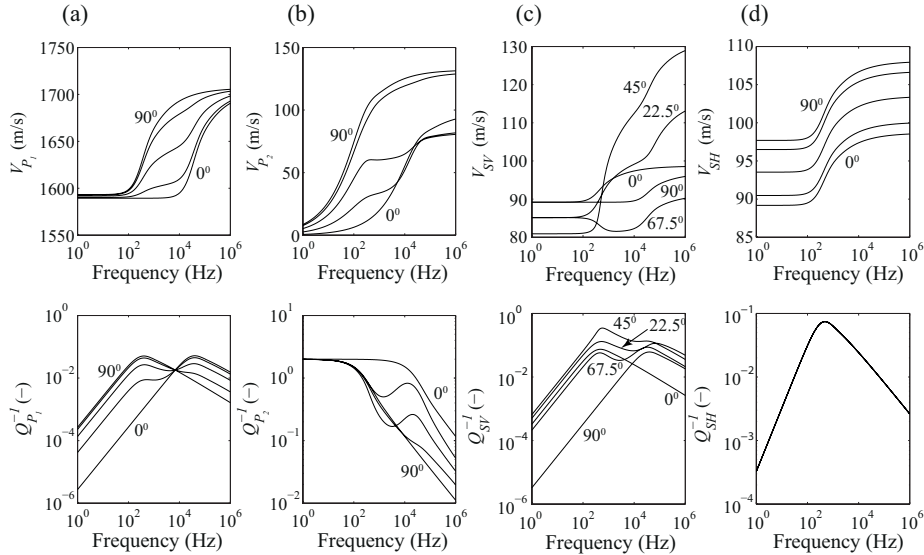


Figure 3.1: Theoretically estimated dispersive velocity and attenuation calculated for different wavetypes: (a) P_1 , (b) P_2 , (c) SV and (d) SH waves. Input parameters are shown in Table 3.1.

Because there are two Biot's characteristic frequencies, i.e. one in the horizontal plane and the other along the vertical direction, one can observe two relaxation peaks for all body waves except SH , when the propagation angle θ is between 0^0 and 90^0 . The polarization direction of the SH wave is always parallel to the symmetry plane ($x_1 - x_2$). Therefore, it peaks only at one characteristic frequency corresponding to the horizontal plane. Note that the Biot characteristic frequencies for P_1 - and SV -waves are different at 0^0 and 90^0 and they coincide only when their propagation directions are perpendicular to each other.

Figure 3.2 shows the phase velocity and the attenuation of all four body waves as a function of the effective stress in the horizontal direction, when τ'_{33} (vertical effective stress) is kept constant. For simplicity, the pore pressure is taken as constant. This is realistic, especially for unconsolidated sandy sediments, where the fluid can freely move in the formation keeping the pore pressure constant. In this case, the effective stress changes are the same as the changes in the confining stress. In this example, we only change the horizontal effective stress τ'_{11} , keeping the effective vertical stress τ'_{33} constant at 200 kPa. The input stress-dependent reference elastic moduli A_{ij} are calculated; they represent stress state $\tau'_{33} = 200$ kPa and $\tau'_{11} = 50$ kPa, using the values shown in Table 3.1. All other parameters in the model are considered to be the same as in Figure 3.1. Then, we change the horizontal effective-stress to $\delta\tau'_{11} = 100, 200$, and 300 kPa. The results are shown for all four body waves in Figure 3.2.

Note that the effect of varying $\delta\tau'_{11}$ is more pronounced in velocity dispersion than in attenuation. The change in velocity dispersion is nonlinear as a function of stress and this nonlinearity is, in turn, angle-dependent (Figures 3.2). Especially, it is more

Parameter	Unit	Value
Permeability, k_1	μm^2	100
Permeability, k_3	μm^2	1
Tortuosity, γ_1	-	1.25
Tortuosity, γ_3	-	1.5
Poisson's ratio ($x_1 - x_2$ plane), ν	-	0.2
Poisson's ratio ($x_3 - x_1$ plane), ν'	-	0.25
Shear rigidity, G'	MPa	20
Material parameter, M_0	-	1.948
Material parameter, λ_0 ,	-	1.419
Degree of anisotropy, n_0 ,	-	2

Table 3.1: Values of parameters used in the Biot model (see Fig. 3.1).

conspicuous for slow P - and SV -waves. This stress- and angle-dependent seismic dispersion provides extra information about the medium, which, to our knowledge was not known before. Theoretical calculations show that the attenuation decreases when the stress increases. Intuitively, this is because an increase in stress closes the voids, and this results in a decrease in the fluid mobility in the formation. As a result, there is a smaller energy dissipation. For the unconsolidated media, attenuations of all body waves are rather insensitive to stress changes in the horizontal direction. This is expected, since the effective stress laws do not provide a dramatic change in the transport properties, especially for relatively small changes in the stress state. In this connection, one may introduce a different effective stress law relevant to a specific medium. In such a case, the stress change may cause a dramatic change in the transport properties. This may be the case for a medium containing compliant cracks. In this case, the permeability change can be conspicuous and may result in a change in attenuation. This is more expected for consolidated materials and rocks. In addition, when the material has an inherent heterogeneity in solids or in fluid phases, the stress change can affect the distribution and the sizes of the heterogeneities. As a consequence, this may change attenuation and velocity dispersion dramatically even at seismic exploration scales. This is left as a topic for future research.

3.3 Conclusions

In this chapter, we have developed a theory which relates the in-situ stress in a porous earth material to the properties of propagating seismic waves. This has been possible by considering separately stress-dependent elastic moduli and stress-dependent transport properties. We have linked these two domains through Lagrangian formulation as was also done by Biot but without incorporation of stress. By constructing the Lagrangian with a dissipative function for fluid-filled granular media, the effect of stress on the kinetic and strain-potential energy has been discussed. Interestingly, the strain-potential energy is nearly independent of the change

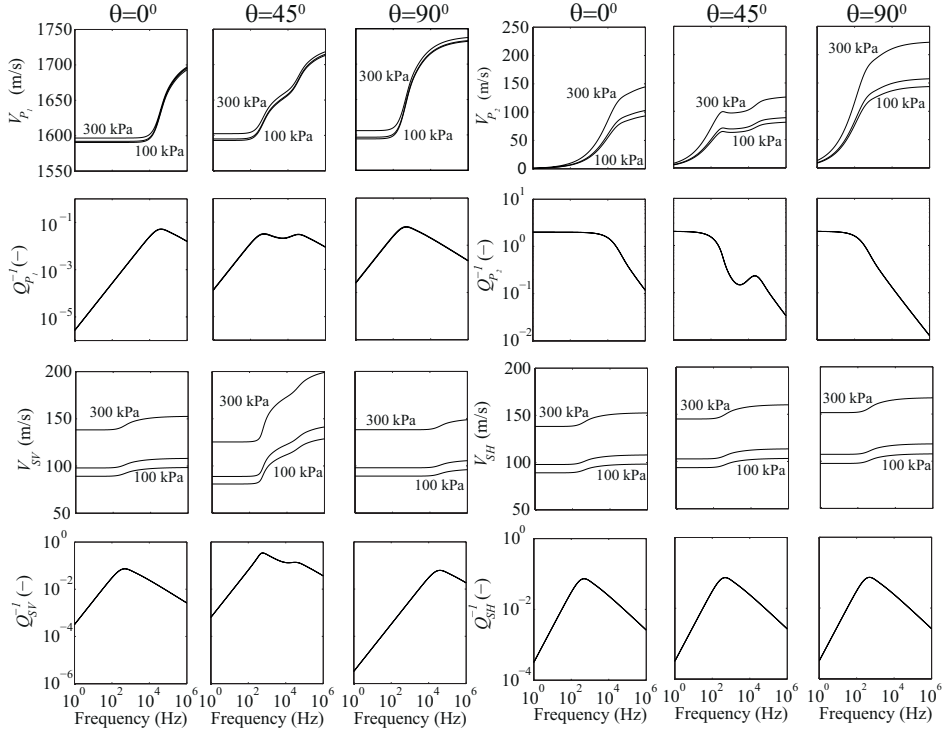


Figure 3.2: Theoretical velocities and attenuations calculated for all four body waves at different $\delta\tau'_{11}$ (100 kPa, 200 kPa, and 300 kPa).

in the transport properties. The primary factors causing the stress change are the elastic moduli. The effects of stress change on the kinetic energy and on the dissipation function of a saturated material are controlled by stress-induced changes in both transport properties and elastic moduli. We have looked at the thermodynamic state of the system which may vary with the applied stress, by considering the dissipative function. This function is strictly dependent on the drag coefficients and on the generalized velocities. We have introduced stress-dependent drag coefficients based on the so-called effective stress laws associated with the permeability. The latter was proposed earlier by Berryman (1992). We have generalized these effective stress laws for the full anisotropic case. In order to describe consistently the change in the relative micro-velocity field of the system with stress, a new effective stress law for the tortuosity has been derived in this chapter. Finally, the effect of effective stress and the angle of wave propagation relative to the axisymmetric axis has been studied for all four body waves. We find that the velocity dispersion is nonlinear with stress, and the stress-dependence is more conspicuous for velocity than for attenuation. It is observed that this nonlinearity in seismic velocity dispersion is more prominent for the slow P and SV waves than for the fast P and SH waves.

3.4 Appendix A: Coefficients and roots of cubic equation

Here we solve the cubic equation given in Eq. (3.54) and obtain explicit expressions for coefficients a_1 , a_2 , a_3 , and a_4 .

By substituting $x = y - a_2/3a_1$ into Eq. (3.54) one can arrive at

$$y^3 + p_1 y + p_2 = 0, \quad (3.60)$$

where

$$p_1 = -\frac{a_2^2}{3a_1^2} + \frac{a_3}{a_1}, \quad (3.61)$$

$$p_2 = \frac{2a_2^3}{27a_1^3} - \frac{a_2a_3}{3a_1^2} + \frac{a_4}{a_1}. \quad (3.62)$$

The roots of Eq. (3.60) can be found from Cardano's formula:

$$y_1 = L_1 + L_2, \quad (3.63)$$

$$y_2 = -\frac{L_1 + L_2}{2} + \frac{L_1 - L_2}{2}\sqrt{3}i, \quad (3.64)$$

$$y_3 = -\frac{L_1 + L_2}{2} - \frac{L_1 - L_2}{2}\sqrt{3}i, \quad (3.65)$$

where

$$L_1 = \left(-\frac{p_2}{2} + \sqrt{\left(\frac{p_2}{2}\right) + \left(\frac{p_1}{3}\right)^3} \right)^{\frac{1}{3}}, \quad (3.66)$$

$$L_2 = \left(-\frac{p_2}{2} - \sqrt{\left(\frac{p_2}{2}\right) + \left(\frac{p_1}{3}\right)^3} \right)^{\frac{1}{3}}. \quad (3.67)$$

The coefficients a_1 , a_2 , a_3 and a_4 are found from calculation of the determinant in Eq. (3.53).

$$\begin{aligned} a_1 = & A_{44}l_3^6M_{33}^2B_{11} - 2l_1^4l_3^2A_{13}M_{33}M_{11}B_{33} - 2l_1^4l_3^2A_{44}M_{33}M_{11}B_{33} \\ & + l_1^4M_{11}^2A_{33}l_3^2B_{33} + l_1^4l_3^2M_{11}^2A_{44}B_{11} + l_1^2l_3^4M_{11}^2A_{33}B_{11} \\ & - A_{44}l_3^4A_{33}l_1^2MB_{33} - 2l_1^2l_3^4A_{44}M_{33}M_{11}B_{11} + A_{44}l_3^4l_1^2M_{33}^2B_{33} \\ & - A_{11}l_1^4A_{44}B_{11}l_3^2M - A_{11}l_1^6A_{44}MB_{33} + l_1^2l_3^4A_{13}^2B_{11}M \\ & - A_{11}l_1^2A_{33}l_3^4B_{11}M - A_{11}l_1^4A_{33}l_3^2MB_{33} + A_{11}l_1^4l_3^2M_{33}^2B_{33} \\ & - 2l_1^2l_3^4A_{13}M_{33}M_{11}B_{11} + A_{11}l_1^2l_3^4M_{33}^2B_{11} + l_1^4l_3^2A_{13}^2MB_{33} \\ & - A_{44}l_3^6A_{33}B_{11}M + 2l_1^2l_3^4A_{13}A_{44}B_{11}M + 2l_1^4l_3^2A_{13}A_{44}MB_{33} + l_1^6M_{11}^2A_{44}B_{33}, \end{aligned} \quad (3.68)$$

$$\begin{aligned}
a_2 = & \rho_f^2 l_3^4 M_{33}^2 + l_1^4 M_{11}^2 \rho_f^2 + 2 \rho_f^2 l_3^2 M_{33} l_1^2 M_{11} - \rho_f^2 A_{33} l_3^4 M \\
& - A_{11} l_1^4 \rho_f^2 M - 2 l_1^2 l_3^2 A_{13} \rho_f^2 M - 4 A_{44} l_3^2 \rho_f^2 l_1^2 M + 2 A_{11} l_1^2 \rho_f l_3^2 M_{33} B_{11} \\
& + A_{44} l_3^4 \rho B_{11} M + A_{44} l_3^2 \rho l_1^2 M B_{33} + A_{44} l_3^4 A_{33} B_{11} B_{33} + \rho A_{33} l_3^4 B_{11} M \\
& + 2 A_{44} l_3^4 \rho_f M_{33} B_{11} + A_{11} l_1^2 \rho B_{11} l_3^2 M + \rho A_{33} l_3^2 l_1^2 M B_{33} \\
& - \rho l_1^2 l_3^2 M_{33}^2 B_{33} - \rho l_3^4 M_{33}^2 B_{11} + A_{11} l_1^4 \rho M B_{33} + A_{11} l_1^4 A_{44} B_{11} B_{33} \\
& + A_{11} l_1^2 A_{33} l_3^2 B_{11} B_{33} - 2 l_1^2 l_3^2 A_{44} M_{33} \rho_f B_{33} - 2 l_1^2 l_3^2 A_{44} \rho_f M_{11} B_{11} \\
& + 2 \rho_f A_{44} l_1^4 M_{11} B_{33} + 2 \rho_f A_{33} l_3^2 l_1^2 M_{11} B_{33} - l_1^4 M_{11}^2 \rho B_{33} \\
& - 2 l_1^2 l_3^2 A_{13} \rho_f M_{11} B_{11} - l_1^2 l_3^2 M_{11}^2 \rho B_{11} - l_1^2 l_3^2 A_{13}^2 B_{11} B_{33} \\
& - 2 l_1^2 l_3^2 A_{13} A_{44} B_{11} B_{33} - 2 l_1^2 l_3^2 A_{13} M_{33} \rho_f B_{33} + \rho A_{44} l_1^2 B_{11} l_3^2 M \\
& + \rho A_{44} l_1^4 M B_{33}, \tag{3.69}
\end{aligned}$$

$$\begin{aligned}
a_3 = & 2 \rho_f^3 l_3^2 M_{33} + \rho_f^2 A_{44} l_1^2 B_{33} - 2 \rho \rho_f l_3^2 M_{33} B_{11} \\
& - \rho A_{33} l_3^2 B_{11} B_{33} - A_{11} l_1^2 \rho B_{11} B_{33} - \rho A_{44} l_1^2 B_{11} B_{33} \\
& - A_{44} l_3^2 \rho B_{11} B_{33} + \rho \rho_f^2 l_1^2 M - \rho^2 B_{11} l_3^2 M - 2 \rho_f \rho l_1^2 M_{11} B_{33} \\
& + 2 \rho_f^3 l_1^2 M_{11} + \rho_f^2 \rho l_3^2 M + A_{11} l_1^2 \rho_f^2 B_{11} \\
& + \rho_f^2 A_{33} l_3^2 B_{33} - \rho^2 l_1^2 M B_{33} + A_{44} l_3^2 \rho_f^2 B_{11} \tag{3.70}
\end{aligned}$$

$$a_4 = -\rho_f^2 \rho B_{33} + \rho_f^4 + \rho^2 B_{11} B_{33} - \rho \rho_f^2 B_{11}, \tag{3.71}$$

where $B_{11} = m_{11} + i\eta F_1/(\omega k_1)$ and $B_{33} = m_{33} + i\eta F_3/(\omega k_3)$.

Chapter 4

Contrasting behaviour between dispersive seismic velocity and attenuation: Advantages in subsoil characterizationⁱ

4.1 Introduction

In the previous chapters, we have derived theoretical formulations to predict frequency-dependent velocities and attenuations in fully- and partially-saturated granular earth media. Relevant extensions of Biot's theory have been investigated in Chapter 2. A new stress-dependent poroelastic formulation has been proposed in Chapter 3.

In this chapter, we focus our attention on the applicability of these poroelasticity theories in the frequency range of exploration seismics for characterization of unconsolidated porous soil layers. A careful look into the pertinent models of poroelasticity reveals that in fluid-saturated sediments or soils, the seismic (P - and S -wave) velocity dispersion and attenuation in the low field-seismic frequency band (20 to 200 Hz) have a contrasting behaviour in different property domains:

1. porosity-permeability,
2. effective stress-permeability, and
3. porosity-water saturation.

This contrasting behaviour can be advantageously used in the optimization algorithms in order to obtain unique, stable and independent estimates of these properties which are otherwise difficult to obtain.

ⁱA part of this chapter (Section 4.2.1) is published as a journal article in the *Journal of the Acoustical Society of America* **131** (2), EL170–EL176 (Zhubayev & Ghose, 2012a). Minor changes have been introduced to make the text consistent with other chapters of this thesis.

We first present the results of our research which concentrates on P - and S -wave dispersion in water-saturated soils and at the field seismic frequency band for soft soils (approximately 20 to 200 Hz). A study on the behaviour of dispersive seismic velocity and attenuation in the n - k domain reveals a significant difference. This contrasting behaviour will be utilized in a cost function integration scheme, leading to stable and unique estimates of both n and k . The effects of using only S -wave and both P - and S -waves and the effect of maximum frequency content in the data will be examined for different soil types (gravel, medium sand, fine sand, sandy clay) through numerical tests using realistic material parameters.

Next making use of the newly developed theory on stress-dependent elastic wave propagation in granular poroelastic media (Chapter 3), we investigate seismic attenuation and velocity dispersion associated with different body waves in case of fully-saturated transverse isotropic media. We shall study how these seismic attributes can be beneficially used in inverting for effective horizontal stress and directional permeability. The utility of additional information of the wave propagation angle on the convergence of the solution will be rigorously investigated.

When a medium is partially saturated with a fluid, the seismic response may change drastically compared to full saturation. Extending Biot-Stoll's model to partial saturation and making use of Gassmann's equation, as discussed in Chapter 2, in this chapter we shall look at the behaviour of seismic velocity and attenuation in the porosity - water saturation domain. This will lead us to propose new ways for deriving soil properties in a partially-saturated medium.

Lastly, in this chapter, we shall study the possibility of a combined use of seismic and GPR velocities to successfully retrieve porosity and water saturation in the shallow subsurface.

4.2 Fully saturated media

In situ properties of geomaterials and the stress state are of primary interest in various disciplines. Often the target zones are at depths which are below the water table, where full saturation can be assumed. Some of the most important yet challenging characterization targets in shallow subsoils are in-situ stress, porosity and fluid mobility in the formation. Here we present an approach to address these key targets based on integration of dispersive seismic attributes governed by the pertinent models of poroelasticity.

4.2.1 Porosity and permeability from integrated velocity and attenuation dispersion

For water-saturated unconsolidated sediments, Stoll's adaptations of Biot's theory (Stoll and Bryan, 1970; Stoll, 1977) have earlier been tested on field seismic data (Holland and Brunson, 1988). These models have been found to be capable of predicting the field-observed seismic dispersion for a variety of soil types. In addition to these models, we have looked into the BICSQS model (Biot model with grain contact squirt flow and shear drag by (Chotiros and Isakson, 2004)) and the

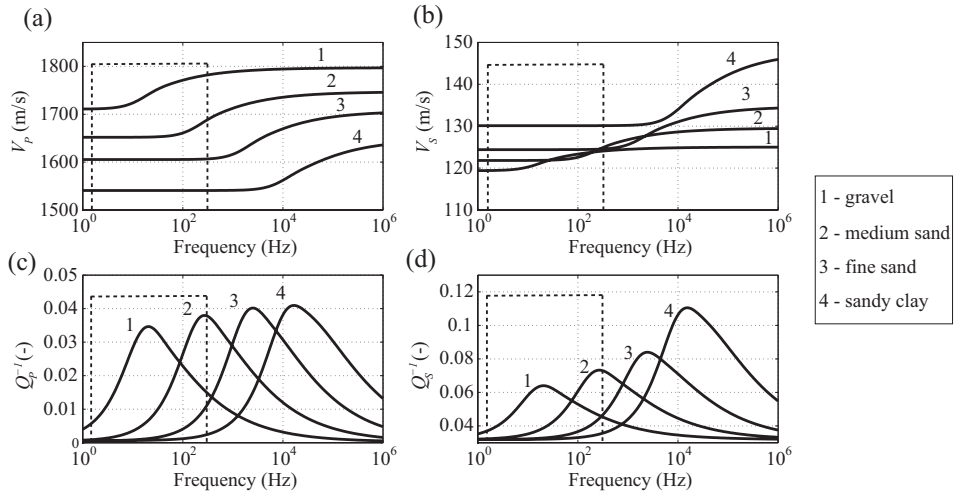


Figure 4.1: P - and S -wave dispersive velocity and attenuation (inverse quality factor) estimated using the Biot-Stoll model for four different permeability (k) and porosity (n) values, representing four different soil types. The dashed box represents the typical field seismic frequency band in soft soil.

Rayleigh-Plesset-Biot model (Smeulders and van Dongen, 1997; Vogelaar, 2009), and have examined them on a compiled database of seismic dispersion observed in soft soil sites. In agreement with Holland and Brunson (1988), we find that the Stoll and Bryan (1970) model (or Biot-Stoll model) can indeed explain well the observed seismic dispersion, except for coarse-grained soils for which BICSQS appears to be more suitable (see Chapter 6). In this Section, we shall illustrate our findings on the behaviour of the dispersive seismic velocity and attenuation in the n - k domain, using the Biot-Stoll model. The above-mentioned behaviour will be little affected if a different model is used. In practice, one may use the model that fits the observed dispersion data best.

Figures 4.1(a) and 4.1(c) illustrate, respectively, the dispersive velocity and attenuation (inverse quality factor) for P -waves in water-saturated soft soil, estimated using Biot-Stoll model. The dispersion curves for four different porosity and permeability values ($n = 0.35$, $k = 1.09 \times 10^{-9} \text{ m}^2$; $n = 0.4$, $k = 1.05 \times 10^{-10} \text{ m}^2$; $n = 0.45$, $k = 1.42 \times 10^{-11} \text{ m}^2$; and $n = 0.55$, $k = 3.31 \times 10^{-12} \text{ m}^2$) are shown. These values generally correspond to gravel, medium sand, fine sand and sandy clay, respectively. As in Holland and Brunson (1988), we have used the Kozeny-Carman relationship to obtain realistic values of k from n :

$$k = \frac{1}{K_0 S_0^2} \frac{n^3}{(1-n)^2}, \quad (4.1)$$

where K_0 is an empirical constant and equal to 5 for spherical grains. S_0 can be defined analytically for a sphere as $S_0 = 6/d_0$, where d_0 is the grain diameter. Following Berryman (1981) and Hovem and Ingram (1979), respectively, the tortuosity

(γ) and the pore size parameter (a) are obtained as:

$$\gamma = 1 - r \left(1 - \frac{1}{n} \right), \quad (4.2)$$

$$a = \frac{d_0 n}{3(1 - n)}, \quad (4.3)$$

where $r=0.5$ for spheres, and lies between 0 and 1 for other families of ellipsoidal surfaces.

Figures 4.1(b) and 4.1(d) show the dispersive velocity and attenuation for S -waves for these four sets of n and k values. The S -wave velocity (V_S) range of 120-150 m/s and P -wave velocity (V_P) range of 1500-1800 m/s represent soft, water-saturated soils. The dashed box in Figure 4.1 indicates the typical field seismic frequency band for soft soils. Note that for gravel and medium sand ($k \sim 10^{-9}\text{m}^2$ and $k \sim 10^{-10}\text{m}^2$), the velocity dispersion is discernible even in the low field-seismic frequency band. The attenuation is, however, sensitive to even finer grain (lower permeability) soils, as we recognize in the field-frequency band changes in the inverse quality factor (Q_P^{-1} and Q_S^{-1}) even for $k \sim 10^{-11}\text{m}^2$. In other words, at field seismic frequencies, seismic attenuation is sensitive to permeability variation over a wider range than seismic velocity. This effect of the maximum frequency content in data on the permeability sensitivity will have an important bearing on the results to be discussed next.

We calculate the changes - separately for velocity and attenuation over the entire frequency (f) range of interest - when n and k both vary, and all other parameters in the model are assigned fixed realistic values. The individual cost functions for velocity and attenuation (C_i^V and C_i^α , respectively) are defined as follows:

$$C_i^V = \left(\frac{\sum_f |\Delta_i^V|^\beta}{\left(\sum_f |\Delta_i^V|^\beta \right)_{max}} \right)^{\frac{1}{\beta}}, \quad (4.4)$$

$$C_i^\alpha = \left(\frac{\sum_f |\Delta_i^\alpha|^\beta}{\left(\sum_f |\Delta_i^\alpha|^\beta \right)_{max}} \right)^{\frac{1}{\beta}}, \quad (4.5)$$

where $\Delta_i^V = (V_i(f, n, k) - \hat{V}_i(f)) / \sigma_i^V(f)$, $V_i(f, n, k)$ being the velocity estimated from the Biot-Stoll model and $\hat{V}_i(f)$ representing the field observed velocity dispersion, with i indicating the different wavetypes (P or S). The notations are similar for attenuation α , shown in Eq. (4.5). The attenuation coefficient α is related to Q as $\alpha \approx 8.686\pi f/(QV)$ dB/m. Here $\sigma_i^V(f)$ and $\sigma_i^\alpha(f)$ denote standard deviation. The denominators in Eqs. (4.4) and (4.5) compensate for the differences in sensitivity and noise or fluctuation in velocity and attenuation data. We have used $\beta=2$ (L_2 -norm) for noise-free data. Figures 4.2(a) and 4.2(b) show, respectively, the cost functions for P -wave velocity and attenuation for a whole range of n and k . Figures 4.2(c) and 4.2(d) illustrate the same for S -wave velocity and attenuation. For this numerical study, the field seismic frequency band (20-200 Hz) is considered. Here,

the dispersion curves representing the observation, obtained also from the Biot-Stoll model, correspond to $n=0.4$ and $k = 5 \times 10^{-11} \text{m}^2$, which are realistic values for fine-grained alluvial sand. The deep blue indicates the cost function minimum.

Remarkably, one can notice in Figures 4.2(a) and 4.2(b) that the orientation of the cost function minima line is sharply different between dispersive velocity and attenuation for P -waves. The same also holds for S -waves (Figure 4.2(c) and 4.2(d)). While for velocity, the cost function minima line is nearly parallel to the k -axis, this line is generally parallel to the n -axis for attenuation. This shows that while dispersive velocity of seismic waves is more sensitive to n and except at very high k (generally corresponding to coarse-grained soils), is nearly insensitive to k , frequency-dependent seismic attenuation is primarily sensitive to k , and n -sensitivity (especially for S -waves) is relatively insignificant. The cost functions (C_P^V and C_P^α) for P -waves show a sharper minimum in the n - k domain than the cost functions for S -waves. (Compare between Figures 4.2(a) and 4.2(c) and Figures 4.2(b) and 4.2(d)).

Clearly, if only seismic velocity or attenuation is used, one gets a whole set of local minima aligned in the n - k domain and no well-defined global minimum (Figures 4.2(a)-4.2(d)). Therefore, it is impossible to obtain unique and robust estimates of either n or k in water-saturated soils from field-observed dispersive velocity or attenuation alone.

The difference between velocity and attenuation in the n - k domain is driven by the underlying physics of seismic wave propagation in water-saturated sediments or soils. We have verified that if a different model of poroelasticity is used (than Biot-Stoll model) then this observed difference between velocity and attenuation remains unaffected. Because the behaviours of dispersive velocity and attenuation are nearly perpendicular to each other in the n - k domain, their integration is expected to result in a sharp convergence into a global minimum. We have defined an integrated cost function as follows:

$$C_{P,S}^{V,\alpha} = \left(\frac{\sum_f |\Delta_i^V|^\beta}{N \left(\sum_f |\Delta_i^V|^\beta \right)_{max}} + \frac{\sum_f |\Delta_i^\alpha|^\beta}{N \left(\sum_f |\Delta_i^\alpha|^\beta \right)_{max}} \right)^{\frac{1}{\beta}}, \quad (4.6)$$

where $C_{P,S}^{V,\alpha}$ is the integrated cost function for P - and S -wave velocity and attenuation. N is the number of attributes (i.e., V_P , α_P , V_S , α_S) to be integrated. Figure 4.2(e) shows the cost function in the n - k domain when V_P , α_P , V_S and α_S are all integrated. Because of the much higher velocity of P -waves compared to S -waves in water-saturated soil, measuring P -wave dispersion in the field is more challenging than S -wave dispersion. We have, therefore, investigated also the cost function in the n - k domain when only V_S and α_S are integrated. The result is shown in Figure 4.2(f). Note that in both Figures 4.2(e) and 4.2(f) the local minima lines have shrunk into sharp global minima points. The global minimum is sharper when both P - and S -wave data are used. However, with only V_S and α_S , the resolution is still very sharp. Unique and accurate estimates of both n and k ($n=0.4$, $k = 5 \times 10^{-11} \text{m}^2$) are obtained.

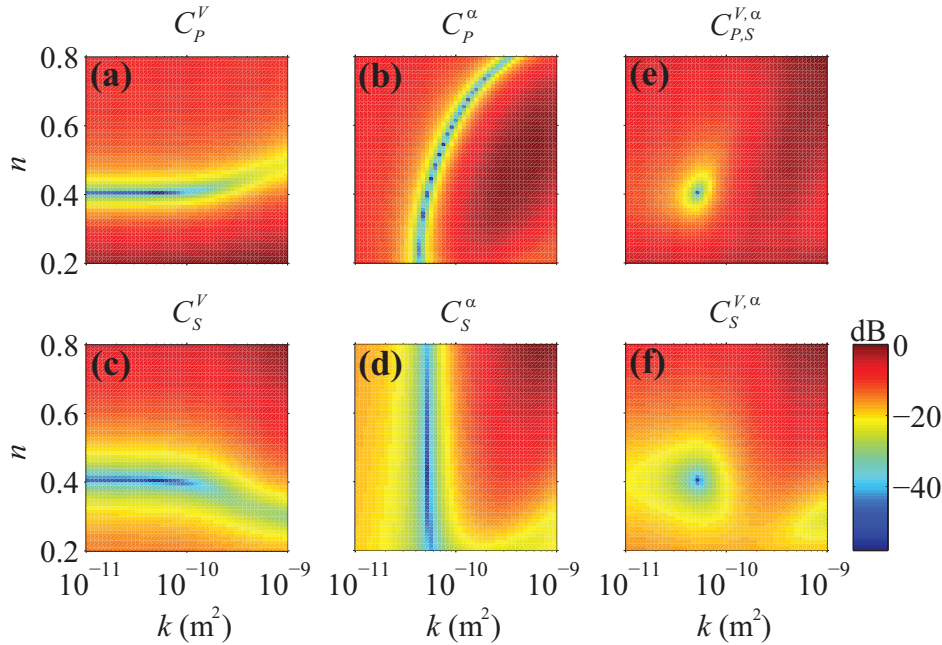


Figure 4.2: Cost functions in the n - k domain (see Eq. (4.4) to Eq. (4.6)) for: (a) V_P , (b) α_P , (c) V_S , (d) α_S , (e) integrated $V_P+\alpha_P+V_S+\alpha_S$, and (f) integrated $V_S+\alpha_S$. The frequency band used in 20-200 Hz. The deep blue colour indicates the cost function minimum. The difference in behaviour between V_P and α_P and that between V_S and α_S in the n - k domain are driven by the underlying physics of poroelasticity pertinent to such media.

In Figure 4.1 we have discussed that the maximum frequency content in field data determines the lowest value of k that is sensed by seismic attenuation. Lower k generally corresponds to finer grain soil. The typical k for gravel, fine sand, and sandy clay are, respectively, 10^{-9}m^2 , 10^{-11}m^2 and 10^{-12}m^2 (Berry and Reid, 1987). k typically ranges between 10^{-10}m^2 and 10^{-12}m^2 for very coarse to very fine grained sands. We have looked into the effect of the maximum frequency content on the nature of the integrated cost function minima in the n - k domain. The result is illustrated in Figure 4.3.

The four rows in Figure 4.3 correspond to four sets of values for n and k . Figures 4.3(a) show the velocity and attenuation integrated cost function (Eq. (4.6)) for S -wave (similar to Figure 4.2(f)). Figures 4.3(b) shows the same when both P -and S -waves are used (similar to Figure 4.2(e)). The three columns in Figure 4.3(a) represent three maximum frequency values in S -wave dispersion data: 80 Hz, 140 Hz and 200 Hz. The three columns in Figure 4.3(b) correspond to three maximum frequencies in P -wave data: 100 Hz, 200 Hz and 300 Hz, while S -wave maximum frequency is constant at 80 Hz. The minimum frequency is 20 Hz for all. These frequency limits are realistic for field data acquired in soft soil with conventional seismic sources.

It is clear from these numerical tests that n can be estimated accurately in

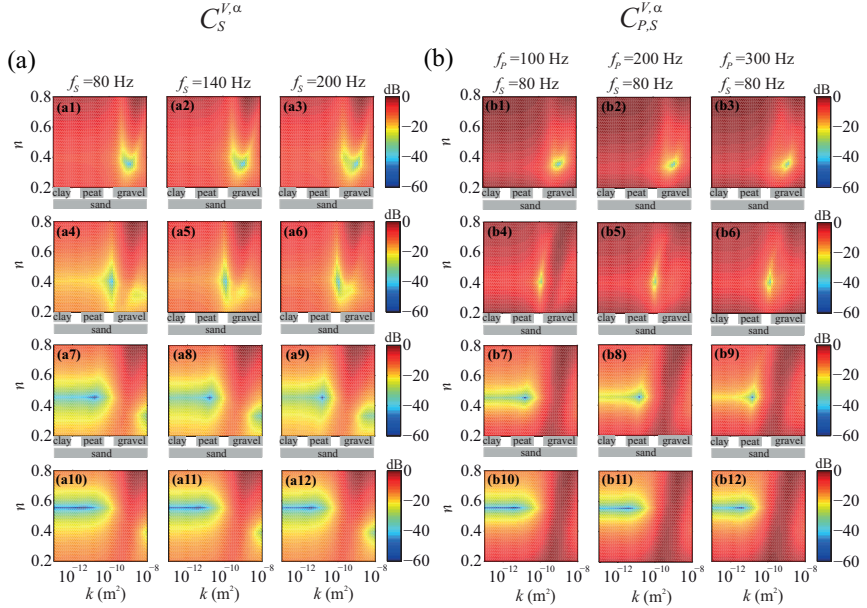


Figure 4.3: Effect of the maximum frequency content in the field-observed seismic dispersion on the n and k estimates when (a) V_S and α_S are integrated, and (b) when V_P , α_P , V_S and α_S are integrated, following Eq. (4.6). The three columns represent three different values of the maximum frequency in the data. The four rows represent four different values of n and k (taken as true values); from top to bottom: $n=0.35$, $k = 1.09 \times 10^{-9} \text{m}^2$; $n=0.40$, $k = 1.05 \times 10^{-10} \text{m}^2$; $n=0.45$, $k = 1.42 \times 10^{-11} \text{m}^2$; and $n=0.55$, $k = 3.31 \times 10^{-12} \text{m}^2$. The typical soil types representing these permeabilities are marked.

all cases. However, estimating correctly the value of k depends strongly on the maximum frequency available in the data, because the k variation is sensed by the higher frequencies, especially attenuation (Figure 4.1). For high k ($\sim 10^{-9} \text{m}^2$), typical in coarse-grained sands and gravels, the integration of dispersive velocity and attenuation of S -wave with only 80 Hz maximum frequency provides a clear global minimum (Figure 4.3(a1)). As the maximum frequency limit for S wave increases to 140 Hz and 200 Hz (Figures 4.3(a2) and 4.3(a3)) or when P -wave is supplemented to S -wave (Figure 4.3(b1)-4.3(b3)), the convergence becomes much sharper. However, when k is low ($\sim 10^{-10} - 10^{-11} \text{m}^2$, typically representing medium to fine grained sand and peat), having higher frequencies in the data or additional P -wave data becomes increasingly advantageous. For instance, for a very low k ($\sim 10^{-11} \text{m}^2$), the 20 to 80 Hz frequency band of S -waves is no longer sufficient to provide a sharp global minimum, and hence one cannot estimate k accurately (Figure 4.3(a7)). However, for this low k , if the S -wave frequency band is extended slightly to 20-140 Hz, then the global minimum becomes quite sharp. The global minimum is unambiguous in the results of inversion. Note that even for a very low value for k ($\sim 10^{-12} \text{m}^2$, typical for sandy clay and very fine sand) a maximum frequency of 200 Hz in the S -wave data or supplementing P data with low-frequency S data (see Figure 4.3(a12) and

4.3(a12)(b12)) leads to a sharp global minimum.

We find that this integrated cost function minimization approach, taking advantage of the contrasting behaviour between dispersive velocity and attenuation, is robust. In the illustrations presented in Figures 4.2 and 4.3 we have considered noise-free data (hence, $\sigma_i^V(f)$ and $\sigma_i^\alpha(f)$ equal to 1 in Eqs. (4.4) to (4.6)). However, we have verified that the presence of $\pm 10\%$ random noise in the velocity dispersion data and $\pm 100\%$ random noise in attenuation data leads to 2% error in n and 20% error in k . The use of standard deviation in the data ($\sigma_i^V(f)$ and $\sigma_i^\alpha(f)$ in Eqs. (4.4) to (4.6)) helps significantly in minimizing the effect of random noise in the observed dispersion curves. The error due to an incorrect model has also been investigated. We have generated the dispersion curves representing the observation using Biot-Stoll model while for estimating n and k we have used the BICSQS model. These two models are considerably different. We notice that the error in the estimated n and k are, respectively, 1.5% and 25%, in case only S -wave data with a frequency band of 20 to 80 Hz is used. The error will be less if more higher frequencies are available in the data and/or P -wave data is supplemented to the S -wave data. Because the difference between the two models is more conspicuous for seismic attenuation than for seismic velocity, and attenuation is primarily sensitive to k , the error due to an inaccurate model is larger for k than for n . All parameters in the model other than n and k have been assigned realistic constant values; if reasonable uncertainties are allowed to those parameters then the errors in the estimated n and k are still small and they do not exceed the above-mentioned effect of model uncertainty.

4.2.2 Effective stress and permeability from integrated velocity and attenuation dispersion: TI media

Stress changes in the subsurface alter both elastic moduli and transport properties from their initial values. As a consequence, the dispersion of the propagating seismic waves also changes. In order to explain the physics of such a change, we have developed in Chapter 3 a stress-dependent poroelastic model by incorporating soil mechanics and effective stress laws of transport properties into Biot's theory. Through recognizing and using efficiently the signatures of stress change in the subsurface on seismic dispersion, we aim to develop an approach in order to address the in-situ stress state.

Generally speaking, stresses are different in different directions, given the tensorial nature of stress. One realistic approach in modelling stress-dependent wave propagation is to consider vertical transverse isotropy (VTI), which represents a horizontally layered subsurface. In this case, it is possible to model the situation where horizontal and vertical stresses differ. Biot's theory requires fifteen parameters. Additionally, six parameters associated with the geomechanics are required in order to model the stress-dependent Biot's (SDB) parameters.

In this section, we analyse the sensitivity of different body waves in the same manner as in Section 4.2.1, with an accent on the effective horizontal stress and the material permeability based on the SDB model. We show that a combined use of body-wave velocity and attenuation can successfully be used in an integrated cost

function to obtain the effective horizontal stress and the permeability tensor. The effect of the angle of propagation of the wave with respect to the vertical on the inversion results is investigated.

For the purpose of synthetic tests, we consider the effective horizontal stress τ'_{11} to change from its reference state at 30 kPa to 120 kPa, whereas the vertical effective stress τ_{33} remains constant at 200 kPa. For simplicity, the pore pressure is assumed to be constant, which is typical of a sandy sediment at a given depth. These stress conditions are representative of the shallow subsurface. 200 kPa τ_{33} corresponds to a depth of about 30 m considering a typical sand-clay layered geology (Ghose, 2010a). For the reference state, all the parameters are given in Table 3.1. Due to the change in τ'_{11} from 30 kPa to 120 kPa, the elastic moduli and the transport properties will change, following the SDB model. Our goal is to retrieve τ'_{11} from the dispersive seismic velocity and attenuation. In this context, investigation of the cost function minima lines associated with velocity and attenuation of different body-waves (same as in Section 4.2.1) in the stress-permeability domain can be insightful.

Figure 4.4 illustrates the results of individual and integrated cost function minimization (similar to Fig. 4.2), calculated assuming the SDB model and using Eqs. (4.4), (4.5) and (4.6). The seismic frequency band is 20 to 300 Hz. In this case, we vary τ'_{11} and k_1 assuming that all other parameters are known (3.1). The results in Figure 4.4a,b show that the cost function minima lines calculated for individual cost function C_i^V and C_i^α , with $i = P, SV, SH$, behave differently in the τ'_{11} - k_1 domain. Notice the change of the minima lines with the angle of propagation, especially for the velocity cost function (C_i^V). The attenuation cost function minima lines C_i^α for different body-waves are almost the same and are very sensitive to horizontal permeability, except for C_P^α at 0° and C_{SV}^α at 90° . In these latter two cases, the attenuation of P - and SV -waves are completely insensitive to permeability k_1 in the plane of isotropy. This can be explained by the fact that a P wave propagating at 0° angle does not see k_1 in the perpendicular direction, whereas the SV wave is absolutely insensitive to k_1 at 90° angle. In this case, the polarization direction of the SV wave is vertical. We also observe that the behaviour of the individual cost functions of P - and SV -wave velocities change with the angle, whereas that for the SH -wave velocity does not change, because the polarization direction of the SH -wave is always in the isotropy plane. Interestingly, SV - and SH -wave velocities are most sensitive to τ'_{11} , while the P -wave velocity offers an additional constraint in permeability identification.

Note, however, that the integrated cost functions for SV - and SH -wave velocity and attenuation ($C_{SV}^{V,\alpha}$ and $C_{SH}^{V,\alpha}$ in Fig. 4.4c) are completely different. For SV and SH waves, one can see a clear global minimum, except for $C_{SV}^{V,\alpha}$. These global minima give true values of k_1 and τ'_{11} . However, for the integrated P -wave velocity and attenuation we do not see a global minimum. As noted previously, additional P -wave information can still be useful in identifying stable and reliable k_1 . Finally, we integrate velocity and attenuation for all body wavetypes (P , SH and SV) in a single cost function ($C_{P,SV,SH}^{V,\alpha}$) and the results are shown in Fig. 4.4d. See the sharp minima in the τ'_{11} - k_1 domain for all angles, but especially for $\theta = 0^\circ$.

Interestingly, the situation is very different if we look at the τ'_{11} - k_3 domain (Figure

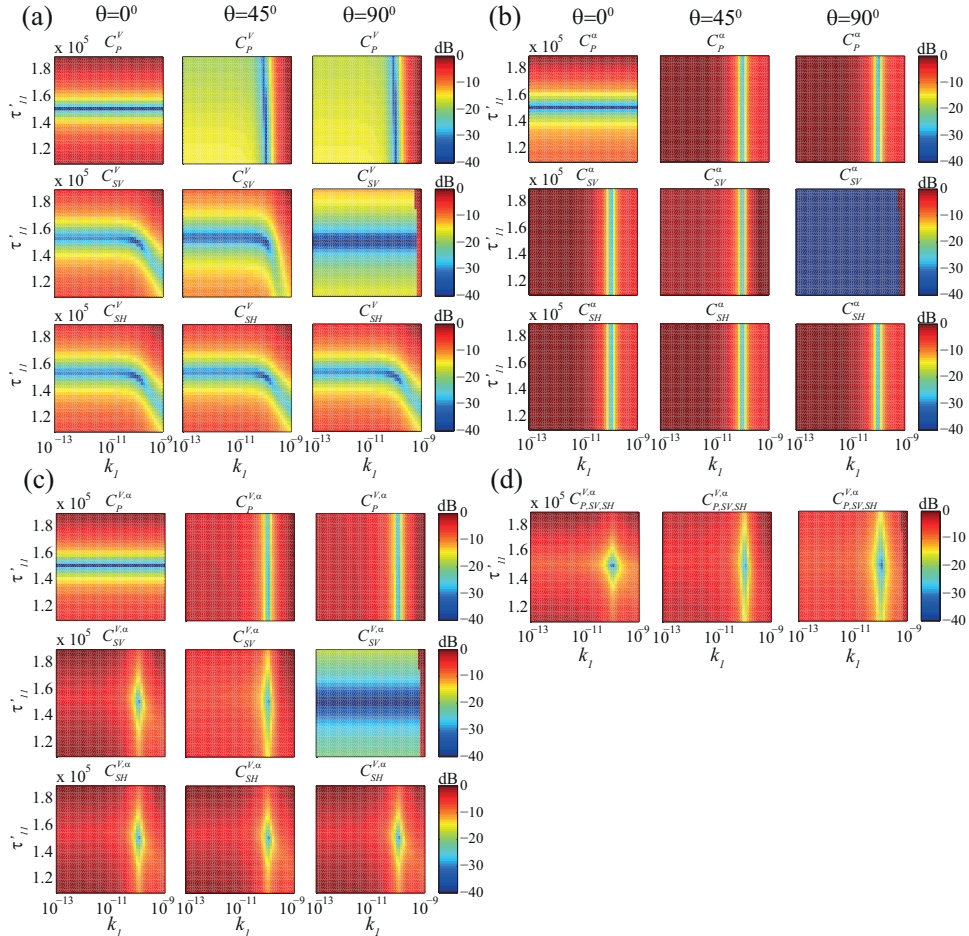


Figure 4.4: Individual and integrated cost functions in the $\tau'_{11} - k_1$ domain using the SDB model developed in this research.

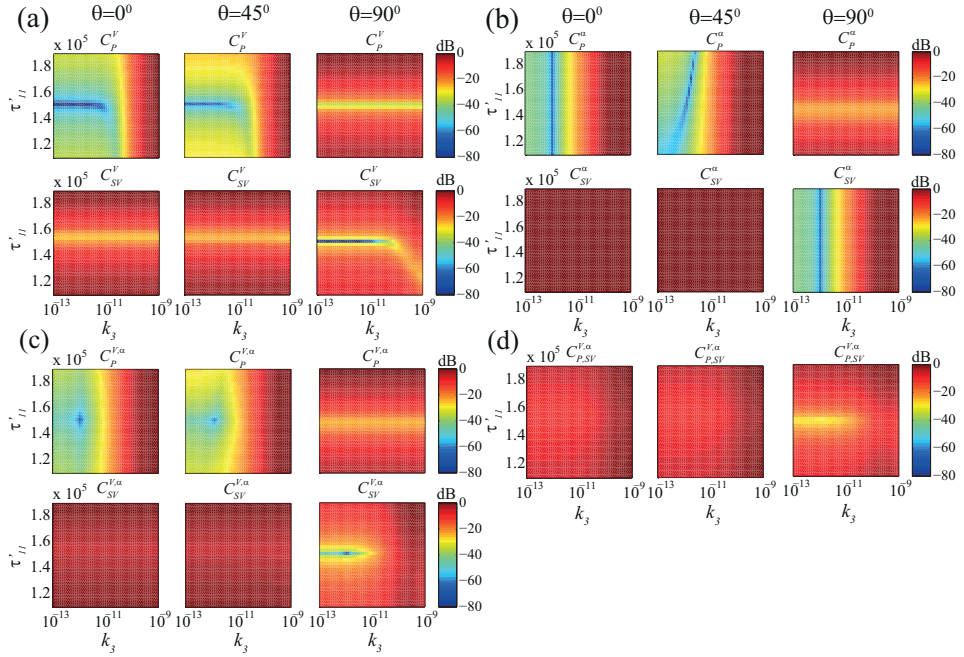


Figure 4.5: Individual and integrated cost functions in the $\tau'_{11} - k_3$ domain using the SDB model developed in this research.

4.5). Note that in this case, we can only use seismic dispersion associated with *P*- and *SV*-waves, since *SH* wave is independent of k_3 (see Eq.(3.57)).

Figure 4.5a illustrates the velocity cost function for *P*- and *SV*-waves. At angles less than 90^0 , we see a good sensitivity of *P*-wave velocity to both τ'_{11} and k_3 . At 90^0 , *P*-waves propagating perpendicular to the vertical direction are completely insensitive to k_3 ; the sensitivity is dominated by τ'_{11} . The situation is reverse for the *SV* wave: the sensitivity to k_3 is greater when it propagates in the horizontal direction; the polarization direction is then vertical. Attenuation of a *P* wave is slightly sensitive to the stress in the horizontal direction at $\theta = 90^0$ (Fig.4.5b), whereas the sensitivity to k_3 is conspicuous at all other angles. For *P*-wave attenuation, the highest sensitivity to τ'_{11} can be achieved when the wave propagates in the horizontal direction. Due to very low sensitivity of the *SV*-wave attenuation, the latter is unable to give any information with respect to τ'_{11} and k_3 at angles $< 90^0$. Sensitivity to k_3 , however, increases as the angle approaches 90^0 .

Importantly, when seismic velocity and attenuation are integrated in a single cost function, the minima lines shrink to a global minimum in the $\tau'_{11}-k_3$ domain (see Fig.4.5c). Integration of appropriate combinations is, therefore, beneficial. Especially, a unique and sharp global minimum is present for $C_P^{v,a}$ at angles less than 90^0 . Opposite results can be seen for $C_{SV}^{v,a}$. Note that k_3 ($= 10^{-12} \text{m}^2$) is smaller than k_1 ($= 10^{-10} \text{m}^2$), which means that the characteristic Biot's frequency in the

vertical direction is higher than that in the horizontal direction. Thus, the seismic dispersion associated with Biot's global flow mechanism, is less in the vertical than in the horizontal direction in the 20 to 300 Hz frequency band. Therefore, the effects of the maximum frequency content in the field-observed seismic dispersion on τ'_{11} and k_3 are similar to those explained in Figure 4.3.

Finally, Figure 4.5d shows the results, when seismic velocity and attenuation of P - and SV -waves are all integrated. Interestingly, due to the very low sensitivity of C_{SV}^{α} at angles less than 90° , the global minimum of $C_{P,SV}^{V,\alpha}$ is poorly defined. One should, therefore, avoid integrating those seismic attributes, where the sensitivity is almost negligible.

In practice, seismic attenuation and velocity dispersion can potentially be extracted in different acquisition geometries, such as vertical seismic profiling (VSP), crosswell seismic, etc. For situations when only a single borehole is available, one can still use a walkaway VSP in order to utilize the angle-dependent information, which can be crucial in reliable and stable identification of the stress state.

Here we have investigated through numerical examples the possibility of inversion of the absolute value of in-situ stress and permeability using seismic dispersion data. In the monitoring mode, one can use this approach for obtaining changes in the stress state and permeability, which are important and relevant in many applications.

4.3 Partially saturated media

For partially saturated soil/rock layers, the quantitative estimates of the degree and type of the fluid saturation is often of critical importance. In Chapter 2, we have already emphasized that a difference in the saturation pattern generally leads to a different velocity-saturation relationship. Therefore, identifying the signatures of patchy or homogeneous pattern from the seismic data should be possible. In this context, Dvorkin & Nur (1998) suggested a practical method for identifying the dominating saturation pattern from the dynamic Poisson's ratio obtained from the sonic logs. They suggested that their method would perform better for soft rocks. Prior to using a model, identifying the type of saturation pattern is indeed important. The theoretical formulations for homogeneous and patchy saturation patterns are given in Chapter 2. Here we investigate which combination of seismic attributes can advantageously be used in addressing efficiently the key soil/rock properties, such as porosity and fluid-saturation.

4.3.1 Porosity and water saturation from dispersive velocity and attenuation: effective-fluid model

We begin with the adaptation of the Biot-Stoll model for partial-saturation (Section 2.4.1). In this case, the cost function can be constructed in a similar way as in Eq.(4.6). The only change comes from the model under consideration. The parameters to be varied are porosity (n) and water saturation (S_w).

Figure 4.6 shows the results for individual and integrated cost function minimization. The value of the input n and S_w are, respectively, 0.44 and 0.6. All other

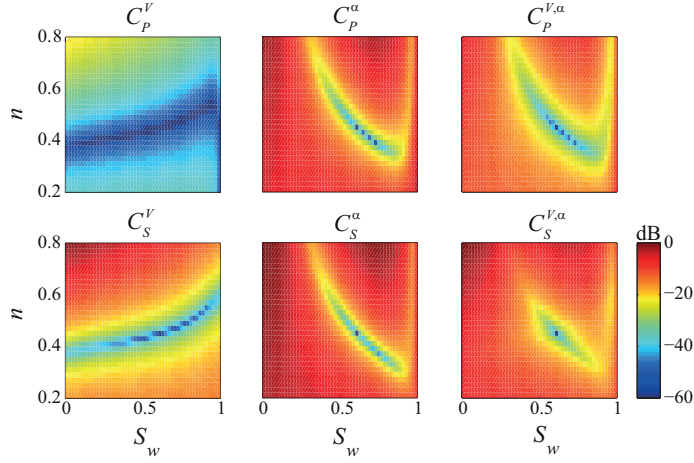


Figure 4.6: Individual and integrated cost functions in the $n - S_w$ domain using the Biot-Stoll model, giving information of water saturation and porosity.

parameters are same as in Section 2.4 and they are assumed to be known. The frequency band in the seismic data is 20-300 Hz. We further assume that the medium behaves as per the effective fluid model. The noise in the seismic data is ignored. In this synthetic test, the behaviours of C_P^V and C_S^V in the n - S_w domain are similar, although their sensitivities are different. One can see a large number of local minima for both C_P^V and C_S^V . Local minima are also present in C_P^α and C_S^α . The behaviour of C_P^α and C_S^α are similar to C_P^V and C_S^V , respectively. But the orientation of the velocity and attenuation minima lines are nearly orthogonal. Therefore, their integration will lead to a unique and sharp minimum giving the correct values of porosity and water saturation.

4.3.2 Porosity and water saturation from elastic P - and S -wave velocity integration: effective-fluid model

Seismic waves propagating through a partially-saturated porous medium, where fluid and gas are finely mixed, may experience negligible dispersion. This holds especially true for low-permeable materials like clay. In this case, Biot's characteristic frequencies are located at much higher frequencies, outside the field seismic frequency band. Therefore, materials with low fluid mobility can behave like elastic bodies at seismic frequencies, i.e. when there is little relative fluid motion and the diffusive processes due to the meso- and micro-scale heterogeneity in the solid and/or fluid phases are ignored. The mathematical formulation is given in Section 2.4.1.

Here we present a new methodology which allows us to obtain simultaneously the in-situ n and S_w from the seismic compressional- and shear-wave velocities only.

From the elasticity theory, P - and S -wave velocities are:

$$V_P = \sqrt{\frac{K_u + \frac{4}{3}G}{\rho}}, \quad (4.7)$$

$$V_S = \sqrt{\frac{G}{\rho}}, \quad (4.8)$$

where K_u is the undrained bulk modulus, G is the shear modulus and ρ is the bulk density. K_u can be calculated using Gassmann's equation applicable in the quasistatic limit (Eq. 2.70). Notice that only K_u and ρ are functions of S_w , whereas G is independent of S_w . The net effect of fluid on V_P comes from K_u and ρ . To separate these two effects from each other, one can use the ratio of V_P to V_S :

$$\frac{V_P^2}{V_S^2} = \frac{K_u}{G} + \frac{4}{3}. \quad (4.9)$$

The effect of fluid on V_P/V_S entirely comes from the undrained bulk modulus. The physical meaning of V_P/V_S becomes clearer through Poisson's ratio (ν):

$$\nu = \frac{1}{2} \frac{V_P^2/V_S^2 - 2}{V_P^2/V_S^2 - 1}. \quad (4.10)$$

Therefore, ν has been used extensively in the exploration industry as a fluid indicator. Further investigation of ν and V_P as a function of S_w is shown in Figure 4.7. See the distinct difference between the two curves. We have checked the behaviour of both V_P^2/V_S^2 and V_P/V_S as a function of S_w . The general trend is similar to the trend of ν as a function of S_w . Therefore, the effect of fluid on Poisson's ratio directly comes from the bulk modulus of the material, and its dependence on S_w is completely different from the dependence of V_P or V_S on S_w .

Since there is no attenuation in a perfectly elastic medium, the minimization can be performed only for the wave velocities and not for the attenuation. One can minimize seismic P - and S -wave velocities as follows:

$$\min = \left\{ V_i(n, S_w) - \hat{V}_i \right\}, \text{ where, } i = P, S. \quad (4.11)$$

The results of minimization are shown in Figure 4.8a,b using Eq.(2.70). The input properties are the same as those used as in Figure 4.6. See the identical behaviour between C_P^V and C_S^V in the n - S_w domain. Clearly, in this situation, individual or integrated V_P and V_S cost function minimization will not provide any extra information. Note also that both V_P and V_S are more sensitive to n than for S_w . It appears that using only seismic velocity information, one is unable to retrieve n and S_w . However, one can obtain a striking result by minimizing the ν in the n - S_w domain. This is illustrated in Figure 4.8c. C^ν is the cost function for ν . One can see clearly the difference in the behaviour of the cost function minima line of C^ν relative to C_P^V or C_S^V , and a pronounced sensitivity of ν to both n and S_w . Thus, integrating ν with one or both of V_P and V_S leads to a unique global

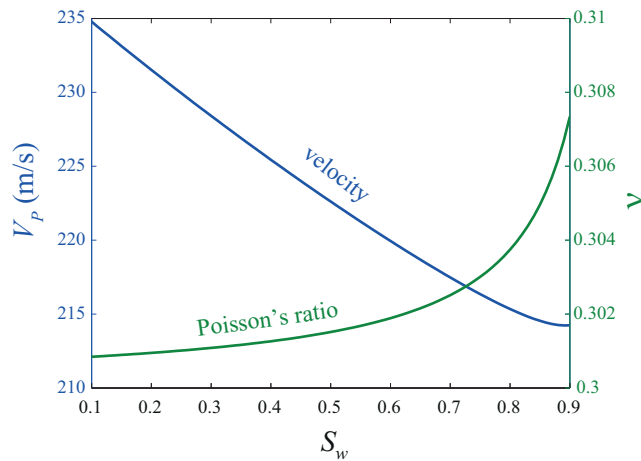


Figure 4.7: Compressional-wave velocity and Poisson's ratio as a function S_w using the effective fluid model.

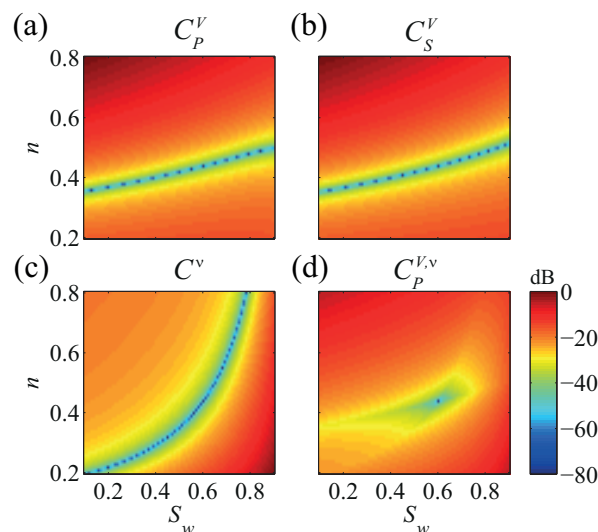


Figure 4.8: Individual and integrated cost functions in the $n - S_w$ domain using the effective fluid model.

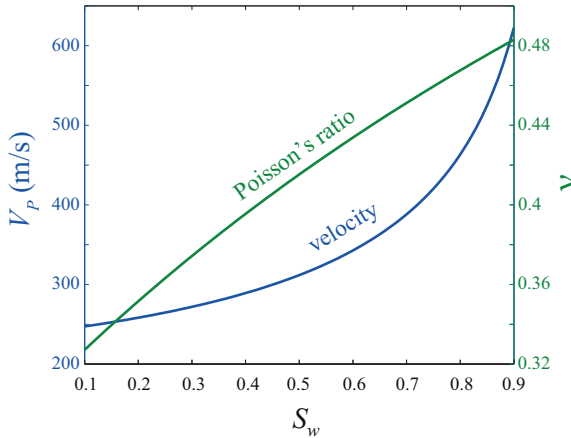


Figure 4.9: Compressional-wave velocity and Poisson's ratio as a function S_w using the patchy saturation model.

minimum. As an example, Figure 4.8d shows the result of integrating V_P and ν . Similar to Eq.(4.6), the integrated cost function can be constructed as:

$$C_P^{V,\nu} = \left(\frac{|\Delta_P^V|^\beta}{2 \left(|\Delta_P^V|^\beta \right)_{max}} + \frac{|\Delta^\nu|^\beta}{2 \left(|\Delta^\nu|^\beta \right)_{max}} \right)^{\frac{1}{\beta}}, \quad (4.12)$$

where $\Delta^\nu = (\nu(n, S_w) - \hat{\nu})/\sigma_\nu$. $\hat{\nu}$ is the observed Poisson's ratio, and σ_ν its standard deviation. Δ_P^V is the model – data residual for V_P . We conclude that an unique estimate of n and S_w can be obtained using the combined information of seismic velocities and ν .

4.3.3 Porosity and water saturation from elastic P - and S -wave velocity integration: patchy saturation model

What will happen if the saturation pattern is patchy? Patchy saturation has been explained in Section 2. Following Eq.(2.71), the undrained bulk modulus K_u will be changed. Consequently, V_P and ν will behave differently with respect to the homogeneous saturation pattern. As was discussed in Chapter 2, V_S will not be affected by a change in the saturation pattern. Theoretical calculations for V_P and ν as a function of S_w using the patchy saturation model are shown in Figure 4.9. The parameters for the dry frame, water and air are taken the same as those in Section 4.3.2.

As we have also seen in Chapter 2, for patchy saturation, V_P increases monotonically with increase of S_w , and the behaviour is different compared to the homogeneous model. The change in V_P as a function of S_w is much larger for the patchy saturation model. Additionally, ν calculated from the patchy saturation model is different

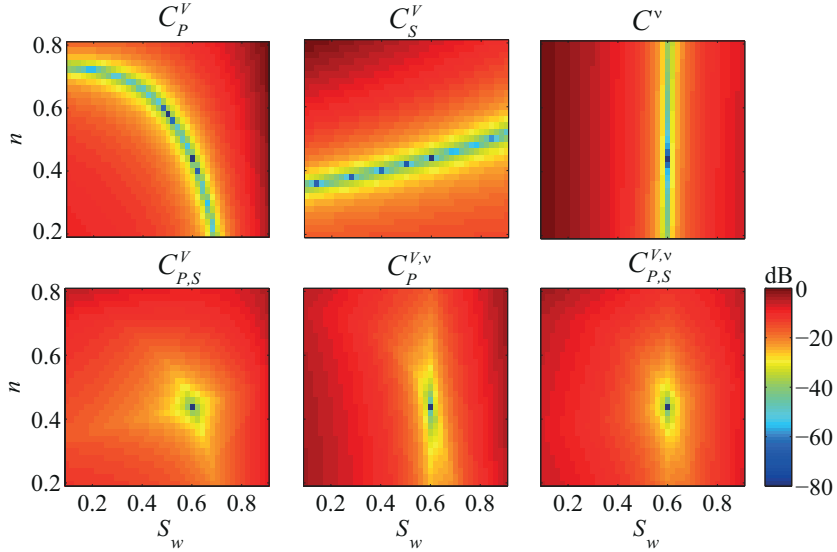


Figure 4.10: Individual and integrated cost functions in the porosity-water saturation domain using the patchy saturation model.

compared to the homogeneous model (compare Figs.4.7 and 4.9). ν increases much faster with S_w in the patchy saturation model than in the homogeneous model.

Let us now investigate the behaviour of C_P^V and C^V associated with the patchy saturation model in the n - S_w domain. These individual cost function minimizations are shown in the upper panels in Figure 4.10. For comparison, C_S^V is also illustrated here. As expected, the behaviours of C_P^V and C^V are different compared to the results shown in Figure 4.8. In this case, the behaviour of C_P^V and C_S^V are quasi-orthogonal to each other. Both V_P and V_S are sensitive to n and S_w . C^V show a very high sensitivity to S_w and almost no sensitivity to n . These results suggest that the combined use of C_P^V and C_S^V will be useful in order to obtain both n and S_w simultaneously, and C^V can be used as an additional constraint for S_w estimation. The results of integrated cost functions are shown in the lower part of Figure 4.10. In all these cases, one can obtain unique estimates of both n and S_w simultaneously using only seismic velocities.

The results obtained here and in Section 4.3.2 can be used for discriminating the saturation pattern in the subsurface, similar to the proposal by Dvorkin & Nur (1998). But in this case, the pattern can be identified from the integrated $C_{P,S}^V$. In case of homogeneous saturation, $C_{P,S}^V$ should behave similar to C_P^V and C_S^V . In this case no convergence is expected in the n - S_w domain. On the contrary, if the saturation is patchy, the convergence is expected from the integrated cost function $C_{P,S}^V$ and V_S . In practice, due to noise in the velocity estimates and in the model, the convergence in the $C_{P,S}^V$ will be less defined or undefined. If it is undefined, then the saturation pattern is homogeneous. If the convergence is more or less defined,

then one may expect the saturation pattern to be patchy.

4.3.4 Porosity and water saturation from integrated seismic and GPR velocities

So far in this thesis, we have only looked at seismic waves propagating through media, which were described by mechanics and thermodynamics. We have shown that seismic data contain signatures of fluid mobility, stress state and fluid saturation, and can be successfully employed to obtain these properties. However, in near-surface geophysics, to compliment seismic measurements, electromagnetic methods are used a lot because of their sensitivity to other subsurface properties. Electromagnetic measurements permit identifying the fluid and chemical contents in the subsurface.

In this study, we focus our attention to high-frequency electromagnetic waves used in ground penetrating radar (GPR), which is capable of providing non-destructive characterization of the hydrogeophysical properties of the subsurface. GPR is widely used for monitoring fluid front (Vellidis *et al.*, 1990), water table (Nakashima *et al.*, 2001), stratigraphy (Davis & Annan, 1989), and for soil-water content identification (Chanzy *et al.*, 1996). Thus, this technique addresses a broad range of issues relevant to the near-surface geophysics.

The main interest of the research to be discussed in this section is to obtain porosity and water saturation estimates from a joint inversion of electromagnetic and seismic wave data. With the recent field hardware, the wavelengths between GPR and seismic waves have become comparable (Ghose *et al.*, 1996). This implies that they both may address the same region. This may allow a meaningful joint inversion of these two datasets. The link of n and S_w to seismic waves have been studied in previous Chapters. In case of GPR data, n and S_w are linked through Archie's equations (Archie, 1942) and effective bulk dielectric permittivity. Archie's empirical relationship gives a direct link between EM measurements to porosity and fluid saturation information and is widely used for resistivity log interpretation. Archie's law is applicable for a wide range of rock types, and well documented in many experimental papers (e.g., Rust (1952); Ransom (1984)). According to Archie (1942), formation conductivity σ can be expressed in terms of n and S_w

$$\sigma = \frac{1}{\alpha} \sigma_w n^m S_w^n, \quad (4.13)$$

where α is an empirical constant close to 1. m is the so-called cementation exponent which increases as the formation becomes more consolidated. It varies between 1.3 and 2.5 and is close to 1.5 for unconsolidated sands (Carothers, 1968). Parameter n is a saturation exponent and depends on the type of fluid saturation. For air-water saturation n is close to 2 (Sharma *et al.*, 1991). Parameter σ_w is the conductivity of the pore fluid. To relate Archie's law to the high-frequency electromagnetic wave phenomenon, we start from the complex wavenumber associated with EM -waves

$$\kappa_{EM} = \beta_{EM} - i\alpha_{EM}, \quad (4.14)$$

in which α_{EM} and β_{EM} are defined as (Bradford, 2007):

$$\alpha_{EM} = \omega \left(\frac{\varepsilon \mu}{2} \left(\sqrt{1 + \left(\frac{\sigma}{\varepsilon \omega} \right)^2} - 1 \right)^{\frac{1}{2}}, \quad (4.15)$$

$$\beta_{EM} = \omega \left(\frac{\varepsilon \mu}{2} \left(\sqrt{1 + \left(\frac{\sigma}{\varepsilon \omega} \right)^2} + 1 \right)^{\frac{1}{2}}, \quad (4.16)$$

where ε , μ and σ are, respectively, dielectric permittivity, magnetic permeability and electric conductivity. In general, they are all complex and frequency-dependent quantities. Eqs. (4.15) and (4.16) can be expressed in terms of real effective permittivity ε_e and real effective electric conductivity σ_e , respectively:

$$\varepsilon_e = \varepsilon' - \frac{\sigma''}{\omega}, \quad (4.17)$$

$$\sigma_e = \sigma' + \varepsilon'' \omega. \quad (4.18)$$

Here ε' and σ' are the real, and ε'' and σ'' are the imaginary parts of the permittivity and conductivity. Since the GPR operational frequency is in the high-frequency range (GHz), displacement currents prevail the conduction currents. This leads to a rather small intrinsic attenuation and phase velocity dispersion of the propagating electromagnetic wave. For GPR, σ' can be taken as the DC conductivity ($\sigma' = \sigma_{DC}$) and $\sigma'' = 0$. In the low-loss approximation $\omega \gg \sigma_e/\varepsilon_e$ and Eq. (4.15) reduces to

$$\alpha_{EM} = \frac{\sigma_e}{2} \sqrt{\frac{\mu_0}{\varepsilon_e}}, \quad (4.19)$$

where μ_0 is the magnetic permeability of the free space. This expression can be realistically used to calculate the attenuation of electromagnetic waves in the frequency range where GPR operates. The electromagnetic phase velocity can be calculated from

$$V_{EM} = \frac{\omega}{\beta_{EM}}. \quad (4.20)$$

The effective bulk dielectric permittivity ε_e for a multiphase system as solid-water-air, can be calculated as follows

$$\varepsilon_e^\alpha = (1 - n)\varepsilon_s^\alpha + S_w n \varepsilon_w^\alpha + (1 - S_w)n \varepsilon_a^\alpha, \quad (4.21)$$

where $\alpha = 0.5$ for sandy soils (Birchak *et al.*, 1974) and $\alpha = 0.65$ for clayey soils (Wang & Schmugge, 1980). The effective bulk electrical conductivity can be calculated from Eq. 4.13.

Velocity-water saturation plots for seismic and GPR waves are shown in Figure 4.11 for typical sand sediments with 44% porosity. Each velocity was normalised by its maximum value. Typical values 4, 80 and 1 for relative dielectric permittivity for sand, water and air are taken, respectively. Note a distinct difference between *EM*

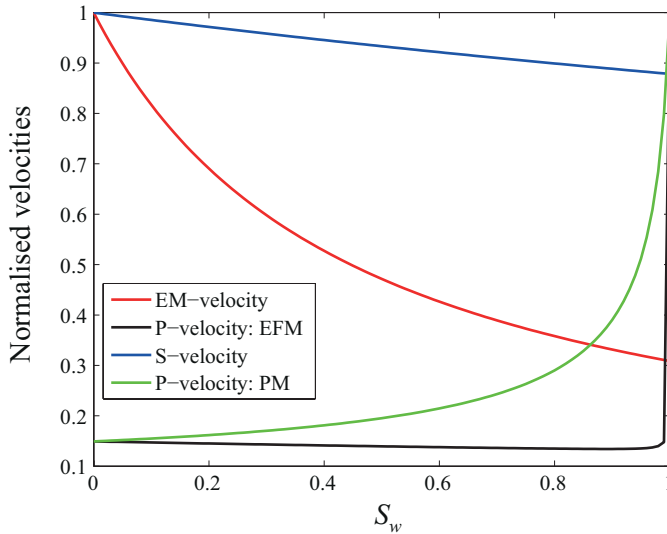


Figure 4.11: Seismic and GPR velocities as a function of S_w .

and seismic wave velocities. An increase of S_w causes a dramatic decrease in EM -velocity. This can be explained by the fact that ϵ_e increases when air is replaced by water. Both seismic and electromagnetic wave velocities decrease with S_w in the range $S_w \in [0, 0.9]$, except when the P -wave velocity is predicted by patchy saturation model.

Similar to Ghose & Slob (2006), we calculate the cost functions for V_P , V_{EM} and α_{EM} as a function of n and S_w . The results are shown in Figure 4.12. One can see that the combinations of n and S_w satisfying the observed EM -velocity and attenuation are the same based on the similar behaviour observed in C_{EM}^V and C_{EM}^α (see upper part of Figure 4.12). This result is opposite to that found for seismic velocity and attenuation in previous sections in the n - k and τ' - k domain. This implies that the quasi-orthogonality between velocity and attenuation in the property domain is not necessarily driven by the Kramers-Kronig relationship. In other words, Kramers-Kronig relationship is not a sufficient condition to explain such quasi-orthogonality in the parameter domain. In fact, the contrasting behaviour between the different physical quantities are simply attributed to their mutually different sensitivity in the domain under consideration. Thus, a stable and unique minimum is found in the n - S_w domain by integrating seismic and EM -wave velocities, thus removing the local minima present in the individual cost functions. Therefore, additional constraints obtained from the high-frequency electromagnetic data, can be useful in retrieving in situ n and S_w in the subsurface.

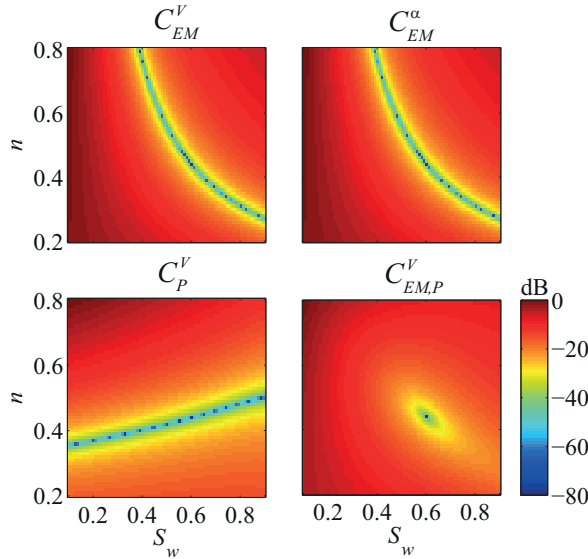


Figure 4.12: Individual and integrated cost functions in the $n - S_w$ domain using effective fluid model and Maxwell's equations

4.4 Conclusions

In this Chapter we have investigated the behaviour of seismic wave attributes in 2-D parameter planes. As an additional constraint, we have briefly looked at the high-frequency electromagnetic wave phenomenon. This has led to interesting results. Measurements involving different underlying physics can exhibit quasi-orthogonal behaviour in the parameter space as were earlier shown by Ghose & Slob (2006) and van Dalen *et al.* (2010). Taking advantage of such contrasts in the property domain, we have constructed new and effective integrated cost functions.

We have found that in the $n-k$ domain, attenuation and velocity dispersion of Biot's model and its adaptions behave very differently. Thus, joint minimization of the data-model residual leads to unique and stable estimates of n and k , solving the problem of local minima in the individual cost function optimization.

We have used the SDB model developed in this research (Chapter 3) to obtain horizontal effective-stress and permeability associated with transverse isotropic media. As in the $n-k$ domain, we have found several combinations of seismic wave velocity and attenuation which have nearly-orthogonal behaviour in the $\tau'_{11}-k_i$ domain. In general, SV - and SH -wave attenuation and velocity dispersion are successful in addressing τ'_{11} and k_1 simultaneously. The integration of SV -wave velocity and attenuation at 90° do not give a unique solution. It was nevertheless good for horizontal stress identification. P -wave velocity and attenuation are found to be most sensitive to k_1 and k_3 and are good constraints for estimation of these properties. Our results reveal that, when utilizing only the acoustic information, the most favourable situation is for the case of estimation of τ'_{11} and k_3 . This holds true especially for

angles around 45^0 . In this case, both velocity and attenuation are most sensitive to these parameters. Additional SV information offers a good constraint to stabilize the inversion results. We have shown how extra angle information can be important in estimating the effective horizontal stress and the permeability tensor.

In case of partial saturation, the extension of Biot's poroelasticity theory developed in this research reveals that a joint inversion of velocity and attenuation can be successful in providing reliable n and S_w estimates. Both P - and S -wave theoretical dispersion curves are affected by the amount of fluid saturation. Attenuation and velocity dispersion are found to behave very differently in the n - S_w domain. This allows us to obtain a single and sharp global minimum.

In practice, extracting dispersion can be challenging. Therefore, we have also looked at the elasticity models. In case of the effective fluid model, we found that it is impossible to obtain n and S_w by inverting V_P and V_S through a single integrated cost function. Interestingly, having the V_P/V_S ratio or Poisson's ratio ν change the situation completely. The calculation of the cost function for Poisson's ratio C^ν reveals a different behaviour with respect to C_P^V and C_S^V . This implies that elastic wave velocity information can only be effectively integrated with V_P/V_S or ν in retrieving reliably n and S_w . ν is sensitive to both n and S_w , while V_P and V_S are more sensitive to porosity.

Applying the same procedure to the patchy saturation model in the quasistatic limit, C_P^V is found to be very different compared to the effective fluid model. In this case, a joint inversion of V_P and V_S shows an excellent convergence in the n - S_w domain. Further investigation of ν in case of the patchy saturation model shows inability to sense n of the formation. It is mainly controlled by S_w . ν is a useful parameter for reliable S_w identification.

Simple numerical analysis of high-frequency EM -wave (GPR) velocity and attenuation as a function n and S_w has shown a monotonic decrease in the velocity and attenuation, when air is replaced by water. Contrary to the quasi-orthogonal behaviour found in the n - k and τ' - k domains for seismic velocity and attenuation, C_{EM}^V and C_{EM}^α behave similar in the n - S_w domain at the high-frequency propagation regime ($\omega \gg \sigma_e/\varepsilon_e$). This implies that the nearly-orthogonal behaviour between velocity and attenuation of GPR waves found in this chapter is not directly associated with the Kramers-Kronig relationship, which relates velocity to attenuation uniquely. Finally, joint seismic and GPR velocity minimization $C_{EM,P}^V$ has yielded a sharp global minimum, which allows reliable estimation of n and S_w .

All synthetic examples are based on noise-free situations. Also, all parameters other than the target ones are assumed to be known. Error in inversion results due to noise in the assigned parameters, data and model errors will be studied in the next chapter. Simultaneous global optimization of all parameters, with no apriori assumption, will be investigated in Chapter 6.

Chapter 5

Physics of shear-wave intrinsic dispersion and estimation of in-situ soil properties: a synthetic VSP appraisalⁱ

5.1 Introduction

In an attempt to explain the intrinsic dispersion of S waves in water-saturated, unconsolidated sediments like soft soil, Biot's theory of poroelasticity was adapted by Stoll & Bryan (1970) and Stoll (1974, 1977, 1986, 1989). These theories and several experimental studies done so far (for a discussion see Schulz & Zabel, 2006) suggest that the two specific soil properties that have a major influence on the dispersive behaviour of S waves propagating in soft, water-saturated sediments are porosity and Darcy permeability. Therefore, understanding the underlying physics of S -wave dispersion may lead to a means to estimating in-situ porosity and permeability in near-surface soil layers.

Values of in-situ porosity n and Darcy permeability k (or hydraulic conductivity K) are critically important to geotechnical, geoenvironmental, agricultural and civil engineers and to hydrogeologists. In saturated soils, k is an important variable for water transport modelling and in all drainage and flow related issues. n and k are related to each other. It has so far been impossible to obtain mutually independent in-situ estimates of both n and k in the shallow soil layers. In case of laboratory tests, the effect of sample disturbance on the estimated soil properties is severe, especially for loose sandy and gravelly soils. Also, widely used empirical approaches relating n to k , e.g., Kozeny-Carman's relation (Kozeny, 1927; Carman, 1937), offer only tentative estimates. In addition to large inherent uncertainties, there is no

ⁱThis chapter is published as a journal article in *Near Surface Geophysics* **10**, 613–629 (Zhubayev & Ghose, 2012b). Minor changes have been introduced to make the text consistent with other chapters of this thesis.

uniqueness in the values obtained by empirical means.

Earlier observations of *S*-wave intrinsic dispersion in soft soils (e.g., Kudo & Shima, 1970; Michaels, 1998) have not led to a quantitative approach for estimation of both n and k from the low-frequency field *S*-wave seismic data. Previous attempts to use seismic wave dispersion for finding n or k have generally used high frequencies (in 1 kHz to tens of kHz range) and/or hard materials or rocks (e.g., Burns, 1990; Yamamoto, 2003; Arroyo *et al.*, 2007; Lin *et al.*, 2009; Baron & Holliger, 2011). Near-surface *S*-wave data acquired in soft soils do not have such high frequencies. A quantitative approach, which exploits the inherent difference in behaviour between dispersive seismic wave velocity and attenuation in the n - k domain, has been proposed in Chapter 4. The effect of maximum frequency content in the data and the integration of different seismic waves on the accuracy and robustness of the estimated n and k have been numerically investigated. However, the success of this new approach on field data remains to be tested. In the present Chapter, we have examined the possibility of estimation of in-situ, layer-specific values of n and k from dispersive *S*-wave velocity and attenuation data in the low field-seismic frequency range. This has been done through realistic tests on synthetic data, for which the n and k are known.

In the following sections, we shall discuss first the different poroelasticity models that are pertinent to the propagation of *S* waves in water-saturated soils and outline the idea of integration of dispersive velocity and attenuation. The concept will then be tested on realistic synthetic VSP datasets with different random noise levels. An approach of extraction for intrinsic velocity dispersion and attenuation from the VSP data will be illustrated. The influence of error in velocity and attenuation will then be examined. Finally, the effect of inadequacy of the used poroelasticity model, with or without noise in the data, on the accuracy of the property estimates will be evaluated.

5.2 Physics of *S*-wave intrinsic dispersion in water-saturated soils

Buchanan (2006) made a useful comparison between the two competing models for seismic dispersion that are valid for unconsolidated water-saturated sediments: (a) Biot's theory and its adaptations for unconsolidated sediments (Stoll & Bryan, 1970; Stoll, 1974, 1977, 1986, 1989), and (b) the model of Buckingham (1997, 1998, 2000). It was concluded that the Biot-Stoll model with its subsequent extensions (Yamamoto & Turgut, 1988; Chotiros & Isakson, 2004, 2008) can explain the experimental results better than the Buckingham model. Moreover, the Buckingham model does not incorporate k . As we are interested in studying the interaction between n and k in the observed intrinsic dispersion, we have concentrated on the Biot-Stoll model in this work (see Chapter 2). Holland & Brunson (1988) tested the Biot-Stoll model on field seismic data, and found that this model predicted accurately the field-observed dispersion for a variety of soil types. We have looked at the following three extensions: (1) the model of Stoll & Bryan (1970) or Biot-Stoll

model; Stoll (1977), (2) the "Biot model with grain contact squirt flow and shear drag" or BICSQS (Chotiros & Isakson, 2004), and (3) the Rayleigh-Plesset-Biot model (Smeulders & van Dongen, 1997; Vogelaar, 2009). Based on examination on a compiled database of field observed dispersion, we find that the Biot-Stoll model can explain quite well the observed dispersion for *S*-waves in unconsolidated soils, excepting for coarse-grained soils for which BICSQS appears to be more suitable. In this chapter, we shall illustrate the main idea using the Biot-Stoll model. In practice, one may use the model that fits best the observed dispersion data.

The Biot-Stoll model requires 9 parameters for predicting dispersion of *S* waves: (1) pore fluid density ρ_f , (2) grain density ρ_s , (3) real part of the frame shear modulus G , (4) shear logarithmic decrement δ_s , (5) porosity n , (6) fluid viscosity η , (7) permeability k , (8) tortuosity γ , and (9) pore size a . Pore size a can be approximated from porosity and grain size (Hovem & Ingram, 1979). Dispersive *S*-wave velocity and attenuation can be obtained from, respectively, the real and the imaginary part of the complex wavenumber (Stoll, 1977; Kimura, 2007). We have examined the relative importance of each of the 9 parameters in predicting previously observed *S*-wave dispersion in soft soils. We have found that n and k are the most important ones in explaining the observation, and other parameters can be assigned realistic constant values for a given soil type without significant loss of accuracy. Therefore, in this study only n and k are considered unknown.

The concept of integration of dispersive *S*-wave velocity and attenuation to estimate simultaneously n and k makes use of the underlying physics of poroelasticity (see Chapter 4 of this thesis). The integration is achieved by combining the residual between the model and the observed (data) dispersion curves, for both velocity and attenuation in a single cost function, which is then minimized as a function of n and k :

$$C_{V+\alpha} = \left(\frac{\sum_f \left(\frac{|V_S(f, n, k) - \hat{V}_S(f)|}{\sigma_V(f)} \right)^\beta}{2 \left(\sum_f \left(\frac{|V_S(f, n, k) - \hat{V}_S(f)|}{\sigma_V(f)} \right)^\beta \right)_{max}} + \frac{\sum_f \left(\frac{|\alpha_S(f, n, k) - \hat{\alpha}_S(f)|}{\sigma_\alpha(f)} \right)^\beta}{2 \left(\sum_f \left(\frac{|\alpha_S(f, n, k) - \hat{\alpha}_S(f)|}{\sigma_\alpha(f)} \right)^\beta \right)_{max}} \right)^{\frac{1}{\beta}}. \quad (5.1)$$

Similar integrated cost functions were used by Ghose & Slob (2006) and van Dalen *et al.* (2010). The first term on the right-hand side of this equation corresponds to the cost function for velocity (C_V), the second term corresponds to the cost function for attenuation (C_α). f is frequency. $\sigma_V(f)$ and $\sigma_\alpha(f)$ are standard deviations normalized to the mean value in data, respectively for velocity and attenuation, due to the presence of noise. For noise free data $\beta = 2$ (L_2 -norm minimization) can be used. In case of noisy data the minimized misfit function is more stable and resistant to outliers when $\beta = 1$ (L_1 -norm minimization). Attenuation and velocity dispersion

of S waves are interrelated; however, they can be estimated from the seismic data mutually independently.

To clarify the concept of integration, we first illustrate the results on noise-free data. In Figure 5.1a and 5.1b, we show respectively the behaviour of C_V and C_α in the n - k domain. In this case, we have assumed $n=0.4$, $k = 5 \times 10^{-11} \text{ m}^2$, representing medium-grained sands. 50-140 Hz is the range of frequency considered available in the S -wave data. Theoretical velocity and attenuation curves have been calculated using Biot-Stoll model. These are taken as input data (measurement): \hat{V}_S and $\hat{\alpha}_S$. Next, the individual cost functions C_V and C_α are minimized (Figures 5.1a and 5.1b). n and k in the model are varied over wide ranges, and C_V and C_α are estimated over the entire frequency range. $\sigma_V(f)$ and $\sigma_\alpha(f)$ are taken as 1, as there is no noise in the data in this case. Figures 5.1a and 5.1b show that the behaviours of C_V and C_α are quite different in the n - k -domain, which is meaningful. The orientation of the cost function minima line (shown in deep blue) is very different between them. While the C_V minima line is oriented nearly parallel to the k -axis, the C_α minima line is aligned more or less parallel to the n axis. This difference is essentially dictated by the underlying physics of poroelasticity, pertinent to unconsolidated soils.

In the new integration scheme (see Chapter 4 of this thesis), this physics-driven difference in behaviour in the n - k domain between C_V and C_α is utilized. This contrasts with the approaches where multiple field measurements are combined based on statistical or empirical relationships between them or through multi-parameter global optimization. In Figure 5.1c the integrated cost function $C_{V+\alpha}$ is shown. Note the very sharp global minimum offering unique estimates of n and k simultaneously. The obtained values of n and k are the same as the input values ($n = 0.4$ and $k = 5 \times 10^{-11} \text{ m}^2$), when there is no noise in the measurement. The minimum is not sharp if we use only C_V or C_α (Figures 5.1a, 5.1b), but the combination of the two gives a sharp minimum (5.1c) because of the very different orientations of the two individual minima lines (for C_V or C_α) in the n - k domain. Further, there are local minima in the individual cost functions, which will be problematic in case of noisy data. The local minima problem is alleviated when C_V and C_α are integrated (Figure 5.1c). The n and k estimates are generally quite robust.

Figures 5.1d-5.1f show the results when there is noise in the measurement. 5% and 20% random noise was added respectively to V_S and α_S dispersion data. $\sigma_V(f)$ and $\sigma_\alpha(f)$ are still taken as 1. The effect of noise is quite detrimental, as we can no longer distinguish any clear global minimum. Further, the positions of the minima lines are moved from their correct positions. The integrated cost function $C_{V+\alpha}$ offers a recognizable global minimum but not at the correct n and k values (Figure 5.1f).

Next we calculate the standard deviations of the noise, normalized with respect to the mean values, over the entire frequency range in V_S and α_S - $\sigma_V(f)$ and $\sigma_\alpha(f)$, respectively. Figures 5.1g-5.1i show the results for the same noisy data as in Figures 5.1d-5.1f but with $\sigma_V(f)$ and $\sigma_\alpha(f)$ used as weights in C_V and C_α . We can now see a very sharp minimum in $C_{V+\alpha}$ at a location that gives the correct values of n and k (Figure 5.1i).

Addressing quantitatively both n and k on S -wave dispersion observed in low-

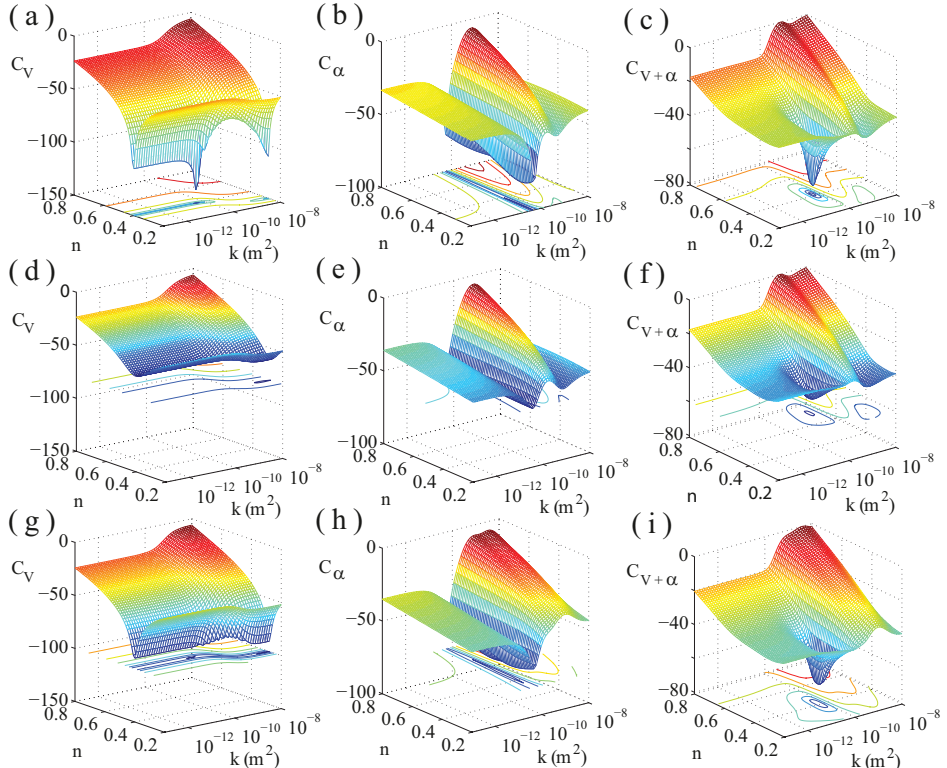


Figure 5.1: (a)-(c) Cost functions (in dB) for velocity (C_V), attenuation (C_α) and integrated velocity+attenuation ($C_{V+\alpha}$), respectively, for noise-free dispersion data. The dispersion curves are generated using the Biot-Stoll model with $n = 0.4$ and $k = 5 \times 10^{-11} \text{ m}^2$. No weights (σ_V and σ_α in equation 5.1) have been used in the cost functions. (d)-(f) the same cost functions but for 5% and 20% random noise respectively in the dispersive velocity and attenuation data. Again no weights have been used in the cost functions. (g)-(i) same as (d)-(f) but, in this case, weights (data standard deviations) have been used. Note that the global minimum is much more focused in the integrated cost functions (see (c), (f) and (i)). For the noisy data the use of the weights calculated from the data clearly enhances the robustness and accuracy of the estimates (compare between (f) and (i)).

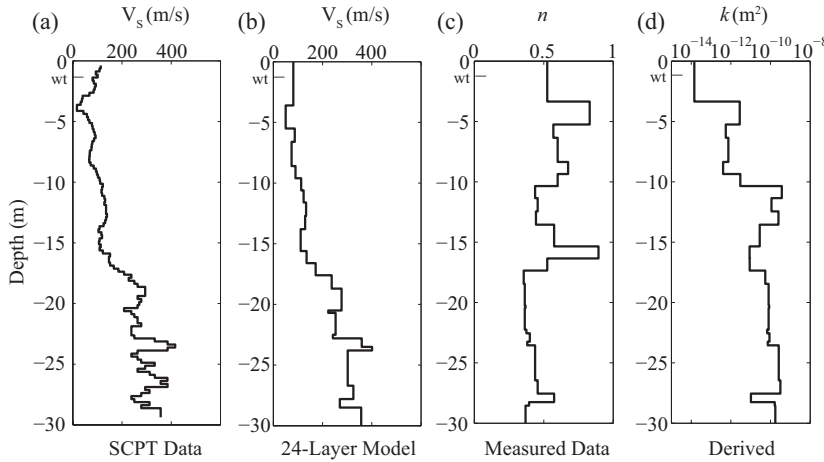


Figure 5.2: (a) High-density V_s profile from SCPT data (Ghose, 2010a), (b) layered model of V_s obtained from (a), (c) porosity (n) profile based on laboratory measurement on samples obtained from a borehole adjacent to the SCPT location and the layer definition in (b), and (d) Darcy permeability (k) obtained from (c) using Kozeny-Carman relation.

frequency field data in soft soil is challenging. The approach discussed above seems to provide a solution. However, it is still difficult to extract good estimates of intrinsic seismic attenuation in the field, which will cause measurement error. Secondly, there will be error due to the inadequacy of the used poroelasticity model to explain the field-observed dispersion. It is important to understand the effect of these errors through realistic synthetic tests.

5.3 Tests on poroelastic synthetic VSP data

There are several obvious reasons for testing the validity of the proposed estimation approach first on realistic synthetic data, before trying on field data:

- (1) In the field, it is very difficult to measure accurately in-situ values of n and k at different depths in the soil; as a result, the goodness of any estimated n and k cannot be objectively checked. In a synthetic test, the n and k values are known.
- (2) In synthetic tests, the errors (e.g., due to noise in data, limited frequency content, model inadequacy) can be varied and the variations are known.
- (3) Extracting reliable, layer-specific, intrinsic dispersion information from the field seismic data, taking into consideration the fine internal layering effects, is very important. On field data it is difficult to check the accuracy of the estimated dispersion. On synthetic data, this can be done.

The main goal of the synthetic tests is, therefore, to critically investigate the feasibility and the accuracy of the new approach. A VSP geometry is chosen because (1) downhole measurements of S waves are more common in engineering site investigation, (2) it is much more realistic and feasible to estimate layer-specific in-

trinsic dispersion on downhole seismic data than on surface seismic data, and (3) the recent development of an array seismic cone penetrometer and the resulting high-quality data make estimation of intrinsic seismic dispersion in shallow subsoil more plausible (Ghose, 2012).

In order to make the synthetic VSP dataset sufficiently realistic, the following measures are taken. First, a realistic soil profile mimicking a sand-clay-peat site is used. The field-measured S -wave velocity (V_S) field and the lab-measured porosity values are used in synthetics generation. Second, a low frequency content, typical of S -wave data in unconsolidated soil, is considered. Third, up to 50% noise has been added to the synthetic data, which is sufficient to represent the real field situation. To evaluate the effect of model error, two poroelasticity models, which are grossly different, have been used - one for data generation and the other for the assumed model in estimation.

5.3.1 Generation of synthetic poroelastic VSP data

Figure 5.2a shows a V_S profile derived from a high-density (receivers at 25 cm interval in depth) seismic cone penetration test (SCPT) at a soft soil site in the western part of the Netherlands (Ghose, 2010b). At this SCPT location, the soil layer composition and n are known from direct sampling and laboratory tests. These are presented in Table 5.1. A detailed, 24-layered V_S profile (Figure 5.2b) is obtained by averaging within a window the V_S profile from SCPT (window length corresponding to the depth intervals for n measurements). The n and k for this 24-layer model is shown in Figures 5.2c and 5.2d, respectively. k is obtained from n using the Kozeny-Carman relation (Carman, 1937):

$$k = \frac{d_0^2}{36k_0} \frac{n^3}{(1-n)^2}, \quad (5.2)$$

where d_0 and k_0 are grain diameter and its shape-related coefficient, respectively. We use $k_0 = 5$, which corresponds to spherical grains. Layer-specific mean grain size has been assumed (Table 5.1) based on laboratory measurements or published data for similar soil types (Berry & Reid, 1987). Appropriate values have been assigned to the remaining parameters of the Biot-Stoll model. These values, constant for all 24 layers, are given in Table 5.2.

The VSP acquisition geometry includes a S -wave source located at 0.5 m distance from the VSP location and seismic sensors positioned in the borehole at 0.25 m interval between 0 and 30 m depths. Such a depth sampling is realisable in SCPT (Ghose, 2010a, 2012).

Poroelastic synthetic S -wave VSP seismograms have been computed using the finite element method implemented in COMSOL multiphysics environment. S -wave source polarization and the downhole horizontal component receiver orientation are in the cross-line direction. We have used the equation-based modelling application (PDE mode) in a 2D space. The equation of motion for S waves (Eqs. (2.46) and (2.47)) is solved within the computational domain (X). The size of X is 80×80 m. This relatively large size is meant to avoid any interfering reflections arriving from

Sample Depth (m)	Composition	Measured Porosity, n	Mean Grain Size (μm)	SCPT Vs (m/s)
3.6	clay, silt	0.525	2 *	81
5.5	peat, silt	0.831	5 *	50
6.6	clay, silt	0.569	10 *	87
8.6	clay, silt, sand	0.6	10 *	74
9.6	clay, silt	0.675	5 *	90
10.6	clay, silt	0.6	20 *	113
11.6	sand, silt	0.438	500 x	123
12.7	sand, clay	0.456	250 x	133
13.8	sand	0.444	400 x	129
15.6	clay, silt	0.575	70 *	111
16.6	peat, clay, silt	0.894	5 *	135
17.6	clay, silt	0.525	50 *	172
18.7	clay, silt	0.356	300 *	237
20.5	sand, silt	0.363	350 x	277
20.7	sand, silt	0.369	350 x	223
22.5	sand, silt	0.363	350 x	253
22.8	sand, silt	0.375	300 x	242
23.5	sand, silt	0.4	300 x	359
23.8	sand, silt	0.381	300 x	401
26.7	sand, silt	0.438	420 x	302
27.8	sand, silt	0.456	420 x	325
28.5	sand, silt	0.575	420 x	270
28.8	sand, silt	0.394	420 x	357
30	sand, silt	0.369	500 x	357

x Laboratory measurement

* Based on published data (Berry and Reid, 1987)

Table 5.1: Soil layer composition and porosity obtained from direct sampling and laboratory tests, mean grain size obtained from laboratory tests and published data, and V_S obtained from high-density SCPT.

Parameter	Unit	Value
Grain density, ρ_s	kg/m^3	2600
Fluid density, ρ_f	kg/m^3	1000
Fluid viscosity, η	$\text{Pa} \cdot \text{s}$	0.001
Tortuosity, γ	-	1.25
Shear logarithmic decrement, δ_s	-	0.1

Table 5.2: Values of parameters in Biot-Stoll model, in addition to those shown in Figure 5.2, used to generate poroelastic *S*-wave VSP synthetics.

the boundaries. The grid interval is 0.05 m. The first derivative of Gaussian with 80 Hz central frequency is used as the source function. Time sampling is 0.5 ms.

The boundary conditions at the interface between two fluid-saturated porous layers are given by the continuity of tangential stress and solid displacement:

$$\sigma_{12}^+ t_2 - \sigma_{12}^- t_2 = 0, \quad (5.3)$$

$$u_2^+ - u_2^- = 0, \quad (5.4)$$

where σ_{12} is the tangential stress, t_2 and u_2 are the unit vector and the solid phase displacement in the x_2 direction, respectively, + and - signs indicate, respectively, the upper and the lower medium with respect to the interface. The discontinuity of relative fluid displacement together with the fluid pressure discontinuity are ignored, as we consider the tangential components of the field variables (Deresiewicz & Skalak, 1963; Gurevich & Schoenberg, 1999). This implies that shear waves induce no pressure and hence no flow at an interface.

Figure 5.3a shows the poroelastic synthetic S -wave VSP data without noise. Figures 5.3b-5.3d show the same synthetic seismograms, but respectively with 10%, 20% and 50% random noise incorporated into the data, in a manner similar to Tonn (1991). The data is filtered between 4 and 250 Hz. The noise level is calculated taking into consideration the average spectral power of noise and signal. 20% and 50% noise level corresponds to signal-to-noise power ratio of 5 and 2, and amplitude ratio of $\sqrt{5}$ and $\sqrt{2}$, respectively. The data with 50% noise level has been stacked 10 times, with the random noise varying at each time. The resulting dataset is shown in Figure 5.3e. The 50% random noise after 10 times source stacking reaches a level which is 15.8% noise in the amplitudes.

5.3.2 Estimation of layer-specific intrinsic dispersion from VSP data: effect on n and k estimates

We have cross-correlated seismograms at two adjacent depths to find the transit time. Using the travel distance and the transit time, the interval velocity for every 0.25 m interval is calculated and is plotted at the middle of this interval. Obviously, such velocity estimation will be highly affected by the noise. The goal here is to examine the effect of error in velocity estimation on the extracted value of intrinsic dispersion. The derived V_S profiles corresponding to data in Figures 5.3a-5.3e are shown in Figures 5.3f-5.3j, respectively. With increasing depth, the signal-to-noise ratio in the VSP data decreases, which translates to increasing error in the estimated velocity. As expected, the stacking of random noise greatly improves the velocity estimates (compare between Figures 5.3i and 5.3j). Each of these V_S profiles is used in calculating the extrinsic attenuation due to multiple scattering (Wapenaar *et al.*, 2003).

The cone tip resistance (q_c) measured in the same SCPT (corresponding to the V_S profile in Figures 5.2a) is shown in Figure 5.3k. Note the correlation between the derived V_S profiles and the measured CPT q_c profile.

The main layer-boundaries can be determined by combined interpretation of changes in the interval travel time versus depth distribution, the depth of origin of the

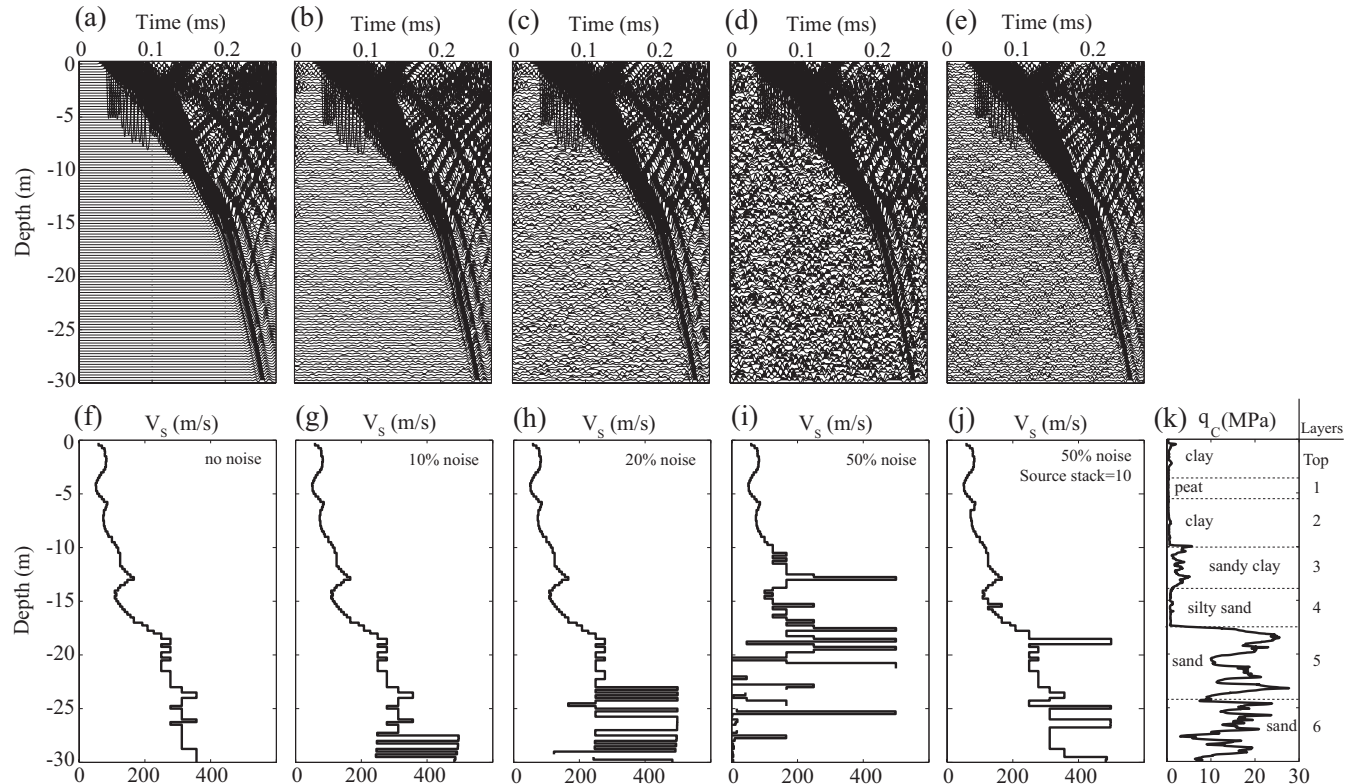


Figure 5.3: (a) Poroelastic synthetic S -wave VSP data without noise, (b)-(d) poroelastic synthetic S -wave VSP data respectively with 10%, 20%, 50% random noise, (e) the same data with 50% random noise but after 10 times source stacking, (f)-(j) V_p profiles obtained by cross-correlation, respectively from datasets shown in (a)-(e), and (k) SCPT cone tip resistance (q_c) field measurement.

upgoing waves in the VSP data, and the CPT data when available. The interpreted six layers are indicated on the right margin in Figure 5.3k. We want to estimate the intrinsic S -wave dispersion in each of these six layers, taking into consideration the loss due to internal reflections within each layer. The partially saturated top layer is excluded, as the present approach is valid for full fluid saturation. We shall first illustrate the estimation procedure and the results using noise-free synthetic VSP data, because otherwise it is not possible to separate the effect of estimation inaccuracy from that of data and/or model error. These results are shown in Figures 5.4-5.6.

The velocity dispersion can be calculated using the relative phase delay time at different frequencies for a given receiver pair positioned at two different depths within a layer (Molyneux & Schmitt, 2000):

$$V(f) = \frac{\Delta x}{\Delta t} = \frac{2\pi\Delta x}{\Delta\phi(f)} f, \quad (5.5)$$

where $\Delta\phi$ is the phase difference for a given frequency and Δx is the travel-distance difference between the receiver pair. In order to calculate the average velocity dispersion within a given layer we take the following approach. Assuming that we have N receivers within a given layer of interest, we choose the topmost (r^{top}) and the lowermost (r^{low}) receivers as the reference receivers. We use all possible receiver combinations with r^{top} and r^{low} , except the combination of the two reference receivers themselves. We have, thus, $2(N - 2)$ combinations. We then calculate the relative phase delay time Δt at different frequencies for all $2(N - 2)$ combinations.

This is shown for one single frequency (75 Hz) for all six layers in the left column of Figure 5.4. The slope of the best-fit line obtained by linear regression of Δx - Δt distribution gives the phase velocity for the given frequency. This estimation is performed for all frequencies to obtain the velocity dispersion curve, which is shown in the right column of Figure 5.4. We restrict ourselves to 50-140 Hz band, because the signal frequency lies in this band. The standard deviations of the estimated velocity dispersion for each frequency are indicated by the vertical bars. This is calculated from the scatter in the Δx - Δt plots. The line with black circles in the right column of Figure 5.4 indicates the mean value for velocity dispersion.

The reliability of velocity dispersion thus estimated from the VSP data can be checked by comparing the estimate with the value obtained from known soil properties in the model. Because the internal stratification within each of the six layers is known for our synthetic model (Figures 5.2b-5.2d), such an analysis is possible. The two red lines in the velocity dispersion plots shown in the right column of Figure 5.4 indicate the theoretical velocity dispersion obtained using the effective n , k and the real part of shear rigidity (G_r) values, calculated from the Voigt upper bound and the Reuss lower bound. The Voigt upper bound for a mixture of M material phases is given by:

$$n_V = \sum_{i=1}^M f_i n_i, \quad k_V = \sum_{i=1}^M f_i k_i, \quad G_V = \sum_{i=1}^M f_i G_i. \quad (5.6)$$

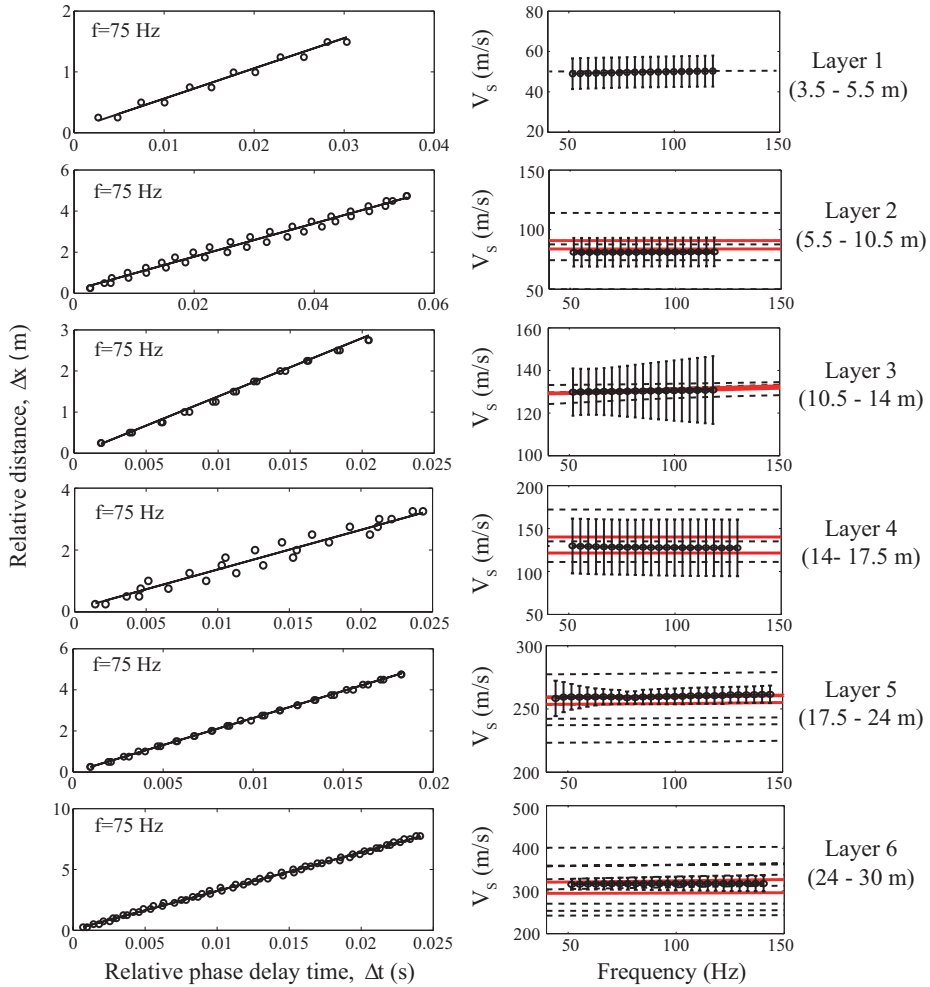


Figure 5.4: Estimation of velocity dispersion in six depth ranges for the noise-free data. Left column: V_S estimation for one frequency (75 Hz) following equation 5.5. The slope of the best-fit line gives V_S . Right column: V_S estimated over the entire frequency range shown by the line with black circles, along with the standard deviation given by the vertical bars. The two red lines indicate the upper and lower bounds for the composite layer computed from the known properties and thicknesses of the constituent internal layers. The dashed lines indicate dispersion curves for each constituent layer, theoretically estimated from the known layer properties (see Figures 5.2c and 5.2d).

The Reuss lower bounds are expressed as:

$$\frac{1}{n_R} = \sum_{i=1}^M \frac{f_i}{n_i}, \quad \frac{1}{k_R} = \sum_{i=1}^M \frac{f_i}{k_i}, \quad \frac{1}{G_R} = \sum_{i=1}^M \frac{f_i}{G_i}. \quad (5.7)$$

In equations 5.6 and 5.7, f_i is the fraction of the i^{th} internal layer, n_i , k_i and G_i are respectively n , k and G of the i^{th} internal layer. G has been estimated from V_S ; for this purpose the bulk density befitting the soil composition (the latter derived from the interpretation of CPT data) has been used. These bounds for layer-specific effective soil properties have been used in the poroelasticity (Biot-Stoll) model to calculate the theoretical dispersion curves. For layer 1 it is not possible to calculate these bounds, as there is no internal layering. For all other layers it is possible (Figure 5.4).

As it will be demonstrated later in this section, the effect of scattering attenuation on seismic dispersion is negligible. Thus, the observed velocity dispersion is due to intrinsic absorption. It is clear that, except marginally for layer 2, velocity dispersion curves estimated from the VSP data (line with black circles) lie nicely between the theoretical upper and lower bounds (red lines) for the effective/composite medium. This is an indication that the approach of estimation of velocity dispersion from VSP data used here is robust and the estimated values are realistic. Each black dashed line in the right column in Figure 5.4 is the theoretical velocity dispersion curve calculated for each internal layer. Note that our estimated velocity dispersion from VSP data is generally in the middle of the spread of all individual curves, further validating the goodness of the estimated layer-specific velocity values.

We have used an adaptation of the spectral ratio method for estimating effective attenuation (Jeng *et al.*, 1999). With only two receivers, the spectral ratio method has large uncertainties. The reliability can, however, be significantly improved if multiple receivers are used within a given layer. This is explained in Figure 5.5 for layer 6 (24-30 m). A time window around the peak amplitude of the first arriving S wave is automatically selected for all depth levels of the VSP data. Figure 5.5a shows the logarithmic spectral amplitude ratio for a given frequency of the first-arrival S wave recorded at all receiver depths within the depth interval of layer 6, with respect to the first-arrival S wave at the uppermost (r^{top}) and at the lowermost (r^{low}) receivers within the same interval (the symmetric distribution between one half of the data points with the other half is due to the two reference receivers used). From the slope of the best fit-line through these data points, the effective attenuation for a given frequency (75 Hz for the illustration in Figure 5.5a) is obtained. This is done for all frequencies in order to obtain the frequency-dependent effective attenuation for this layer, which is shown in Figure 5.5b. The vertical bars indicate the standard deviations estimated from the data. Effective attenuation is the sum of intrinsic attenuation and extrinsic attenuation due to multiple scattering. We have estimated multiple scattering due to internal layering using the formulation of Wapenaar *et al.* (2003), which relates the codas between transmission and reflection responses.

In order to calculate the extrinsic attenuation due to scattering, we use the velocity profile derived from the VSP data (Figure 5.3f) and a realistic assumption of

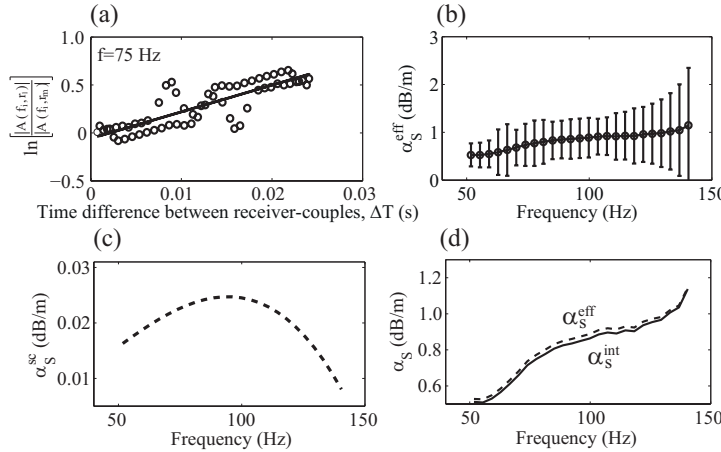


Figure 5.5: Estimation of frequency-dependent intrinsic attenuation, illustrated for layer 6 (24-30 m) for the noise-free data: (a) logarithmic ratio of the spectral amplitudes versus arrival-time difference, for 75 Hz, (b) effective attenuation (α_S^{eff}), (c) scattering attenuation (α_S^{sc}), (d) scattering attenuation subtracted from effective attenuation giving intrinsic attenuation (α_S^{int}).

the layer-specific bulk density. Figure 5.5c shows the estimated extrinsic attenuation due to multiple scattering. Note that the vertical axis in Figure 5.5c is much exaggerated compared to that in Figure 5.5b. In other words, the scattering attenuation is rather small. When the scattering attenuation is subtracted from the observed effective attenuation (Figure 5.5b), what remains is the intrinsic attenuation. This is shown in Figure 5.5d (solid line), along with the effective attenuation (dashed line).

Figure 5.6 shows for all six layers the estimated frequency-dependent attenuation. The left column shows effective attenuation together with the standard deviation, the middle column shows the intrinsic and the effective attenuations, and the right column illustrates the intrinsic attenuation (line with black circles) along with the standard deviations. Intrinsic attenuation theoretically calculated for all the internal layers that constitute a composite layer is also shown in the right column of Figure 5.6 (dashed lines), together with the theoretical upper and lower bounds for the effective medium (red lines). Note that for almost all layers the upper and lower bounds are rather close, and the estimated intrinsic attenuation is not far from these bounds and lies within the spread of the attenuation curves for all individual layers. This suggests that the calculated values of intrinsic attenuation are realistic. For layer 4 the estimate is slightly outside the range of the theoretical bounds. This can be explained by the fact that within layer 4 there is a thin peat layer (at 15.6-16.6 m depth) with an extremely high porosity compared to the porosity in the surrounding layers (see Figure 5.2c and Table 5.1).

These results (Figures 5.4-5.6) generally suggest that it is possible to achieve reasonable accuracy in extracting *S*-wave intrinsic dispersion (both velocity and attenuation) from the VSP data, in case multiple receivers are located within each layer.

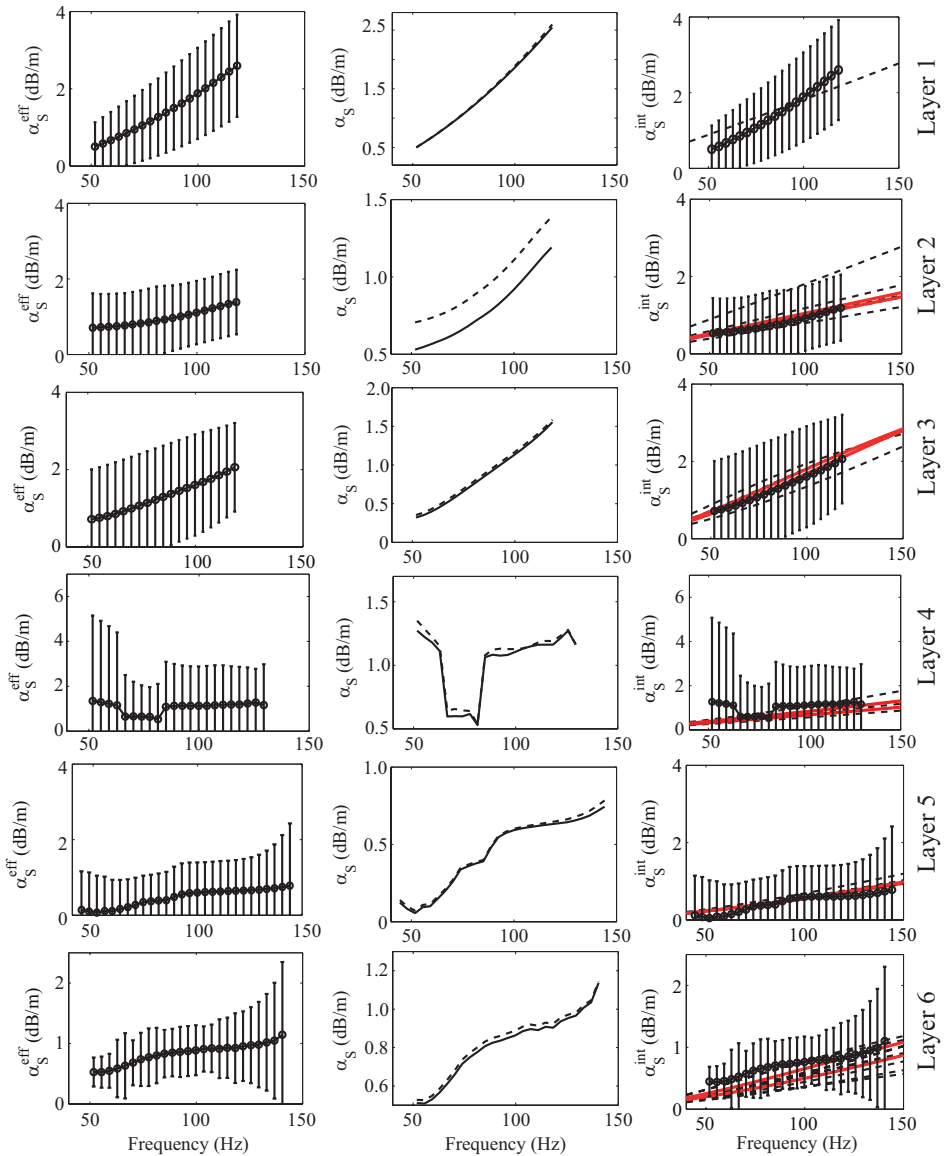


Figure 5.6: Left column shows effective attenuation for all six composite layers for the noise-free data. Middle column illustrates the estimated intrinsic attenuation (solid line) and the effective attenuation (dashed line), same as in Figure 5.5(d). Right column shows the intrinsic attenuation (line with the black circles) along with standard deviations (vertical bars) and the theoretically estimated bounds (red lines), as well as the theoretical dispersion curves for the individual thin layers (dashed lines) within each composite layer.

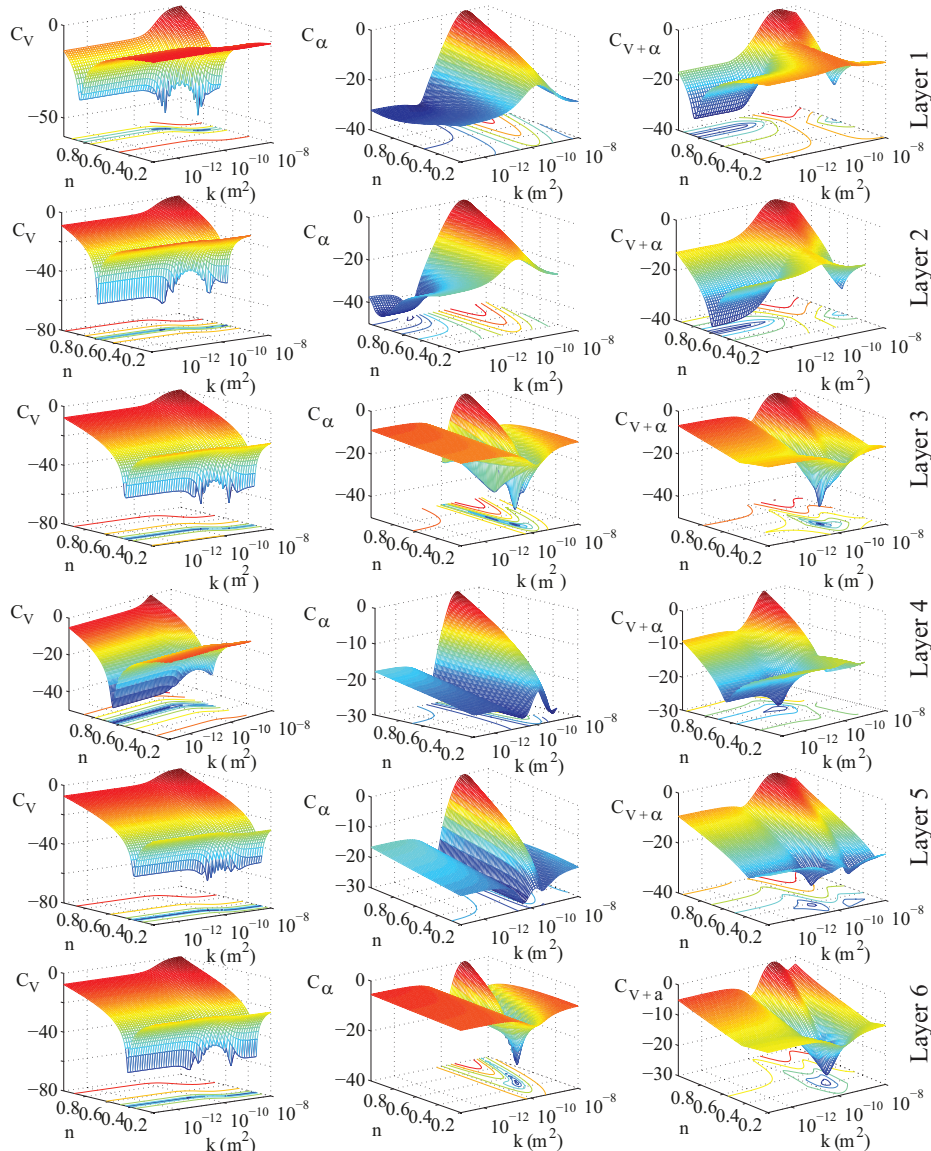


Figure 5.7: Cost functions (in dB) for velocity (C_V), attenuation (C_α) and integrated velocity+attenuation ($C_{V+\alpha}$) following equation 5.1, for all six layers for the noise-free data. Standard deviation of data has been used as the weight in cost function minimization. The cost function scale differs between the plots; this is because the minimum has been made visible in the contours drawn on the n - k plane.

Finally, we will discuss the effect of inaccuracy in extracting the dispersion on estimated n and k , by illustrating results on noise-free data and using the same model which has generated the data for the model in estimation. Figure 5.7 shows the individual costs functions C_V and C_α and the integrated cost function $C_{V+\alpha}$ in the $n - k$ domain for all six layers, for noise free data (see Figures 5.3a, 5.4 and 5.6). We find that, for all layers except layer 2, the integrated cost function shows a sharp minimum in the $n - k$ domain, from which unique estimates of n and k can be obtained. For layer 2, no minima can be found for the frequency range available in the data. This is due to the rather low (of the order of 10^{-12} m^2) k in this very clayey layer (see Figure 5.2d), which asks for higher frequencies in the dispersion data than what we have (50-140 Hz) in the synthetic data. The critical frequency of dispersion increases as k decreases. If we had higher frequencies in data, then n and k for layer 2 could also be resolved. This is explained in Zhubayev & Ghose (2012a).

In Table 5.3a and 5.3b the estimated n and k values for 0% noise in data and using the Biot-Stoll model are listed for all six layers. The theoretical ranges are also given. Clearly, if there is no noise in data and the model is also error-free, then the effect of error in extraction of layer-specific values of intrinsic dispersion from the VSP data is quite small on the n estimates and the estimated k is comfortably in the same order of magnitude as the theoretically expected range.

5.3.3 Noisy data and error in estimated dispersion: effect on n and k estimates

Now, we will look in detail at the effect of noise in data. The VSP datasets of various noise levels are presented earlier in Figure 5.3. Figure 5.8a-5.8d show, for layer 6, V_S estimation for 75 Hz frequency following equation 5.5, respectively for data with no noise, 10% noise, 20% noise and 50% noise. The straight line in these plots is the best-fit line. Figure 5.8e shows the same V_S estimation for 75 Hz, for data with 50% random noise but with 10 times source stacking. Evidently, when there are multiple receivers within a given layer thickness and when all these receivers are used for estimating the layer-specific velocity dispersion, the estimate is generally quite stable and accurate. Figures 5.8f-5.8i show, for the same layer 6, logarithmic ratio of spectral amplitudes versus arrival time difference between various receiver pairs, respectively for data with no noise, 10% noise, 20% noise and 50% noise. Here also, the straight line is the best-fit line, giving the effective attenuation for 75 Hz. Figure 5.8j corresponds to 50% random noise in data but with 10 times source stacking. Remarkably, note that unlike for velocity dispersion (Figures 5.8a-5.8e) where the slope of the best-fit line changes little with changing noise level, for attenuation (Figures 5.8f-5.8j) there is a clear change, especially for 50% noise level. 10 times source stacking greatly helps in bringing the error in attenuation estimate back to 0-10% noise level of the unstacked data.

The effect of noise in data and the benefit of source stacking on the estimates of intrinsic dispersion in layer 6 are illustrated in Figures 5.8k and 5.8l, for velocity and attenuation, respectively. The black lines in these figures correspond to different noise levels. The dispersion for 50% random noise level with 10 times source stacking

(a) Porosity estimates

Layer Number	Depth Range (m)	Porosity Reuss-Voigt, $n_R - n_V$	n_{est}											
			Using Biot-Stoll model						Using BICSQS model					
			noise in data (%)					0 10 20 50 50 st	noise in data (%)					0 10 20 50 50 st
Top	0 - 3.6	-	-	-	-	-	-	-	-	-	-	-	-	-
1	3.5 - 5.5	0.83 - 0.83	0.86	0.86	0.86	0.86	0.86	0.86	0.86	0.86	0.85	0.85	0.86	0.86
2	5.5 - 10.5	0.59 - 0.62	-	-	-	-	-	-	-	-	-	-	-	-
3	10.5 - 14	0.44 - 0.45	0.45	0.45	0.46	0.47	0.45	0.44	0.43	0.45	0.43	0.43	0.43	0.44
4	14 - 17.5	0.61 - 0.68	0.65	0.65	0.66	0.68	0.65	0.65	0.65	0.65	0.65	-	0.65	-
5	17.5 - 24	0.36 - 0.37	0.37	0.38	0.39	-	0.38	0.39	0.38	0.39	-	0.38	-	0.38
6	24 - 30	0.40 - 0.43	0.42	0.40	0.40	-	0.39	0.36	0.34	-	-	-	-	-

(b) Permeability estimates

Layer Number	Depth Range (m)	Permeability Reuss-Voigt, $k_R - k_V \times 10^{-12} (\text{m}^2)$	$k_{est} \times 10^{-12} (\text{m}^2)$											
			Using Biot-Stoll model						Using BICSQS model					
			noise in data (%)					0 10 20 50 50 st	noise in data (%)					0 10 20 50 50 st
Top	0 - 3.6	-	-	-	-	-	-	-	-	-	-	-	-	-
1	3.5 - 5.5	2.8 - 2.8	3.3	7.5	2.4	1.2	5.2	60	49	72	49	60	-	-
2	5.5 - 10.5	0.7 - 1.1	-	-	-	-	-	-	-	-	-	-	-	-
3	10.5 - 14	180 - 240	170	150	126	87	126	184	222	268	41	222	-	-
4	14 - 17.5	5 - 12	23	26	49	42	19.3	60	60	41	-	60	-	-
5	17.5 - 24	72 - 76	48	15.9	23.3	-	15.9	87	153	127	-	87	-	-
6	24 - 30	70 - 180	290	327	285	-	305	596	754	-	-	-	-	-

Table 5.3: Layer-specific porosity (n) and permeability (k) values. n_{est} and k_{est} are the estimates using the new approach tested in this research. Reuss and Voigt bounds are obtained from the known properties and thicknesses of the internal layers.

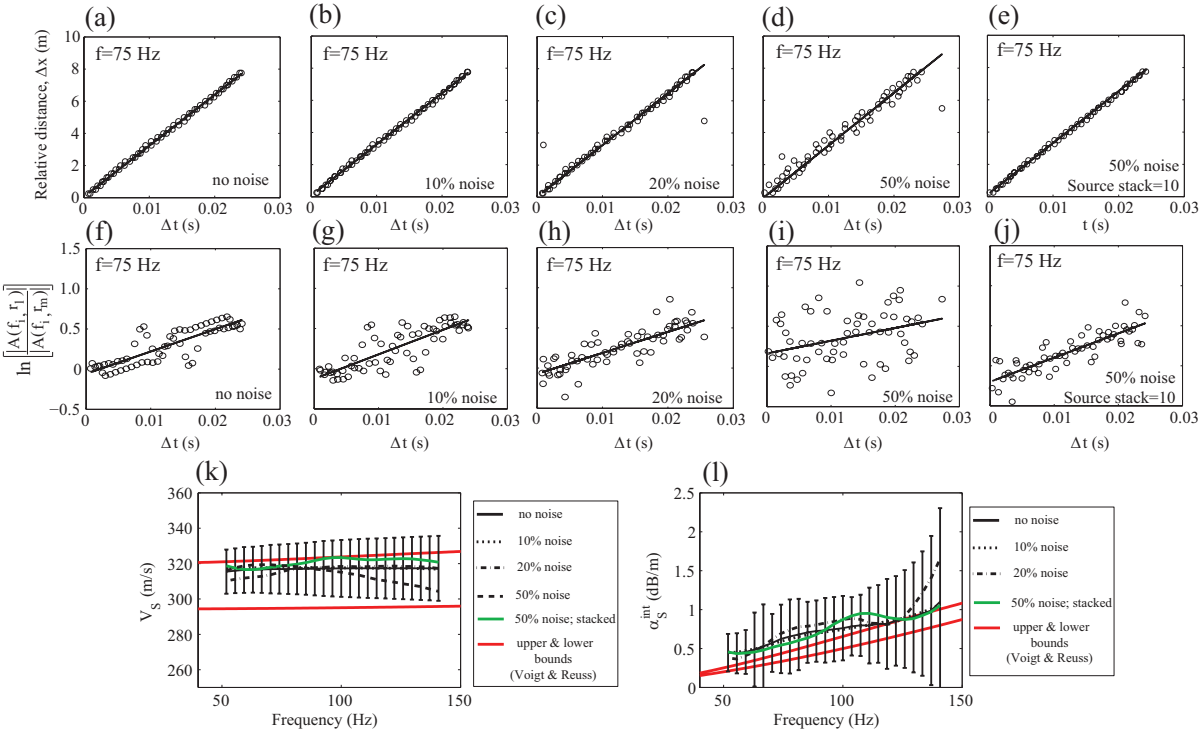


Figure 5.8: Effect of noise in the VSP data (illustrated for layer 6) on estimation of velocity and attenuation dispersion: (a)-(e) V_s estimation for 75 Hz following equation 5.5, for different noise levels in the data. (f)-(j) Logarithmic ratio of the spectral amplitudes versus arrival-time difference for 75 Hz, for different noise levels in the data. (k) S -wave velocity dispersion in the 50-150 Hz band for various noise levels. (l) S -wave attenuation in the 50-150 Hz band for various noise levels. The two red lines show the theoretical bounds calculated from known n , k and V_s distribution in the composite layer.

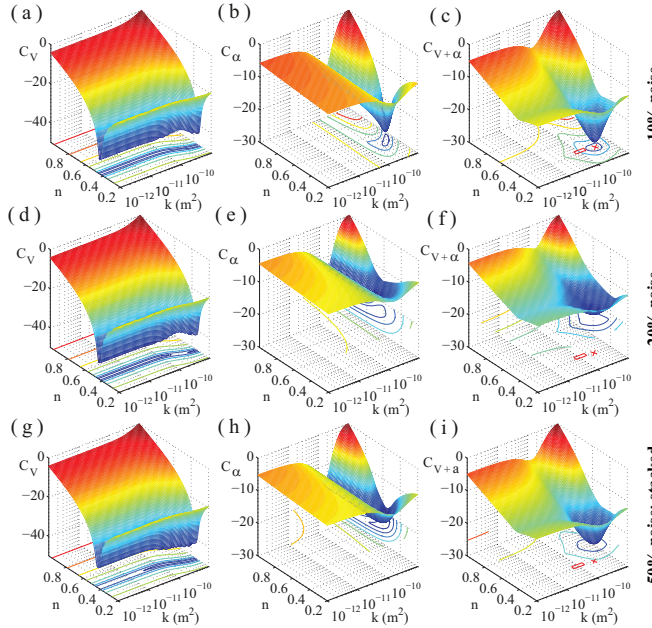


Figure 5.9: Effect of noise in the VSP data (illustrated for layer 6) on the cost functions (in dB) for velocity (C_V), attenuation (C_α) and integrated velocity+attenuation ($C_{V+\alpha}$) following equation 5.1: (a)-(c) for 10% random noise, (d)-(f) for 20% random noise, and (g)-(i) for 50% random noise with 10 times source stacking. The red cross and the red rectangle in (c), (f) and (i) denote, respectively, the cost-function minimum and the theoretical bounds for the composite layer.

is shown by the green line. The two red lines indicate the theoretical upper and lower bounds estimated from the known distribution n , k and V_S within each layer. For intrinsic attenuation (Figure 5.8l), the curve for 50% noise without source stacking is not shown, as it is not possible to estimate good intrinsic attenuation (the extrinsic attenuation, due to the large noise, becomes unrealistically large, exceeding the effective attenuation). For velocity, all estimates (even for 50% noise and no source stacking) fall within the theoretical bounds and within the estimation error bars. Till 20% noise in the unstacked data and 50% noise in case of 10 times stacking, the estimated dispersion curves are not much different from the no-noise situation; however when the noise is very large (50%) and there is no source stacking, the attenuation estimate becomes quite erroneous. For velocity, the estimates fall slightly outside the theoretical bounds, even for the noise-free case; this is probably due to the presence of a thin, sharply low-permeability lens (at ~ 28.5 depth, see Figure 5.2) within a relatively high-permeability sand layer.

If there are many receivers within the thickness of a given layer and the source stack count is large (> 10), then it is possible to obtain quite reliable estimates of intrinsic dispersion (both velocity and attenuation) even when the random noise level is high. Figure 5.9 shows the effect of noise in VSP data and hence in the estimated

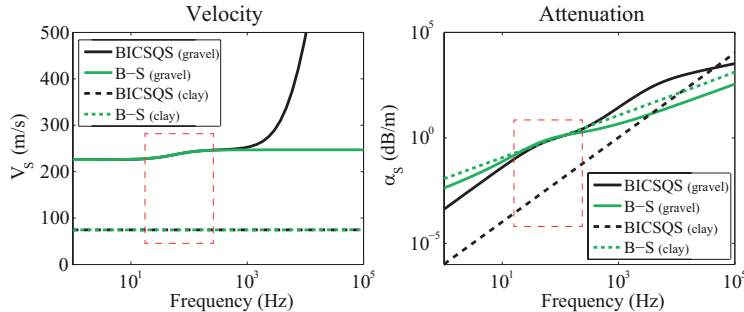


Figure 5.10: Theoretical dispersion curves for Biot-Stoll and BICSQS models for two soil types - fine-grained (clay) and coarse-grained (gravel). The red-dashed box marks the typical frequency range for S -wave seismic data in soft soil. The values of the parameters used to calculate these curves are presented in Table 5.4.

layer-specific dispersion on the n and k values estimated from the integration of dispersive S -wave velocity and attenuation. The individual cost functions for velocity and attenuation and the integrated velocity+attenuation cost function for 10% noise, 20% noise, and 50% noise with 10 times source stacking are shown. While for 10% noise we see a very sharp minimum in the integrated cost function in the n - k domain, the minimum is present but much less sharp when the random noise is 20%. However, even for a noise level as high as 50%, 10 times source stacking results in a quite sharp global minimum.

Table 5.3 summarizes the estimated n and k values for data with random noise of 0%, 10%, 20%, 50% and 50% with 10 times source stacking and when the model used is accurate (i.e., Biot-Stoll model). When the noise level is very high (50%) and there is no source stacking, it is still possible to estimate n within 2-3% absolute error for the shallow layers (layers 1, 3 and 4), but the error in permeability is twice as large compared to the low-noise case. With such high noise in the data and no stacking, it is not possible to estimate n and k at large depths (layers 5 and 6), where the signal-to-noise ratio drops significantly. However, if the data with 50% random noise is stacked for 10 times, then stable estimates of both n and k can be obtained and the error in the estimates is comparable to the 10-20% noise case (without stacking).

5.3.4 Error in model: effect on n and k estimates

So far we have considered the issue of noise in the data only, assuming a perfect model. However, in reality, the model is never known and there will always be a deviation between the model assumed and the model that perfectly fits the observed dispersion. In order to understand the effect of this model error on the estimated n and k , we consider two models which are grossly different - one representing the truth (field reality) and the other corresponding to the assumed model. For field data, we still use the Biot-Stoll model; we consider BICSQS as the assumed model in the cost-function minimization scheme.

Compared to the Biot-Stoll model, the BICSQS model is known to explain better the high seismic dispersion in relatively coarse-grained, high-permeability sediments. However, if the dispersion is not large, then both models offer a good prediction. Figure 5.10 shows a comparison of these two very different models for *S*-wave dispersion in typical fine-grained (clay) and coarse-grained (gravel) soils. Table 5.4 shows the values of all parameters that have been used to estimate these dispersion curves. We have used representative values for those few parameters which are not common between the two models, viz. shear logarithmic decrement (δ_S) in the Biot-Stoll model, and shear relaxation frequency (f_c) and half gap width (a_1) in the BICSQS model. The main difference in the dispersion behaviour between these two models that we see in Figure 5.10 is due to the difference in the models themselves, and not due to the difference in the values of the parameters. Clearly, at the low frequencies corresponding to field *S*-wave data in soft soil (red dashed boxes in Figure 5.10), the velocity dispersion is the same in the two models. However, in the same frequency range, the attenuation is grossly different between them for fine-grained sediments (e.g., clay). For relatively high-permeability coarse-grained sediments, these models are rather close in case of attenuation at field seismic frequencies.

The green crosses and the black diamonds in Figure 5.11 indicate the n and k estimates using, respectively, Biot-Stoll model and BICSQS model as the assumed model. The VSP data used (representing field observation and generated using the Biot-Stoll model) is the same for the two assumed models and are shown in Figure 5.3. Layer 2 is excluded in this plot because, given the low frequency-content in the VSP data, it is not possible to get estimates of n and k for this very low-permeability clay, as explained earlier. The horizontal axis in Figure 5.11 shows noise levels in the synthetic data - 0% (no noise), 10%, 20%, 50%, and 50% noise with 10 times source stacking. The red lines indicate the theoretical bounds estimated using the known n and k distribution within each layer. For layer 1, there is no internal layering, so there is only one estimate and no bounds.

The difference at 0% data noise is indicative of the effect of model error only. Dispersive *S*-wave velocity and attenuation are affected by both n and k . In general, n has a strong effect on velocity, while attenuation is primarily sensitive to k . For the n estimate, the effect of only model error (i.e., 0% data noise) is negligible for the shallow layers 1, 3 and 4, because the two models are the same for velocity dispersion. However for layer 5 and layer 6, there is some difference (by about 2% in the absolute scale). We believe that this is due to attenuation being estimated slightly different between the two assumed models. The effect of only model error on the k estimates, shown on the right column in Figure 5.11, is more significant. Evidently, this effect is large in layers 1 and 4, and quite small in layers 3 and 5. Layers 1 and 4 are fine-grained soils and less sandy than layers 3 and 6 (see CPT q_c in Figure 5.3k). Figure 5.10 shows that for fine-grained soils the difference in attenuation between Biot-Stoll and BICSQS models is very large, but this difference is rather small when the soil is coarse-grained. This explains the effect of only model error on the k estimates. Layer 6 has some clay alterations; therefore, the two models differ in attenuation; this is probably the reason why we notice some difference in the estimated k between the two models.

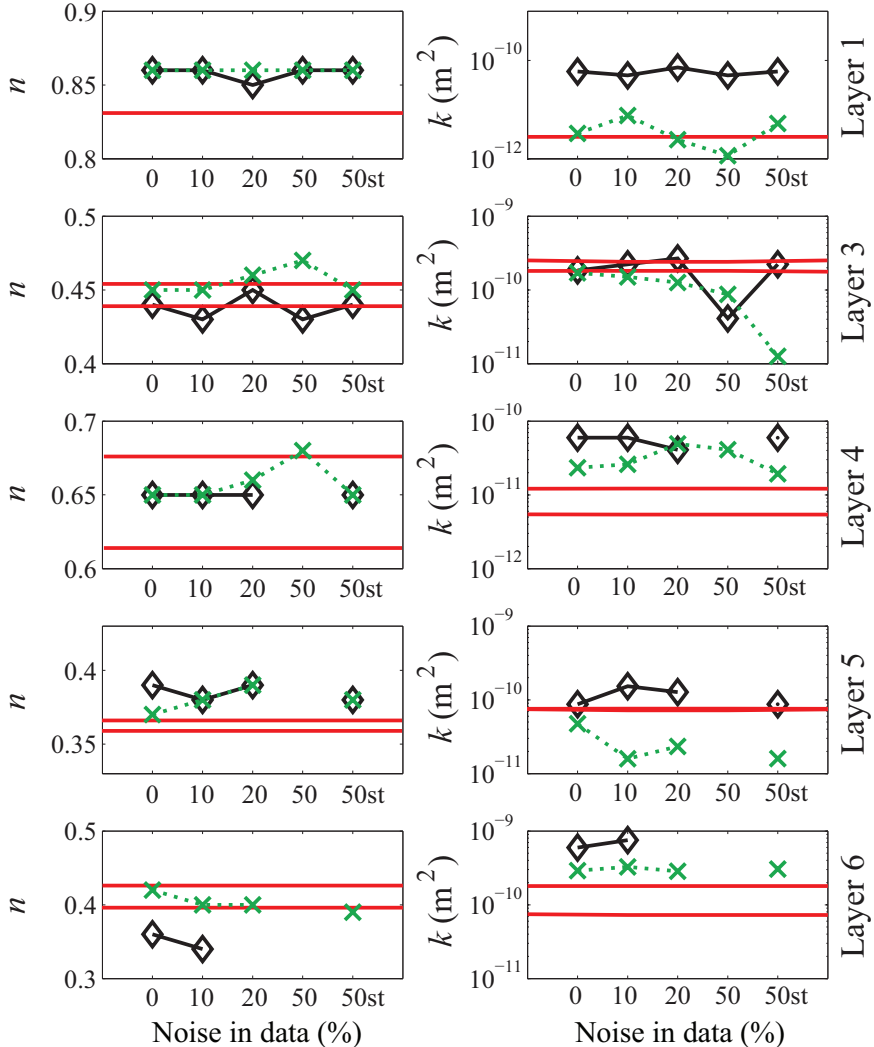


Figure 5.11: Effect of error in model used and error in data on n and k estimates. The synthetic VSP data (representing field observation) is generated using Biot-Stoll model. For estimating n and k , the assumed model in cost-function minimization is either Biot-Stoll (green cross) or BICSQS (black diamond). The red lines are the theoretical bounds for the composite layer.

Parameter	Unit	Biot-Stoll		BICSQS	
		gravel	clay	gravel	clay
Porosity, n	-	0.4	0.5	0.4	0.5
Permeability, k	μm^2	1000	0.1	1000	0.1
Grain density, ρ_s	kg/m^3	2600	2600	2600	2600
Fluid density, ρ_f	kg/m^3	1000	1000	1000	1000
Fluid viscosity, η	$\text{Pa}\cdot\text{s}$	0.001	0.001	0.001	0.001
Tortuosity, γ	-	1.25	1.25	1.25	1.25
Pore size, a	μm	10	0.1	10	0.1
Frame shear modulus, G	GPa	0.1	0.01	0.1	0.01
Shear logarithmic decrement, δ_s	-	0.1	0.1	-	-
Shear relaxation frequency, f_c	kHz	-	-	4	400
Half gap width, a_l	μm	-	-	1	0.1

Table 5.4: Values of parameters in Biot-Stoll and BICSQS models for calculating *S*-wave dispersion shown in Figure 5.10.

If the data has noise and the assumed model is also inadequate, then the combined effect of these errors on n and k estimates can be evaluated on synthetic data. There is a trend in Figure 5.11 that, for both n and k , as the data becomes increasingly noisy, the estimates diverge from the limit of the theoretical bounds (red lines). However, source stacking of the noisy data is generally helpful in reducing this error. Here, we have considered the Biot-Stoll and the BICSQS models, because the difference between them is very large for fine-grained sediments in the field-seismic frequency range. The effect of model error that we have discussed are, therefore, not underestimated. In reality, one should check first, using typical values of soil parameters, which of the available poroelasticity models fits best an observed *S*-wave dispersion dataset, and then use this model in the scheme of integration of velocity and attenuation, to obtain the estimates of in-situ n and k in saturated soil layers.

The results presented here indicate that if the model error is not large, then both n and k estimates should be quite accurate even when the data is rather noisy. Source stacking helps greatly to improve the accuracy further. However, when the model used is grossly inaccurate (e.g., using BICSQS model for fine-grained soils) and there is also much noise in the data and hence a large error in the estimated dispersion, then though the absolute error in n is still within 2-3%, k can be off by an order of magnitude (see in Figure 5.11 the estimated k for layers 1 and 4 using BICSQS model instead of Biot-Stoll model). In general, if the poroelasticity model is so chosen that it explains reasonably well the observed dispersion, then the

estimates of in-situ n and k should both be quite accurate.

5.4 Discussion

It has so far been impossible to obtain reliable, in-situ values of n and k in the near-surface, water-saturated soil layers. Geophysical logging tools for n estimation which are used for hard rocks do not work well for soft soils. Laboratory estimation on samples is generally problematic, especially for loose, sandy soils for which undisturbed sample collection is very difficult. In this Chapter, we have investigated the feasibility of a proposed approach for estimation of in-situ n and k in unconsolidated soils from S waves at the field-frequency band (see Chapter 4). We have tested the approach on a synthetic S -wave VSP dataset with various degrees of added random noise. The synthetic dataset is realistic. The effect of inaccuracy in the estimated S -wave dispersion on the property estimates has been analysed. To understand the influence of model error, a model which is grossly different from the one representing field reality has been used.

We have considered the noise in VSP data to be random. In practice, the noise is generally also source- and receiver-related. The receiver coupling in a VSP can and does change from depth to depth. This makes estimation of depth-dependent dispersion, especially attenuation, very difficult. Further, the source function can also vary from shot to shot. That makes it challenging to use data from two different sources to estimate intrinsic seismic dispersion. Solving these problems needs extra attention.

For field application we use a vibratory S -wave source which is well-monitored, including the source coupling (Ghose *et al.*, 1996; Ghose & Goudswaard, 2004; Ghose, 2012). It is possible to correct for the source-coupling variation through deterministic source-signature deconvolution. In this case, the effective source wavelet after raw vibrogram compression is quite uniform from shot to shot (Ghose, 2002). This is useful in measuring the S -wave amplitude change in the subsoil, decoupled from the source effect.

To minimize the effect of receiver coupling variation, we propose the use of closely spaced receivers in depth, covering densely the thickness of the layer of interest. We have shown in this chapter that having multiple receivers results in many receiver pair combinations and the use of the best-fit line to obtain the dispersion. This increases stability and reliability of the estimate. Tonn (1991), while comparing various methods for frequency-independent quality factor (Q) estimation from VSP, also recommended the use of a sufficient number of geophones within a layer. In this way, the error is addressed in a statistical manner.

Recently, a digital array seismic cone penetrometer based on micro-electromechanical systems (MEMS) has been developed (Ghose, 2012). In SCPT, because the cone is pushed into the ground, the coupling of the cone with the surrounding soil is generally very good. This usually results in high-quality VSP data. In the new array SCPT system, an array of (7 at present) closely spaced seismic sensors is located within the cone. The advantage is that the source function is constant within an array. If deterministic source signature deconvolution is performed on raw vibroseis

data acquired with the array SCPT system, then the amplitude fidelity is greatly improved.

The frequency band in shallow VSP data in soil can be extended if high-frequency, controlled seismic sources, like electromagnetic vibrators (Ghose *et al.*, 1996; Ghose *et al.*, 1998), are used instead of traditional impulsive sources, like a sledge-hammer. If the frequency band is extended, then the extracted dispersion will contain information of n and k for soils with finer grain size and the accuracy will also increase.

5.5 Conclusions

We have tested, on a synthetic VSP dataset, a concept of quantitative integration of dispersive S -wave velocity and attenuation in unconsolidated soils, based on the underlying physics, to estimate in-situ, layer-specific values of n and k . The soil profile, the V_S field, and n and grain size values have been taken from field measurements at a sand-clay-peat site. The low frequency content and sufficient added noise make the S -wave synthetic VSP dataset further realistic. The effect of inaccuracy in the extraction of intrinsic dispersion information from the VSP data even when there is no noise, the effect of random noise in data on the estimated dispersion and hence on the estimated n and k , and finally the effect of inadequacy of the assumed model with and without data error have been investigated in details. Having a sufficient number of seismic receivers within the thickness of the soil layer of interest greatly helps in obtaining reliable and stable estimates of layer-specific S -wave dispersion. Our test results show that in general, in this approach, if the poroelasticity model is so chosen that it explains reasonably well the observed dispersion, then the estimates of in-situ n and k are quite accurate even when the data has large noise. However, when the model used is grossly inaccurate and there is large noise in data, then although the absolute error in n is still within 2-3%, k can be off by an order of magnitude.

Chapter 6

Global optimization using poroelasticity theory

6.1 Introduction

Laboratory and field-seismic measurements have indicated in the past the dispersive nature of seismic wave propagation through partially or fully saturated geomaterials (e.g., Kudo & Shima, 1970; Michaels, 1998; Sams *et al.*, 1997; Batzle *et al.*, 2006; Adam *et al.*, 2009). In this context, elasticity theory - which requires only two elastic coefficients (assuming isotropy) and density to calculate seismic velocities, or viscoelasticity theory - which incorporates fluid viscosity in order to explain seismic attenuation, are generally unable to predict the broadband seismic dispersion data. This suggests the insufficiency of these models and/or incompleteness of the parameterization. The poroelasticity models, e.g., those of Biot-Stoll and BICSQS, as described in Chapter 2, on the other hand, require up to 13 parameters for a complete description of seismic wave dispersion. Some of these parameters are difficult to virtually impossible to measure in reality. Having such a multitude of parameters results in extra difficulty in forward modelling and inversion.

Compared to elasticity or viscoelasticity theory, the presence of more unknown parameters in the poroelasticity models makes identifying a global solution for the involved parameters a complex problem. In many cases, the parameters are interrelated or coupled. Thus, an uncertainty in one parameter causes an uncertainty in the other. Further, some model parameters are significantly more influential than the remaining parameters to changes in the cost function representing the data-model residual (Chapters 4 and 5), while some others have almost no influence. Information such as parameter *hierarchy* and parameter coupling can be useful in improving the reliability/stability and efficiency of an optimization approach for property estimation.

In this chapter, we introduce a non-invasive method to determine the independent soil/rock properties within a poroelastic framework, using frequency-dependent seismic transmission data. We consider a multiparameter cost function and look for a

global optimization method that minimizes this cost function. In order to efficiently navigate the parameter space in the global search algorithm, relative sensitivities of different parameters and their intrinsic coupling are studied prior to the inversion. We apply this approach to the compiled near-surface shear-wave dispersion data in fully saturated onshore sediments. Finally, we discuss and summarize our results.

6.2 Optimization

In order to find the global solution in a multivariate or combinatorial problem, the optimization techniques must have the ability to avoid local minima. In this vein, one efficient approach was proposed by Kirkpatrick *et al.* (1983). These authors found a useful connection between the statistical mechanics (the behaviour of systems with many degrees of freedom in a thermal equilibrium at a finite temperature) and the global optimization. The analogy with annealing in solids provided a new framework for optimization of these very large and complex systems through simulated annealing (SA).

Although the SA global search algorithms have the ability to escape a local minimum, they may have difficulty to navigate through long valleys and other complex features of the parameter landscape (Collins & Fishman, 1995). To improve the situation, the latter authors proposed an idea to efficiently navigate the search, taking benefit of the global nature of the parameter landscapes. There are several advantages of this approach, including an increase in reliability, reduction of the number of parameters, and optimized resolution.

In the context of the shallow subsurface (say 1 to 30 m), extraction of shear-wave (*S*-wave) intrinsic dispersion can be more feasible compared to compressional-wave (*P*-wave) dispersion. *P* waves propagating through fully saturated unconsolidated sediments have a much higher velocity than the *S* waves. With the development of high-frequency *S*-wave source and receiver systems for near-surface applications (e.g., Ghose *et al.*, 1996; Ghose & Goudswaard, 2004; Ghose, 2012), the frequency-bandwidth of *S*-wave data on/in near-surface soils has increased. Considering comparable frequencies between *P* and *S* waves in shallow seismic datasets, a much shorter wavelength is expected for the *S* waves than for the *P* waves.

We have computed synthetic seismograms in a VSP geometry for a homogeneous, fully-saturated porous medium using the Biot-Stoll poroelasticity model for propagating *P* and *S* waves. The depth interval is short: 10 to 15 m. Realistic soil (sand) properties are considered here and they mimic the water-saturated shallow subsurface situation. In the VSP geometry, the downhole receivers are positioned at 0.5 m depth interval. For simplicity, a zero-offset surface seismic source is taken. The time sampling interval is 0.2 ms. For both *P* and *S* waves, a 10 to 500 Hz frequency range is taken. For the source, a Ricker wavelet $\mathcal{N}(f)$ with a peak frequency of 300 Hz (f_0) is used:

$$\mathcal{N}(f) = f^2 \exp(-f^2/f_0^2). \quad (6.1)$$

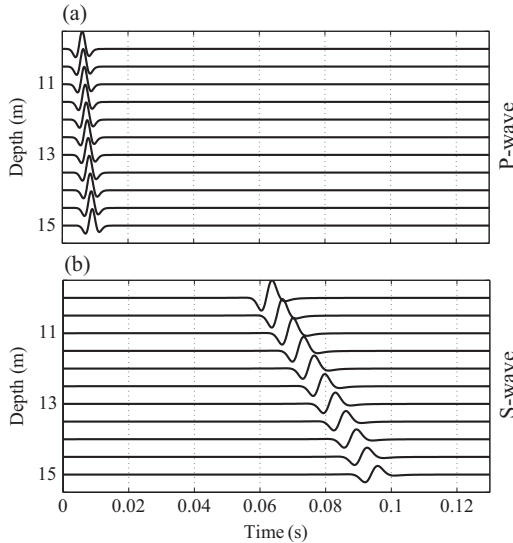


Figure 6.1: Poroelastic synthetic seismograms between 10 and 15 m depths using the Biot-Stoll model for: (a) P wave and (b) S wave.

Figure 6.1 illustrates the synthetic seismograms. One can directly see an amplitude decay for the propagating S waves, whereas the decrease in amplitude for the propagating P waves is less obvious. The attenuation of S waves is larger than that of P waves. The resolution with P waves is inferior to that with S waves in soft soil. This has also been the general observation in field S -wave data in soft soil. Extraction of attenuation information from the P -wave data is difficult and/or unstable in the scale of near-surface seismic surveys, as we notice in Figure 6.1 negligible change in the P -wave amplitude over the 5 m interval. Additional factors, like the effects of receiver coupling and external noise, will further add complexity to the intrinsic loss measurements for the P waves, even though the sensitivity of P wave to transport properties (especially permeability) is larger. One may, therefore, need higher (e.g., sonic or ultrasonic) frequencies to effectively use P -wave dispersion data. Therefore, in the context of shallow subsoil (short distances for wave propagation) and field-seismic (low) frequencies, S -wave data appear to be more attractive. Finally, because the S -wave velocity is directly related to the small-strain dynamic shear modulus, linking geotechnical parameters to intrinsic seismic dispersion and related properties, the use of S wave is more meaningful (Ghose & Goudsward, 2004). In this chapter, therefore, we concentrate on investigating the possibility of multivariate poroelastic optimization on the S -wave dispersion datasets.

6.2.1 Cost function

The cost function to be minimized in this chapter is similar to that introduced in Chapter 4, but in this case all parameters are considered unknown. Thus,

$$C^{V,\alpha} = \left(W_1 \sum_f |\Delta_S^V|^\beta + W_2 \sum_f |\Delta_S^\alpha|^\beta \right)^{\frac{1}{\beta}}, \quad (6.2)$$

where $\Delta_S^V = \frac{V(f, \vec{x}) - \hat{V}(f)}{\sigma_V(f)}$, $V(f, \vec{x})$ being the S -wave velocity estimated from a pertinent model of poroelasticity, and $\hat{V}(f)$ representing the S -wave intrinsic velocity dispersion extracted from the field data. The term \vec{x} represents the input parameter vector in the model, and $\sigma_V(f)$ denotes the standard deviation in the velocity estimate for field data. For attenuation (Δ_S^α), the notations are analogous. W_1 and W_2 are the appropriate data scaling factors, which can be calculated prior to the inversion. Since $C^{V,\alpha}$ is an analytical function, it is expected to have continuous and finite derivatives. To invert this multidimensional cost function, we use SA. SA is commonly used when the number of inputs parameters are large and the cost function has many local minima.

In the following inversion examples on synthetic data, we consider S waves and the Biot-Stoll model. In this case \vec{x} includes eight parameters. Prior to inversion, a rotation of coordinates is performed to enhance the efficiency of SA (Collins & Fishman, 1995).

6.2.2 Coordinate rotation

Optimization techniques can have difficulty searching the deepest point in long valleys that are oriented obliquely to the parameter axis in the multiparameter space. The approach of Collins & Fishman (1995) forces the global search to perturb a position in such a way that the displacement is always parallel to the prominent valleys in the parameter space. In this way, the search finds quickly the deepest point. They also showed that the prominent valleys are parallel to the eigenvectors of the covariance matrix of the gradient of the cost function. In other words, a newly identified orthogonal basis (eigenvectors) that includes the information of the prominent directions can be used as the new (rotated) coordinates to efficiently navigate in the global search algorithm. Following Collins & Fishman (1995) the covariance matrix can be calculated as follows:

$$\Psi = \int_{\Omega} \nabla C^{V,\alpha} (\nabla C^{V,\alpha})^t d\Omega, \quad (6.3)$$

where Ω is the parameter space,

$$\Omega = \{\vec{x} | a_i < x_i < b_i\}, \quad (6.4)$$

where a_i and b_i are the bounds on the i th parameter. Parameter vector \vec{x} contains the parameters x_i for $i = \overline{1, N}$. In order to meaningfully compare between the

elements in \vec{x} , the dimensions are removed by dividing x_i by $b_i - a_i$. Monte Carlo integration is performed to efficiently calculate the multidimensional integral (Eq. 6.3).

The N eigenvectors \vec{e}_i (or rotated coordinates) of the covariance matrix Ψ have the information of how parameters are coupled to each other. The rotated coordinates \vec{e}_i and the corresponding eigenvalues λ_i provide additional information about the relative sensitivity of the cost function to changes in the individual parameters. For example, the eigenvector corresponding to the maximum eigenvalue is the most sensitive direction, and thus leads to the most efficient way to decrease (or increase) the cost function. On the contrary, the eigenvector corresponding to the smallest eigenvalue is the least sensitive direction. In this way, the number of parameters can eventually be reduced by apriori assigning realistic, constant values to the most insensitive parameters. In our analyses, we have allowed all parameters to vary. The details are given in the next section. This approach has been used to minimize the cost function involving S -wave intrinsic dispersion as shown in Eq. 6.2.

Figures 6.2a,b,c illustrate the eigenvectors of Ψ calculated over the bounds specified in Table 6.1 for data-model misfit between seismic velocity (C^V), seismic attenuation (C^α) and their integration ($C^{V,\alpha}$), respectively, for the frequency range 10–200 Hz. The frequency range is realistic for near-surface S -wave data in soft soils. 1000 sample points are used to calculate the integral shown in Eq. 6.3. For this purpose, the Monte Carlo technique is used within the bounds shown in Table 6.1. Each eigenvector is plotted as a row in Figure 6.2a,b,c and is sorted according to the eigenvalues in Figure 6.2d,e,f. The deviation of the circles in Figure 6.2a,b,c from the null vector (horizontal dashed line) corresponds to the coordinates of the eigenvector in the original parameter basis. For example, the eigenvectors corresponding to the largest and the smallest eigenvalues are shown, respectively, by number 8 and 1 in 6.2a,b,c.

Clearly, when we have only velocity information ($C^V = \left(W_1 \sum_f |\Delta_S^V|^\beta \right)^{1/\beta}$ with $W_1 = 1$), the most sensitive parameters are then shear modulus of the frame (G), permeability (k) and porosity (n) (see eigenvectors 8, 7 and 6 in Figure 6.2a). Moreover, these parameters are coupled. The sensitivity of k relative to all other parameters is most pronounced (the biggest displacement) in the direction of the eigenvector 7. The most insensitive parameter in this case is the fluid viscosity (η). This is expected, because the assigned viscosity variation is rather small in this study (Table 6.1). We also see from this analysis that the fluid and the solid densities are insensitive parameters (in Figure 6.2a eigenvector 2 and 3, respectively). The eigenvalues normalized with respect to the maximum eigenvalue of C^V are shown in Figure 6.2d.

The results of eigenanalysis of the covariance matrix calculated using only attenuation information (C^α) are different. In this case, the most sensitive parameters are the shear logarithmic decrement (δ_s) and the permeability (k), which correspond to the highest displacements of the largest eigenvector corresponding to the maximum eigenvalue. In fact, they are the main parameters which control the seismic attenuation according to the Biot-Stoll model (Chapter 2). C^α shows also insensitivity to viscosity (η), solid density (ρ_s) and fluid density (ρ_f). The ratios of individual eigenvalues to the maximum eigenvalue of C^α are illustrated in Figure 6.2e.

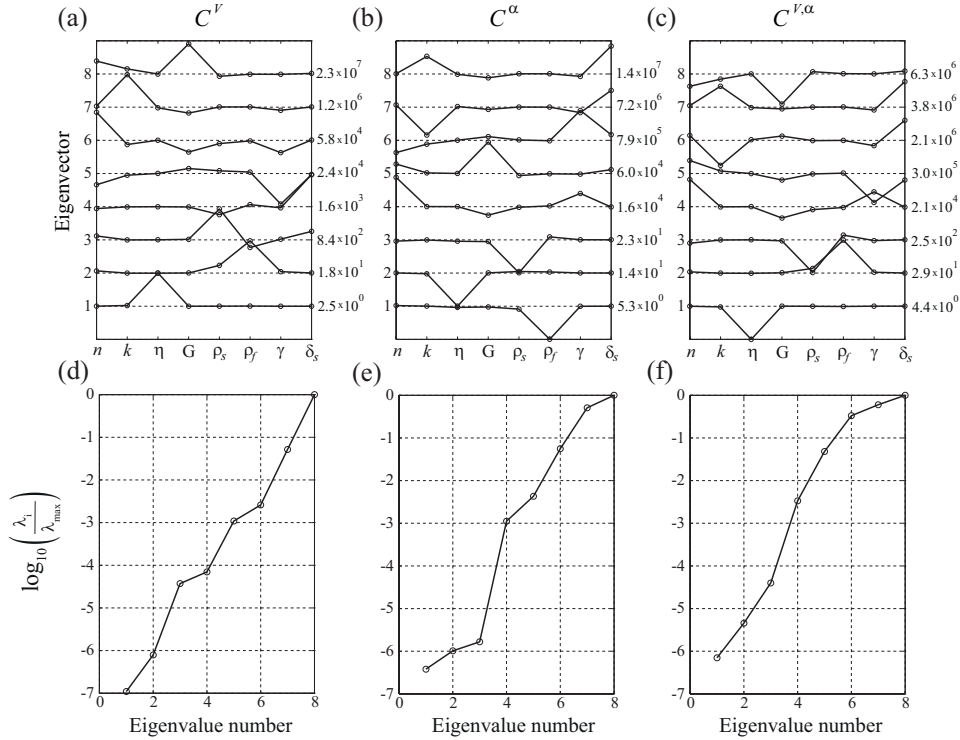


Figure 6.2: (a)-(b)-(c) Eigenvectors of the covariance matrix Ψ calculated over the bounds specified in Table 6.1. The frequency band is 10 to 200 Hz. The numbers on the right margin represent the eigenvalues. (d)-(e)-(f) Eigenvalues scaled by the maximum eigenvalue of the covariance matrix Ψ .

The results for the integrated cost function $C^{V,\alpha}$ can be analysed in the same manner. In this case, the result tends to show sensitivity lying between the sensitivity values for C^V and C^α . The advantage of $C^{V,\alpha}$ compared to C^V or C^α will be discussed in the next section.

Parameter	Unit	True	Min	Max
Porosity, n	-	0.4	0.26	0.47
Permeability, k	μm^2	50	0.1	1000
Viscosity, η	$\text{Pa}\cdot\text{s}$	0.001	0.0009	0.0011
Shear rigidity, G	MPa	50	43	63
Density of solid, ρ_s	kg/m^3	2650	2600	2700
Density of fluid, ρ_f	kg/m^3	1000	998	1023
Tortuosity, γ	-	1.25	1	3
Shear log decrement, δ_s	-	0.1	0.01	0.3

Table 6.1: Values of the parameters used in the Biot-Stoll model to calculate the covariance matrix Ψ .

6.2.3 Simulated annealing

Simulated annealing (SA) is a stochastic global search method to find a ground state. It models the physical process of heating of a material; the material is gradually quenched in order to find an optimum state (or global minimum energy). The algorithm was first proposed by Metropolis *et al.* (1953), where a constant-noise temperature of a many-body system was assumed. Later, the algorithm was generalized by Kirkpatrick *et al.* (1983) to include a temperature schedule (change in noise temperature) for an efficient search of the ground state.

The inversion procedure in SA is iterative. The algorithm first generates a random point in the solution space (Ω), and then using a forward model, it computes the replica dataset. Then the cost function ($C(\vec{x})$) is evaluated. The distance between the new (\vec{x}_{k+1}) and the current (\vec{x}_k) trial point is based on the probability distribution with a scale depending on the current temperature. In our case we use

$$\vec{x}_{k+1} = \vec{x}_k + \beta T, \quad (6.5)$$

where T is the current temperature of the system and β is a random number uniformly distributed between -1 and 1 . The probability of acceptance of a new trial point is based on the Boltzmann distribution function which is defined as:

$$\begin{aligned} \mathcal{P}(\Delta C) &= \frac{\exp(-C_{k+1}/T)}{\exp(-C_{k+1}/T) + \exp(-C_k/T)} \\ &= \frac{1}{1 + \exp(\Delta C/T)} \approx \exp(-\Delta C/T), \end{aligned} \quad (6.6)$$

where $\Delta C = C_{k+1} - C_k$ represents the cost function (or energy) difference between new and current states. Perturbations that decrease the cost function C are always accepted. A perturbation that increases the cost function is accepted with a probability $\mathcal{P}(\Delta C)$ (Eq. 6.6). This is also known as Metropolis Criterion (Metropolis *et al.*, 1953). Thus, the acceptance of points which increase the cost function residual ($\Delta C > 0$) is necessary to prevent the search from getting trapped in a local minimum. Following Eq. 6.6, uphill perturbations become less likely as the temperature decreases. Also, the larger the ΔC the smaller is the acceptance probability.

In this study, we implement the SA algorithm with an exponential cooling schedule:

$$T = T_0 \cdot 0.95^\varsigma, \quad (6.7)$$

where $T_0 = 100$ K is the initial temperature and ς is the annealing parameter. The annealing parameter is same as the iteration number until reannealing.

As can be seen from Eq. 6.5 the perturbation directions of the new points are random. These perturbation approaches may have difficulty to navigate the search over long valleys. We incorporate in our navigation the rotated coordinate system explained in the previous section, to efficiently run the SA algorithm. This has been achieved by adding one eigenvector at a time to the random perturbation defined in

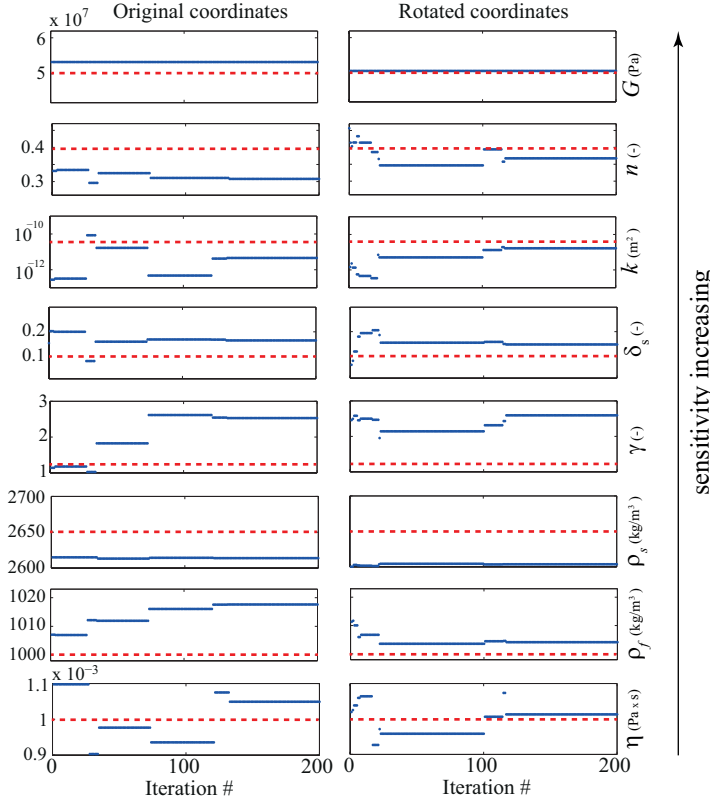


Figure 6.3: The optimization of Eq. 6.2 in original and rotated coordinates by SA, using Biot-Stoll model. The solid blue dots represent the optimum values found during the search for noise-free situation. The red dashed lines indicate the true values.

Eq. 6.5. Following Collins *et al.* (1992) and Collins & Fishman (1995), the new k th perturbation for the j th eigenvector is of the form:

$$\vec{x}_{k+1}^{\text{rc}} = \vec{x}_{k+1} + \frac{1}{2} \beta_{k,j}^3 \vec{e}_j, \quad (6.8)$$

where $\vec{x}_{k+1}^{\text{rc}}$ is the perturbed parameter vector and the $\beta_{k,j}$ are the random numbers that are uniformly distributed between -1 and 1 . No summation over repeated subscripts is applied in the above equation. The second term in this equation incorporates the rotated coordinates.

The inversion can be terminated based on the tolerance value and the number of iterations specified by the user. In this study, the tolerance value is 10^{-6} and there is no constraint imposed on the iteration number.

Next, we illustrate the results of poroelastic inversion for properties of the shallow subsoil. The unknowns to be estimated are the parameters of the Biot-Stoll model as discussed in Section 6.2.2. A comparison of the optimization results between the original and the rotated coordinates is shown in Figure 6.3 for $C^{V,\alpha}$. $C^{V,\alpha}$

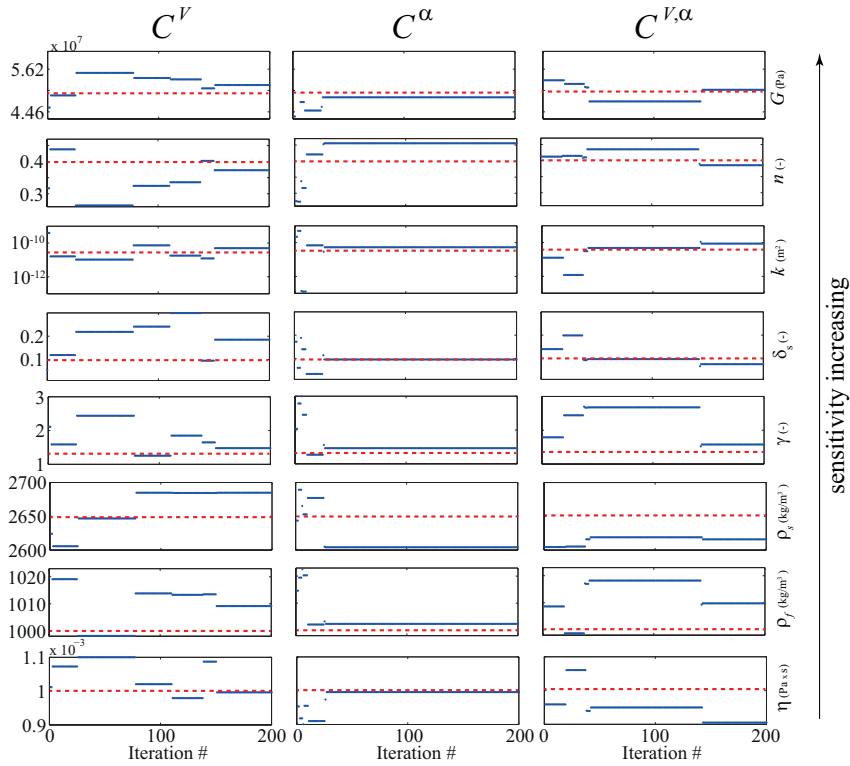


Figure 6.4: The optimization of C^V , C^α and $C^{V,\alpha}$ in the rotated coordinates by SA, using Biot-Stoll model. The solid blue dots represent the optimum values found during the search for noise-free situation. The red dashed lines indicate the true values.

involves eight parameters. The order of the parameters in the column is based on the sensitivity hierarchy found for $C^{V,\alpha}$ in Figure 6.2c. In other words, the most influential parameters G, n, k and δ_s on $C^{V,\alpha}$ are shown in the top 4 rows. Remaining less sensitive parameters are shown in the bottom rows. Figure 6.3 shows the optimum values encountered during the search by SA in original and rotated coordinates. The frequency content (10–200 Hz) in the data is the same for both original and rotated coordinates. The data are generated using the Biot-Stoll model with the correct (representing the truth in nature) input parameters. No noise has been added to the generated data. The ranges for these parameters considered in inversion are given in Table 6.1. In the rotated coordinates, five of the parameters that converge well are n, k, η, G and δ_s . In case of the original coordinates, only two parameters converge: k and δ_s . In general, the search results in an earlier convergence in the rotated coordinates than in the original coordinates. Note also the active jumps toward the true values at earlier iterations of the search in the rotated coordinates compared to search in the original coordinates. As expected,

for a given frequency band, the parameters that have the largest displacements in the eigenvectors associated with the largest eigenvalues are best resolved (see Figure 6.2c,f).

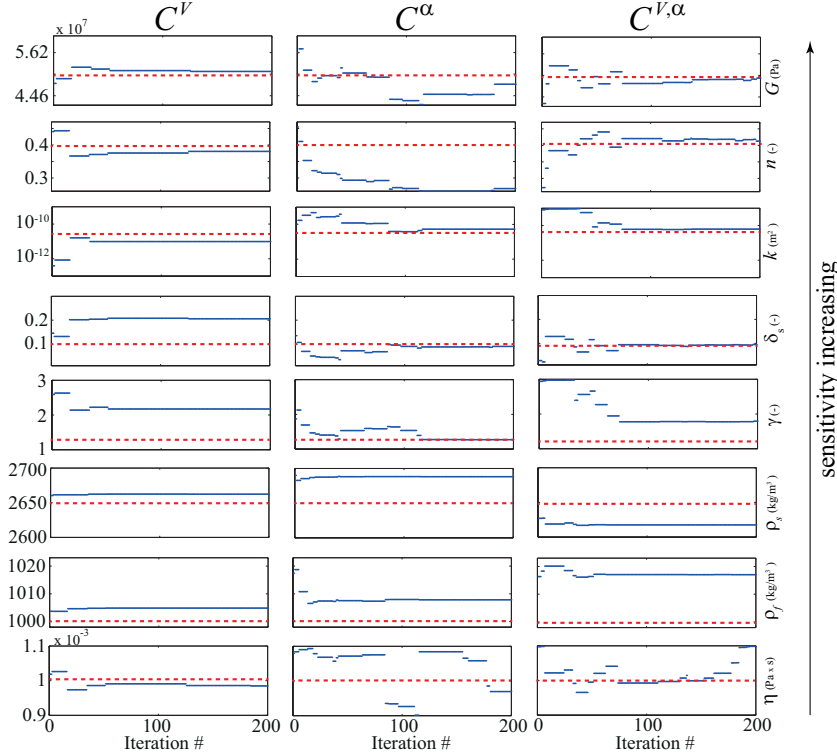


Figure 6.5: The optimization of C^V , C^α and $C^{V,\alpha}$ in the rotated coordinates by SA, using Biot-Stoll model. The solid blue dots represent the optimum values found during the search with added noise in the velocity and attenuation data. The red dashed lines indicate the true values.

Figure 6.4 illustrates the results of SA algorithm applied to C^V , C^α and $C^{V,\alpha}$ in the rotated coordinate system. The frequency band is the same for all three. Input parameters are given in Table 6.1. As in the previous example, clearly the most sensitive parameters are better resolved. Again, a noise-free situation is considered. For instance, the minimization of the velocity dispersion residual (C^V) gives a fairly good convergence to the true value of n , k , γ and G . However, δ_s does not converge. This is because C^V is almost insensitive to δ_s , as shown in the previous section (Figure 6.2a,d). Contrarily, δ_s is the most sensitive parameter in C^α . As a result, δ_s converges very quickly to its correct value in C^α minimization, where a very good convergence is also found to all other parameters except n and ρ_f . The sensitivity of C^α to n is less than the sensitivity of C^V to n . The converged parameters that are associated with the eigenvectors corresponding to the smallest eigenvalues are found to be rather unstable. Finally, the minimization of the integrated cost function $C^{V,\alpha}$

gives a good convergence in both δ_s and n , in addition to k and G .

To demonstrate a cogent advantage of having $C^{V,\alpha}$ for subsurface property characterization, we add 5% and 20% noise to the velocity dispersion and attenuation data, respectively. The results of the SA algorithm applied to C^V , C^α and $C^{V,\alpha}$ in the rotated coordinate system are shown in Figure 6.5. $C^{V,\alpha}$ appears to be more resistant to the added noise and give overall a better convergence for n , k , G and δ_s compared to C^V and C^α . In Section 6.3, we will use this approach to retrieve soil properties from an S -wave dispersion database.

6.2.4 Is viscosity change discernible?

In Section 6.2.2, fluid viscosity is found to be an insensitive parameter. However, this may change, if the viscosity range is enhanced. Such a situation can represent, for example, contamination of water in the shallow subsoil by a dense non-aqueous phase liquid (DNAPL). Chemicals representing DNAPL may change the viscosity of the fluid by several orders of magnitude. As a result, the seismic response will change because of the viscosity change in the porous matrix. Since the permeability and viscosity enter into the macroscopic Biot and Biot-Stoll models as k to η ratio (also known as fluid mobility), this leads to the resolvability of fluid viscosity, provided k is known. Fluid mobility can then be resolved uniquely. However, in models where both macro- to microscale losses are present (e.g., BICSQS model), both k and η can be resolved uniquely at certain frequency bands. This will be illustrated for a separate model (BISQ) in Chapter 8.

6.3 Application to field database of shear wave dispersion

6.3.1 Dispersion in field database

We have found only a few papers reporting S -wave dispersion in soft soils, and none for P -wave dispersion. We have compiled a database made of twelve well-selected datasets. They are used to check the approach explained in the previous section. The database satisfies the following criteria: (a) fully saturated land/onshore data, (b) field-seismic frequency band, and (c) at least two independently measured phase velocity and attenuation values available for a given location. There are no datasets found for P wave satisfying these criteria. Four out of twelve datasets are reported by Kudo & Shima (1970). These are field experiments from Adachi, Sunamachi, Yukigaya and Yayoi test sites in Japan. Another frequency-dependent S -wave velocity and attenuation dataset was presented by Michaels (1998) from four locations in Utah and Idaho, USA. Here the lithology information is available. In all these cases, there are no attempts made to separate the scattering attenuation from the intrinsic attenuation. Finally, four datasets were obtained from our own field experiments using array seismic cone penetration tests (Ghose, 2012). These tests were conducted in Friesland, in the northern part of the Netherlands. In the case of our own data, we could separate the scattering attenuation from the intrinsic attenuation, using the

velocity distribution estimated from the array-seismic data. More detailed discussions on these tests will be given in Chapter 7. All these cases represent dispersion data for vertically propagating SH waves. Information of soil properties (porosity, permeability, etc.) are not available. However, realistic bounds can be assigned to them, given the known soil type. Soil type, depth and the location are summarized in Table 6.2.

No.	Location	Lithology	Depth range (m)
1	Adachi, Japan ^a	Diluvial sand	22–43
2	Sunamachi, Japan ^a	Alluvial silt	11–23
3	Yukigaya, Japan ^a	Tertiary mudstone	6–16
4	Yayoi, Japan ^a	Kwanto loam	3–8
5	Utah, USA ^b	Sand	8–13
6	Utah, USA ^b	Silt, clay	2–7
7	Idaho, USA ^b	Cobbles	5–10
8	Idaho, USA ^b	Sand, cobbles	10–15
9	Heerenveen, The Netherlands ^c	Sand	1.5–3
10	Heerenveen, The Netherlands ^c	Sand, clay	2.75–4.25
11	Heerenveen, The Netherlands ^c	Clay, peat, sand	4–5.5
12	Heerenveen, The Netherlands ^c	Sand, clay	4.4–5.9

^a Kudo & Shima (1970)

^b Michaels (1998)

^c This study

Table 6.2: Location, soil type and depth range for the field datasets of S -wave dispersion in soil.

Although there are several definitions for attenuation (Bourbie *et al.*, 1987), the reported attenuation (α_S) values in two previous works – Kudo & Shima (1970) and Michaels (1998) – are in $1/m$ ($8.686 \cdot 1/m = \text{dB}/m$). By definition, α_S controls the exponential decay of the wave amplitude with the propagation distance. It is sometimes convenient to use the quality factor Q as the measure of attenuation:

$$Q = \frac{\Delta E}{2\pi E} \approx \frac{\pi f}{\alpha V}, \quad (6.9)$$

where E which is defined as the loss in one cycle and divided by the averaged stored strain energy and divided by 2π .

Q gives a better idea of whether the porous medium at a given frequency band is in the low- (relaxed) or in the high- (unrelaxed) frequency regime. The frequency-dependence of Q in hard rocks with small porosity has generally been ignored; a single Q value for a whole frequency band is estimated using the spectral ratio method (SRM). However, for porous rocks and near-surface sediments, this approach is not valid. Jeng *et al.* (1999) proposed an improved method of determining near-surface Q without making the constant Q assumption. They found that both P -and S -wave quality factors (Q_P and Q_S) are highly frequency-dependent between 50 and 300 Hz at three experimental sites consisting of silt and sand. In this study, we consider frequency-dependent Q_S computed from V_S and α_S (Eq.6.9).

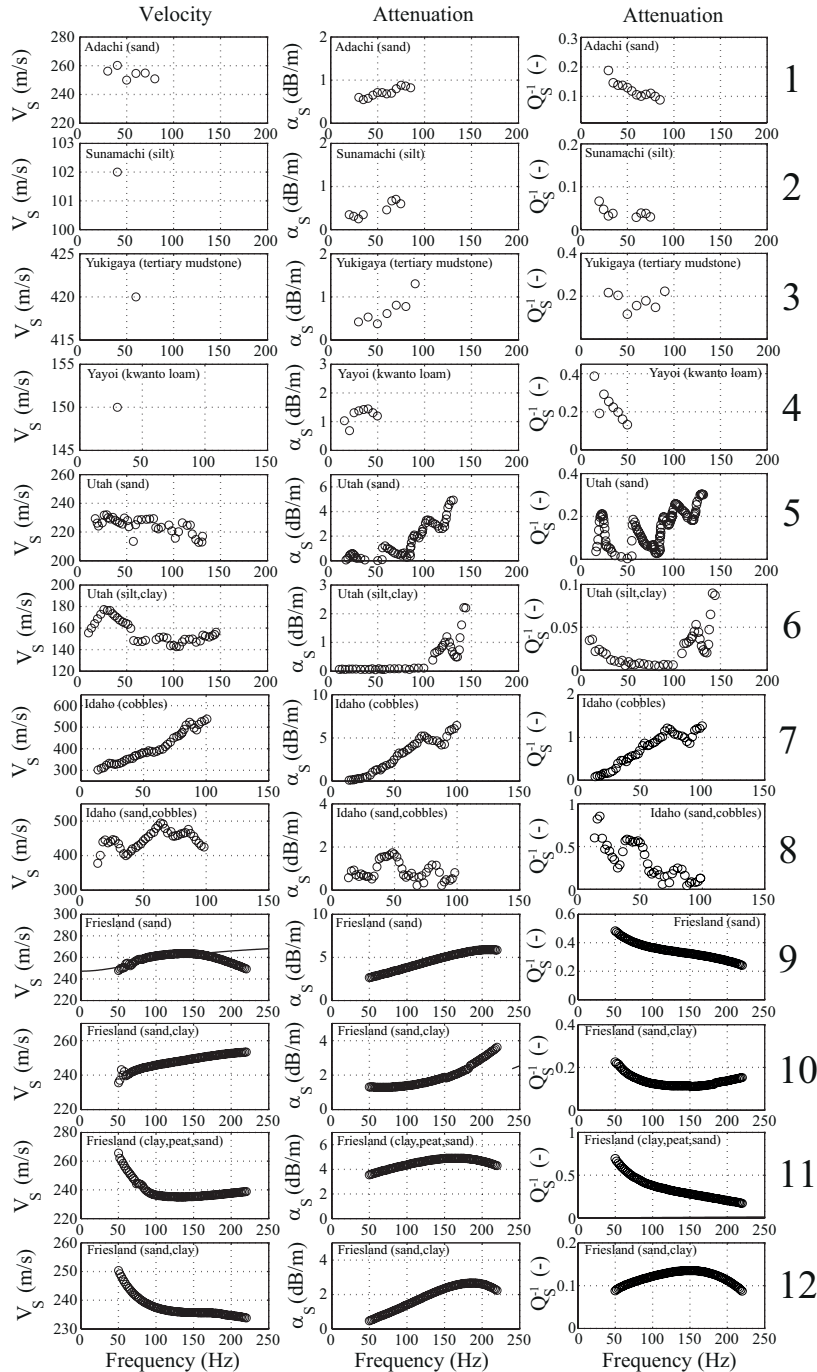


Figure 6.6: Field-observed S -wave velocity and attenuation dispersion at twelve different locations.

Field-observed S -wave velocity and attenuation data are shown in Figure 6.8 and 6.9 by black circles. Velocity dispersion of the S -wave is distinct, especially for sandy sediments at locations 7, 8, 9 and 10. Attenuation defined as α_S , generally, increases with frequency at all locations. For the sediments with relatively low permeability (based on the lithology information) or sands with clay inclusions at locations 2, 3, 10 and 12, α_S shows a linear change with frequency. For the same 4 locations, Q_S^{-1} show nearly frequency-independent behaviour. A conspicuous increase of Q_S^{-1} with frequency is observed at locations 5 and 7, suggesting the existence of a low-frequency regime at field-seismic frequency bands. Note, however, that the behaviour of Q_S^{-1} at location 8 differs from that at locations 5 and 7, in spite of the similarity in lithology. According to lithology information, relatively high permeability values are expected at all three sites. A clear decrease of Q_S^{-1} with frequency is observed at locations with sand and silt/clay mixtures, i.e., 1, 4, 9 and 11. Such a trend and the level of measured Q_S^{-1} are consistent with the measurements reported by Jeng *et al.* (1999) for near-surface mixtures of sand and silt. This indicates that even at low field-seismic frequencies, these materials are still unrelaxed and need more time (lower frequencies) for equilibration. Finally, the trend of Q_S^{-1} at location 6 is ambiguous, which makes interpretation difficult.

In general, one can observe V_S dispersion for unconsolidated sandy sediments even at low frequency bands. Also, Q_S^{-1} is found to be highly frequency-dependent, especially in sand/gravel sediments. Q_S^{-1} in near-surface, fully-saturated sediments is in the range of $10^{-2} < Q_S^{-1} < 10^0$. Both velocity and attenuation can be used in retrieving in-situ soil properties provided the model for the loss mechanism is reasonably accurate. In the next section, we show the results of poroelastic inversion.

6.3.2 Results and discussion

Prior to inversion, rotated coordinates are calculated in order to increase the efficiency of the SA algorithm. We need to identify the parameter search space Ω . Since there is no information available about most of the parameters involved in minimization, realistic bounds are taken based on early publications (Berry & Reid, 1987; Stoll, 1977; Chotiros & Isakson, 2004; Isakson & Neilsen, 2006). These bounds are given in Table 6.3.

Parameter bounds for η , γ , ρ_s and ρ_f are considered to be same for all locations. They are, respectively, 0.0009–0.0011 (Pa·s), 1–3 (-), 2600–2700 (kg/m³) and 998–1023 (kg/m³). Similar to Isakson & Neilsen (2006), shear rigidity ($G = \rho V_S^2$) bounds are calculated from the velocity range observed in the dispersion data and the density range from the assumed porosity range (Table 6.3).

The inversion is accomplished by minimizing Eq. 6.2 for three different models, viz. Biot, Biot-Stoll and BICSQS. These models are explained in Chapter 2. The model parameters are obtained for 50 realizations of SA at each location. The median of the 50 vector outputs are then calculated for each location. The inverted median values of n and k , for all locations, are shown in Figure 6.7. The green-shaded rectangles in Figure 6.7 represent the same bounds as shown in Table 6.3. Since there are no earlier independent n and k measurements available, the goodness

No.	n (-)	k (m^2)	δ_s (-)	f_c (kHz)
1	0.26-0.47	10^{-15} - 10^{-9}	0.01-0.3	0.1-50
2	0.35-0.55	10^{-15} - 10^{-11}	0.01-0.3	1-70
3	0.3-0.7	10^{-22} - 10^{-16}	0.01-0.5	100-1000
4	0.3-0.65	10^{-15} - 10^{-10}	0.01-0.5	50-100
5	0.26-0.47	10^{-15} - 10^{-9}	0.01-0.3	0.1-50
6	0.35-0.55	10^{-15} - 10^{-11}	0.01-0.3	1-100
7	0.26-0.4	10^{-12} - 10^{-8}	0.01-0.3	0.01-10
8	0.26-0.47	10^{-13} - 10^{-8}	0.01-0.3	0.1-50
9	0.26-0.47	10^{-15} - 10^{-9}	0.01-0.3	0.1-100
10	0.3-0.65	10^{-15} - 10^{-10}	0.01-0.35	1-500
11	0.3-0.7	10^{-16} - 10^{-11}	0.01-0.5	10-1000
12	0.3-0.7	10^{-15} - 10^{-10}	0.01-0.3	1-500

Table 6.3: Parameter bounds for porosity (n), permeability (k), shear logarithmic decrement (δ_s) in the Biot-Stoll model, and the shear relaxation frequency (f_c) in the BICSQS model, based on lithology information. These bounds are used in the SA algorithm and in calculating the rotated coordinates.

of the inverted n and k can only be examined based on the lithology information. Practically, all porosity and permeability values obtained from the Biot model are found to be high and close to their upper bounds. This is because the Biot model systematically underestimates attenuation, as also reported earlier.

In order to examine more closely the goodness of the inverted parameters and the pertinence of the poroelasticity models, we compare the model prediction of the dispersion curve (using the inverted values of all model parameters) with the observed dispersion curve. In Figure 6.8 and 6.9 the solid lines of three different colours show the theoretical dispersion curves for Biot, Biot-Stoll and BICSQS models, calculated from the inverted model parameters. Note that the Biot model is unable to predict the high values of S -wave attenuation. In contrast, the Biot-Stoll model is good for seven of the twelve datasets and the estimated values of soil properties (n and k) seems to be realistic. Both Biot and Biot-Stoll models fail for soils where the observed dispersion (both velocity and attenuation) is high, as reported by Michaels (1998) for fluid-saturated cobbles. In this case, the BICSQS model by Chotiros & Isakson (2004), which incorporates the wave-induced flow occurring at the grain contacts, is much more successful. The estimated values of n and k should be more accurate for highly permeable soils, if the BICSQS model is used in the inversion.

The underprediction of attenuation by the Biot model is more conspicuous for low-permeable sediments like clay, silty clay, mudstone, etc. The macroscopic Biot's loss is not sufficient to explain not only the conversion of P -wave energy into heat but also S -wave energy. The same conclusion was previously drawn for hard rocks for P -wave attenuation (Dvorkin & Nur, 1993; Dvorkin *et al.*, 1994; Pride *et al.*, 2004). Our finding for S -wave attenuation in soft soils is new. Loss mechanisms like grain-to-grain shearing or other contact relaxations, wave-induced flow at meso and micro scales are likely to be more dominant in such soil types. To explain the

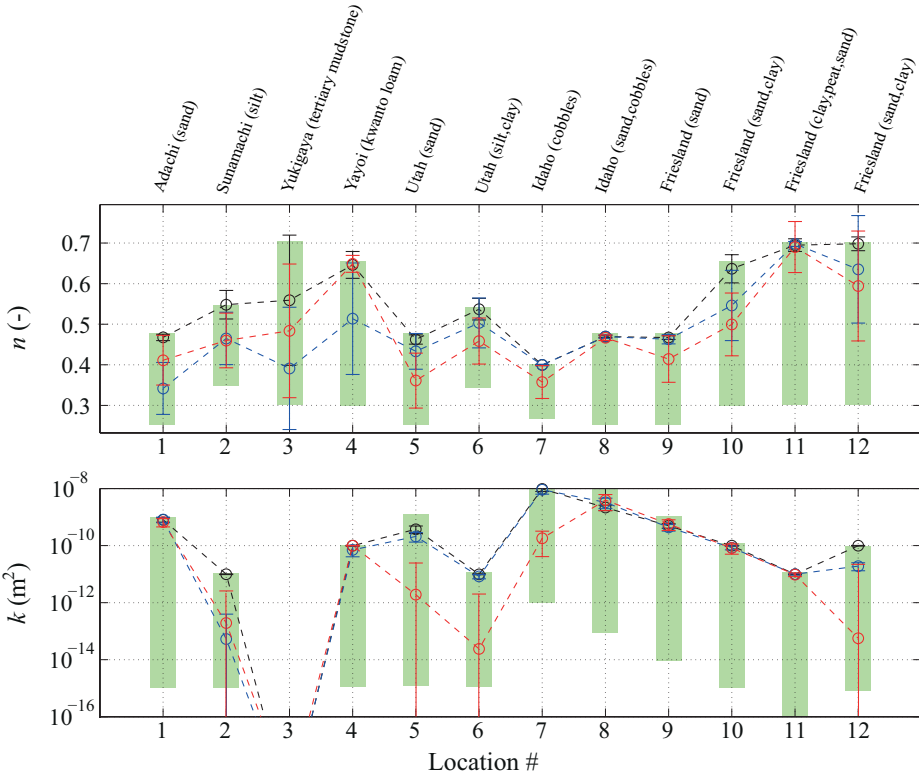


Figure 6.7: Porosity (n) and permeability (k) obtained by inversion of S -wave dispersion data using Biot (black circles), Biot-Stoll (blue circles) and BICSQS (red circles) models. Vertical bars and green-shaded rectangles represent, respectively, standard deviation in the inverted parameters and the bounds used in the inversion scheme.

observed attenuation, an increase in porosity and permeability in soil is the only way to increase the value of attenuation according to the Biot model.

When we use the Biot-Stoll model, which has additional loss coming from the inelastic response of the frame, we can explain better the observed high attenuation values at seven of the twelve test locations. For the five test locations – 6, 7, 8, 9 and 11 – where the Biot-Stoll model fails, the estimated n and k values are similar to the estimates from the Biot model (close to the upper bounds). Both Biot and Biot-Stoll models have difficulty to explain high velocity dispersion and high attenuation as observed in highly permeable soil (location 7). However, in this case the BICSQS model gives a perfect match with the observed S -wave dispersion data, suggesting the likelihood of wave-induced flow at micro (or grain) scale, also proposed by Chotiros & Isakson (2004) for saturated sandy or gravelly sediments. The prediction by the BICSQS model for locations 5, 6 and 7 is generally good. The estimated n and k using BICSQS model are different from the values obtained using Biot and Biot-Stoll

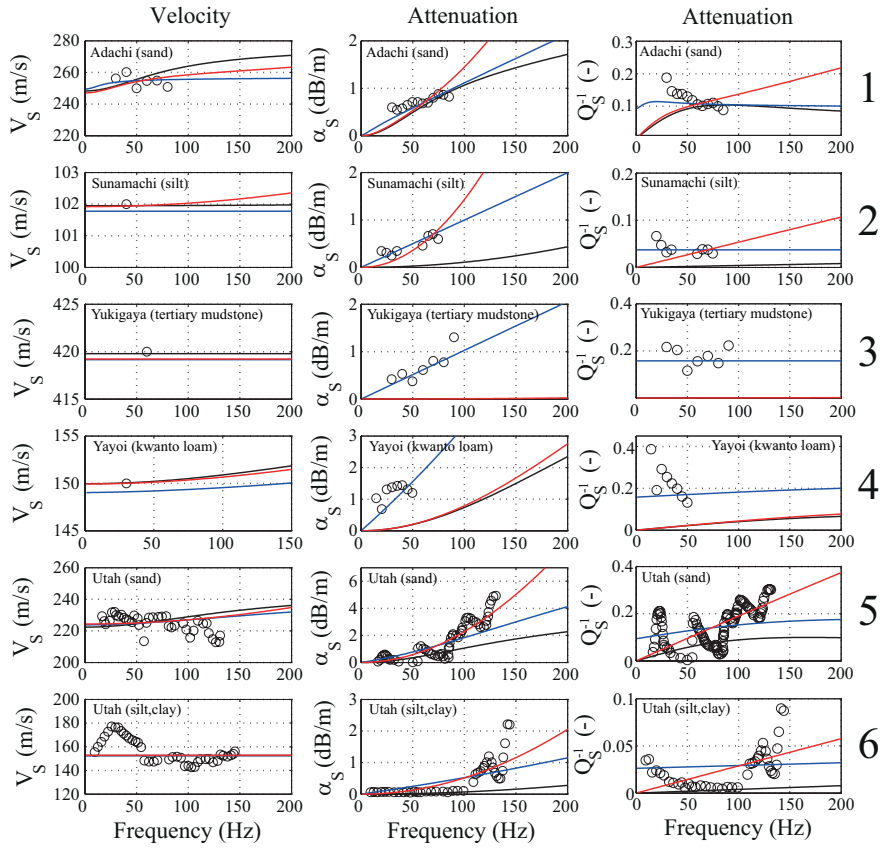


Figure 6.8: Data (circles) and model (lines) comparison at locations 1 to 6. Theoretical predictions of Biot, Biot-Stoll and BICSQS models are shown, respectively, by the black, blue and red solid lines.

models, and they are not as high and seem to be more realistic for highly permeable sands and gravels.

High attenuation values are observed at a very shallow depth at location 9. This is possibly a near-field effect. In this case, the recorded displacement field is likely to be not elastic. At location 11, the thin layer of peat is possibly the reason for the high S -wave attenuation. The overall prediction of velocity dispersion by all three models has a very good agreement with the observation. Needless to mention, having broadband dispersion data for both P and S waves and well-log measurements would give better estimates of n and k and improved insights on the underlying mechanisms.

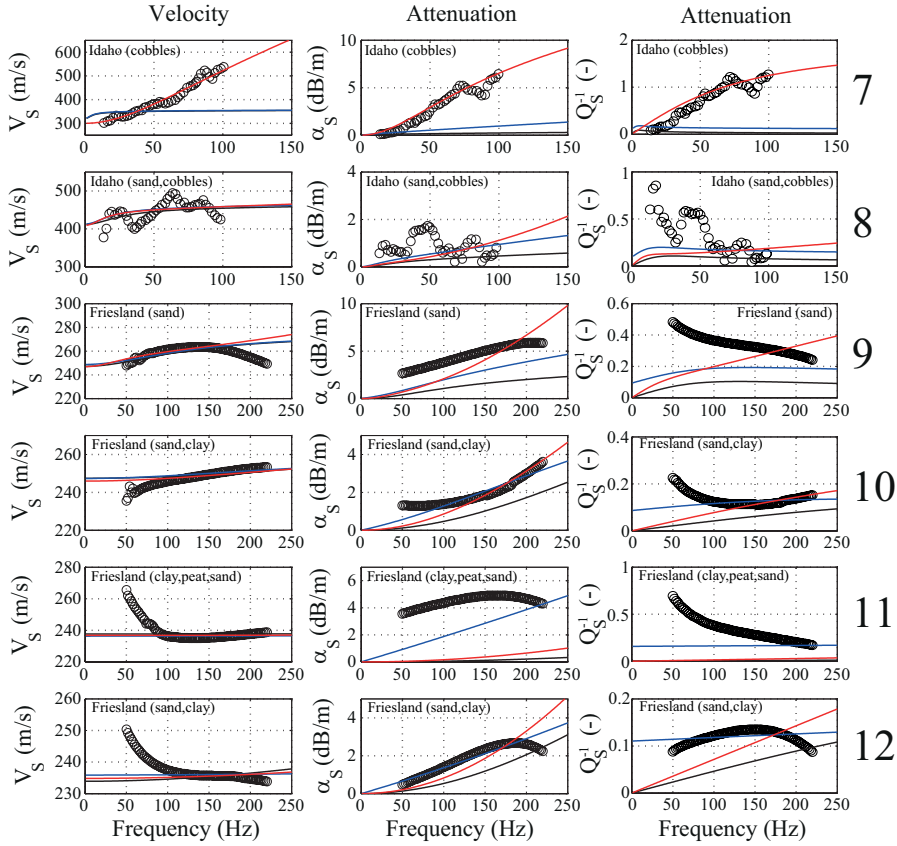


Figure 6.9: Data (circles) and model (lines) comparison at locations 7 to 12. Theoretical predictions of Biot, Biot-Stoll and BICSQS models are shown, respectively, by the black, blue and red solid lines.

6.4 Conclusions

A global optimization technique has been discussed within the framework of poroelasticity, to retrieve soil parameters. We have tested the efficiency of SA in a rotated coordinate system. The rotated coordinates are found from the eigenvectors of the covariance matrix of the gradient of the cost function. The covariance matrix has been calculated using the Monte Carlo integration technique. It contains information about the intrinsic parameter coupling and the relative importance of all model parameters in the optimization.

Optimization by SA is more efficient in the rotated coordinates than in the original coordinates. Synthetic studies with and without noise in the data have shown a very good convergence of the most sensitive parameters that are associated with the eigenvectors corresponding to the largest eigenvalues.

A database made of twelve S -wave dispersion datasets gathered from fully-

saturated, unconsolidated soils have been studied. We have found that *S*-wave attenuation (Q_S^{-1}) is frequency-dependent, which strongly depends on the soil type. For example, high-permeability sands and gravels exhibit very high velocity dispersion and Q_S^{-1} increases with frequency, indicating the prevalence of a low-frequency (relaxed) regime. Contrarily, sandy silts show a decrease of Q_S^{-1} with frequency, supporting the prevalence of a high-frequency (unrelaxed) regime. Finally, low-permeable soils (assumed based on known lithology), such as mudstone or sand/silt with clay inclusions, show a nearly frequency-independent Q_S^{-1} . For such clayey soils, the inelastic loss (grain-to-grain shearing, inelastic frame response) is possibly dominant. The loss due to wave-induced fluid flow can be more important for high-permeability sands and gravels at field-seismic frequencies.

We have tested the SA algorithm using the rotated coordinate system on the database containing twelve *S*-wave dispersion datasets. Soil properties have been obtained and checked with the known lithology information. No independent measurements of soil properties are available. We find that the Biot model is unable to predict the high values of *S*-wave attenuation. In contrast, the Biot-Stoll model is found to be good for seven of the twelve datasets and the estimated values of soil properties (n and k) seems to be realistic. Both Biot and Biot-Stoll models fail for soils where the observed dispersion (both velocity and attenuation) is high, as reported by Michaels (1998) for fluid-saturated cobbles. In this case, the BICSQS model by Chotiros & Isakson (2004), which incorporates the wave-induced flow occurring at the grain contacts, is found to be much more successful. The estimated values of n and k should be more accurate for highly permeable soils, if the BICSQS model is used in the inversion.

Chapter 7

Soil properties from *S*-wave dispersion: tests on shallow downhole field data

7.1 Introduction

The Darcy permeability (k) and porosity (n) of saturated soils are the two most important parameters in hydrogeological modelling, in drainage and swelling considerations in geotechnical engineering, in estimating soil susceptibility to erosion - with major implications on sustainable soil management and in efficient irrigation planning. They control transport and infiltration processes, surface runoff, leaching of chemicals or pesticides, and migration of pollutants to the groundwater. Permeability and porosity depend strongly on soil texture and structure, and can vary widely in space.

Although k and n are essential in diverse applications, their in-situ estimation is considered virtually impossible. Permeability is determined either experimentally (in field or in laboratory) using methods based on Darcy's law, or through empirical correlation involving another measured parameter e.g., n , pore or grain size distribution, soil texture. All these approaches have major technical difficulties and the estimates are generally grossly uncertain.

In the past, the intrinsic dispersion of seismic waves in porous media was used to predict k and n , because k and n have major influences on poroelastic wave propagation. This is true for soft sediments or soils (e.g. Badiey *et al.*, 1998; Buchanan, 2006). The inversion of compressional (P) wave dispersion for water-saturated marine sands or sediments was attempted to derive the sediment parameters, including k and n . However these studies used frequencies in kHz to tens of kHz range (e.g. Burns, 1990; Chotiros & Isakson, 2004; Yamamoto, 2003; Isakson & Neilsen, 2006; Lin *et al.*, 2009). Such high frequencies are not observed in land seismic data. The inversion of *S* wave dispersion has not yet been accomplished on field data. However, field observation of intrinsic dispersion, for the relatively short propagation

distances in the shallow subsoil, is more practicable for *S* waves than for *P* waves (Chapter 5 and 6), because *S* waves typically have a significantly lower velocity in soft, water-saturated soils.

A new concept for determining simultaneously k and n using seismic dispersion in the field-seismic frequency band has been discussed in Chapter 4. The concept utilizes the contrasting behaviour dictated by the underlying physics between dispersive seismic velocity and attenuation in the k - n domain. In Chapters 4 and 5, the idea is tested on synthetic data and considering all model parameters other than k and n to be known or to have small effects.

In this chapter, we first examine, using synthetic data, the effect of noise in data and the unknown parameter values in the poroelasticity model. Next, we present results on a near-surface *S*-wave field-dataset, illustrating the possibility of estimating in-situ, layer-specific k and n at a typical sand-clay-silt site and the effect of model uncertainty.

7.2 *k* and *n* from *S*-wave dispersion: effect of noise and unknown parameter values

In Chapters 4 and 5, we have shown that dispersive *S*-wave velocity $V_S(f)$ and attenuation $\alpha_S(f)$ can be efficiently used in an integrated cost function to obtain porosity (n) and permeability (k) simultaneously. The effect of noise in data have been critically studied in Chapter 5. In this section, we investigate the simultaneous effect of noise in the dispersion data and errors in the assigned parameters which are considered to be constant in the inversion.

To study the effect of noise and unknown parameter values, *S*-wave dispersion data is generated using the Biot-Stoll model (Chapter 2). This model is known to be good for a wide variety of soil types (e.g., Holland & Brunson, 1988, Chapter 6). The *S*-wave frequency band used is 20-200 Hz. The input values of permeability and porosity for typical sandy sediments are, respectively, $k = 5 \times 10^{-11} \text{ m}^2$ and $n=0.4$. Realistic values are also taken for the remaining model parameters: viscosity $\eta=0.001 \text{ Pa}\cdot\text{s}$, solid density $\rho_s=2650 \text{ kg}\cdot\text{m}^{-3}$, fluid density $\rho_f=1000 \text{ kg}\cdot\text{m}^{-3}$, shear rigidity $G=30 \text{ MPa}$, tortuosity $\gamma=1.25$, shear log decrement $\delta_s=0.1$, and pore size a calculated from (Carman, 1937):

$$a = \sqrt{\frac{8\gamma k}{n}}. \quad (7.1)$$

In order to study the effect of the unknown parameter values in the poroelasticity model, we consider large ranges for each parameter: $\eta=0.0009\text{--}0.0011 \text{ Pa}\cdot\text{s}$, $\gamma=1\text{--}3$, $\delta_s=0.05\text{--}0.15$, $\rho_f=998\text{--}1023 \text{ kg}\cdot\text{m}^{-3}$ and $\rho_s=2600\text{--}2700 \text{ kg}\cdot\text{m}^{-3}$. The range for the frame shear modulus G is calculated using the elastic relationship between G and V_S :

$$V_S = \sqrt{\frac{G}{\rho}}, \quad (7.2)$$

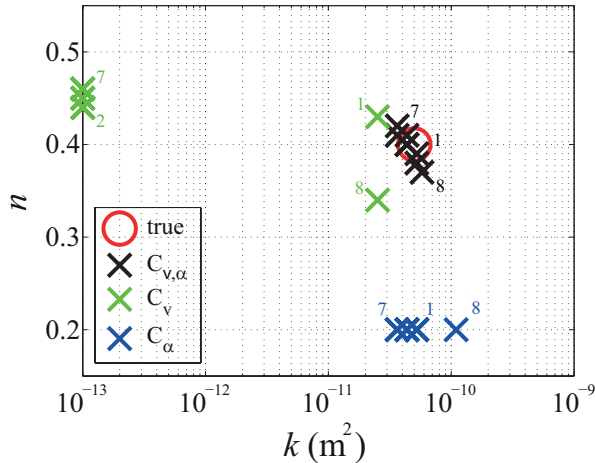


Figure 7.1: Results of cost function minimization in the k - n domain when the model parameters vary within a large range. The median values of the estimates are shown.

where the bulk density ρ has a range of 1900-2100 kg·m⁻³. Next, random values are picked within the assigned range for all parameters except k and n . The solution space for k and n is kept as: $k = 10^{-13}$ - 10^{-9} m², $n = 0.2$ - 0.8 . 200 sets of model parameters are chosen. The cost function minimization is performed for all 200 random sets. The median of the 200 estimates of k and n are plotted in Figure 7.1. Here, the input $V_S(f)$ and $\alpha_S(f)$ are assigned different maximum random errors, denoted by numbers 1–8: 1 ($\delta V=1\%$, $\delta \alpha=5\%$), 2 ($\delta V=3\%$, $\delta \alpha=15\%$), 3 ($\delta V=5\%$, $\delta \alpha=25\%$), 4 ($\delta V=7\%$, $\delta \alpha=35\%$), 5 ($\delta V=9\%$, $\delta \alpha=45\%$), 6 ($\delta V=11\%$, $\delta \alpha=55\%$), 7 ($\delta V=13\%$, $\delta \alpha=65\%$) and 8 ($\delta V=15\%$, $\delta \alpha=75\%$). The data standard deviations are used in minimization. The red circle in Figure 7.1 indicates the true k and n (5×10^{-11} m² and 0.4, respectively). Green, blue and black crosses denote the median values of k and n estimated by minimization of C_V , C_α and $C_{V,\alpha}$, respectively.

The merits of integration of $V_S(f)$ and $\alpha_S(f)$ are evident in Figure 7.1. Note that from the global minimum of $C_{V,\alpha}$ (black crosses), one can predict n within 2-3% error margin and k within 20% error margin, even when the values of all model parameters are unknown and the data has errors as large as 75% in $\alpha_S(f)$ and 15% in $V_S(f)$. For the same conditions, the cost function minimization of either $V_S(f)$ or $\alpha_S(f)$ cannot give accurate estimates of both k and n . From C_V minimization (green crosses), n can be predicted with a maximum error of 6-7%, but the error in k is extremely large (several orders of magnitude). From C_α minimization (blue crosses), the k estimates are less inaccurate, but the error in n estimates is very large. Note that some green crosses are close to the true value. This is due to the random assignment of model parameter values. $C_{V,\alpha}$, however, offers consistently accurate values for both k and n .

7.3 Field experiment

7.3.1 Estimating dispersion

The layer-specific k and n in the shallowest few meters of the saturated subsoil are crucial in hydrology, environmental and civil engineering. We deploy a downhole seismic array for reliable observation of *S*-wave dispersion. A microelectromechanical system (MEMS) digital array seismic cone penetrometer (SCPT), housing seven 3C accelerometers at 25 cm interval, is pushed into the soil (Ghose, 2012). *S* waves from a surface source are recorded at the 1.5 m downhole array. As source, we use an electromagnetic horizontal vibrator (Ghose *et al.*, 1996). The vibrator-SCPT offset is 0.9 m. The vibrator sweep is 100–450 Hz; sweep and record lengths are 3.7 s and 4.2 s, respectively. Because the source motion is well-monitored, a deterministic source signature deconvolution is performed for compressing the raw vibrograms (Ghose, 2002; Ghose & Goudswaard, 2004). The effective source function is constant at all depth levels in the array and the receiver coupling is good due to direct push in soil. The resulting data is of high quality.

Raw and rotated data of the two horizontal accelerometer components (X and Y) are shown in Figures 7.2a and 7.2b, respectively. Figure 7.2c shows CPT data from the same downhole tool: tip resistance (q_c), sleeve friction (f_s) and pore pressure (u). The friction ratio, f_s/q_c , is a good indicator of the soil layering. The data quality allows estimation of a reliable V_S profile by cross-correlation of the rotated traces between two adjacent depths. We choose four depth ranges (A, B, C and D in Figure 7.2c) corresponding to four downhole arrays. From prior geological knowledge and interpretation of CPT data, the soil compositions are known. Zone A is primarily sandy showing relatively high q_c and V_S , low friction ratio, and u following the hydrostatic gradient (marked by the dashed line in Figure 7.2c). Zone B is clayey, with low q_c , a generally high friction ratio, and low V_S . Zone C is clayey but contains a low-strength peat lens with low q_c , very low f_s , low V_S and also low u . Zone D has clay in the upper part and a sharp transition to sand in the lower part.

For *S*-wave velocity dispersion, we utilize multiple sensors in the downhole array and calculate the relative phase delay time (Δt) between receivers at two depth levels from the unwrapped phase difference ($\Delta\phi$) and travel distance (Δx) between the receiver pair, as shown in equation (5.5). With topmost and bottommost receivers as the reference ones, all possible receiver combinations within the array are used. The slope of the best-fit line in $\Delta x - \Delta t$ gives the phase velocity. This is shown for 140 Hz in Figure 7.3a. This estimation is performed for all frequencies to obtain the velocity dispersion (Figure 7.3b). We restrict to 50–220 Hz band because the signal lies in that band. The standard deviation at each frequency is indicated by the vertical bar.

For estimating effective attenuation α_{eff} , we use an adaptation of the spectral ratio method (Jeng *et al.*, 1999) which does not make constant Q assumption. This is illustrated in Figure 7.3c. The extrinsic attenuation α_{sc} due to internal multiple scattering is estimated using the formulation of Wapenaar *et al.* (2004). For this purpose we use the velocity profile in Figure 7.2c and bulk density information. Since

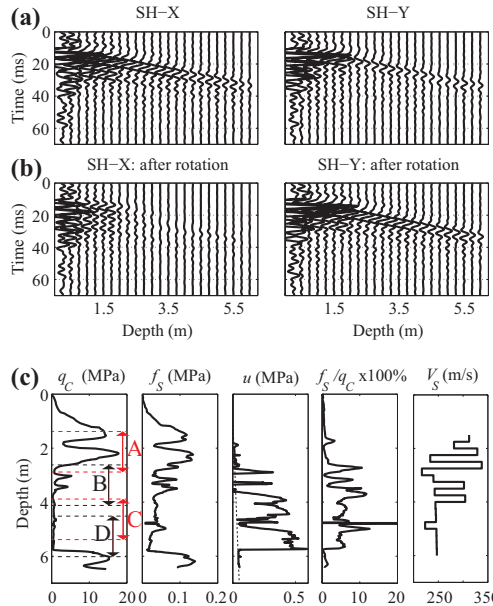


Figure 7.2: Horizontal components of the downhole S -wave data from array SCPT: (a) before and (b) after trace rotation. (c) CPT data and the derived V_s profile.

there were no data available about bulk density, the latter has been approximated based on the CPT information. α_{sc} is subtracted from α_{eff} to obtain the intrinsic attenuation α_{int} . This approach offers quite stable and reliable estimates of intrinsic dispersion (Zhubayev & Ghose, 2012b).

Figure 7.3d shows the estimated α_{eff} and α_{int} for four depth zones. The intrinsic attenuation, together with standard deviations, are shown in Figure 7.3e. Note that α_{int} is higher in zones A and C than in zones B and D (Figure 7.3c–7.3e). Zone B and D are predominantly clayey, zone A is sandy, and zone C has a conspicuous peat lens.

7.3.2 Results and discussion

Quantitative estimation of both k and n simultaneously from the low-frequency field-seismic dispersion data in soft soil has so far been not possible. In order to test if the new approach discussed above provides realistic estimates on field data, we have used at first the Biot-Stoll model. For the known soil types, representative values are used for the model parameters other than k and n (Table 7.1).

The result is shown in Figure 7.4. Clearly, there is a sharp global minimum for $C_{V,\alpha}$, giving unique estimates for both k and n simultaneously. Sand is well-known to have lower n and higher k than clay. The depth zone A is mostly sandy, B is clayey, C is clayey but contains a peat lens which is highly porous and permeable, and zone D contains both clay and sand. Using the Biot-Stoll model, for depth zones

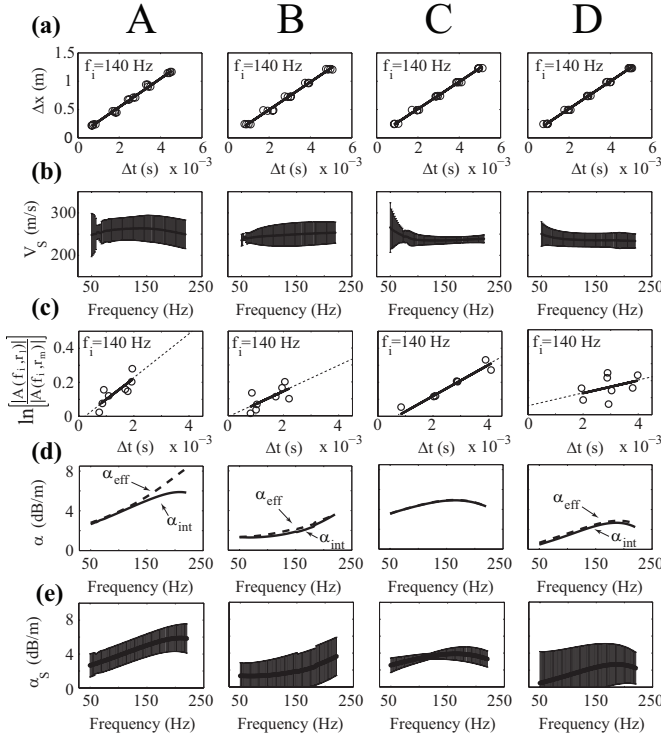


Figure 7.3: Estimating S-wave intrinsic dispersion. A, B, C, D are four depth zones shown in Figure 7.2.

A, B, C and D the estimated n is 0.44, 0.53, 0.55 and 0.46, and the estimated k is $3.3 \times 10^{-10} \text{ m}^2$, $6.0 \times 10^{-11} \text{ m}^2$, $2.2 \times 10^{-10} \text{ m}^2$ and $4.8 \times 10^{-11} \text{ m}^2$, respectively. The estimated values are realistic (Berry & Reid, 1987). Note that the global minimum is either poorly defined or erroneous in C_V and C_α (Figure 7.4).

The Biot-Stoll model is known to explain well the intrinsic dispersion for a wide variety of sediments. The crucial question is how sensitive the estimates are to the used model. In order to test this, we consider two different models – Biot-Stoll model and "Biot model with grain contact squirt flow and shear drag" or BICSQS by Chotiros & Isakson (2004). For highly permeable sands and gravels, BICSQS models predicts the intrinsic dispersion better than Biot-Stoll model, for normal sands both models are good, and for fine-grained soils like clay and peat, Biot-Stoll model works better.

Figure 7.5a shows theoretical estimates for $V_S(f)$ and $\alpha_S(f)$ for gravel and clay, using the two models. The dashed box indicates the field-frequency band for S-wave in soil. Table 7.1 presents realistic values for the model parameters that have been used. Note that, for the two models, all parameters are the same, except shear logarithmic decrement δ_s in the Biot-Stoll model and shear relaxation frequency f_c and half-gap width a_1 in the BICSQS model. The difference between the two models

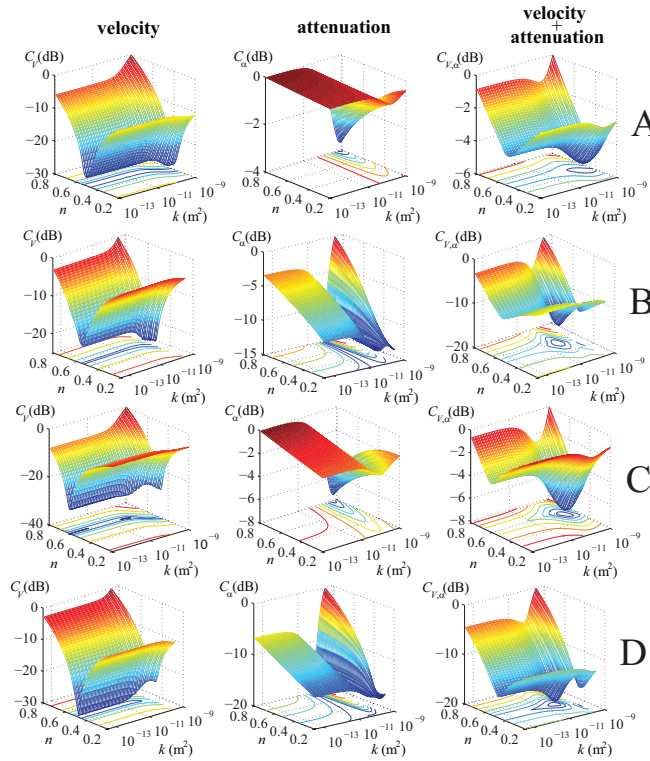


Figure 7.4: Result of cost-function minimization in the k - n domain for S -wave field data.

seen in Figure 7.5a is due to the model itself and not due to different parameter values. Clearly, for $V_S(f)$ there is no difference between the two models in the field frequency band. However, for $\alpha_S(f)$, although the two models are nearly the same for gravel, they are grossly different for clay.

The red circles in Figure 7.5b show k and n estimated from field data by $C_{V,\alpha}$ minimization using Biot-Stoll and BICSQS models and with realistic values (mean of the assumed ranges) for all parameters but k and n (Table 7.1). The estimates are shown at the top in each panel. Note that for depth zones A (sandy) and C (clay but with a highly permeable peat lens), which are expected to have a not-low overall permeability, both models predict very close values for k and n . However, for depth zones B (clay) and D (clay and sand), which are likely to have rather low to moderate overall permeability, we find a large difference between the estimates using the two models. Theoretical dispersion curves can sufficiently explain this difference (Figure 7.5a). When the model used is pertinent to the soil type, the estimates are quite robust.

Lastly, we investigate the effect of the unknown model parameters on the estimated k and n . The result is illustrated by the green, blue and black lines in Figure 7.5b, respectively for C_V , C_α and $C_{V,\alpha}$ minimization. The line lengths represent the

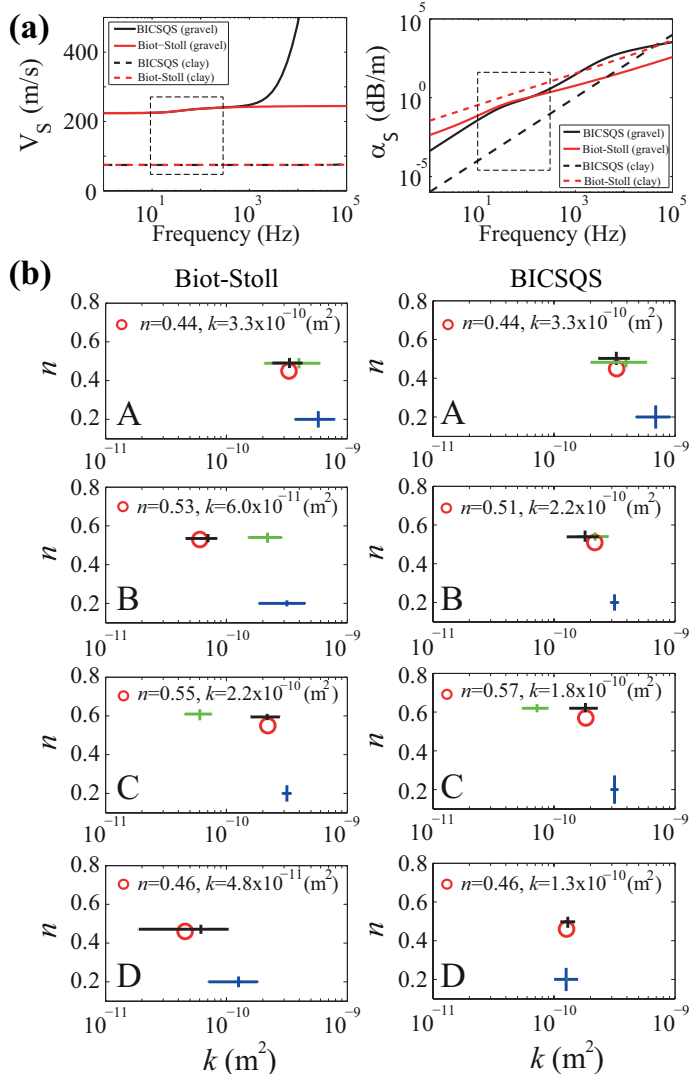


Figure 7.5: (a) $V_S(f)$ and $\alpha_S(f)$ in gravel and clay from Biot-Stoll and BICSQS models. (b) Estimated k and n from field data using the two models. Green, blue and black crosses denote the median values of k and n estimated by minimization of C_V , C_α and $C_{V,\alpha}$, respectively. Red circles the values of k and n estimated by $C_{V,\alpha}$ minimization using the mean of the assumed ranges (read the text).

Table I

Parameter	Unit	Biot-Stoll		BICSQS	
		gravel	clay	gravel	clay
Porosity, n	-	0.4	0.5	0.4	0.5
Permeability, k	μm^2	1000	0.1	1000	0.1
Grain density, ρ_s	kg/m^3	2650	2600	2650	2600
Fluid density, ρ_f	kg/m^3	1000	1000	1000	1000
Fluid viscosity, η	$\text{Pa}\cdot\text{s}$	0.001	0.001	0.001	0.001
Tortuosity, γ	-	1.25	3	1.25	3
Pore size, a	μm	158	2.2	158	2.2
Frame shear modulus, G	GPa	0.1	0.01	0.1	0.01
Shear logarithmic decrement, δ_s	-	0.1	0.3	-	-
Shear relaxation frequency, f_c	kHz	-	-	4	400
Half gap width, a_l	μm	-	-	1	0.01

Table 7.1: Values of parameters in Biot-Stoll and BICSQS models for calculating S -wave dispersion shown in Figures 7.4 and 7.5.

ranges of the estimated values. Permeability ranges are in log scale. The assigned ranges for parameter values are the same as in Figure 7.1. For ρ , δ_s , f_c and a_l , different ranges are used for the four different depth zones: A [$\rho = 1900\text{--}2100 \text{ kg}\cdot\text{m}^{-3}$, $\delta_s = 0.05\text{--}0.15$, $f_c = 4\text{--}50 \text{ kHz}$, $a_l = 0.1\text{--}1 \mu\text{m}$], B [$\rho = 1800\text{--}2000 \text{ kg}\cdot\text{m}^{-3}$, $\delta_s = 0.25\text{--}0.35$, $f_c = 30\text{--}500 \text{ kHz}$, $a_l = 0.01\text{--}1 \mu\text{m}$], C [$\rho = 1600\text{--}1900 \text{ kg}\cdot\text{m}^{-3}$, $\delta_s = 0.25\text{--}0.5$, $f_c = 30\text{--}100 \text{ kHz}$, $a_l = 0.01\text{--}1 \mu\text{m}$] and D [$\rho = 1800\text{--}2000 \text{ kg}\cdot\text{m}^{-3}$, $\delta_s = 0.25\text{--}0.35$, $f_c = 30\text{--}500 \text{ kHz}$, $a_l = 0.01\text{--}1 \mu\text{m}$].

In case of $C_{V,\alpha}$ minimization, the estimated k and n values (range given by the black lines) for varying model parameters are very close to those obtained by using the realistic model parameter values (red circles). These results on field data are in good agreement with those obtained on synthetic data (Figure 7.1). On the contrary, in case of C_V or C_α minimization, either the k or the n estimate has a large error. Note also that the difference in the estimated k and n values between Biot-Stoll and BICSQS models is small for depth zones A and C, but generally large for zones B and D. This is because both models are good for zones A and C, but not so for zones B and D. Clearly, if the model of poroelasticity is chosen such that it can explain the observed dispersion data well, then the integrated cost function $C_{V,\alpha}$ will give reliable and robust estimates of both k and n .

Independent field verifications of the goodness of the in-situ k and n estimates as derived in this research are not possible. Synthetic tests show that the estimates obtained by $C_{V,\alpha}$ minimization is quite accurate and robust, even in the presence of high noise and when the values of other model parameters are unknown. On field

data, we have succeeded to obtain reliable estimates of k and n for all four depth zones. However, if k is much smaller, then more high-frequency frequency content in the *S*-wave data will be necessary for a stable estimation (Zhubayev & Ghose, 2012a).

7.4 Conclusions

Estimates of k and n in water-saturated soil layers are essential in many important projects, but in-situ estimation of these flow properties remained impossible so far. We have shown that the integrated cost function minimization of dispersive *S*-wave velocity and attenuation can offer quite accurate and robust estimates of both k and n , even when the dispersion data has large error and the values of other model parameters have realistic uncertainties. We have tested the methodology on both noisy synthetic data and field data. Obtaining reliable *S*-wave dispersion information in the shallow soil layers has been possible through deployment of a downhole seismic array. We have found on field data that when the used model of poroelasticity is pertinent to the soil type, the estimated k and n are quite robust.

Chapter 8

Seismic signatures of fluid mobility: Field observation

8.1 Introduction

In all previous chapters, we have looked into seismic dispersion in unconsolidated soils or sediments and into the possibility of extracting soil properties from the observed seismic dispersion. Subsequently, we have also had the opportunity to test the approach developed in this research on a deeper exploration seismic dataset acquired in consolidated rock formations. In this chapter, we shall discuss these results.

The physics underlying the conversion of seismic energy into heat in porous rocks is not fully understood. The main reason is perhaps a lack of exhaustive experimental datasets allowing a reliable investigation of such phenomena. Extraction of intrinsic attenuation from seismic data itself is additionally challenging, which inhibits studies in this direction. In this chapter, we show distinct seismic signatures of fluid mobility in reservoir rocks at exploration-seismic frequencies (10–120 Hz). This can be regarded as a field evidence for wave-induced flow as to be a dominant mechanism for seismic attenuation.

Although it is widely accepted that wave-induced fluid flow can be an important mechanism for attenuation, there are few laboratory and even fewer field experiments which unambiguously confirm such a mechanism. Perhaps the most well-known field experiments were carried out at the Imperial College borehole site to measure velocity dispersion and frequency-dependent intrinsic attenuation (Q^{-1}) in a layered sequence of water-saturated sandstones, siltstones, limestones, and mudstones (Sams *et al.*, 1997). Four sets of experiments were conducted at depths ranging from 50 to 250 m, namely VSP (30–280 Hz), crosswell measurements (200–2300 Hz), sonic logging (8–24 kHz) and ultrasonic laboratory experiments (300–900 kHz). In the same year, Quan & Harris (1997) used crosswell experimental data in a layered sequence of shaly sandstones and limestones at BP’s Devine test site (depths ranging from 500 to 900 m) to estimate intrinsic attenuation. They found correlations between the

estimated Q^{-1} and the lithology. No permeability measurements were available for either site. Payne *et al.* (2007) tried to invert for permeability using crosswell seismic data (100–4000 Hz) in a fractured chalk (depths ranging from 20 to 50 m), where extensive hydrogeological investigations, including in situ estimation of permeability, were performed. Relatively high attenuation values were observed at relatively high-permeability (20–50 D) zones, suggesting seismic signatures of wave-induced fluid flow. Thus, correlations between seismic Q^{-1} and permeability were reported. However, the authors did not succeed to obtain rock permeability estimates due to the difficulty arising from the inherent parameter coupling in the poroelasticity models and the relatively high scattering attenuation. All these studies made a constant Q assumption in attenuation estimation and found $10^{-2} < Q^{-1} < 10^{-1}$ in sedimentary rocks.

Laboratory experiments were more successful in studying seismic energy dissipation in sedimentary rocks. This is mainly because of a better control in the experiments and meticulous knowledge of the geomaterial. The experimental results of Winkler *et al.* (1979) dramatically influenced the future course of investigations on the possible mechanisms of seismic intrinsic attenuation. The authors concluded that the loss of seismic energy caused by grain-boundary friction is important only at low confining pressures and at strains larger than about 10^{-6} . Their experimental results indicated that important mechanisms, like fluid flow, must be more dominant (than friction) in seismic attenuation.

More recent experiments by Batzle *et al.* (2006) over a broad frequency band (5 Hz–800 kHz), demonstrated a significant velocity dispersion in rock samples at low seismic-strain amplitudes (10^{-7}). They reported a strong fluid mobility effect on the seismic velocity dispersion. Both mesoscopic and microscopic (grain scale) fluid-flow models could explain their data. Adam *et al.* (2009) investigated experimentally the fluid effect on P -wave, S -wave, extensional wave and bulk compressibility attenuations at both seismic (10–1000 Hz) and ultrasonic (0.8 MHz) frequencies in five carbonate rocks. Porosity and permeability ranges were, respectively, 20%–30% and 0.03–58.1 mD. Only one out of five samples—the most permeable (58.1 mD) one—showed a significant frequency-dependent seismic attenuation at exploration-seismic frequencies (10–100 Hz) under partially and fully saturated conditions. Saturated fluids were, respectively, liquid butane (0.2 centipoise (cP)) and brine (1 cP). Additionally, the magnitude of seismic attenuation observed in this sample was significantly higher than that in four other samples, especially for brine saturation. In general, attenuation measurements of compressional waves showed $10^{-2} < Q^{-1} < 10^{-1}$, except for the most permeable sample with brine saturation $10^{-1} < Q^{-1} < 0.5$.

Compared to experimental studies, theoretical models evolved more rapidly. Different theoretical quantifications of seismic wave attenuation were proposed (e.g., Frenkel, 1944; Biot, 1956a,b, 1962; Mavko & Nur, 1975; White, 1975; Budiansky & O'Connell, 1976; Dutta & Ode, 1979b,a; Dvorkin & Nur, 1993; Dvorkin *et al.*, 1994, 1995; Smeulders & van Dongen, 1997; Johnson, 2001; Chapman *et al.*, 2002; Pride & Berryman, 2003a,b; Muller & Gurevich, 2005). Importantly, it was found that attenuation can peak at seismic frequencies because of a diffusive process (pore-fluid

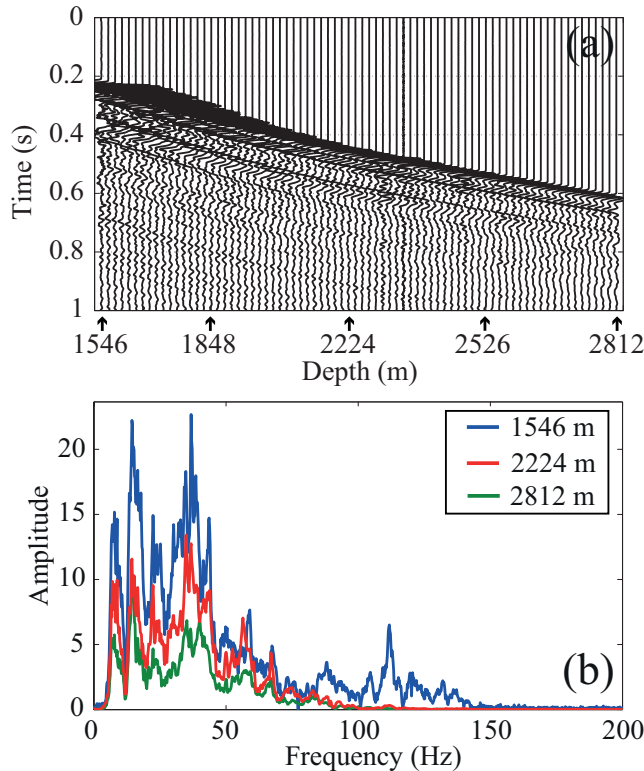


Figure 8.1: (a) Raw zero-offset VSP data (compressional wave) from an offshore field in China. (b) Amplitude spectra of seismograms at three depth levels.

pressure equilibration) at mesoscopic and microscopic (grain) scales. This may occur because of the heterogeneous nature of the solid and fluid phases at different scales. As a result, strong attenuation and velocity dispersion can be observed at seismic frequencies.

The structure of this chapter is as follows. In section 8.2, we discuss a zero-offset VSP experiment carried out in China, where exhaustive well log measurements were also performed. In section 8.3, we estimate seismic attenuation and velocity dispersion of compressional waves from this zero-offset VSP data. P -wave velocities from the VSP are compared with sonic velocities in Section 8.4. Scattering attenuation due to multiple layering is quantified in Section 8.5. In Section 8.6, we discuss intrinsic attenuation in high- and low-mobility zones in our data. We investigate briefly the Biot and squirt (BISQ) model (Dvorkin & Nur, 1993) in Section 8.7.1, and show that it provides a possible mechanism for the observed attenuation. We then use the extracted intrinsic dispersion information from VSP data complemented with well log data to invert for fluid mobilities using simulated annealing. In Section 8.8 we discuss and summarize our results.

8.2 Field zero-offset VSP and well log measurements

High-quality zero-offset VSP in the depth interval 522 m–3190 m were acquired on a layered sequence of fluid-saturated sandstone, siltstone and shale at an offshore test site in China. Stacked raw seismograms for compressional waves between 1546 and 2812 m are shown in Figure 8.1a. The frequency content is between 10 and 120 Hz (Figure 8.1b). In VSP acquisition, seismic sensors were positioned in the vertical borehole at alternating 15 m and 30 m intervals in the depth range 522 m–2178 m. At depths below 2178 m, the sensors were positioned at 15 m interval. The time sampling interval was 1 ms. The amplitude spectra shown in Figure 8.1b are for the entire trace length. The similarity among the spectra at three widely separated depth levels is indicative of the measurement stability.

In addition to VSP, exhaustive wireline logging (Figure 8.2) was carried out every 15 cm in the same borehole. The measurements included bulk density, porosity, Stoneley wave-based mobility, sonic P - and S -wave velocities, and temperature. Two independent porosity estimates were available. A detailed interpretation of lithology and fluid content were available between 2250 and 2960 m depths. As this depth interval was of particular interest because of light hydrocarbon accumulation, it was subjected to more detailed investigations. Hydrocarbon accumulations were found primarily inside the high fluid mobility (10^1 – 10^3 mD/cP) zones. In addition, high-resolution magnetic resonance and dynamic formation test measurements were performed to obtain independent estimates of fluid mobility. All three independent fluid mobility measurements (i.e., Stoneley wave-based, high-resolution magnetic resonance, and dynamic formation test) were found to be in good agreement with each other.

8.3 Estimation of effective attenuation and velocity dispersion from VSP data

The physics of seismic intrinsic attenuation in a porous medium (see e.g., Pride *et al.*, 2003) suggests that Q^{-1} is not constant at the seismic-frequency band and is more likely to vary by one or even two orders of magnitude in the frequency range 1 Hz–1000 Hz. The behaviour of Q^{-1} can be complicated, especially at the characteristic frequencies, which can sometimes fall into the seismic band. The characteristic frequency defines the boundary between relaxed and unrelaxed regimes. Although widely used (e.g., Sams *et al.*, 1997; Quan & Harris, 1997; Payne *et al.*, 2007), the constant Q assumption is not strictly correct for many fluid-saturated geomaterials. This assumption may hinder capturing the signatures of permeability from the seismic amplitude.

The viability of different techniques for estimation of attenuation from the VSP data were rigorously studied by Tonn (1991). White (1992) quantified the accuracy that can be expected in Q estimation. In this study, we use an adaption of the spectral ratio method (Jeng *et al.*, 1999) to calculate seismic attenuation, without

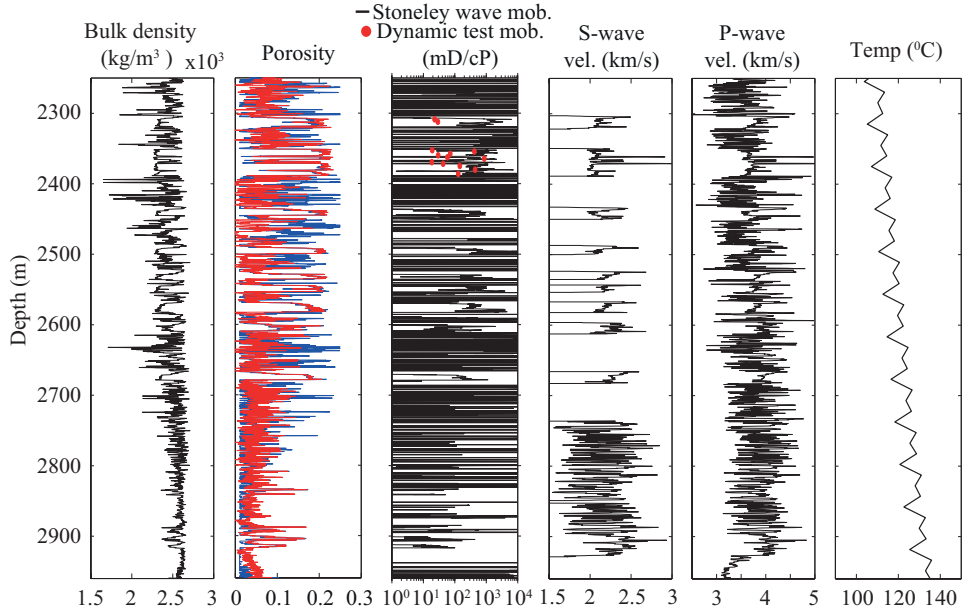


Figure 8.2: Wireline logs and the interpreted data. Logs were acquired in the same well as the VSP data.

making constant Q assumption.

The VSP data (Figure 8.1) are used to extract layer-specific seismic intrinsic attenuation and velocity dispersion. No processing is done to the stacked raw seismograms in order to preserve the amplitude information. To extract velocity dispersion and attenuation within a given layer, we follow the approach of Zhubayev & Ghose (2012b).

A time window around the peak amplitude of the direct P -wave first arrival is automatically chosen. The velocity dispersion is calculated, as in Section 5.3.2, using the relative phase delay time ($\Delta t = t_2 - t_1$) at different frequencies (f) for a given receiver pair positioned at $\Delta x = x_2 - x_1$ distance apart from each other. The delay time Δt is found from the unwrapped phase difference $\Delta\phi$ (Eq. (5.5)). Two reference receivers—one at the top and another at the bottom of a given depth interval—are selected. To calculate the average velocity dispersion within the interval, we use all possible receiver combinations with respect to the reference receivers, except the combination of the two reference receivers themselves.

Similarly, to calculate the average effective attenuation within a depth interval, we use an adaptation of the spectral ratio method (Jeng *et al.*, 1999):

$$\ln \frac{A_1(f, x_1)}{A_2(f, x_2)} = \text{const} + \frac{\pi f}{Q(f)} \Delta t, \quad (8.1)$$

where A_1 and A_2 are recorded amplitudes for a given frequency (f) at receivers at depths x_1 and x_2 , respectively.

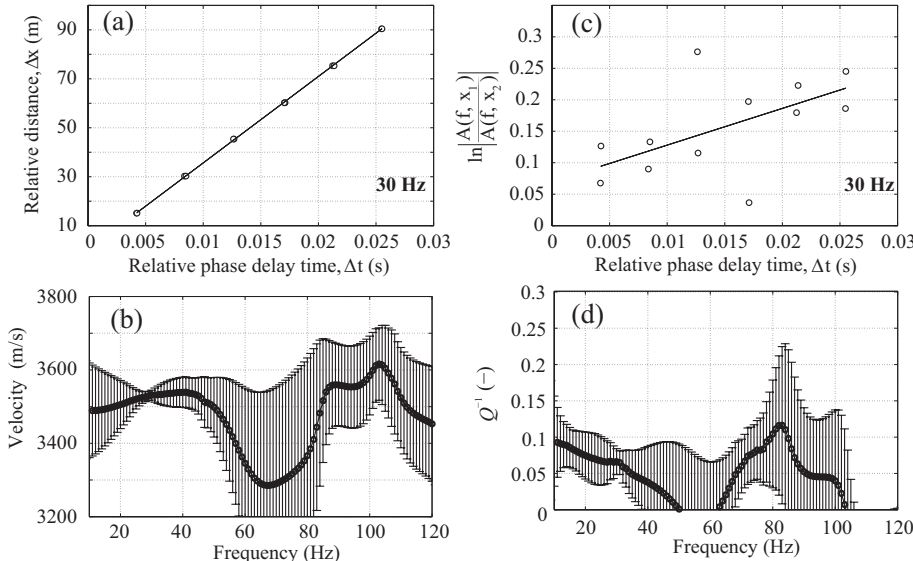


Figure 8.3: Estimation of phase velocity and attenuation dispersion for 2300 m–2405 m depth interval. (a) The slope of the best-fit line gives V_P at 30 Hz. (b) Estimated phase velocity (black line) over the entire frequency range and the standard deviation denoted by the vertical bars. (c) Logarithmic ratio of the spectral amplitudes versus phase-delay time at 30 Hz. The slope of the best-fit line gives $\pi f/Q$. (d) Estimated Q^{-1} (black line) over the entire frequency range; the standard deviation is indicated by the vertical bars. The standard deviations are relatively small in the frequency band (10 Hz–55 Hz) where the signal-to-noise ratio is high (Figure 8.1b)

Figure 8.3 illustrates the results of estimation of seismic velocity dispersion and attenuation within 2300 m–2405 m depth interval. Eight seismic sensors are available in this interval. The standard deviations of the estimated velocity and attenuation for each frequency are calculated from the scatter plots (Figures 8.3a, 8.3c). In Figure 8.3b and 8.3d, the estimated velocity dispersion and attenuation (black lines), together with their standard deviations (vertical bars), are shown for the frequency range 10 Hz–120 Hz. Note that the errors in velocity and attenuation estimates are smaller in the dominant frequency range (10 Hz–55 Hz). The errors outside this range are relatively large. Large errors are primarily associated with the low signal-to-noise ratio. Errors also enter because of multiple scattering within the depth interval.

Next, we calculate the layer-specific effective velocity dispersion and attenuation for all depths in the VSP data (Figure 8.1). Figures 8.4b and 8.4c show the dispersion estimates for the depth interval where VSP data are available at four consecutive depths. In other words, four traces are used within each sliding window to calculate layer-specific attenuation and velocity dispersion. The window is moved by one trace each time. The reason behind using four traces is to minimize the effect of averaging over different lithologies on the velocity and attenuation estimates. Admittedly, a decrease in the number of traces in a window does cause an increase in the uncertainty in the estimated velocity and attenuation. The use of a step of one

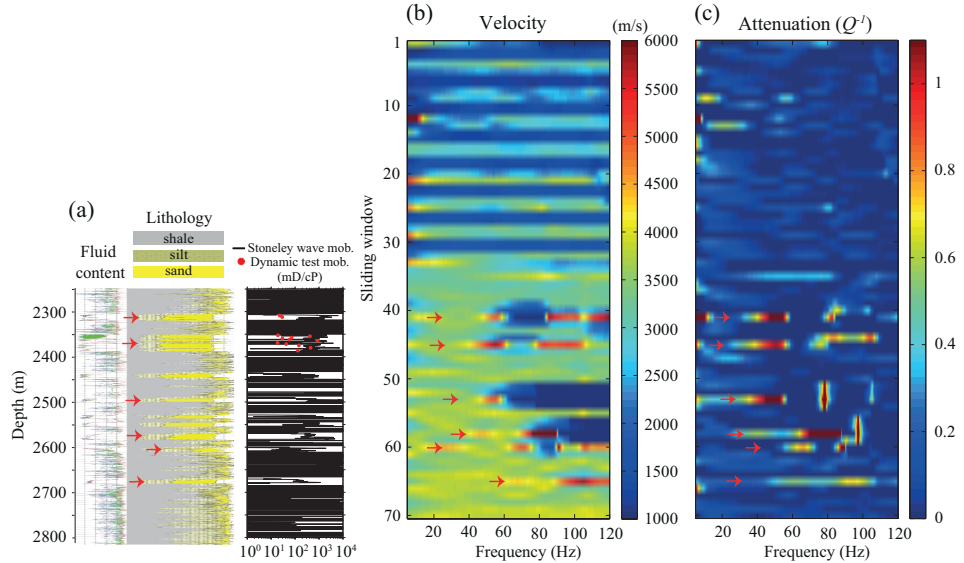


Figure 8.4: Vertical profiles showing (a) fluid content (green colour is oil), lithology, and mobility of the formation, (b) estimated interval velocity, and (c) estimated attenuation dispersion between 1546 m and 2750 m depth. Note the correlation (see red arrows) between lithology, independently measured fluid mobilities, and the seismic dispersion estimated from VSP data.

single trace helped in obtaining good depth resolution of the estimated dispersion.

The effective velocity dispersion and attenuation reveal a striking correlation in depth with well log data (Figure 8.4). These correlations are marked by the red arrows. The velocity dispersion and attenuation are conspicuous in the sandy zones with high fluid mobility, where the hydrocarbons are accumulated. It is also evident that the contrast in attenuation in the sandy zones relative to the surrounding is much higher compared to the contrast in velocity, indicating greater sensitivity of effective seismic attenuation to the fluid flow properties. The effective seismic dispersion could discriminate between high- and low-mobility layers.

For the high-permeability sandstones, the estimated attenuation is in the range $10^{-1} < Q^{-1} < 10^0$, while for the low-permeability shales, the range is $10^{-2} < Q^{-1} < 10^{-1}$, as shown in Figure 8.4c (and subsequently, more clearly in Figure 8.8). The most accurate, independent estimates of fluid mobility in the hydrocarbon-bearing sandstone are known from the dynamic formation tests in the same borehole (shown by red dots in Figure 8.4a); they range between 15 mD/cP and 800 mD/cP. The porosity range in the experiments of Adam *et al.* (2009) is between 20% and 30%, which is the same range as that in the high-permeability sandstones in our study. Adam *et al.* (2009) has reported a mobility value of 58.1 mD/cP, for the most permeable sample, which falls into the range of mobility estimated from the dynamic formation tests in our study. Interestingly, we find that our estimated range of Q^{-1} from the effective seismic dispersion in VSP data is the same as that ($10^{-1} < Q^{-1} < 0.5 \cdot 10^0$) of the measurements of Adam *et al.* (2009). For the shales,

our estimated range of Q^{-1} is representative for typical low-permeability formations (e.g., Quan & Harris, 1997; Sams *et al.*, 1997; Pride *et al.*, 2004; Payne *et al.*, 2007; Adam *et al.*, 2009).

Note that the effective attenuation for high fluid-mobility sandstones peaks at different frequencies than that for shales. This is possibly due to the difference in the size of heterogeneity and the macroscopic fluid mobility. It was not possible to resolve the high-mobility layer at around 2450 m depth, possibly because the layer is surrounded by thick low-permeability shale layers. In general, distinct signatures of mobility changes on the seismic amplitudes can be delineated. To evaluate the quality of our velocity estimates, next, we look at the sonic logs.

8.4 P-wave velocities from VSP and sonic log data

Before a quantitative comparison between VSP and sonic velocities is carried out, we need to look at the influence of fluid mobility on the seismic dispersion. According to earlier theoretical and experimental observations (Pride *et al.*, 2003, 2004; Batzle *et al.*, 2006), the fluid mobility of rocks largely controls the pore-fluid motion and the interaction between heterogeneous regions of different scales. As a result, the overall response of a propagating seismic wave in rocks with highly different fluid mobilities can vary greatly. A schematic illustration of such difference (assuming the same scale for the heterogeneities) in terms of the frequency-dependent velocity and attenuation is shown in Figure 8.5. It shows that the pore-pressure equilibration process (caused by wave-induced disturbance) between the pores or between solid/fluid heterogeneous regions takes longer time in low-mobility rocks like shales and siltstones than in high-mobility rocks like sandstones and carbonates. The low-mobility rocks are generally in the high-frequency regime at seismic and higher frequencies. Therefore, the velocity values measured in the VSP should be close to the sonic and ultrasonic velocities. In contrast, high-mobility rocks are in the low-frequency regime at the seismic frequency band. For this type of rocks, one can observe large discrepancies in the measured velocity values using different techniques (e.g., VSP, sonic logging, ultrasonic tests).

To investigate the VSP and the sonic velocities, we focus on velocities at 30 Hz in the spectra shown in Figure 8.4b. We have the maximum signal-to-noise ratio at this frequency (Figures 8.1b and 8.3b) and the standard deviation of velocity here is small (4%). The average standard deviation in the estimated VSP velocities over the frequency band 10 Hz–120 Hz is about 8%. These velocity values are compared with the smoothed sonic logs shown in Figure 8.2. The results are illustrated in Figure 8.6. The velocity values obtained from the VSP are generally lower than those measured from the sonic logs. Similar observations were reported by De *et al.* (1994). The result is consistent with theoretical velocity dispersion illustrated in Figure 8.5. The difference in the velocity values between the VSP and the sonic logs is more apparent for high-permeability sandstones with a relatively high Q^{-1} (marked by arrows in Figure 8.6). This is also in agreement with the theoretical expectation (Figure 8.5). These explain the discrepancy between the VSP and sonic velocities that we find in the high-permeability sandstones.

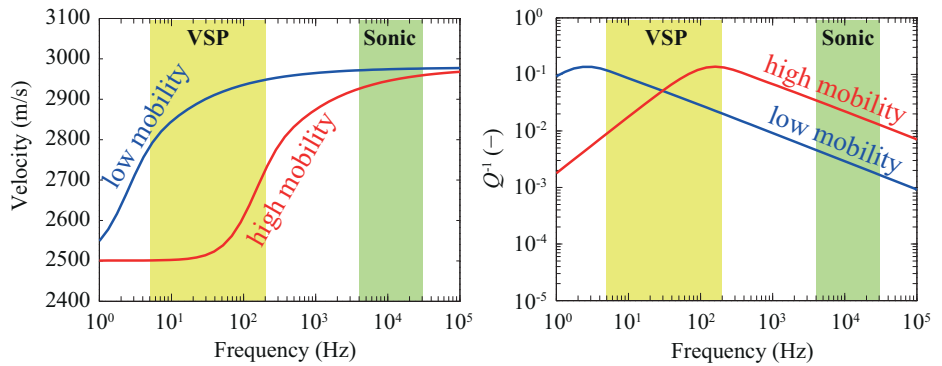


Figure 8.5: Schematic illustration of the expected dispersion (velocity and attenuation) in high-mobility (red line) and low-mobility (blue line) rocks. Yellow- and green-shaded areas correspond to the operating frequency bands for VSP data and sonic logs, respectively.

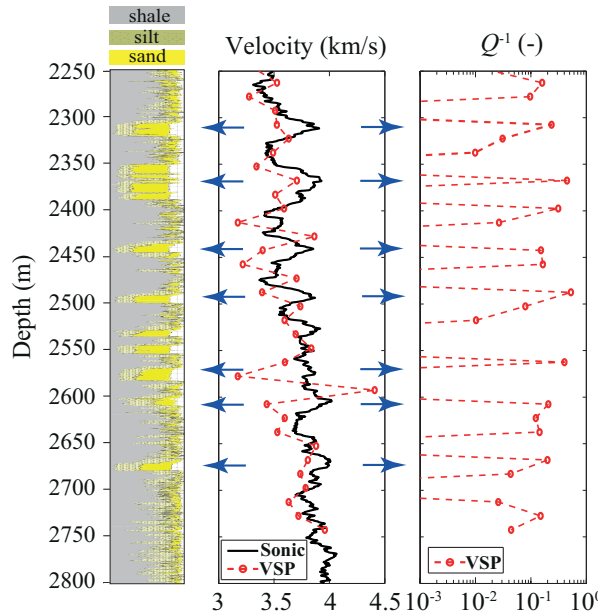


Figure 8.6: Comparison of *P*-wave velocity from VSP and sonic log data, and Q^{-1} from VSP data. Note large discrepancies between VSP and sonic velocities at sandy zones with high fluid mobility. These zones also show high attenuation (Q^{-1}), marked by arrows.

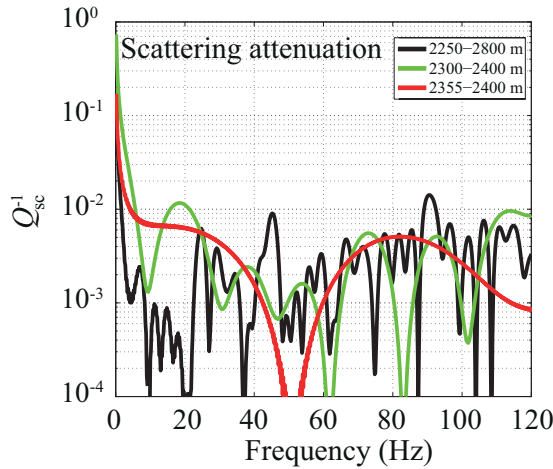


Figure 8.7: Calculated scattering attenuation over three different depth intervals: 2355 m–2400 m (red), 2300 m–2400 m (green), and 2250 m–2800 m (black).

8.5 Estimation of scattering attenuation

The observed effective attenuation is the sum of intrinsic attenuation (Q^{-1}) and scattering attenuation (Q_{sc}^{-1}). An analysis of the relative importance of inelastic absorption and scattering attenuation on the effective attenuation is necessary. Previous studies (O'Doherty & Anstey, 1971; Schoenberger & Levin, 1974) suggest that, in the scale of seismic wavelengths, the primary extrinsic loss may be caused by multiple scattering in the internal layers. There are several available techniques which allow us to separate scattering attenuation from intrinsic attenuation (e.g., O'Doherty & Anstey, 1971; Wapenaar *et al.*, 2003; Wapenaar *et al.*, 2004). To quantify the attenuation which can be attributed to multiple scattering in our VSP data, we use the deterministic approach proposed by Wapenaar *et al.* (2003, 2004), which uses the velocity and density information of the subsurface.

Seismic wave transmission between depths z_1 and z_2 for a given frequency (ω) can be expressed in terms of the 1-D primary propagator (W_p) and the coda waves (\hat{C}):

$$T_0^+(z_2, z_1, \omega) = W_p^+(z_2, z_1, \omega) \hat{C}(z_2, z_1, \omega), \quad (8.2)$$

where + indicates the downgoing wave. In our case, P -wave velocity and density logs are available (Figure 8.2). The calculated reflection responses (R_0) for a given frequency (ω) give the coda waves (\hat{C}) due to multiple scattering for wave propagation between depths z_1 and z_2 :

$$\left\{ \hat{C}(z_2, z_1, \omega) \right\}^* \hat{C}(z_2, z_1, \omega) = 1 - \{ R_0^+(z_2, z_1, \omega) \}^* R_0^+(z_2, z_1, \omega), \quad (8.3)$$

where $*$ denotes a complex conjugate. The amplitude (\hat{A}) of the coda part decays

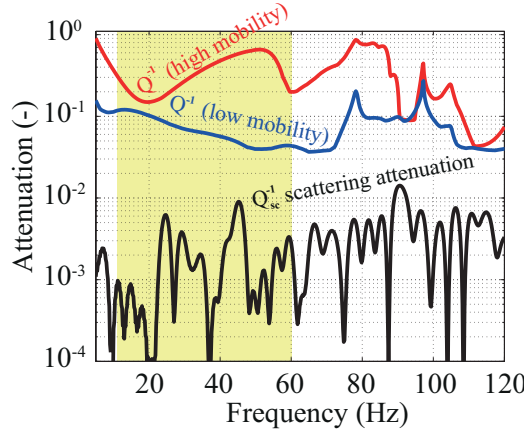


Figure 8.8: Estimated average intrinsic attenuation for high-mobility (red line) and low-mobility (blue line) zones in 2250 m–2750 m depth interval. Calculated attenuation due to multiple scattering between depths 2250 and 2800 m is shown by the black line. The yellow-shaded area corresponds to the frequency band with high signal-to-noise ratio in the VSP data (Figures 8.1b, 8.3b and 8.3d).

exponentially:

$$\hat{C}(z_2, z_1, \omega) = e^{-\hat{A}(\omega)}, \quad (8.4)$$

where \hat{A} is related to the extra delay time (τ) and attenuation Q_{sc}^{-1} due to multiple scattering:

$$\tau(\omega) = \frac{\text{Im}(\hat{A}(\omega))}{\omega}, \quad (8.5)$$

$$Q_{\text{sc}}(\omega) = \frac{\omega t_p}{2\text{Re}(\hat{A}(\omega))}, \quad (8.6)$$

where t_p is the primary (one-way) traveltime from z_1 to z_2 . Eq. 8.6 is used to estimate Q_{sc}^{-1} .

The estimated Q_{sc}^{-1} for three depth intervals is shown in Figure 8.7. In all three cases, it is found that $Q_{\text{sc}}^{-1} < 10^{-2}$. Further comparison with the apparent attenuation estimated from the VSP data (red and blue lines in Figure 8.8) shows that the contribution of the scattering attenuation to the observed effective attenuation, in the case of our data, is negligible. The scattering attenuation cannot predict the relatively high attenuation for almost all depth zones, and even more so for attenuation values observed in the high-mobility layers. The effective attenuation is primarily due to intrinsic loss resulting from fluid flow, especially in high-mobility layers.

8.6 Intrinsic attenuation in high- and low-mobility zones

Based on lithology interpretation and direct measurements of fluid mobility (Figure 8.4a), it is possible to divide the depth range into two categories—high-mobility (sand) zones and low-mobility (shale) zones. Next, we calculate the average effective Q_{eff}^{-1} for these two zones.

As it is demonstrated in the previous section, the attenuation due to multiple scattering is negligible for this dataset, and the effective attenuation calculated from the VSP data can be regarded as the intrinsic attenuation ($Q_{\text{eff}}^{-1} \approx Q^{-1}$). Figure 8.8 shows the comparison between the average attenuation Q_{eff}^{-1} calculated for high-mobility (red line) and low-mobility (blue line) zones in the depth range 2250 m–2750 m. These curves are obtained from attenuation estimates shown in Figure 8.4c. Interestingly, one can mark at least two distinct differences in the frequency band with high signal-to-noise ratio (10 Hz–55 Hz).

The first conspicuous difference is in the attenuation range found for the high- and the low-mobility zones. The level of attenuation for the high-mobility layers is found to be $10^{-1} < Q^{-1} < 10^0$, while the level for the low-mobility zones is $10^{-2} < Q^{-1} < 10^{-1}$. The latter range is consistent with previous studies (e.g., Sams *et al.*, 1997; Quan & Harris, 1997; Payne *et al.*, 2007). Our observation of relatively high Q^{-1} values for high-mobility zones are also in agreement with the recent attenuation measurements (10–1000 Hz) in carbonates reported by Adam *et al.* (2009) for a sample with 58.1 mD permeability and full saturation with brine of viscosity 1 cP. Moreover, the fluid mobility value (58 mD/cP) of Adam *et al.* (2009) falls into the fluid mobility range (10^1 – 10^3 mD/cP) estimated in this field experiment (from Stoneley waves and dynamic formation tests) for high mobility formations. In addition to this, in our study, the behaviour of Q^{-1} as a function of frequency for the high-mobility zones (Figure 8.8) is found to be similar to those reported by Adam *et al.* (2009).

The second difference between the high- and the low-mobility zones is the behaviour of Q^{-1} with frequency, which is found to be opposite in the frequency band corresponding to high signal-to-noise ratio. Q^{-1} increases with frequency for the high-mobility zones, while it decreases with frequency for the low-mobility zones (Figure 8.8). This is in accordance with the theoretical results from the BISQ model, illustrated in Figure 8.5. The multiple peaks in the attenuation-versus-frequency plots (Figure 8.8), especially for the high-mobility zone are due to averaging. These results indicate that the low-mobility zones are located in the high-frequency regime—even at exploration seismic frequencies, whereas high-mobility sandstones are still in the low-frequency regime. In the following sections we will investigate the viability of the BISQ model and discuss an inversion strategy to obtain the transport properties from the seismic intrinsic dispersion.

8.7 Poroelastic inversion using a rotated coordinate system and simulated annealing

8.7.1 Forward model

The squirt flow is one of the possible mechanisms that can explain seismic attenuation at exploration seismic frequencies (Pride *et al.*, 2003). The loss due to a squirt flow is a microscale loss due to grain-level heterogeneities. Dvorkin & Nur (1993) proposed the unified Biot and squirt flow (BISQ) model to predict the high levels of seismic attenuation. Most of the tests involving the BISQ model, so far, use ultrasonic frequencies and there is little check on the validity of loss associated with squirt flow in the exploration seismic frequency band. For instance, (Dvorkin & Nur, 1993; Dvorkin *et al.*, 1994) tested the model on typical sandstones at 1 MHz and found it to be good in predicting seismic attenuation and velocity dispersion. A rigorous test on the applicability of the BISQ model to different types of sandstones was performed at 800 kHz by Marketos & Best (2010). These authors concluded that the BISQ model was able to predict the observed velocity and attenuation dispersion. Batzle *et al.* (2006) conducted laboratory experiments to measure velocity dispersion in rocks over a wide frequency range (from 5 Hz to 800 kHz) using different fluid types for rock saturation. They concluded that both mesoscopic and microscopic (squirt flow) loss mechanisms were consistent with the measured velocity dispersion. However, there are still concerns (e.g., Pride *et al.*, 2004) about whether the squirt flow mechanism is capable of reproducing the high levels of seismic attenuation at exploration seismic frequencies (10–1000 Hz). Therefore, we test the BISQ model using the low-frequency dispersion data obtained in Section 8.3. A brief description of the BISQ model will be given first.

The BISQ model unifies two loss mechanisms: 1) the Biot loss mechanism, which incorporates the viscous loss due to fluid flow in the direction of the solid motion (global flow), and 2) the squirt flow, which occurs when the fluid is squeezed out of the thin cracks to the stiff pores as the seismic wave propagates through a partially saturated porous medium. The model assumes that the (Newtonian) fluid and the solid phases are statistically homogeneous and isotropic. This fluid can flow not only parallel, but also perpendicular to the direction of wave propagation. All thermal and chemical effects are ignored. The derivation of this model can be found in Dvorkin & Nur (1993). The fast and the slow P -wave velocities ($V_{P_{1,2}}$) and attenuations ($Q_{P_{1,2}}$) are given by:

$$V_{P_{1,2}} = \frac{1}{\text{Re}(\sqrt{Y_{1,2}})}, \quad (8.7)$$

$$Q_{P_{1,2}} = \frac{\text{Re}(\sqrt{Y_{1,2}})}{2\text{Im}(\sqrt{Y_{1,2}})}, \quad (8.8)$$

where

$$Y_{1,2} = -\frac{B}{2A} \mp \sqrt{\left(\frac{B}{2A}\right)^2 - \frac{C}{A}}, \quad (8.9)$$

$$A = \frac{F_{sq}M}{n\rho_f^2}, \quad (8.10)$$

$$B = \frac{F_{sq}(2\gamma - n - (1-n)\rho_s/\rho_f)}{n\rho_f} - \frac{(M + F_{sq}\gamma^2/n)(1 + \rho_a/n\rho_f + i\omega_c/\omega)}{n\rho_f}, \quad (8.11)$$

$$C = \frac{(1-n)\rho_s}{n\rho_f} + \left(1 + \frac{(1-n)\rho_s}{n\rho_f}\right) \left(\frac{\rho_a}{n\rho_f} + i\frac{\omega_c}{\omega}\right), \quad (8.12)$$

$$\rho_a = (\tilde{\alpha} - 1)n\rho_f, \quad (8.13)$$

$$\omega_c = \frac{\eta n}{k\rho_f}, \quad (8.14)$$

$$\lambda^2 = \frac{\rho_f\omega^2}{F} \left(\frac{n + \frac{\rho_a}{\rho_f}}{n} + i\frac{\omega_c}{\omega}\right), \quad (8.15)$$

$$F = \left(\frac{1}{K_f} + \frac{1-\gamma}{nK}\right)^{-1}, \text{ and} \quad (8.16)$$

$$F_{sq} = F \left(1 - \frac{2J_1(\lambda R)}{\lambda R J_0(\lambda R)}\right). \quad (8.17)$$

Here, $\gamma = 1 - K/K_s$, where K is the bulk modulus of the rock in drained condition and K_s is the bulk modulus of the solid grain. $M = 2G(1 - \nu)/(1 - 2\nu)$ is the dry uniaxial modulus, where G is the shear modulus and ν is the dry Poisson's ratio. K_f is the fluid bulk modulus, η is the viscosity of the fluid, k is the permeability, ρ_s is the density of the grain, ρ_f is the density of the fluid, n is the porosity, ω and ω_c , respectively, are the cyclic and Biot characteristic frequencies, and R is the characteristic squirt flow length. J_0 and J_1 are the Bessel functions of zero and first order, respectively. Dynamic tortuosity is modeled according to Johnson *et al.* (1987) as:

$$\tilde{\alpha}(\omega) = \alpha_\infty \left[1 + i\frac{\omega_c}{\omega} \left(1 - i\frac{M_0}{2} \frac{\omega}{\omega_c}\right)^{\frac{1}{2}}\right], \quad (8.18)$$

where α_∞ is the tortuosity in the high-frequency regime ($\lim_{\omega \rightarrow \infty} \tilde{\alpha}(\omega) = \alpha_\infty$). The pore-shape factor M_0 is generally close to 1 (Johnson *et al.*, 1987).

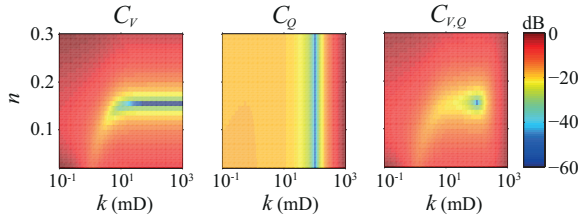


Figure 8.9: Results of cost function minimization in the porosity (n)–permeability (k) domain. The values of the parameters other than n and k in the BISQ model, used in this calculation, are shown in Table 8.1.

8.7.2 Cost-function

In this section, we investigate whether the quasi-orthogonal behaviour in the porosity–permeability domain between frequency-dependent P -wave velocity and attenuation is observable also in the case of the BISQ model and when using Q instead of α for attenuation.

Thus, the dispersive fast P -wave velocity $V(\omega, \vec{x})$ and attenuation $Q(\omega, \vec{x})$ in an integrated cost function can be written as:

$$C_{V,Q} = \left(W_1 \sum_{\omega} |\Delta_P^V|^{\beta} + W_2 \sum_{\omega} |\Delta_P^Q|^{\beta} \right)^{\frac{1}{\beta}}, \quad (8.19)$$

where $\Delta_P^V = \frac{V(\omega, \vec{x}) - \hat{V}(\omega)}{\sigma_V(\omega)}$, $V(\omega, \vec{x})$ being the velocity estimated from a pertinent model of poroelasticity and $\hat{V}(\omega)$ representing the intrinsic velocity dispersion extracted from field data. The term \vec{x} is the input parameter vector, and $\sigma_V(\omega)$ denotes the standard deviation in the velocity estimate. For attenuation, the notations for Δ_P^Q are similar. W_1 and W_2 are appropriate scaling coefficients, which can be calculated prior to the inversion.

Figure 8.9 illustrates the results of cost function minimization in the n – k domain. P -wave dispersion data are generated between 10 and 200 Hz using the BISQ model. All model parameters other than n and k ($\vec{x} = (n, k)^t$) are assumed to be known (see Table 8.1). When only $V(\omega)$ or $Q(\omega)$ is used (i.e., equation 8.19 has only the first (C_V) or the second (C_Q) term), the cost function minimum offers no unique estimate. The results will be even worse if the data are noisy. But when we minimize an integrated cost function ($C_{V,Q}$), we find a unique minimum in the n – k domain, which corresponds to the correct value. The approach is robust against noise (Zhubayev & Ghose, 2012b). Such difference in dispersive V and Q can be applied as an additional constraint in the multiparameter optimization problem, which will be discussed next.

8.7.3 Estimation of rotated coordinates and parameter bounds

As discussed in details in Chapter 6, the inversion becomes more challenging when the numbers of unknown parameters (\vec{x}) in the cost function increases. The BISQ

Parameter	Unit	True	Min	Max
Porosity, n	-	0.15	0.02	0.30
Permeability, k	mD	100	0.1	10000
Viscosity, η	cP	8	1	20
Shear rigidity, G	GPa	12	8.86	17
Poisson's ratio, ν	-	0.22	0.17	0.3
Frame bulk modulus, K	GPa	15	10	30
Grain bulk modulus, K_s	GPa	38	36	39
Fluid bulk modulus, K_f	GPa	2	1.25	2.2
Density of solid, ρ_s	kg/m ³	2650	2600	2700
Density of fluid, ρ_f	kg/m ³	880	800	1000
Tortuosity, α_∞	-	1.8	1	3
Squirt length, R	mm	5	0.01	1000

Table 8.1: Values of Parameters (BISQ model) used to Compute the Covariance Matrix Ψ

model requires twelve parameters (Table 8.1). As before, we use here simulated annealing (Kirkpatrick *et al.*, 1983; Metropolis *et al.*, 1953) in order to obtain the parameters in the model by minimizing the cost function in equation 8.19. To improve the optimization efficiency, we navigate again the global search using rotated coordinates (Collins & Fishman, 1995).

The covariance matrix of the gradient of the cost function is estimated using Eqs. (6.3) and (6.4).

The parameter search space Ω can be identified based on analyses of an exhaustive openhole dataset (Figure 8.2), which was available. Ten out of twelve parameters of the BISQ model can be extracted with reasonable accuracy from the well log data. The remaining two rock properties—tortuosity (α_∞) and characteristic squirt length (R)—are virtually impossible to measure. Stoll (1977) suggested that tortuosity may range between 1 and 3. From eigenvector analysis of the covariance matrix (Ψ), the effect of tortuosity to dispersive velocity and attenuation is found to be rather small, for a formation with 100 mD permeability. In the case of field VSP data, we are at much lower frequencies compared to the Biot's characteristic frequency. Sensitivity of seismic intrinsic dispersion to tortuosity, however, may increase in low-permeability layers, which are in the high-frequency regime even at exploration seismic frequencies. Information concerning the characteristic squirt length is not known and can only be obtained by inverting the observed dispersion data using the BISQ model. A broad range—0.01 mm to 1000 mm—for the squirt flow length is, therefore, chosen. The squirt-flow length for the reservoir sandstones was rigorously studied by Marketos & Best (2010).

Temperature logs were available in our case. Therefore, realistic bounds for the fluid properties e.g., viscosity, density and bulk modulus, could be obtained from the fluid-content information and then be evaluated using thermodynamic relationships and empirical trends (Batzle & Wang, 1992). Similar to Isakson & Neilsen (2006), shear rigidity ($G = \rho V_S^2$) bounds are calculated from the available shear velocity

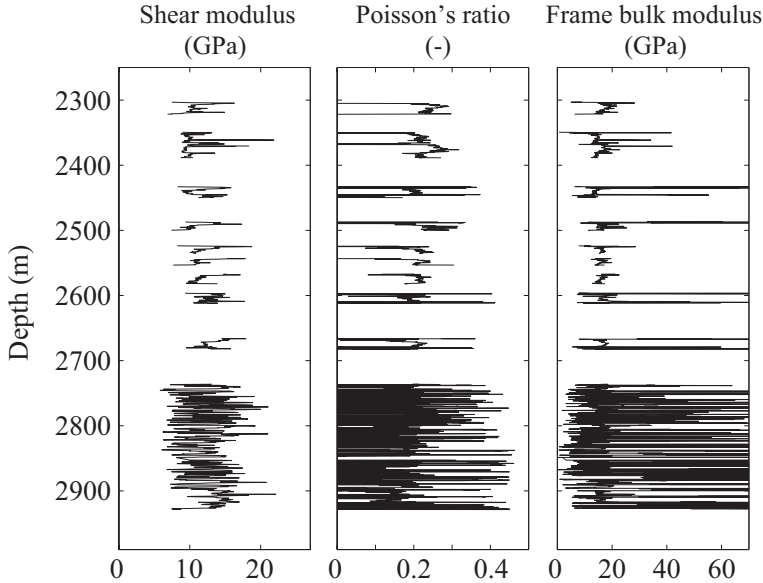


Figure 8.10: Calculated shear modulus (G), Poisson's ratio (ν), and bulk modulus (K) for the dry frame.

(V_S) logs and bulk density. V_S is mostly available in the high-permeability zones and in a limited depth range (2736 m–2929 m) for the shale (see Figure 8.2). For these layers, undrained bulk moduli are approximated from sonic P -and S -wave velocities and bulk density ($K_b = \rho(V_P^2 - (4/3)V_S^2)$). Although this value of K_b is pertinent to sonic frequencies, a maximum of 10% variation between VSP and sonic log velocities (Section 8.4) will introduce only a small uncertainty (in MPa scale) in K_b . Substituting this value of K_b into the Gassmann's equation provide the bounds for the frame bulk modulus K . Representative ranges are taken for the grain density and grain bulk modulus. Poisson's ratio for the dry frame is calculated using K and G information: $\nu = (3K - 2G)/(2(3K + G))$. Calculated shear modulus (G), Poisson's ratio (ν), and bulk modulus (K) for the dry frame are shown in Figure 8.10. In this way, realistic bounds for all parameters are obtained; they are listed in Table 8.1.

Figure 8.11a shows the eigenvectors of Ψ calculated over the bounds specified in Table 8.1 and for 10 Hz–200 Hz frequency band. Each eigenvector is plotted as a row in Figure 8.11a. The rows are sorted according to the eigenvalues. For instance, the eigenvector corresponding to the maximum eigenvalue is shown by row number 12. This eigenvector gives the most sensitive direction of the cost function. The eigenvector corresponding to the minimum eigenvalue is shown by row number 1, and it is the least sensitive direction. The deviation of the circles from the null vector (horizontal dashed line) of the corresponding eigenvector represents the coordinates of this eigenvector in the original parameter basis (\vec{x}).

Based on this eigenvector–eigenvalue analysis, it is clear that permeability (k),

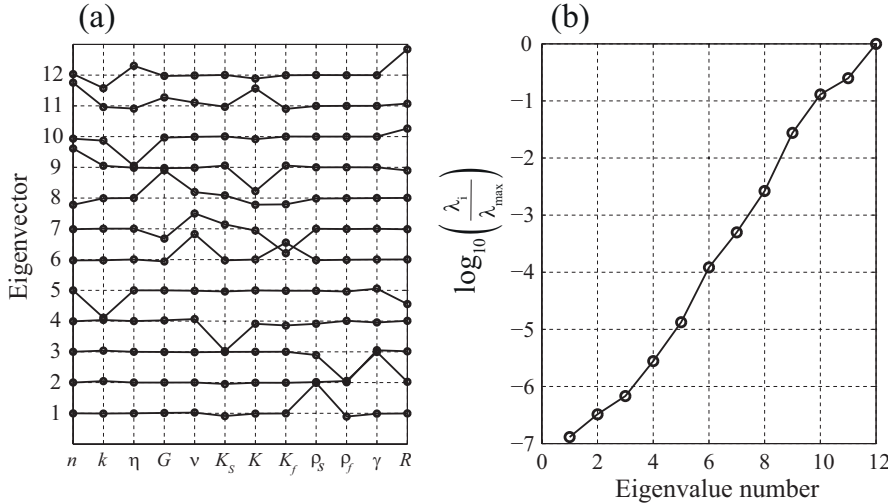


Figure 8.11: (a) Eigenvectors of the covariance matrix Ψ calculated over the bounds specified in Table 8.1 and for 10 Hz–200 Hz frequency band. (b) Eigenvalues scaled by maximum eigenvalue of the covariance matrix Ψ .

viscosity (η), and squirt-flow length (R) are the most influential parameters (see eigenvector 12 in Figure 8.11a). This is because the projection of this eigenvector to the original parameter basis has the largest value for k , η and R (see eigenvector 12). In addition to this, k has opposite influence to $C_{V,Q}$ compared to η and R , for the same eigenvector. This is expected, because k and η usually enter as the k/η ratio (fluid mobility) in the Biot equations.

It is also clear that these parameters are coupled. The effect of porosity (n), frame shear modulus (G), and frame bulk modulus (K) becomes more conspicuous in the direction of eigenvector 11. The parameters, which have a large amplitude in the eigenvectors corresponding to the large eigenvalues, can be resolved from seismic velocity dispersion and attenuation, in the frequency range 10 Hz–200 Hz and for the bounds specified in Table 8.1. As anticipated, other parameters have a much larger effect on the cost function than grain bulk modulus (K_s), tortuosity (α_∞), solid density (ρ_s), and fluid density (ρ_f). This is because the largest displacements of K_s , α_∞ , ρ_s and ρ_f appear at the eigenvectors corresponding to the smaller eigenvalues (eigenvector 4, 3, 2, and 1, respectively, in Figure 8.11a). All other eigenvectors can be analysed in the same way. The ratios of the i th eigenvalue λ_i to the maximum eigenvalue λ_{\max} are shown in logarithmic scale in Figure 8.11b. This analysis allows us to identify less sensitive parameters in Ω . Parameters which have small influence on the cost function can be kept realistically constant. The knowledge of the parameter hierarchy, thus, helps to reduce the dimension of the problem, which leads to increased efficiency and more stable inversion. In our case, however, all parameters are varied utilizing the deduced importance of various parameters in the inversion scheme (details are given in Section 6.2 of this thesis).

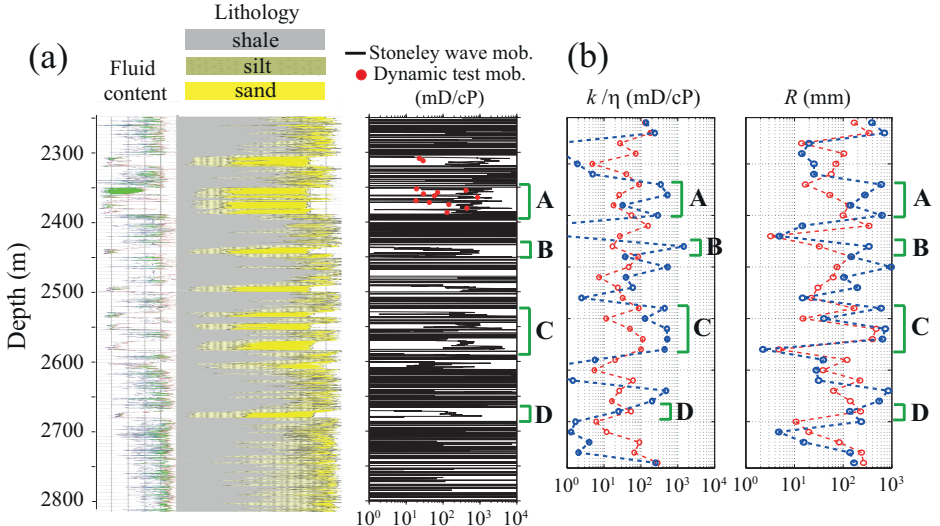


Figure 8.12: Vertical well profiles showing (a) fluid content, lithology and fluid mobility; (b) inverted best-fit (blue circles) and median (red circles) interval mobility (k/η) and squirt length (R) calculated from seismic dispersion observed in the VSP data, using the approach discussed here.

Tests of this inversion algorithm on synthetic data show encouraging results. The more influential parameters to the cost function (Equation 8.19) are found to be stably resolvable. In simulated annealing, we have used an exponential cooling schedule $T = T_0 \cdot 0.95^\chi$ with the initial temperature $T_0 = 100$ K, where χ is the annealing parameter and is the same as the iteration number until reannealing.

8.7.4 Inversion results and discussion

The inversion of the dispersion data is performed at each sliding depth-window (containing traces for four consecutive depth levels in VSP). Extensive well log measurements are available between windows 37 to 70 (see Figure 8.4). The cost function $C_{V,Q}$ in equation 8.19 is minimized using simulated annealing navigated by the information of the rotated coordinates. For 50 realizations of the simulated annealing at each depth interval, the layer-specific output parameters are obtained. The best-fit and median values are then obtained from the 50 vector outputs for each layer. The values of the best-fit and median fluid mobility and squirt-flow length inverted from the VSP and the well-log data are shown in Figure 8.12b. The best-fit and median values from the VSP dispersion data are marked by blue and red circles, respectively. These properties (k/η and R) represent the most influential parameters (Figure 8.11). Note the good correlation (A, B, C and D in Figure 8.12) between the Stoneley wave-based mobility, dynamic formation test mobility, and fluid mobility obtained from seismic dispersion extracted from the VSP data. Although the scale (of averaging over depth) of the inverted fluid mobility from the VSP data

is different from that obtained from Stoneley waves and formation tests, yet the estimated mobility magnitude is comparable with those independent estimates at several depth levels. The uncertainties in the inverted mobility values vary up to two orders of magnitude. This degree of uncertainty is also present in the estimates from the well logs. Model imperfectness, parameter coupling, and the uncertainty in the estimated dispersion—all influence the output.

The goodness of the mobility estimates and the model are further checked through comparison of the observed dispersion curves with the dispersion curves obtained using the inverted layer-specific parameters plugged into the BISQ model. This is illustrated in Figure 8.13 for all 34 windows. The BISQ model, in general, fits the data well in the frequency band corresponding to the high signal-to-noise ratio, suggesting that the squirt flow mechanism is possibly dominant and responsible for the observed loss at the exploration seismic frequencies. The squirt flow mechanism can be used in addressing reservoir transport properties in such cases. However, the BISQ model is unable to explain the high level of attenuation observed at high-mobility zones, although the trend is found to be consistent with the observed attenuation and the attenuation predicted by the BISQ model falls into the uncertainty bounds for attenuation calculated from the VSP data. In this case, other mechanisms such as mesoscopic losses are more plausible.

In this study, we see only a small part of the seismic dispersion. Having broadband seismic velocity dispersion and attenuation measurements (sonic, ultrasonic) would improve the stability and the reliability of this approach. That will also offer more insights into the physics of conversion of seismic energy to heat.

8.8 Conclusions

Frequency-dependent seismic velocity and attenuation estimates were obtained from a VSP dataset (10–120 Hz) in a layered sequence of fluid-saturated sandstones, siltstones, and shales at depths ranging from 1546–2812 m, where comprehensive well log measurements were available. The sandstone layers are known to contain light hydrocarbons. Our analyses showed that Q^{-1} is strongly frequency-dependent and can vary up to one order of magnitude even at the exploration seismic frequency band. For shales, Q^{-1} was found to decrease with frequency, indicating a high-frequency regime. Conversely, sandstones with a high fluid mobility showed an increase in Q^{-1} with frequency, suggesting a low-frequency regime. For shales, which has the lowest permeability at this site, the level of attenuation ($10^{-2} < Q^{-1} < 10^{-1}$) was consistent with earlier results (Sams *et al.*, 1997; Quan & Harris, 1997; Payne *et al.*, 2007). In contrast, higher levels of attenuation (10^{-1} and 10^0) were found in the high-permeability sandstones. The same levels of Q^{-1} were previously reported by Adam *et al.* (2009) for high-permeability carbonates saturated with brine. Such marked difference in attenuation is a diagnostic of low- and high-mobility zones within the depth range of consideration. The velocity values obtained from VSP were lower than those measured from the sonic logs. Relatively large discrepancies between the VSP and sonic velocities were found in high-permeability sandstones; this is consistent with earlier theoretical and experimental observations.

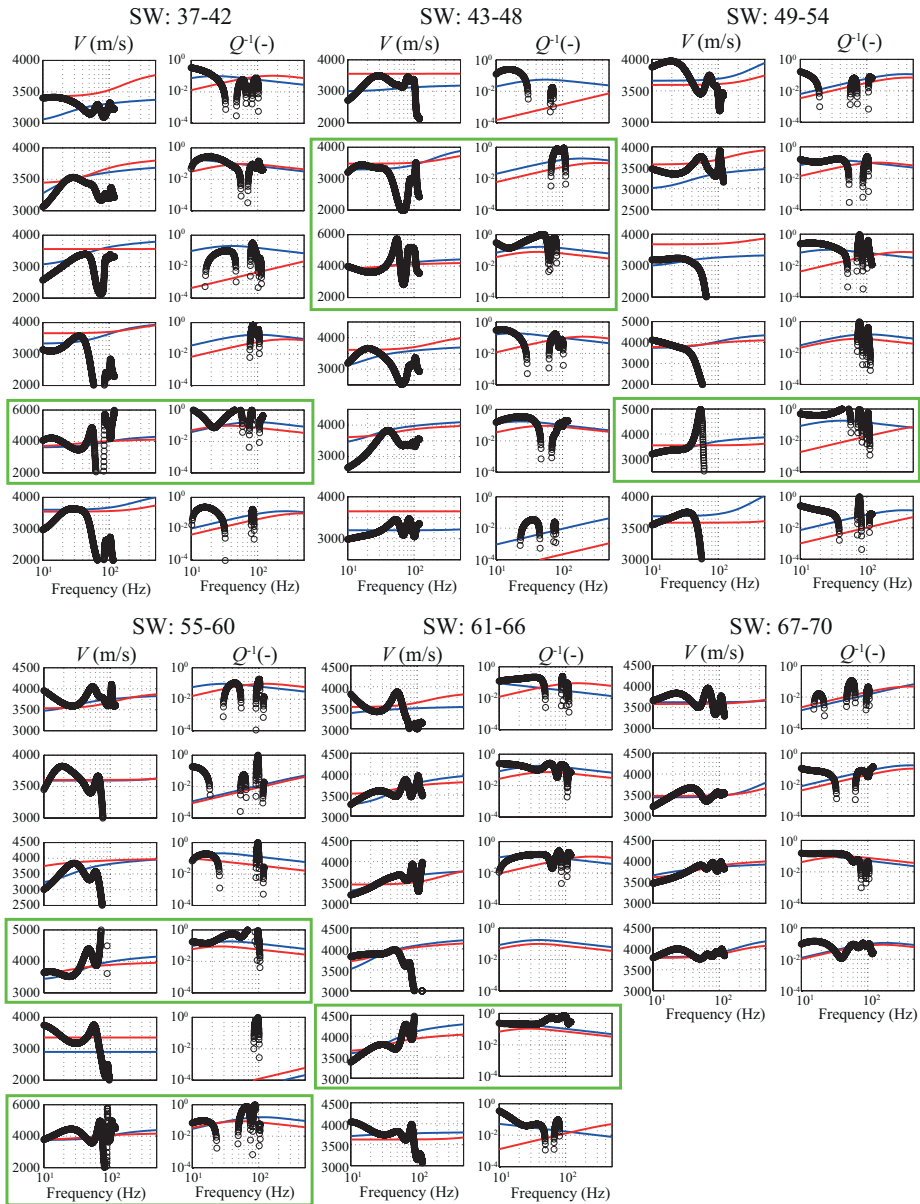


Figure 8.13: Estimated intrinsic velocity and attenuation dispersion (black circles) from the VSP data in 2250 m–2750 m depth range, for sliding windows (SW) 37 to 70, in comparison with the BISQ model predictions (solid lines). Blue and red lines correspond to the inverted best-fit and median values, respectively. The green boxes mark the zones showing high attenuation, where the BISQ model underestimates. These zones match with the high-mobility, sandy formations known from the lithology information and independent fluid-mobility measurements. The model fits the observation in the frequency band corresponding to the high signal-to-noise ratio, due to the relatively small standard deviations at those frequencies (Figures 8.3b and 8.3d).

We looked into the impact of attenuation due to multiple scattering (Q_{sc}^{-1}) on the observed effective attenuation. We found that $Q_{\text{sc}}^{-1} < 10^{-2}$. In general, the scattering attenuation is much smaller than the effective attenuation in our data.

We used the BISQ model to invert the observed dispersion, using simulated annealing navigated by a rotated coordinate system. Eigenanalysis of the covariance matrix Ψ calculated using the BISQ model and realistic parameter bounds (Table 8.1) showed that in the 10 Hz–200 Hz band, the rock permeability (k), the fluid viscosity (η) and the squirt flow length (R) are the most influential parameters to the cost function representing the residual between model and observed dispersion. In general, the theoretical prediction from the BISQ model is in good agreement with the observation. Despite different scales (depth averaging) between the inverted fluid mobility values from VSP data and the independent estimates of mobility based on Stoneley-wave analyses and dynamic formation tests, the absolute magnitudes and the general trend in depth of the extracted fluid mobilities are quite similar. The squirt flow appears to be a dominant dissipative mechanism for the formation under consideration. The BISQ model is unable to explain the high level of attenuation observed in high-mobility zones. In this case, other mechanisms such as mesoscopic losses are more plausible.

Chapter 9

Conclusions

This thesis intends to advance our understanding on the dispersion of seismic waves primarily in unconsolidated, granular earth materials, and to define new possibilities for subsurface characterization using dispersive seismic waves in the field-seismic frequency band. In this pursuit, the research has been focused on theoretical considerations together with new methodology developments and elaborate tests on synthetic and field experimental datasets.

The research results in this thesis are presented in seven chapters. These results comprise new theoretical developments linking in-situ stress to dispersive seismic wave propagation in a transversely isotropic medium, evidence of a contrasting behaviour between seismic velocity dispersion and attenuation levering crucial advantages in subsoil characterization, and new methodologies and data inversion approaches for extracting important properties of porous, fluid-bearing formations in the subsurface, tested on synthetic and field data.

In Chapter 2 of this thesis, starting from the Lagrangian mechanics and incorporating dissipation, we have derived equations of motions and have looked at different loss mechanisms that are pertinent to unconsolidated soils/sediments. With a statistical isotropy assumption for the grain contact orientation, the microscale loss mechanism has been upscaled to describe the macroscale seismic attenuation. Biot's theory has been extended to partial fluid saturation by considering an average, effective fluid modulus. It has finally been shown that the behaviour of the bulk modulus as a function of saturation, in the quasistatic limit, can change dramatically between the effective fluid model and the patchy saturation model. Theoretical expressions derived in this chapter have been used in the subsequent chapters.

In Chapter 3 we have developed a model which relates in-situ stress in a transverse isotropic medium to the properties of propagating seismic waves. This has been possible by incorporating stress-dependent elastic moduli and effective stress laws for transport properties. We have shown that the strain potential energy is nearly independent of the changes in the transport properties caused by stress and is primarily controlled by the stress-dependent elastic moduli. The kinetic energy and the dissipation function of the mechanical system are sensitive to stress; they are controlled by stress-induced changes in both transport properties and elastic

moduli. We have demonstrated that the frequency-dependent velocity is nonlinear with stress and is more prominent for the slow P and SV waves than for the fast P and SH waves. The model predicts nearly independent behaviour of attenuation dispersion with the applied stress.

The work of Chapter 4 is inspired by earlier findings that nearly orthogonal behaviour in the domain of multiple parameters that commonly affect two or more independently measured quantities can be utilized to obtain stable and unique estimates of those causative parameters. We have found that dispersive seismic velocity and attenuation, in reality, can exhibit such quasi-orthogonal behaviour in multiple property domains at the field-seismic frequency band. This is due to the underlying physics of poroelasticity. Especially, we have observed this highly contrasting behaviour in porosity-permeability, effective-stress-permeability, and porosity-water saturation domains. We have found that seismic and high-frequency electromagnetic wave velocities can also be advantageously integrated in a cost function to obtain unique and stable estimates of porosity and water saturation. Also, porosity and water saturation can be uniquely obtained from seismic velocities alone (e.g., from V_P and V_S).

In Chapter 5, we have shown on a realistic, near-surface vertical seismic profile (VSP) dataset that in-situ estimates of porosity and permeability can be obtained from the frequency-dependent V_S and α_S extracted from the data, provided the assumption of the underlying loss mechanism is reasonably good. The estimates are stable against model and data uncertainties. We have illustrated the possibility of separating the effect of multiple scattering from the observed dispersion and deriving sufficiently accurate estimates of intrinsic dispersion, which are then useful in subsoil property estimation. It is challenging to estimate reliable values of in-situ porosity and permeability for loose granular soils, although these are important in many practical applications. The outcome of this research provides an answer to this challenge.

Because the theories of poroelasticity involve a multitude of parameters, an inversion for these parameter values is a daunting task. In Chapter 6, we take up this challenge. A global optimization technique using simulating annealing (SA) in a rotated coordinate system has been discussed within the framework of poroelasticity. The rotated coordinates are found from the eigenvectors of the covariance matrix of the gradient of the cost function representing the data-model residual. This covariance matrix, calculated using a Monte Carlo integration technique, contains information about the parameter coupling and the relative importance of different model parameters in the optimization. We have found that the optimization by SA is more efficient in the rotated coordinates than in the original coordinates. Synthetic studies with and without noise in the data show very good convergence for the more sensitive parameters corresponding to the larger eigenvalues. The approach was tested on a database consisting of twelve well-selected S -wave dispersion datasets from fully-saturated, unconsolidated soils. The analyses provide interesting insights on different relaxation mechanisms in different soil types. We have found that the Biot model is unable to predict the high S -wave attenuation in field data; however the Biot-Stoll model is good for seven of the twelve datasets, giving reasonable values

of porosity and permeability. For high-dispersion formations, the Biot-Stoll model also fails. In this case, the BICSQS model of Chotiros & Isakson (2004), which includes wave-induced fluid flow at grain boundaries, is quite successful and offers very reasonable estimates of porosity and permeability.

Finally, in Chapter 7 we have tested the approach discussed in Chapters 5 and 6 on a very shallow field VSP dataset collected at a soft soil site in the Netherlands. In the field data acquisition, we have used a recently developed array seismic cone penetrometer (SCPT) housing seven 3C accelerometers at 25 cm interval. An *S*-wave vibrator has been used as the seismic source. The soil type is known from the CPT. Obtaining reliable values of *S*-wave dispersion (50–220 Hz) in the very shallow soil layers has been possible using the high-quality array-seismic data. We have illustrated on the field data that when the assumed model of poroelasticity is pertinent to the soil type, the estimated values of porosity and permeability are quite robust and reasonable. We can distinguish in the field-observed *S*-wave dispersion these soil properties among sand, clay and peat layers.

Because we have had the opportunity to test the approach developed in this research on a deeper, exploration-seismic (VSP) dataset acquired in consolidated rock formations, in Chapter 8 we present these results as an additional proof of the concept. *P*-wave velocity and attenuation dispersion (10–120 Hz) estimates are obtained from the VSP data in a layered sequence of fluid-saturated sandstones, siltstones and shales. The sandstone layers are known to contain light hydrocarbons. We have found that in shales, the attenuation, expressed as the inverse quality factor (Q^{-1}), decreases with frequency, indicating a high-frequency regime. On the other hand, in the sandstones with a high fluid mobility (permeability to viscosity ratio), we find Q^{-1} to increase with frequency, suggesting a low-frequency regime. We observe a high level of attenuation in the high-permeability sandstones, as reported also in earlier studies. The BISQ model of Dvorkin & Nur (1993) and simulated annealing in a rotated coordinate system (presented in Chapter 6) have been used to invert the observed dispersion and estimate the fluid mobility values. Despite different scales (depth averaging) between the inverted fluid mobility values from VSP dispersion data and independent estimates of mobility based on Stoneley-wave analyses and dynamic formation tests, the absolute magnitudes and the general trend in depth of the fluid mobility are quite similar.

Seismic dispersion did not receive much attention in the past in the investigation of the near-surface soil layers. Earlier attempts to utilize seismic dispersion for evaluating shallow marine sediments or deeper hydrocarbon-bearing formations generally considered very high (ultrasonic, acoustic) frequencies; such high frequencies are not available in usual field-seismic data on land. In-depth studies of seismic dispersion in the low field-frequency band and its possible utilization in quantitative subsurface characterization are few and far between. This thesis has shown the value of seismic dispersion in the field-frequency band in quantitative, in-situ estimation of the properties of the porous subsoil layers. The properties that can advantageously be addressed are in-situ stress, fluid saturation, porosity, permeability or fluid mobility. These are properties that are extremely difficult to be estimated otherwise, especially at in-situ condition and in unconsolidated/loose, granular soils.

There are generally large uncertainties in the invasive field estimation approaches and in laboratory estimates on disturbed samples. The methodology proposed in this thesis offers a solution to this problem. Except in Chapter 8, the presented results are valid for unconsolidated granular earth materials like soils or sediments. However, the concept of subsurface characterization developed here is valid for deeper, consolidated formations as well, as evidenced in Chapter 8. Future development of this concept should consider extension from VSP to surface seismic data, full-waveform inversion of near-surface seismic data considering poroelasticity, further tests on stress-sensitivity of seismic dispersion and possible estimation of stress in the subsurface, (time-lapse) monitoring of dynamic properties using seismic dispersion, and suitable field-acquisition system for efficient and reliable seismic dispersion measurements.

Bibliography

Adam, L., Batzle, M., Lewallen, K.T., & van Wijk, K. 2009. Seismic wave attenuation in carbonates. *Journal of Geophysical Research*, **114**, B06208.

Aki, K., & Wu, R.-S. 1988. *Scattering and attenuation of seismic waves, Part I*. Basel: Springer Basel AG.

Archie, G.E. 1942. The electrical resistivity log as an aid in determining some reservoir characteristics. *Petroleum Transactions of AIME*, **146**, 54–62.

Arroyo, M., Ferreira, C., & Sukorlat, J. 2007. Dynamic measurements and porosity in saturated triaxial specimens. *Soil Mechanics and Its Applications*, **146**, 537–546.

Badiey, M., Cheng, A. H-D., & Mu, Y. 1998. From geology to geoacoustics - Evaluation of Biot-Stoll sound speed and attenuation for shallow water acoustics. *Journal of the Acoustical Society of America*, **103**(1), 309–320.

Badri, M., & Mooney, H.M. 1987. Q measurements from compressional seismic waves in unconsolidated sediments. *Geophysics*, **52**, 772–784.

Baron, L., & Holliger, K. 2011. Constraints on the permeability structure of alluvial aquifers from the poro-elastic inversion of multifrequency P-wave sonic velocity logs. *IEEE transactions on geoscience and remote sensing*, **49**, 1937–1948.

Batzle, M., & Wang, Z. 1992. Seismic properties of pore fluids. *Geophysics*, **57**, 1396–1408.

Batzle, M.L., Han, D., & Hofmann, R. 2006. Fluid mobility and frequency-dependent seismic velocity-Direct measurements. *Geophysics*, **71**, N1–N9.

Beebe, J.H. 1982. Shallow-water transmission loss prediction using the Biot sediment model. *Journal of the Acoustical Society of America*, **71**, 1417–1426.

Berry, P.L., & Reid, D. 1987. *Introduction to soil mechanics*. McGraw-Hill.

Berryman, J.G. 1992. Effective stress for transport properties of inhomogeneous porous rock. *Journal of Geophysical Research*, **97**, 17409–17424.

Berryman, J.G., Berge, P.A., & Bonner, B.P. 2002. Estimating rock porosity and fluid saturation using only seismic velocities. *Geophysics*, **67**(2), 391–404.

Biot, M.A. 1956a. Theory of propagation of elastic waves in a fluid-saturated porous solid. I. Lower frequency range. *Journal of the Acoustical Society of America*, **28**, 168–178.

Biot, M.A. 1956b. Theory of propagation of elastic waves in a fluid-saturated porous solid. II. Higher frequency range. *Journal of the Acoustical Society of America*, **28**, 179–191.

Biot, M.A. 1962. Mechanics of deformation and acoustic propagation in porous media. *Journal of Applied Physics*, **33**, 1482–1498.

Biot, M.A., & Willis, D.G. 1957. The elastic coefficients of the theory of consolidation. *Journal of Applied Mechanics*, **24**, 594–601.

Birchak, J.R., Gardner, L.G., Hipp, J. W., & Victor, J.M. 1974. High electric constant microwave probes for sensing soil moisture. *Proceedings of the IEEE*, **62**(1), 93–98.

Bourbie, T., Coussy, O., & Zinszner, B. 1987. *Acoustics of porous media*. Houston, TX: Gulf Publishing Co.

Bowles, F.A. 1997. Observations on attenuation and shear-wave velocity in fine-grained, marine sediments. *Journal of the Acoustical Society of America*, **101**(6), 3385–3397.

Bradford, J.H. 2007. Frequency-dependent attenuation analysis of ground-penetrating radar data. *Geophysics*, **72**(3), J7–J16.

Buchanan, J.L. 2006. A comparison of broadband models for sand sediments. *Journal of the Acoustical Society of America*, **120**, 3584–3598.

Buckingham, M.J. 1997. Theory of acoustic attenuation, dispersion, and pulse propagation in unconsolidated granular materials including marine sediments. *Journal of the Acoustical Society of America*, **102**, 2579–2596.

Buckingham, M.J. 1998. Theory of compressional and shear waves in fluidlike marine sediments. *Journal of the Acoustical Society of America*, **103**, 288–299.

Buckingham, M.J. 2000. Wave propagation, stress relaxation, and grain-to-grain shearing in saturated, unconsolidated marine sediments. *Journal of the Acoustical Society of America*, **108**, 2796–2815.

Buckingham, M.J. 2004. Compressional and shear wave properties of marines sediments: Comparisons between theory and data. *Journal of the Acoustical Society of America*, **117**, 137–152.

Budiansky, B., & O'Connell, R. J. 1976. Elastic moduli of a cracked solid. *International Journal of Solids and Structures*, **12**, 81–97.

Burns, D.R. 1990. Acoustic waveform logs and the in-situ measurement of permeability - a review. *Geophysical Applications for Geotechnical Investigations, ASTM, Philadelphia*, 65–78.

Carman, P.C. 1937. Fluid flow through granular beds. *Transactions of the Institution of Chemical Engineers*, **15**, 150–166.

Carothers, J.E. 1968. A statistical study of the formation factor relation to porosity. *The Log Analyst*, **9**(5), 13–20.

Chanzy, A., Tarussov, A., Judge, A., & Bonn, F. 1996. Soil water content determination using digital ground penetrating radar. *Soil Science Society of America Journal*, **60**, 1318–1326.

Chapman, M., Zatsepin, S. V., & Crampin, S. 2002. Derivation of a microstructural poroelastic model. *Geophysical Journal International*, **151**, 427–451.

Cheng, A. H.-D. 1997. Material coefficients of anisotropic poroelasticity. *International Journal of Rock Mechanics and Mining Sciences*, **34**, 199–205.

Chotiros, N.P., & Isakson, M.J. 2004. A broadband model of sandy ocean sediments: Biot-Stoll with contact squirt flow and shear drag. *Journal of the Acoustical Society of America*, **116**, 2011–2022.

Chotiros, N.P., & Isakson, M.J. 2008. High-frequency dispersion from viscous drag at the grain-grain contact in water-saturated sand. *Journal of the Acoustical Society of America*, **124**, EL296–EL301.

Collins, M.D., & Fishman, L. 1995. Efficient navigation of parameter landscapes. *Journal of Acoustical Society of America*, **98**, 1637–1644.

Collins, M.D., Kuperman, W.A., & Schmidt, H. 1992. Nonlinear inversion for ocean-bottom properties. *Journal of Acoustical Society of America*, **92**, 2770–2783.

Davis, J.L., & Annan, A.P. 1989. Ground penetrating radar for high resolution mapping of soil and rock stratigraphy. *Geophysical Prospecting*, **37**, 531–551.

De, G. S., Winterstein, D. F., & Meadows, M. A. 1994. Comparison of P- and S-wave velocities and Q's from VSP and sonic log data. *Geophysics*, **59**, 1512–1529.

De Barros, L., Dietrich, M., & Valette, B. 2010. Full waveform inversion of seismic waves reflected in a stratified porous medium. *Geophysical Journal International*, **182**, 1543–1556.

Deresiewicz, H., & Skalak, R. 1963. On uniqueness in dynamic poroelasticity. *Bulletin of the Seismological Society of America*, **53**, 783–788.

Deresiewicz, V.P. 1974. *Bodies in contact with applications of granular media*, In *Geo Herrmann, Mindlin R.D. and applied mechanics (ed.)*. New York: Pergamon.

Drnevich, V. P., & Richart, F. E. 1970. Dynamic restraining of dry sand. *Journal of the Soil Mechanics Foundation Division*, **96**, 453–469.

Dutta, N. C., & Ode, H. 1979a. Attenuation and dispersion of compressional waves in fluid-filled porous rocks with partial gas saturation (White model)-part II: Results. *Geophysics*, **44**, 789–805.

Dutta, N. C., & Ode, H. 1979b. Attenuation and dispersion of compressional waves in fluid-filled porous rocks with partial gas saturation (White model)-part I: Biot theory. *Geophysics*, **44**, 1777–1788.

Dvorkin, J., & Nur, A. 1993. Dynamic poroelasticity: A unified model with the squirt and the Biot mechanisms. *Geophysics*, **58**(4), 524–533.

Dvorkin, J., & Nur, A. 1998. Acoustic signatures of patchy saturation. *International Journal of Solids and Structures*, **35**, 4803–4810.

Dvorkin, J., Nolen-Hoeksema, R., & Nur, A. 1994. The squirt-flow mechanism: Macroscopic description. *Geophysics*, **59**, 428–438.

Dvorkin, J., Mavko, G., & Nur, A. 1995. Squirt flow in fully saturated rocks. *Geophysics*, **60**, 97–107.

El Hosri, M.S. 1984. Contribution a l'etude des proprietes macanique des materiaux. *These d'Etat, University of Paris VI, Paris, France (in French)*.

Eshelby, J.B. 1957. The determination of the elastic field of an ellipsoidal inclusion, and related problems. *Proceedings of the Royal Society of London A*, **241**, 376–396.

Frenkel, J. 1944. On the theory of seismic and seismoelectric phenomena in a moist soil. *Journal of Physics*, **3**(4), 230–241.

Ghose, R. 2002. High-frequency shear wave reflections from shallow subsoil layers using a vibrator source; sweep cross-correlation versus deconvolution with groundforce derivative. *Proceedings of the Society of Exploration Geophysicists*, 1408–1411.

Ghose, R. 2010a. *Estimating in-situ horizontal stress in soil using time-lapse VS measurements*, In *Advances in Near-Surface Seismology and Ground-Penetrating Radar*, Bradford, J.H. and Holliger, K. (eds.). Tulsa, OK: Society of Exploration Geophysicists.

Ghose, R. 2010b. Possibilities for multidisciplinary, integrated approaches in near-surface geophysics. *72nd EAGE Conference, WS 4*.

Ghose, R. 2012. A micro-electromechanical system digital 3-C array seismic cone penetrometer. *Geophysics*, **77**(3), WA99–WA107.

Ghose, R., & Goudswaard, J. 2004. Integrating S-wave seismic reflection data and cone-penetration-test data using a multiangle multiscale approach. *Geophysics*, **69**, 440–459.

Ghose, R., & Slob, E. 2006. Quantitative integration of seismic and GPR reflections to derive unique estimates for water saturation and porosity in subsoil. *Geophysical Research Letters*, **33**, L05404.

Ghose, R., Brower, J., & Nijhof, V. 1996. A portable S-wave vibrator for high-resolution imaging of the shallow subsurface. *Proceedings of the 59th European Association of Geoscientists and Engineers*.

Ghose, R., Nijhof, V., Brower, J., Matsubara, Y., Kaida, Y., & Takahashi, T. 1998. Shallow to very shallow, high-resolution reflection seismic using a portable vibrator system. *Geophysics*, **63**, 1295–1309.

Gurevich, B. 2004. A simple derivation of the effective stress coefficient for seismic velocities in porous rocks. *Geophysics*, **69**, 393–397.

Gurevich, B., & Schoenberg, M. 1999. Interface conditions for Biot's equations of poroelasticity. *Journal of the Acoustical Society of America*, **105**, 2585–2589.

Hamilton, E.L. 1980. Geoacoustic modeling of the sea floor. *Journal of the Acoustical Society of America*, **68**(5), 1313–1340.

Hardin, B.O., & Black, W.L. 1968. Vibration modulus of normally consolidated clay. *Journal of the Soil Mechanics Foundation Division*, **94**(2), 353–369.

Hardin, B.O., & Richart, F.E. 1963. Elastic wave velocities in granular soils. *Journal of the Soil Mechanics Foundation Division*, **89**, 33–65.

Holland, C.W., & Brunson, B.A. 1988. The Biot-Stoll sediment model: an experimental assessment. *Journal of the Acoustical Society of America*, **84**, 1437–1443.

Hovem, J.M., & Ingram, G.D. 1979. Viscous attenuation of sound in saturated sand. *Journal of the Acoustical Society of America*, **66**, 1807–1812.

Isakson, M.J., & Neilsen, T.B. 2006. The viability of reflection loss measurement inversion to predict broadband acoustic behavior. *Journal of Acoustical Society of America*, **120**, 135–144.

Jamiolkowski, M., & Lo Presti, D.C.F. 1994. Validity of in situ tests related to real behaviour. *Proceedings of the 13th International Conference on Soil Mechanics and Foundation Engineering*, **5**, 51–55.

Jeng, Y., Tsai, J., & Chen, S. 1999. An improved method of determining near-surface Q. *Geophysics*, **64**, 1608–1617.

Johnson, D. L. 2001. Theory of frequency dependent acoustics in patchy saturated porous media. *Journal of the Acoustical Society of America*, **110**, 682–694.

Johnson, D.L., Koplik, J., & Dashen, R. 1987. Theory of dynamic permeability and tortuosity in fluid-saturated porous media. *Journal of Fluid Mechanics*, **176**, 379–402.

Jongmans, D. 1990. In-situ attenuation measurements in soils. *Engineering Geology*, **29**, 99–118.

Kimura, M. 2007. Study on the Biot-Stoll model for porous marine sediments. *Acoustical Science and Technology*, **28**, 230–243.

Kirkpatrick, S., Gellatt, C.D., & Vecchi, M.P. 1983. Optimization by simulated annealing inversion. *Science*, **220**, 671–680.

Kozeny, J. 1927. Ueber Kapillare Leitung des Wassers im Boden. *Stizungsber. Akad. Wiss. Wien*, **136**, 271–306.

Kudo, K., & Shima, E. 1970. Attenuation of shear waves in soil. *Bulletin of the Earthquake Research Institute*, **48**, 145–158.

Lade, P.V., & Nelson, R.B. 1987. Modeling of elastic behavior of granular materials. *International Journal for Numerical and Analytical Methods in Geomechanics*, **11**(5), 521–542.

Landau, L.D., & Lifshitz, E.M. 1970. *The course of theoretical physics. The theory of elasticity*. second edn. Vol. 7. Pergamon Press, Oxford.

Landau, L.D., & Lifshitz, E.M. 1976. *The course of theoretical physics. Mechanics*. third edn. Vol. 1. Pergamon Press, Oxford.

Landau, L.D., & Lifshitz, E.M. 1980. *The course of theoretical physics. Statistical physics, part 1*. third edn. Vol. 5. Pergamon Press, Oxford.

Landau, L.D., & Lifshitz, E.M. 1987. *The course of theoretical physics. Fluid mechanics*. second edn. Vol. 6. Pergamon Press, Oxford.

Leurer, K. C. 1997. Attenuation in fine-grained marine sediments: Extension of the Biot-Stoll model by the effective grain model. *Geophysics*, **62**, 1465–1479.

Lin, L., Peterson, M.L., Greenberg, A.R., & McCool, B.A. 2009. In situ measurement of permeability. *Journal of the Acoustical Society of America*, **125**(4), EL123–EL128.

Marketos, G., & Best, A.I. 2010. Application of the BISQ model to clay squirt flow in reservoir sandstones. *Journal of Geophysical Research*, **115**, B06209.

Mavko, G., & Nur, A. 1975. Melt squirt in asthenosphere. *Journal of Geophysical Research*, **80**, 1444–1448.

Mavko, G., Mukerji, T., & Dvorkin, J. 2009. *The Rock Physics Handbook*. second edn. Cambridge University Press.

Metropolis, E.T., Rosenbluth, A.W., Rosenbluth, M.N., & Teller, A.H. 1953. Equation of state calculations by fast computing machines. *Journal of Chemical Physics*, **21**, 1087–1092.

Michaels, P. 1998. In-situ determination of soil stiffness and damping. *Journal of Geotechnical and Geoenvironmental Engineering, ASCE*, **124**, 709–719.

Mindlin, R. D. 1949. Compliance of elastic bodies in contact. *Journal of Applied Mechanics*, **16**, 259–268.

Molyneux, J.B., & Schmitt, D.R. 2000. Compressional-wave velocities in attenuating media: A laboratory physical model study. *Geophysics*, **65**, 1162–1167.

Muller, T.M., & Gurevich, B. 2005. Wave-induced fluid flow in random porous media: Attenuation and dispersion of elastic waves. *Journal of Acoustical Society of America*, **117**, 2732–2741.

Nakashima, Y., Zhou, H., & Sato, M. 2001. Estimation of groundwater level by GPR in an area with multiple ambiguous reflections. *Journal of Applied Geophysics*, **47**, 241–249.

Nur, A. 1971. Effects of stress on velocity anisotropy in rocks with cracks. *Journal of Geophysical Research*, **76**, 2022–2034.

O'Doherty, R.F., & Anstey, N.A. 1971. Reflections on amplitudes. *Geophysical Prospecting*, **19**, 430–458.

Payne, S. S., Worthington, M. H., Odling, N. E., & West, L. J. 2007. Estimating permeability from field measurements of seismic attenuation in fractured chalk. *Geophysical Prospecting*, **55**, 643–653.

Pride, S.R., & Berryman, J.G. 2003a. Linear dynamics of double-porosity dual-permeability materials I. Governing equations and acoustic attenuation. *Physical Review E*, **68**, 036603.

Pride, S.R., & Berryman, J.G. 2003b. Linear dynamics of double-porosity dual-permeability materials II. Fluid transport equations. *Physical Review E*, **68**, 036604.

Pride, S.R., Harris, J.M., Johnson, D.L., Mateeva, A., Nihei, K.T., Nowack, R.L., Rector, J.W., Spetzler, H., Wu, R., Yamamoto, T., Berryman, J.G., & Fehler, M. 2003. Permeability dependence of seismic amplitudes. *The Leading Edge*, **22**(6), 518–525.

Pride, S.R., Berryman, J.G., & Harris, J.M. 2004. Seismic attenuation due to wave-induced flow. *Journal of Geophysical Research*, **109**, B01201.

Quan, Y., & Harris, J. M. 1997. Seismic attenuation tomography using the frequency shift method. *Geophysics*, **62**, 895–905.

Ransom, R.C. 1984. A contribution towards a better understanding of the modified Archie formation resistivity factor relationship. *The Log Analyst*, **25**(2), 7–15.

Rust, C.F. 1952. Electrical resistivity measurements on reservoir rock samples by the two-electrode and 4-electrode methods. *Transactions AZME*, **195**, 217–224.

Sams, M. S., Neep, J. P., Worthington, M. H., & King, M. H. 1997. The measurement of velocity dispersion and frequency-dependent intrinsic attenuation in sedimentary rocks. *Geophysics*, **62**, 1456–1464.

Schoenberger, M., & Levin, F.K. 1974. Apparent attenuation due to intrabed multiples. *Geophysics*, **18**, 10–40.

Schulz, H.G., & Zabel, M. 2006. *Marine Geochemistry*. 2nd edition edn. Springer.

Sharma, M.M., Garrouch, A., & Dunlap, H.F. 1991. Effects of wettability, pore geometry, and stress on electrical conduction in fluid-saturated rocks. *The Log Analyst*, **32**, 511–526.

Sivukhin, D.V. 2005. *The course of general physics. Mechanics*. Vol. 1. Fizmatlit/MFTI (in Russian).

Smeulders, D.M.J., & van Dongen, M.E.H. 1997. Wave propagation in porous media containing a dilute gas-liquid mixture: Theory and experiments. *Journal of Fluid Mechanics*, **343**, 351–373.

Stokoe, K. H., H., Lee S., & Knox, D. P. 1985. *Shear moduli measurements under true triaxial stresses*, In *Advances in the art of testing soils under cyclic conditions*, Khosla, V. (ed.). New York: ASCE.

Stoll, R.D. 1974. *Acoustic waves in saturated sediments*, In *Physics of Sound in marine sediments*, Hamilton L. (ed.). New York: Plenum.

Stoll, R.D. 1977. Acoustic waves in ocean sediments. *Geophysics*, **42**, 715–725.

Stoll, R.D. 1986. *Acoustic waves in marine sediments*, In *Ocean seismo-acoustics*, Akal T. & Berkson M. (eds.). New York: Plenum.

Stoll, R.D. 1989. *Sediment acoustics*. Lecture Notes in Earth Sciences, Springer-Verlag.

Stoll, R.D. 2002. Velocity dispersion in water-saturated granular sediment. *Journal of the Acoustical Society of America*, **111**(2), 785–793.

Stoll, R.D., & Bryan, G.M. 1970. Wave attenuation in saturated sediments. *Journal of the Acoustical Society of America*, **47**, 1440–1447.

Tonn, R. 1991. The determination of the seismic quality factor Q from VSP data: A comparison of different computational methods. *Geophysical Prospecting*, **39**, 1–27.

van Dalen, K.N., Ghose, R., Drikkoningen, G.G., & Smeulders, D.M. 2010. In-situ permeability estimation from integrated poroelastic reflection coefficients. *Geophysical Research Letters*, **37**, L12303.

Vellidis, G., Smith, M.C., Thomas, D.L., & Asmussen, L.E. 1990. Detecting wetting front movement in a sandy soil with ground penetrating radar. *Transactions of ASAE*, **33**, 1867–1874.

Vogelaar, B.B.S.A. 2009. Fluid effect on wave propagation in heterogeneous porous media. *PhD thesis. Delft University of Technology*.

Wang, J.R., & Schmugge, T.J. 1980. An empirical model for the complex dielectric permittivity of soils as a function of water content. *IEEE Transactions on Geoscience and Remote Sensing*, **18**, 288–295.

Wapenaar, C.P.A., Draganov, D., & Thorbecke, J. 2003. Relations between codas in reflection and transmission data and their applications in seismic imaging. *6th SEGJ International Symposium on Imaging Technology, Tokyo, Japan*.

Wapenaar, K., Thorbecke, J., & Draganov, D. 2004. Relations between reflection and transmission responses of three-dimensional inhomogeneous media. *Geophysical Journal International*, **156**, 179–194.

White, J. E. 1975. Computed seismic speeds and attenuation in rocks with partial gas saturation. *Geophysics*, **40**, 224–232.

White, R.E. 1992. The accuracy of estimating Q from seismic data. *Geophysics*, **57**, 1508–1511.

Winkler, K., Nur, A., & Gladwin, M. 1979. Friction and seismic attenuation in rocks. *Nature*, **277**, 528–531.

Yamamoto, T. 2003. Imaging permeability structure within the highly permeable carbonate earth: Inverse theory and experiment. *Geophysics*, **68**, 1189–1201.

Yamamoto, T., & Turgut, A. 1988. Acoustic wave propagation through porous media with arbitrary pore size distributions. *Journal of the Acoustical Society of America*, **83**, 1744–1751.

Yokota, K., & Konno, M. 1980. Dynamic Poisson's ratio of soil. *Proceedings of 7th World Conference on Earthquake Engineering, Istanbul, Turkey*, **3**, 475–478.

Yu, S., & Dakoulas, P. 1993. General stress-dependent elastic moduli for cross-anisotropic soils. *Journal of Geotechnical Engineering*, **119**(10), 1568–1586.

Zhubayev, A., & Ghose, R. 2012a. Contrasting behavior between dispersive seismic velocity and attenuation: Advantages in subsoil characterization. *Journal of the Acoustical Society of America*, **131**, EL170–EL176.

Zhubayev, A., & Ghose, R. 2012b. Physics of shear-wave intrinsic dispersion and estimation of in situ soil properties: A synthetic VSP appraisal. *Near Surface Geophysics*, **10**, 613–629.

Zimmerman, R.W. 1989. *Compressibility of sandstones*. Elsevier, New York.

Summary

Soil properties from seismic intrinsic dispersion

Theoretical and experimental studies in the past have shown the sensitivity of seismic waves to soil/rock properties, such as composition, porosity, pore fluid, and permeability. However, quantitative characterization of these properties has remained challenging. In case of unconsolidated soils, the inherently loose and heterogeneous nature complicates the task of obtaining the *in situ* properties and spatial variations. In this thesis, we investigate the possibility of exploiting the information of seismic intrinsic dispersion in the low frequency band (10–200 Hz), which is relevant to onshore field data, in order to quantify these physical properties, with special focus on soil porosity and permeability. *In situ* values of these properties are crucial in many different projects.

We first investigate the frequency-dependent seismic velocity and attenuation caused by inelastic losses at grain contacts and wave-induced fluid flow at different scales (from grain size to seismic wavelength), using the theory of poroelasticity first proposed by Biot and many subsequent extensions and modifications. Several pertinent models of poroelasticity are looked at in order to find out their applicability in explaining the observed seismic dispersion. The observed dispersion can vary greatly between various unconsolidated, fully-saturated soils. Further, we develop a stress-dependent Biot (SDB) model in order to study the behaviour of seismic waves propagating through a fully-saturated porous medium subjected to different stress conditions. This is achieved by combining the mechanics of granular soils with the effective-stress laws, finally coupling with Biot's theory.

Careful analyses of the underlying soil/rock physics that relate geophysical observations to the physical properties reveal an interesting feature in the property domain among several different measurements. This is an extention to some recent work done by others. We have found that it is possible to find two or more measured quantities, showing contrasting (sometimes quasi-orthogonal) behaviour in the common parameter space, such that a combination of those measured quantities leads to a physics-based uniqueness in the property estimation. This quasi-orthogonality in the common property domain among different measured quantities is advantageously used for estimation of porosity, permeability, water saturation, and effective stress. Several numerical examples are presented where P - and S -wave velocity and attenuation are efficiently integrated in order to obtain soil properties. In addition

to seismic waves, electromagnetic waves are briefly considered for extracting extra soil properties.

In this research, considerable attention has been paid to the investigation of S waves travelling through a porous medium, since S waves have well-known significance in the context of shallow subsurface characterization. Twelve selected datasets of frequency-dependent S -wave velocity and attenuation from various soft-soil sites are used in this study. Data for fully-saturated, unconsolidated soils from land/onshore environment are only considered. It is found that the behaviour of seismic intrinsic dispersion can vary greatly with the soil-type.

One of the main challenges in property estimation using intrinsic dispersion relates to reliable extraction of the information of intrinsic dispersion from the recorded seismic data. The difficulty lies in the quantification of scattering attenuation, the effect of which is always present in the recorded seismograms due to the wavelength-scale and smaller heterogeneities in the subsurface. Scattering has an absorption-like effect on the transmitted seismic energy. Accordingly, determining and subtracting the scattering attenuation from the total (or apparent) attenuation is critically important. We have discussed and successfully tested an approach, achieving this goal.

Several shallow vertical seismic profiling (VSP) measurements are conducted in the field using a recently developed digital, array-seismic cone penetrometer (CPT) system. CPT provides information on cone-tip resistance, sleeve friction, and pore pressure, thus offering direct, additional knowledge on geological layering, that is used to calculate the scattering attenuation.

To obtain the soil properties, an inversion algorithm is presented based on simulated annealing and the poroelasticity theory. We study the sensitivity of different parameters involved in the cost function to be minimized. The most and the least sensitive parameters are discriminated based on the eigenanalyses of the covariance matrix of the gradient of the cost function. The eigenvectors and the corresponding eigenvalues of the covariance matrix are used to navigate efficiently the search algorithm in the multidimensional space and find a relatively stable, global solution of the cost function.

Finally, we apply the methodology developed in this research to a VSP dataset acquired in a layered sequence of siltstone, shale and sandstone. The porous sandstone contains hydrocarbon accumulations. The influence of fluid mobility (permeability-to-viscosity ratio) on the estimated P -wave intrinsic dispersion is distinctly observed. Using optimization by simulated annealing together with VSP and well-log measurements, the Biot and squirt flow (BISQ) model is found to provide one possible mechanism for the observed dispersion. The layer-specific fluid mobility values are estimated using our approach; they are found to be close to the independent measurements of mobility using Stoneley waves and from dynamic formation-tests carried out at the same borehole. The depth distribution of fluid mobility matches well between our estimate and the independent measurements.

The methodology developed and the results obtained in this research pave the way to a new direction for in situ, quantitative soil/rock characterization using seismic waves.

Samenvatting

Grondeigenschappen uit intrinsieke seismische dispersie

Theoretische en experimentele studies in het verleden hebben de gevoelighed van seismische golven aangetoond voor grond- en gesteente-eigenschappen, zoals samenstelling, porositeit, porievloeistof en permeabiliteit. De kwantitatieve karakterisatie van deze eigenschappen is echter nog steeds een uitdaging. In het geval van ongeconsolideerde grond bemoeilijken het inherente gebrek aan samenhang en de heterogene aard het verkrijgen van de *in situ* eigenschappen en de ruimtelijke variaties. In dit proefschrift onderzoeken we de mogelijkheid van het benutten van informatie uit intrinsieke seismische dispersie in de laagfrequente band (20–200 Hz), die relevant is bij veld data van het vaste land, om deze fysische eigenschappen te kwantificeren, met speciale aandacht voor grondporositeit en-permeabiliteit. *In situ* waarden van deze eigenschappen zijn cruciaal bij veel verschillende projecten.

Allereerst onderzoeken we de frequentie-afhankelijke seismische snelheid en demping veroorzaakt door inelastisch verlies aan de korrelkontakten en door golven veroorzaakte vloeistofstroming op verschillende schalen (van korrelgrootte tot seismische golflengten), gebruikmakend van de poro-elastische theorie van Biot en vele daaropvolgende aanpassingen en uitbreidingen. Verscheidene relevante modellen van poro-elasticiteit worden bekeken om te bepalen welke van toepassing kunnen zijn om de waargenomen seismische dispersie te verklaren. De waargenomen dispersie kan sterk variëren tussen verscheidene ongeconsolideerde, volledig verzadigde grondsoorten. Verder hebben we een spanningsafhankelijk Biot (stress-dependent Biot, SDB) model ontwikkeld om het gedrag te bestuderen van seismische golven die zich voortplanten door een volledig verzadigd poreus medium, onderworpen aan verschillende spanningstoestanden. Dit is bereikt door een combinatie van grondmechanica met “effectieve-stress” wetten en deze uiteindelijk te koppelen aan de Biot-theorie.

Zorgvuldige analyse van de principes van de grond- en gesteentefysica die geofysische waarnemingen verbinden met fysische eigenschappen openbaart bij verschillende metingen een interessant kenmerk binnen het domein van eigenschappen. Dit bouwt voort op recent werk van anderen. We hebben gevonden dat het mogelijk is om twee of meer gemeten grootheden die contrasterend (soms quasi-orthogonaal) gedrag vertonen in de algemene parameterruimte zodanig te combineren dat die gemeten grootheden leiden tot een op fysica gebaseerde uniciteit in de bepaling van de

eigenschappen. Deze quasi-orthogonaliteit in het domein van algemene eigenschappen tussen gemeten grootheden is nuttig voor de bepaling van porositeit, permeabiliteit, watersaturatie en effectieve spanning. Verschillende numerieke voorbeelden worden gepresenteerd waarin P - en S -golf snelheid en demping efficient worden geïntegreerd om grondeigenschappen te bepalen. Om extra grondeigenschappen te bepalen wordt, naast seismische golven, ook beknopt gekeken naar elektromagnetische golven.

In dit onderzoek is veel aandacht besteed aan zich in een poreus medium voortplantende S -golven, daar het bekend is dat S -golven van belang zijn bij de karakterisatie van de ondiepe ondergrond. Twaalf geselecteerde data-sets van frequentie-afhankelijke S -golf snelheid en demping, van verscheidene locaties, worden in deze studie gebruikt. Alleen data uit volledig verzadigde, ongeconsolideerde grond, wordt beschouwd. Er wordt vastgesteld dat het gedrag van intrinsieke seismische dispersie sterk kan variëren afhankelijk van de grondsoort.

Eén van de uitdagingen in de eigenschap-bepaling met behulp van intrinsieke dispersie heeft te maken met het op een betrouwbare manier verkrijgen van de dispersie-informatie uit de opgenomen seismische gegevens. De moeilijkheid zit in de kwantificering van de demping veroorzaakt door verstrooiing, die altijd aanwezig is in de opgenomen seismogrammen als gevolg van de golflengte-schaal en kleine heterogeniteiten in de ondergrond. Deze verstrooiing heeft een absorptie-achtig effect op de propagerende seismische energie. Een goede bepaling op zich en het aftrekken van de demping ten gevolge van verstrooiing van de totale demping is van groot belang. Een aanpak om dit doel te bereiken is behandeld en succesvol getest.

Verschidene ondiepe “vertical seismic profiling” (VSP) metingen zijn in het veld uitgevoerd met behulp van een recentelijk ontwikkeld digitaal sondeerinstrument voorzien van een aantal seismische opnemers op rij (array-seismic cone penetrometer, CPT). Dit instrument geeft informatie over de conusweerstand, de kleefmantelwrijving en de poriedruk. Op deze manier wordt direct extra informatie verkregen over de geologische gelaagdheid die gebruikt wordt om de demping door verstrooiing te berekenen.

Om de eigenschappen van de grond te bepalen wordt een inversie algoritme gepresenteerd dat gebaseerd is op een stochastische optimalisatie procedure (simulated annealing) en poro-elastische theorie. We onderzoeken de gevoeligheid van verschillende parameters in de te minimaliseren kostfunctie. De meest en de minst gevoelige parameters worden onderscheiden op basis van de eigenanalyse van de covariantiematrix van de gradiënt van de kostfunctie. De eigenvectoren en de corresponderende eigenwaarden van de covariantiematrix worden gebruikt om het algoritme effectief te navigeren binnen de multidimensionale ruimte om een relatief stabiele, algemene oplossing van de kostfunctie te vinden.

Tenslotte passen we de in dit onderzoek ontwikkelde methodologie toe op een VSP dataset verkregen in een gelaagde structuur van siltsteen, schalie en zandsteen. De poreuze zandsteen bevat ophopingen van koolwaterstoffen. De invloed van vloeistofmobiliteit (permeabiliteit-viscositeitsverhouding) op de geschatte intrinsieke dispersie van de P -golf wordt duidelijk waargenomen. Door optimalisatie met ‘simulated annealing’, samen met VSP en boorgat metingen geeft het ‘Biot en squirt-

flow' model (BISQ) een mogelijk mechanisme voor de waargenomen dispersie. De waarden van de laag-specifieke vloeistofmobiliteit worden geschat, gebruikmakend van onze aanpak; ze benaderen onafhankelijke mobiliteitsmetingen verkregen met behulp van Stoneley golven en uit dynamische formatietesten in hetzelfde boorgat. Onze schatting van de verdeling van vloeistofmobiliteit over de diepte komt goed overeen met onafhankelijke metingen.

De ontwikkelde methodologie en de verkregen resultaten in dit onderzoek effenen de weg naar een nieuwe richting in in situ, kwantitatieve grond- en gesteentekarakterisatie, gebruik makend van seismische golven.

Acknowledgments

First of all, I would like to thank my supervisor, Ranajit Ghose, who determined to a large extent the direction of the research presented in this thesis. His constant support and enthusiasm, as well as given freedom, made my study at TU Delft enjoyable. Many hours of discussions on different aspects of this research have largely shaped me as a scientist and have influenced my development.

I am grateful to my promotor Kees Wapenaar for his constant support throughout my years in Delft. This thesis has benefited a lot from his critical comments and suggestions. His keen eye for weak points in the work and an impressive arsenal of mathematical skills can only be admired. Despite being famous, he is always open and warm towards his students and I was lucky to be one of them.

This PhD project is supported by Deltares and the Delft Earth research programme of the Delft University of Technology for which I am very grateful. Especially, I am thankful to Jurjen van Deen (Deltares), Rogier Westerhoff (Deltares), Pauline Kruiver (Deltares), Dominique Ngan-Tillard (TU Delft) and Michael Hicks (TU Delft) for participating at users committee meetings and for many useful comments and suggestions that have improved this thesis. I would also like to acknowledge the members of my PhD committee for their questions and comments.

My special thanks go to David Smeulders, who has solidified my understanding of the physics of poroelasticity. Discussions with David helped me to see physics from a new perspective.

I would like to thank Igor Borodin and Francois Daube from Schlumberger, who made my research internship possible at WesternGeco Houston Technology Center. There, I had a great opportunity to work with seismic field data and test some of the methods developed in this thesis. Some of our results were incorporated in this thesis. I thank China National Offshore Oil Corporation (CNOOC) Ltd., especially Yang Jihai and Cai Jun for permission to publish their data in chapter 8. My special thanks go to Henry Menkiti for his enthusiasm and support during my stay at Schlumberger. It was a pleasure to collaborate with Takashi Mizuno and Kui (Karl) Lin from Schlumberger.

I would like to thank Nico Koster and Eric Landskroon from A.P. van den Berg for the design and manufacturing of the 3C array-SCPT system that we used to acquire the seismic data in chapter 7.

During my years at TU Delft, I had the great opportunity to work with Karel Heller. His outstanding experimental skills and a remarkable physical intuition have always been inspiring. Our endless discussions about history of famous physicists

and their discoveries were especially interesting. I learnt a lot from Karel. Of course, I would like to thank him for the translation of the summary and propositions into Dutch. Many people helped me a lot during my frequent visits to the laboratory. I am deeply indebted to Alber, Arno, Dirk, Ellen, Han, Jan, Jolanda, Marc and Wim. Thank you all for the great coffee breaks and cakes.

I am especially thankful to Auke Barnhoorn for giving me a great opportunity to continue developing my skills and understanding in rock physics and certainly for being exposed to geology. I shall never forget our geological trip to Whitby!

My study at TU Delft would not have been possible without Oleg Zhuravlev, who brought the university to my attention, while I was working on my MSc project in Schlumberger Moscow Research. I would like to thank Dima Chuprakov from Schlumberger-Doll Research for his help, support, and kind heart.

Deyan Draganov and Karel van Dalen have played a special role in my development. Their tremendous love of science always reminds me why I love and do my research.

I would like to thank Asha, Hannie, Lydia, Margot, Marlijn, Marijke, Ralf and all other staff members for making the department feel like home. Thanks to our academic staff, Evert Slob, Guy Drijkonigen, and Wim Mulder. I am extremely grateful to my officemates—Adrian, Ali, Amerjeet, Amin, Andrea, Andreas, Araz, Bobby, Boris, Carlos, Christiaan, Chunfang, Claudio, Daria, Elham, Geertje, Guus, Huajun, Ilja, Iris, Laura, Leon, Liang, Jan, Jiaguang, Joost, Marwan, Max, Menne, Menno, Michel, Mohammad, Mohsen, Narjes, Niels, Nihed, Nikita, Panos, Pawan, Ralph, Rik, Saskia, Shohei, Simone, Thomas, Tomohide, Tristan, Wiebke, Wieske, Yohei—who made the atmosphere in our office enjoyable, positive and productive. Every coffee break with you was like a charging time with energy and getting new ideas. I would like to thank Jürg and Elmer for their endless help in Matlab, Latex and Illustrator. This thesis definitely benefited a lot from their help. I thank Asiya for always keeping me informed with the latest publications, upcoming workshops and conferences on poroelasticity. My special thanks go to Alex Kirichek with whom these years at Delft became much different. His thorough knowledge of history, broad thinking and sense of humour made my last three years unforgettable. Talking to Alex is always easy and enjoyable.

Physics lectures by Gimalin Doskeyev were very special to me during my high school study. His strong logic, love of physics, exceptional clarity of thinking, and the ability of explaining difficult physical phenomena in a simple way made me love this subject. No less important role in my life played Onlasyn Imambekov, who has been training young Kazakh physicist for several decades. On behalf of all of your students, I would like to thank for the energy and love you are sharing with us.

I thank my dear friends, Arman B., Aidos, Anuar B., Boris, Deniska, Danik, Eldar, Lesha, Misha, Maksat, Nurlybek, Nurzhan, Rafael and Saken for being always like a family to me. Eldarchik advices were very useful on some of my scripts developed in this work. Almushka, Amina, Bunya, Dinka, Irisha and Sholpan, thank you all for taking care of my friends. I would like to thank my “Dutch” friends, Medet, Altynbek, Amirkin, Anuar A., Arman A., Berik, Nurlan, Olzhas, and Zharas, who made our stay in the Netherlands enjoyable and rewarding.

My family is always in my heart. I am grateful to my grandfather Saki for getting me interested in mathematics in childhood. I am especially thankful to my parents-in-law Akbaken and Gulaim for their support and efforts which made every visit to my hometown Aktobe unforgettable. I would also like to express my sincere thanks to my tetya Gulya for being like a mother to me. My uncles—Kadirzhan, Akimzhan and Azad—are especially acknowledged. Thanks to Dostan for taking care of my sister Ainur and my little niece Araileka. Thanks to my little sisters-in-law and brother Bakyt, Kuralai and Sadyk. I am thankful to Bakusya and Kura for always finding some time to take care of my little kids Sarbinaz and Ansar, while I was working on my PhD in one of the library of Aktobe.

This thesis would not have been possible without my parents Sabyrzhan and Zhanar, and my sister Ainur. Your love, care and support always keep me up. You are always in my mind.

My wife Raushan is my main source of motivation. Thank you for your love, care, patience and the most beautiful smile in the world. And of course, thank you for taking care of our little kids Sarbinoka and Anseka. You are the meaning of my life. I love you all!

This thesis is dedicated to my friend, brother, Adilet Imambekov, who made a tremendous contribution to science, physical society and my development. He will always be a role model for me. I will miss you deeply.

Alimzhan Zhubayev
Delft, April, 2014

Curriculum Vitae

Personal information

Name Alimzhan Sabyrzhanovich Zhubayev
Date of birth 5th of February 1986
Place of birth Aktobe, Kazakhstan
Civil state Married

Education and work

Since June 2014 Geophysicist, NAM–Royal Dutch Shell
Assen, the Netherlands

2013–2014 Postdoctoral researcher, Applied Geophysics and Petrophysics
Delft University of Technology, Delft, the Netherlands

2008–2013 PhD in Applied Physics
Delft University of Technology, Delft, the Netherlands

2012 (Summer) Research intern, WesternGeco, Houston Technology Center
Schlumberger, Houston, USA

2006–2008 Research associate
Schlumberger Moscow Research, Moscow, Russia

2006–2008 MSc in Physics and Applied Mathematics
Moscow Institute of Physics and Technology, Moscow, Russia

2002–2006 BSc in Physics and Applied Mathematics
Moscow Institute of Physics and Technology, Moscow, Russia

1992–2002 High school #6 named after G. Aktayev
Aktobe, Kazakhstan

Journal papers

- Zhubayev A., Ghose R., Borodin I. and Menkiti H., 2014, Seismic signatures of fluid mobility: Field observation. *Journal of Geophysical Research*, (under review).
- Zhubayev A. and Ghose R., 2012, Contrasting behavior between dispersive seismic velocity and attenuation: Advantages in subsoil characterization. *Journal of the Acoustical Society of America*, 131(2), EL170-EL176.
- Zhubayev A. and Ghose R., 2012, Physics of *S*-wave intrinsic dispersion and estimation of in-situ soil properties: A synthetic VSP appraisal. *Near Surface Geophysics*, 10, 613-629.
- Chuprakov D.A. and Zhubayev A.S., 2010, A variational approach to analyze a natural fault with hydraulic fracture based on the strain energy density criterion. *Theoretical and Applied Fracture Mechanics*, 53, 221-232.

Conference abstracts

- Zhubayev A., Houben M., Smeulders D., and Barnhoorn A., 2014, Geomechanical and anisotropic acoustic properties of Lower Jurassic Posidonia shales from Whitby (UK), *Geophysical Research Abstracts*, EGU2014-11246, Vienna, Austria.
- Zhubayev A., Jihai Y., Jun C., Borodin I., Sanders M., Lim T.K., Menkiti H., and Ghose R. , 2013, Fluid mobility in reservoir rocks from integrated VSP and openhole data, 83rd annual SEG meeting, Houston, USA.
- Zhubayev A. and Ghose R., 2012, Flow properties in saturated soils from dispersive seismic velocity and attenuation: Test on field data, 74th annual EAGE meeting, Copenhagen, Denmark.
- Ghose R. and Zhubayev A., 2012, Flow Properties in saturated soils from differing behaviour of dispersive seismic velocity and attenuation, 74th annual EAGE meeting, Copenhagen, Denmark.
- Zhubayev A. and Ghose R., 2011, Physics-based integration of shear wave dispersion properties for soil property estimation: Laboratory investigation, 81st annual SEG meeting, San Antonio, USA.
- Ghose R. and Zhubayev A., 2011, Stress-dependent seismic dispersion in fluid-saturated granular media, 81st annual SEG meeting, San Antonio, USA.
- Zhubayev A. and Ghose R., 2011, Simultaneous estimates of in-situ porosity and permeability in the near-surface soil from seismic dispersion at the low frequencies, SAGEEP, South Carolina, USA.
- Ghose R. and Zhubayev A., 2011, Extension of the poroelasticity theory to address in-situ stress in shallow subsoil, SAGEEP, South Carolina, USA.

- Zhubayev A. and Ghose R., 2010, In-situ soil properties from integrated poro-elastic models, 80th annual SEG meeting, Denver, USA.
- Zhubayev A. and Ghose R., 2010, In-situ porosity and permeability estimation from the VSP data using integrated poroelastic model, 72nd annual EAGE meeting, Barcelona, Spain.
- Zhubayev A. and Ghose R., 2010, In-situ soil properties from the integrated poroelastic model, 72nd annual EAGE meeting, ws04, Barcelona, Spain.
- Zhubayev A. and Ghose R., 2010, Physics-based integration of poroelastic wave propagation properties to derive near-surface soil properties, FSST (Frontiers in Shallow Subsurface Technology), Delft, The Netherlands.